

# Electric-pump Rocket Engines

Comparative analysis of the electric-pump cycle  
using Rocket Cycle Analysis Tool (RoCAT)

R.J.F. van den Berg



# Electric-pump Rocket Engines

Comparative analysis of the electric-pump  
cycle using Rocket Cycle Analysis Tool  
(RoCAT)

by

R.J.F. van den Berg

to obtain the degree of Master of Science  
at the Delft University of Technology,

Student number:	4268997		
Date:	Tuesday 29 <sup>th</sup> of August, 2023		
Thesis committee:	Ir. B.T.C. Zandbergen	TU Delft	Thesis supervisor
	Prof. Dr. E.K.A. Gill	TU Delft	Committee Chair
	Dr. A. Cervone	TU Delft	Examiner



# Preface

First, I would like to thank my parents, Jos van den Berg and Ilona van Beers, who have always inspired me in my studies. They have been a great support during the highs and lows of this research and continuously stood at the ready to encourage me and facilitate a perfect place to study whenever required.

I also would like to thank my supervisor, ir. Barry Zandbergen, for his help and guidance. Our meetings always left me enthused about rocket engines and full of new ideas.

Furthermore, I'd like to thank the people who helped me gain new insights and tackle issues with both the code and report: Sparsh Garg, Ruwan Ernst, and Bart van Zegbroeck.

Lastly, I want to thank my friends, Eric de Gruyter, Jan Scheurer, and Joost Zwart, for patiently listening to my monologues about rocket engines and, as peers, providing companionship while writing this report.

*R.J.F van den Berg*  
*Delft, Tuesday 29<sup>th</sup> August, 2023*

*Cover Image: Launch of an Electron rocket powered by 9 Rutherford engines for the mission "As The Crow Flies".  
Credit: Andrew Burns & Simon Moffatt*



# Executive Summary

The electric-pump cycle is a configuration in which an electric motor powers the pumps in a rocket engine instead of a turbine found in conventional engine configurations. This has several advantages among which are simpler design, cheaper development, no need for intricate pump seals, and easy restartability. These advantages come at the cost of performance, as identified by previous research. However, detailed analysis of the electric-pump cycle's performance has mainly compared this cycle with the gas generator cycle and only for equal inputs, while individual cycles might have different optimal inputs. Furthermore, the main technologies used in the electric-pump cycle, i.e. electric motors and batteries, have been improving in the past decades and this improvement is even accelerating with the advent of the electric car. Therefore, this research set out to define the current performance of the electric-pump cycle in the context of conventional cycles and predict the performance it will have in the future.

To this end a modular rocket cycle analysis tool, called RoCAT, has been built, which combines ideal rocket theory and previous research to analyze the electric-pump, gas generator, and open expander cycle in a broad design space for several propellants and configurations. It was verified and validated by comparing it to engine designs, engine simulations, and existing engines. The performance of all cycles was found to be modeled quite accurately with room for improvement in the modeling of pressure drops and heat transfer. The mass model was found to severely underestimate the engine dry mass, which makes the mass modeling of RoCAT unsuited for calculating absolute values, but this inaccuracy was accepted for this research as it is only needed for comparative purposes.

Following this determination for accuracy RoCAT was used to compare the cycles over a broad range of thrust levels, burn times, and chamber pressures. It was found that the electric-pump cycle performs worse than the gas generator and open expander for all considered performance parameters, i.e. initial mass, specific impulse, mass ratio and velocity change. This is in line with previous research with the exception of initial mass. Previous research found the initial mass of the electric-pump cycle engine to be lower than that of the gas generator cycle for burn times above 390 seconds, which was not confirmed by this research. Subsequently, the cycles were compared for selected thrust and burn times with optimized chamber pressure and mixture ratio. The electric pump cycle was found to have a velocity change that is 9.4-9.9% lower than that of the gas generator and 7.7-8.4% lower than the open expander cycle, respectively. With the smaller difference corresponding to higher burn times and vice versa. Additionally, the optimal chamber pressure was found to be around only 15 bar irrespective of burn time. Unlike the conventional cycles whose optimal chamber pressure does change with burn time. The differences in optimal mixture ratio were found to be almost completely dependent on the differences in optimal chamber pressure.

Finally, the development trends for batteries and electric motors were used to approximate the future performance of the electric-pump cycle. It was estimated that it will still take several decades for the electric-pump cycle to match the performance of the conventional cycles. Electric motor specific power will need to increase by two orders of magnitude, while battery specific energy will need to at least double. In conclusion: Despite continuous expected improvement, breakthroughs in both electric motor and battery technology are required to bring the performance of the electric-pump cycle on par with the turbine driven cycles.

RoCAT is available on GitHub at: <https://github.com/RubenvdBerg/RoCAT>



# Nomenclature

## Symbols

$\gamma$	Heat capacity ratio	–	$D$	Diameter	$m$
$\delta_E$	Specific energy	$J/kg$	$E$	Energy	$J$
$\delta_P$	Specific power	$W/kg$	$F$	Force	$N$
$\varepsilon$	Expansion-ratio $A_e/A_{th}$	–	$H$	Height	$m$
$\eta$	Efficiency	–	$h$	Specific enthalpy	$J/kg$
$\kappa$	Factor (e.g. safety/margin)	–	$h$	Heat transfer coeff.	$W/(m^2K)$
$\Lambda$	Mass ratio $m_0/m_f$	–	$I_{sp}$	Specific impulse	$s$
$\mu$	Dynamic viscosity	$Pa\ s$	$L$	Length	$m$
$\nu$	Poisson's ratio	$Pa$	$L^*$	Characteristic length	$m$
$\rho$	Density	$kg/m^3$	$M$	Mach-number	–
$\sigma$	Yield strength	$Pa$	$m$	Mass	$kg$
$\tau$	Torque	$Nm$	$\dot{m}$	Mass flow	$kg/s$
$\theta$	(Half) Angle	$rad$	$\mathfrak{M}$	Molar mass	$kg/mol$
$\omega$	Angular velocity	$rad/s$	$o/F$	Oxidizer-to-Fuel ratio	–
$A$	Area	$m^2$	$P$	Power	$W$
$a$	Acceleration	$m/s^2$	$p$	Pressure	$Pa$
$C_F$	Thrust coefficient	–	$Pr$	Prandlt number	–
$C_p$	Molar heat capacity at const. pressure	$J/(mol\ K)$	$\dot{Q}$	Heat flow rate	$W$
$C_v$	Molar heat capacity at const. volume	$J/(mol\ K)$	$R$	Specific gas constant	$J/(kg\ K)$
$c^*$	Characteristic velocity	$m/s$	$r$	Radius	$m$
$c_p$	Specific heat capacity at const. pressure	$J/(kg\ K)$	$S$	Surface area	$m^2$
$c_v$	Specific heat capacity at const. volume	$J/(kg\ K)$	$T$	Temperature	$K$
			$t$	Thickness	$m$
			$t$	Time	$s$
			$V$	Volume	$m^3$

## Constants

$\bar{\sigma}$	Stefan's	56.7037 $nW/(m^2K^4)$	$g_0$	Standard gravity	9.80665 $m/s^2$
$\bar{R}$	Universal Gas	8.31446 $J/(K mol)$			

## Subscripts

$X_*$	Sonic (or throat conditions)	$X_{inv}$	Inverter
$X_0$	Initial	$X_{isp}$	Specific Impulse (Correction)
$X_\alpha$	Convective	$X_m$	Material
$X_a$	Ambient	$X_{max}$	Maximum
$X_b$	Burn	$X_{noz}$	Nozzle
$X_{bat}$	Battery	$X_{op}$	Oxidizer pump
$X_{bc}$	Battery cooler	$X_{ot}$	Oxidizer tank
$X_{bp}$	Battery pack	$X_{ox}$	Oxidizer
$X_c$	Combustion	$X_p$	Power
$X_{c^*}$	Characteristic velocity	$X_p$	Propellant
$X_{cap}$	Cap of sphere (for ullage)	$X_{pr}$	Pressurant
$X_{cc}$	Combustion chamber	$X_{prt}$	Pressurant tank
$X_{cl}$	Coolant	$X_{pu}$	Pump
$X_{conv}$	Convergent	$X_{rad}$	Radiative
$X_{con}$	Continuous	$X_{ref}$	Reference
$X_{cs}$	Cooling section	$X_{req}$	Required
$X_d$	Discharge	$X_s$	Stay (time)
$X_{div}$	Divergent	$X_{sf}$	Safety
$X_e$	Exit	$X_{st}$	Structural
$X_E$	Energy	$X_T$	Thrust
$X_{em}$	Electric motor	$X_t$	Tank
$X_{ep}$	Electric pump cycle	$X_{tc}$	Thrust Chamber
$X_{exh}$	(Turbine) Exhaust	$X_{th}$	Throat
$X_f$	Final	$X_{tot}$	Total
$X_{fp}$	Fuel pump	$X_{tp}$	Turbopump(s)
$X_{ft}$	Fuel tank	$X_{tu}$	Turbine
$X_{fu}$	Fuel	$X_{ull}$	Ullage
$X_{gg}$	Gas generator (cycle)	$X_w$	Wall

## Acronyms

APM	Auxiliary Power Module	LH2	Liquid Hydrogen
BEV	Battery Electric Vehicle	Li-ion	Lithium Ion (battery)
BLDC	Brushless Direct Current (Motor)	LiPo	Lithium-ion Polymer (battery)
BMS	Battery Management System	LOX	Liquid Oxygen
CB	Coolant Bleed (Cycle)	LTO	Lithium Titanite Oxide (battery)
CC	Combustion Chamber	MCC	Main Combustion Chamber
CE	Closed Expander (Cycle)	MCDC	Maximum Continuous Discharge Current
CEA	Chemical Equilibrium with Applications [40]	NASA	National Aeronautics & Space Administration
COTS	Commercial Off-The-Shelf	OE	Open Expander (Cycle)
CSI	Current Source Inverter	OOP	Object-Oriented Programming
DMC	Dimethyl Carbonate	PE	Poly Ethylene
EC	Ethylene Carbonate	PET	Poly Ethylene Terephthalate
EP	Electric Pump (Cycle)	PHEV	Plug-in Hybrid Electric Vehicle
EPFS	Electric-pump Propellant Feed System	PP	Poly Propylene
ESA	European Space Agency	RC	Radio-Controlled
ESC	Electronic Speed Controller	RoCAT	Rocket Cycle Analysis Tool
FPV	First Person View (Quadcopter)	RP-1	Rocket Propellant-1
GG	Gas Generator (Cycle)	RSE	Relative Standard Error
HEV	Hybrid Electric Vehicle	SC	Staged Combustion (Cycle)
IRT	Ideal Rocket Theory	TO	Tap-Off (Cycle)
LCH4	Liquid Methane	UML	Unified Modelling Language
LFP	Lithium Metal(Ferrous) Phosphate	VSI	Voltage Source Inverter



# List of Figures

1.1	Stylized schematic of rocket engine cycles . . . . .	1
1.2	Historic trend of battery specific energy (Adapted from Tiede et al. [59]) . . . . .	2
3.1	Schematic overview of the cycles as defined above . . . . .	8
3.2	Original graph showing battery coolant flow for a 100 kN, 300 s EP-cycle engine [34] . . . . .	13
3.3	Replications of fig. 3.2 . . . . .	13
4.1	Possible open expander cycle configurations based on location of turbine flow split . . . . .	17
4.2	Schematic overview of cycle configurations . . . . .	18
5.1	Schematic overview of the thrust chamber and injector shell components . . . . .	24
5.2	Schematic overview of nozzle longitudinal cross-section . . . . .	26
5.3	Fuel-rich RP-1/LOX Combustion Temperature (Engine Data from McHugh [41]) . . . . .	32
5.4	Schematic overview of electric-pump cycle component connections . . . . .	35
6.1	Overview of main (blue) cycles' dependence on the abstract (red) base classes. . . . .	39
6.2	Cycle schematic of the abstract base class "Engine Cycle" . . . . .	39
6.3	Cycle schematic of the abstract base class "Open Cycle" . . . . .	42
6.4	Circular dependence for the turbine mass flow and turbine exhaust thrust in an open cycle. . . . .	43
6.5	Cycle schematic of the main class "Electric-Pump Cycle" . . . . .	45
6.6	Circular dependence in the electric-pump cycle. (Purple arrows indicate dependence) . . . . .	45
6.7	Cycle schematic of the main class "Gas Generator Cycle" . . . . .	46
6.8	Cycle schematic of the main class "Coolant Bleed Cycle" . . . . .	47
6.9	Cycle schematic of the main class "Open Expander Cycle" . . . . .	48
6.10	Detail schematic overview of double fuel pump configuration . . . . .	49
6.11	Detail schematic overview of parallel double turbine configuration . . . . .	50
6.12	Detail schematic overview of series double turbine configuration . . . . .	50
6.13	Detail schematic overview of double motor configuration . . . . .	50
6.14	Overview of mass aggregations . . . . .	51
7.1	Schematic overview of performance and flow parameters for an electric-pump cycle engine ( $F_T=100\text{kN}, p_{cc}=10\text{MPa}, t_b=300\text{s}$ ) as simulated with RoCAT . . . . .	54
7.2	Schematic overview of performance and flow parameters for an electric-pump cycle engine ( $F_T=100\text{kN}, p_{cc}=10\text{MPa}, t_b=300\text{s}$ ) as simulated with Adjusted Replication of Kwak's model [34] . . . . .	55
7.3	Schematic overview of performance parameters and flow parameters for the Vulcain as simulated with RoCAT . . . . .	57
7.4	Schematic overview of performance parameters and flow parameters for the Vulcain as simulated by Mota [43] . . . . .	58
7.5	Schematic overview of performance parameters and flow parameters for the SE21D as simulated by RoCAT . . . . .	61
7.6	Schematic overview of performance parameters and flow parameters for the SE21D as simulated by Sippel [53] . . . . .	62
8.1	Performance schematic of an electric-pump cycle engine with $F_T=100\text{kN}, t_b=500\text{s}, p_{cc}=50\text{bar}$ . . . . .	68
8.2	Performance schematic of a gas generator cycle engine with $F_T=100\text{kN}, t_b=500\text{s}, p_{cc}=50\text{bar}$ . . . . .	69
8.3	Performance schematic of an open expander cycle engine with $F_T=100\text{kN}, t_b=500\text{s}, p_{cc}=50\text{bar}$ . . . . .	70
8.4	Comparison of initial mass between EP-, GG-, and OE-cycle . . . . .	71
8.5	Development of thrust chamber mass and feed system mass with chamber pressure . . . . .	73
8.6	Development of energy source mass and cc prop. group mass with chamber pressure . . . . .	73
8.7	Turbine inlet properties versus chamber pressure for the GG- and OE-cycle . . . . .	74

8.8	Development of feed system mass and thrust chamber mass with burn time . . . . .	75
8.9	Development of energy source mass with burn time . . . . .	75
8.10	Development of chamber propellant group mass with burn time . . . . .	76
8.11	Comparison of mass ratio between EP-, GG-, and OE-cycle . . . . .	77
8.12	Comparison of specific impulse between EP-, GG-, and OE-cycle . . . . .	78
8.13	Properties of (Decomposed) RP-1 according to CEA and CoolProp . . . . .	79
8.14	Comparison of idealized velocity change between EP-, GG-, and OE-cycle . . . . .	80
8.15	Optimization space for velocity change with $F_T=100\text{kN}$ , $t_b=300\text{s}$ . . . . .	82
8.16	Optimization space for velocity change with $F_T=100\text{kN}$ , $t_b=1200\text{s}$ . . . . .	83
8.17	Effect of chamber pressure on optimal O/F-ratio for specific impulse ( $p_e=.002\text{ MPa}$ Found from CEA with "frozen at throat" assumption) . . . . .	84
8.18	Effect of battery specific energy on performance of electric-pump cycle . . . . .	86
8.19	Effect of battery specific energy without specific power limit . . . . .	86
8.20	Projected development of EP-cycle in the future . . . . .	88
8.21	Effect of battery specific energy on electric-pump cycle optimal chamber pressure . . . . .	90
A.1	Specific impulse graph taken from Fig.10 in reference [34] . . . . .	99
A.2	Comparison between EP- and GG-cycle for idealized change in velocity . . . . .	102
A.3	Comparison between EP- and GG-cycle for mass ratio . . . . .	103
A.4	Comparison between EP- and GG-cycle for initial mass . . . . .	103
A.5	Comparison between EP- and GG-cycle for specific impulse . . . . .	103
C.1	Schematic overview of performance parameters and flow state of the HM60 engine as simulated by RoCAT . . . . .	112
C.2	Schematic overview of performance parameters and flow state of the J-2 engine as simulated by RoCAT . . . . .	113
C.3	Schematic overview of performance parameters and flow state of the HM7B engine as simulated by RoCAT . . . . .	114
C.4	Schematic overview of performance parameters and flow state of the RS-27 engine as simulated by RoCAT . . . . .	115
C.5	Schematic overview of performance parameters and flow state of the H-1 engine as simulated by RoCAT . . . . .	116
C.6	Schematic overview of performance parameters and flow state of the F-1 engine as simulated by RoCAT . . . . .	117

# List of Tables

3.1	Comparison of replication model and data from Kwak et al. [34] ( $t_b = 300$ s, $F_T = 100$ kN, $p_{cc} = 10$ MPa) . . . . .	8
3.2	Data shows the GG-cycle thrust is not consistent with the 1% thrust contribution. (Data from paper [34] in italics) . . . . .	10
3.3	Data shows the GG-cycle specific impulse to be around 350s (Data for 100 kN engines, original data in italics) . . . . .	11
3.4	Comparison of adjusted model and data from Kwak et al. [34] ( $t_b = 390$ s, $F_T = 100$ kN, $p_{cc} = 10$ MPa) . . . . .	14
4.1	Overview of components and in which cycles they are present. The components are referred to by number in most schematics in this report. . . . .	15
5.1	Data from Humble [28] . . . . .	25
5.2	Coefficients for the calculation of the convective heat transfer coefficient for two methods. . . . .	28
5.3	Gas generator pressures for engines shown in fig. 5.3 . . . . .	32
5.4	Default input values . . . . .	36
5.5	Default inputs based on propellant or propellant mixture. . . . .	36
5.6	Default materials and fluids. . . . .	37
5.7	Default inputs for the electric-pump cycle. . . . .	37
5.8	Default input for the gas generator cycle and open expander cycle . . . . .	37
6.1	Relative difference for key outputs for engines iterated to 1E-3 relative error and iterated to 1E-14 relative error. . . . .	43
7.1	Comparison of performance parameters for an electric-pump cycle engine ( $F_T=100\text{kN}, p_{cc}=10\text{MPa}, t_b=300\text{s}$ ) as produced by RoCAT and by a replication of Kwak's model [43] . . . . .	54
7.2	Comparison of performance parameters for the Vulcain (HM60) engine as produced by RoCAT and Mota's model [43] . . . . .	56
7.3	Differences between performance data from McHugh and RoCAT for selected engines as well as average of absolute differences . . . . .	59
7.4	Comparison between SE21D performance values as expected from the Sippel paper [53], estimated by RoCAT, and estimated with several extra inputs . . . . .	60
7.5	Exit conditions of the SE21D as found by Sippel and from CEA . . . . .	61
7.6	Comparison between real data and RoCAT output for LE-5B open expander engine . . . . .	63
7.7	Comparison of RoCAT and Lee et al.[35] masses for an electric-pump cycle engine *Battery, Inverter, Electric Motor, and Pumps - **Total mass without Feed line mass . . . . .	64
7.8	Differences between mass data from McHugh [41] and RoCAT for selected GG engines . . . . .	64
7.9	Comparison between RoCAT and real data for LE-5B engine dry mass . . . . .	65
8.1	Expected effect of an increase in chamber pressure and burn time on component masses . . . . .	72
8.2	Detailed initial mass composition of all cycles with optimized chamber pressure and O/F-ratio. For $t_b=500\text{s}$ . . . . .	87
8.3	Number of years after 2023 at which EP-cycle overtakes the performance of the other cycles . . . . .	88
8.4	Specific powers and energy as expected at surpassing of conventional cycles . . . . .	89
A.1	Specific impulses extracted from fig. A.1 . . . . .	99
A.2	Comparison of replication model and data from Kwak et al. [34] ( $t_b = 300$ s, $F_T = 100$ kN, $p_{cc} = 10$ MPa) . . . . .	100
A.3	Comparison of replication model and data from Kwak et al. [34] ( $t_b = 390$ s, $F_T = 100$ kN, $p_{cc} = 10$ MPa) . . . . .	101

A.4	Comparison of replication model and data from Kwak et al. [34] ( $t_b = 1200$ s, $F_T = 100$ kN, $p_{cc} = 10$ MPa) . . . . .	101
A.5	Comparison of adjusted model and data from Kwak et al. [34] ( $t_b = 300$ s, $F_T = 100$ kN, $p_{cc} = 10$ MPa) . . . . .	101
A.6	Comparison of adjusted model and data from Kwak et al. [34] ( $t_b = 390$ s, $F_T = 100$ kN, $p_{cc} = 10$ MPa) . . . . .	102
A.7	Comparison of adjusted model and data from Kwak et al. [34] ( $t_b = 1200$ s, $F_T = 100$ kN, $p_{cc} = 10$ MPa) . . . . .	102
B.1	Inputs used in the replication of Kwak's model [34] . . . . .	105
B.2	Predefined materials in RoCAT and their properties . . . . .	106
B.3	D . . . . .	106
B.4	inputs used for simulating the F-1 engine . . . . .	107
B.5	inputs used for simulating the H-1 engine . . . . .	107
B.6	inputs used for simulating the HM60 engine . . . . .	107
B.7	inputs used for simulating the HM7B engine . . . . .	108
B.8	inputs used for simulating the J-2 engine . . . . .	108
B.9	inputs used for simulating the RS-27 engine . . . . .	108
B.10	Inputs used for simulating the LE-5B engine . . . . .	109
B.11	inputs used for simulating the SE21D engine . . . . .	109
C.1	Overview of components and in which cycles they are present. The components are referred to by number in most schematics in this report. . . . .	111
D.1	Overview of centaur mass data in pounds. Taken from [18] (Continues next page) . . . . .	119
D.2	Continuation of Centaur mass data in pounds. Taken from [18] . . . . .	120
D.3	Various mass ratios calculated from tables D.1 and D.2 . . . . .	120
E.1	Overview of parameters for various gas generator engines . . . . .	123
E.1	Overview of parameters for various gas generator engines . . . . .	124

# Contents

Executive Summary	v
Nomenclature	ix
List of Figures	xi
List of Tables	xiii
1 Introduction	1
2 Literature Review	5
3 Replication of Kwak's Model	7
3.1 Kwak's Model . . . . .	7
3.2 Replication Model. . . . .	8
3.3 Detailed Analysis of Kwak's approach . . . . .	9
3.3.1 Gas-generator mass flow. . . . .	9
3.3.2 Gas-generator specific impulse . . . . .	11
3.3.3 Gas generator propellant masses. . . . .	11
3.3.4 Electric-pump battery coolant flow . . . . .	12
3.4 Adjusted Replication Model. . . . .	14
4 Engine Cycles	15
4.1 Modeled Components . . . . .	16
4.2 General Configuration . . . . .	16
4.3 Individual Cycle Configuration . . . . .	16
4.3.1 Electric Pump Cycle . . . . .	16
4.3.2 Gas Generator Cycle . . . . .	16
4.3.3 Expander Differentiation. . . . .	17
4.3.4 Coolant Bleed Cycle . . . . .	17
4.3.5 Open Expander Cycle . . . . .	17
5 Engine Components	19
5.1 Base Classes. . . . .	19
5.1.1 Flow State . . . . .	19
5.1.2 Flow Component . . . . .	20
5.1.3 Material . . . . .	20
5.1.4 Pressure Structure . . . . .	20
5.2 Main Components . . . . .	21
5.2.1 Propellant . . . . .	21
5.2.2 Tank . . . . .	21
5.2.3 Pressurant . . . . .	22
5.2.4 Pressurant Tank . . . . .	23
5.2.5 Pump . . . . .	23
5.2.6 Injector . . . . .	24
5.2.7 Thrust Chamber . . . . .	25
5.2.8 Combustion Chamber . . . . .	25
5.2.9 Nozzle . . . . .	26
5.2.10 Heat Exchanger . . . . .	27
5.2.11 Heat Transfer Section . . . . .	27
5.2.12 Splitter. . . . .	29
5.2.13 Merger. . . . .	29

5.3	Open Cycle Components . . . . .	29
5.3.1	Turbine . . . . .	30
5.3.2	Turbine Exhaust . . . . .	30
5.4	Class Specific Components . . . . .	31
5.4.1	Gas Generator . . . . .	31
5.4.2	Electrical Component . . . . .	33
5.4.3	Electric Motor . . . . .	33
5.4.4	Inverter . . . . .	33
5.4.5	Battery . . . . .	34
5.4.6	Battery Cooler . . . . .	34
5.5	Component Connection . . . . .	35
6	Engine Cycle Implementation . . . . .	39
6.1	Engine Cycle . . . . .	40
6.1.1	Component Integration . . . . .	40
6.1.2	Parameter Calculation . . . . .	40
6.1.3	Checks . . . . .	41
6.2	Open Cycle . . . . .	42
6.2.1	Iteration . . . . .	43
6.2.2	Parameter Calculation . . . . .	44
6.3	Electric Pump Cycle . . . . .	44
6.3.1	Check . . . . .	45
6.4	Gas Generator Cycle . . . . .	46
6.5	Coolant Bleed Cycle . . . . .	47
6.6	Open Expander Cycle . . . . .	48
6.7	Additional Cycle Configuration . . . . .	49
6.7.1	Double Fuel Pumps . . . . .	49
6.7.2	Parallel Double Turbines . . . . .	49
6.7.3	Series Double Turbines . . . . .	49
6.7.4	Double Electric Motor . . . . .	50
6.8	Other Parameters . . . . .	50
6.8.1	Mass Aggregation . . . . .	50
6.8.2	Mass Factor . . . . .	51
6.8.3	Change in velocity . . . . .	52
7	Verification&Validation . . . . .	53
7.1	Performance . . . . .	53
7.1.1	Performance Schematics . . . . .	53
7.1.2	Electric-Pump Verification . . . . .	53
7.1.3	Gas Generator Verification . . . . .	56
7.1.4	Gas Generator Validation . . . . .	59
7.1.5	Open Expander Verification . . . . .	59
7.1.6	Open Expander Validation . . . . .	62
7.1.7	Performance Conclusions . . . . .	63
7.2	Mass . . . . .	64
7.2.1	Electric-Pump . . . . .	64
7.2.2	Gas Generator . . . . .	64
7.2.3	Open Expander . . . . .	65
7.2.4	Mass Conclusions . . . . .	65
8	Results & Discussion . . . . .	67
8.1	Direct Cycle Comparison . . . . .	67
8.1.1	Initial Mass . . . . .	71
8.1.2	Mass Ratio . . . . .	77
8.1.3	Specific Impulse . . . . .	78
8.1.4	Change in Velocity . . . . .	80
8.2	Optimized Cycle Comparison . . . . .	81
8.3	Future of Electric-Pump Cycle . . . . .	85

9	Conclusion	91
9.1	Conclusions	91
9.2	Recommendations	92
	Bibliography	95
A	Detailed Data for Kwak Replication Model	99
A.1	Specific Impulse	99
A.2	Minor modeling details	100
A.3	Replication Model Comparison	100
A.4	Adjusted Model Comparison	101
A.5	Adjusted Model Figures	102
B	Inputs	105
B.1	Kwak Replication Inputs	105
B.2	Predefined Materials	106
B.3	Non-Default Inputs for Engines	106
B.3.1	Electric-pump	106
B.3.2	Gas Generator	106
B.3.3	Open Expander	109
C	Gas Generator Performance Schematics	111
C.1	HM60	112
C.2	J-2	113
C.3	HM7B	114
C.4	RS-27	115
C.5	H-1	116
C.6	F-1	117
D	Centaur Mass Data	119
E	Assumptions & Differences	121
E.1	Differences w.r.t Kwak	121
E.2	List of assumptions	122
F	Detailed Gas Generator Validation Data	123



# Introduction

This research focuses on the analysis of the electric-pump cycle for rocket engines. Conventional rocket engines use a turbine driven by hot gas to drive the pumps, while the electric-pump cycle uses an electric motor powered by a battery to drive the pumps instead, as schematically shown in fig. 1.1a and fig. 1.1b respectively. An electric-pump cycle was first demonstrated by the Agena for in-space propulsion in 1973 [19], but only recently has this cycle been applied successfully to the rocket engine of a launch vehicle: namely the Rutherford engine. This engine was developed by Rocket Lab and used in both stages of the Electron launch vehicle, which first successfully launched in 2017. However, since its introduction little further application of the electric-pump cycle has been seen. Does this mean the electric-pump rocket engine is a one-off or will the future see many launch vehicles use electric-pump rocket engines? This question can only be answered by first identifying its potential advantages and disadvantages.

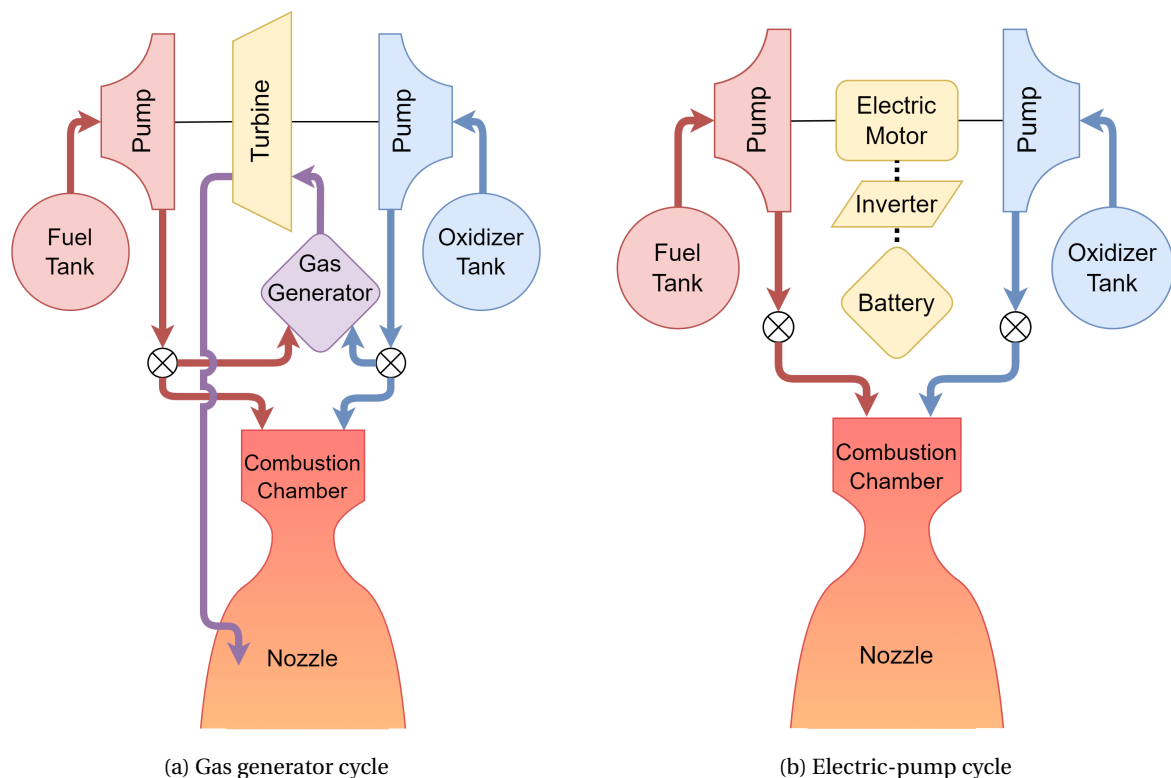


Figure 1.1: Stylized schematic of rocket engine cycles

There are several expected advantages to the electric-pump cycle, most of which derive from its relative simplicity. They are listed below:

- Lower development time than conventional turbo-pump designs [63]
- Reduced complexity and number of components [12]. It is estimated that compared to a gas generator cycle, an EPFS cycle will have 26% less components [34]
- This lower complexity is expected to lead to higher reliability [12]. Additionally, out of the 380 Rutherford engines flown there have only been 2 malfunctions [49]
- Unlimited restartability and very simple ignition sequence [61] [34]

- No issues that follow from a hot turbine attached to a cold pump for cryogenic propellants [14], which is seen as a serious failure mode [62]. Additionally, the seal required to protect for this type of failure was deemed the most critical component of a liquid pump-fed rocket engine by NASA [10]
- Iterative power/pressure balance is not necessary
- Uncomplicated pump speed control leading to possible reduction of combustion instability [56]
- Commercially readily available components [35]

The advantages mentioned above only concern aspects besides performance, while performance is of course also an important aspect, if not the most important. Here the electric-pump cycle also has an advantage, but also two large disadvantages. The electric-pump cycle's advantage is due to being a closed cycle, i.e. all of the propellant flows through the combustion chamber. This leads to a higher overall specific impulse compared to open cycle engines, like the gas generator cycle, where part of the propellant is dumped overboard or in the nozzle.

Its major disadvantages are related to the battery: Firstly, the battery mass is not expelled like the turbine drive gasses in a conventional cycle, which negatively impacts the mass ratio and thus the change in velocity that can be achieved. This first issue can be somewhat mitigated by dropping part of the battery somewhere throughout the flight as has already been demonstrated by Electron's second stage [49]. Secondly, batteries carry much less energy per kilogram than conventional propellants. The energy released by the combustion of 1 kg of RP-1 and oxygen is 9 times higher than the energy contained in 1 kg of a high performance lithium-ion battery [6]. This lower specific energy is partly mitigated by a much higher efficiency when converting the battery energy into pump work than converting the heat energy of a hot gas into pump work. Nonetheless, it is estimated that current batteries deliver 40% less energy to the pump per kg than RP-1 and oxygen [6].

In spite of these clear limitations, the electric-pump cycle has already flown successfully and its crucial technologies are steadily increasing in performance every year [6], see for example the development of the battery specific energy as shown in fig. 1.2.

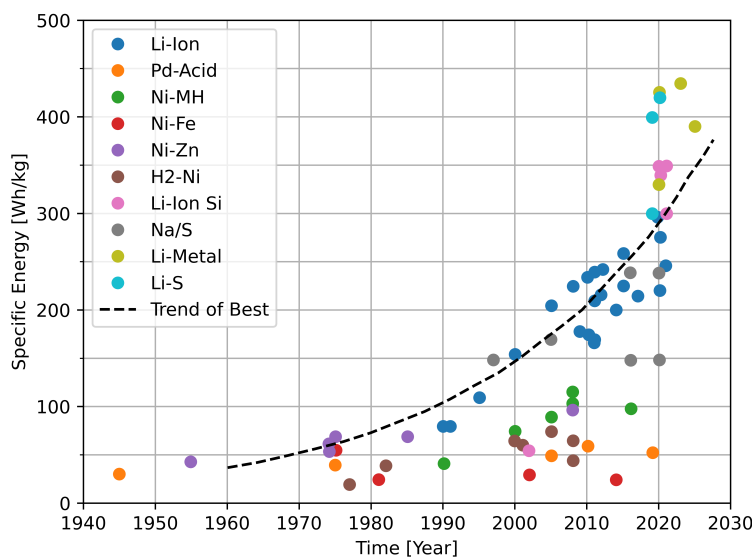


Figure 1.2: Historic trend of battery specific energy (Adapted from Tiede et al. [59])

The steady development of electric motors and batteries has already been going on for a few decades, but is further urged on by the advent of the electric car and the general electrification driven by the abandonment of fossil fuels. This not only makes it worth reevaluating now, but also indicates the electric-pump cycle might be of even greater interest in the future. This continuous improvement has driven interest in the electric feed system, which was already observed by Lentini in 2013 [36]: "... as a result of technological advances of the last decade in the field of electric motors, ... , and batteries, it is now worth reevaluating the viability of electric-pump feed systems." and this is true once again a decade later.

There have been several recent studies into the electric-pump cycle, most notably the work by Kwak et al. [34]. It is of greatest interest since it is the only one to account for the need for active cooling of the battery. Cooling is crucial since the performance of lithium-ion batteries, which currently have the best specific energy, is quite sensitive to temperature changes. The main conclusions of Kwak's work are that, for equal inputs, the electric-pump cycle delivers a 8-25% lower change in velocity than the gas generator cycle and the initial mass is generally lower except for burn times below 390 seconds. For both properties the electric-pump cycle improves relative to the gas generator cycle when the chamber pressure is decreased and the burn time increased.

Despite these clear conclusions, the work by Kwak and other previous studies have been limited in several aspects. Firstly, all previous studies compare the electric-pump cycle solely with the gas generator cycle. A comparison with the expander cycle would be more fruitful, because this cycle is a more probable candidate to be replaced by the electric-pump cycle when considering its limits in thrust and specific impulse. On top of that, almost all studies have made direct comparisons where the cycles are compared for completely equal inputs. However, different cycle types operate best at different chamber pressures. Therefore, it would be more realistic to compare the cycles at individually optimized chamber pressure. Finally, previous comparative studies consider only RP-1 and LOX as propellant combination, while the performance using other propellants like hydrogen and methane could also be of interest.

Consequently, this research attempts to address these limitations and perform a broad scope analysis of the performance of the electric-pump cycle for a wide range of thrusts and burn-times, which could better place it in the context of conventional rocket engine cycles. Additionally, this research explores the electric-pump cycle's potential in the future and answer the question if and when the electric-pump's performance will match that of the conventional cycles. The research focuses mainly on the performance and mass of the electric-pump cycle engine, leaving possible gains in cost, development time and reliability for future research. Key factors here are the velocity change and initial mass. With the former largely determining what payload can be brought to which orbit through the rocket equation, while the initial mass largely determines the payload mass of a lower stage. Furthermore, the mass of the stage is indicative of the cost of the rocket [58]. Additionally, this research is mainly focused on thrust values that best match with the second stages of launch vehicles, but some minor conclusions for first stage and spacecraft application are also drawn.

To be able to compare the electric-pump cycle over a wide scope of conditions and optimize it, simulation is perfectly suited. Simulation lends itself well to the analysis of conceptual systems as well as analysis over a wide array of parameters [55]. Although various software tools for the simulation and analysis of rocket engines are available, see for example RPA and REDTOP [8, 47], many are not free, nor within the budget for this research. Furthermore, none of these tools have the integrated possibility for directly simulating electric-pump cycles or only to a very limited extent [6]. Therefore, for this research, a rocket cycle analysis tool has been built; the Rocket Cycle Analysis Tool or RoCAT for short. The steps undertaken to build this tool as well as its final capabilities are also discussed in this report.

So, to summarize, in this report the performance of the electric-pump cycle is compared to that of several conventional cycles. It is determined for what conditions this cycle performs close to the other cycles and for what conditions it is clearly outperformed. Additionally, this research explores how much better the core technologies of the electric-pump cycle need to become to match the performance of conventional cycles. For this purpose a modular rocket engine cycle analysis tool is built, whose models and implementation are described in this report.

As starting point for building RoCAT the work done by Kwak et al. has been selected [34]. The replication of this work and its comparison to the original results is done in chapter 3. With the foundation for the tool created, chapter 4 follows with a description of the general configurations of the electric-pump cycle as well as the selected conventional cycles. Additionally this chapter identifies the crucial components of all of these cycles. With the components of interest identified chapter 5 discusses the components, their models, and their implementation in detail. Subsequently, chapter 6 contains the detailed implementation of the cycles, which expands upon the component integration, cycle iteration, and additional configuration options. After this complete description of RoCAT, it can be verified and validated, which is done in chapter 7. The final chapters present the results and conclusion, which also includes the recommendations.



# 2

## Literature Review

Several previous studies on the electric-pump cycle have already been conducted and will be highlighted in this chapter. For a more detailed discussion of the previous studies that are of interest for this research the reader is referred to the literature study [6]. It also discusses existing rocket analysis software and its limitations for use in this research.

Since the first successful flight of the electric-pump cycle as in-space propulsion in 1973 there have been conducted quite some studies about it. In the initial two decades afterwards the research was still limited and mostly done by Bell Aerosystems as well as ESA, which led to several papers [7, 13, 30]. One of those already suggests that higher thrust applications than in-space propulsion could be possible and in the latter half of the 2000's several studies are made into the application of electric pumps to liquid fueled rocket engines, see for example the work by Schneider [52], Solda et al. [56], and Rachov [48]. As the quote by Lentini in the introduction exemplifies improvements in battery and electric motor technologies led to even more studies at the start of the previous decade, which culminated in the first successful launch of an electric-pump cycle rocket engine in 2017 by Rocket Lab. This sparked further research internationally as German [61], Korean [34], and Russian [14] studies were completed the following year.

It should be clear that there is clear interest in the electric-pump cycle, which has gone from tiny space propulsion to first stage application in the last three decades. Consequently, a study into its performance is warranted. As already identified in the introduction the work by Kwak et al. [34] is most interesting as it clearly details its modeling of both electric-pump and gas generator cycles and compares them. It combines several aspects of previous work concerning the electric pump cycle, most importantly the work of Rachov [48], Solda & Lentini [56], and Spiller et al. [57], and it is the only study to consider active cooling of the battery. This is crucial since non-optimal temperatures can greatly diminish battery performance.

Kwak analyzed the performance of the electric-pump cycle relative to the gas generator and did so within the following engine ranges: 10 - 100 kN of thrust, 3 - 10 MPa of chamber pressure, and 300 - 1200 s of burn time and for RP-1/LOX as propellant choice. Subsequently, the following conclusions were drawn for the electric-pump cycle relative to the gas generator cycle:

1. It performs worse on mass ratio and velocity change
2. It performs better on specific impulse
3. It performs better on initial mass, but only for burn times higher than 390 s
4. It performs better with longer burn times due to a gain in battery efficiency for longer discharge times
5. It performs better with higher thrusts, although the effect is almost negligible
6. It performs worse with higher chamber pressures

These are already quite interesting conclusions and give more reason for further research as it would be of great interest if similar conclusions can be drawn when the electric-pump cycle is compared to the open expander cycle or for different propellants. Additionally, the last point also begs the question how the cycles would compare if they each operate at their optimal chamber pressure (if the electric-pump cycle has a clear optimum). This work thus should be extended, which this research sets out to do.

Despite several shortcomings with respect to the ideal set forth in the introduction, it would be frivolous to build an analysis tool from scratch instead of using this existing work. Especially when it is as well clearly documented as is done in the work of Kwak et al.. So let us stand on the shoulders of giants and use this work as a foundation for the Rocket Cycle Analysis Tool to be developed.



# Replication of Kwak's Model

In the previous chapter existing research was highlighted and the work by Kwak et al. [34] was identified as a great starting point for the cycle analysis tool. Consequently, an attempt is made to replicate the model of Kwak, such that this replication model can be used as a foundation for RoCAT as envisioned in the introduction. Thus, this chapter summarizes the model as discussed by Kwak, discusses the replication of this model, and present the results from this replication.

## 3.1. Kwak's Model

To not simply repeat previous research, the reader is referred to the original paper of Kwak et al. [34] for the detailed explanation of modeling the gas generator and electric pump cycle. In this section only some main assumptions and approaches are summarized. The list below contains the main assumptions and approach to Kwak's modeling.

- The components modeled by Kwak are as follows:

<b>Both</b>	Propellant Tank, Pressurant Tank, Propellant, Pressurant, Pump
<b>EP</b>	Electric Motor, Inverter, Battery
<b>GG</b>	Gas Generator, Turbine

- The cooling and thrust chamber of both cycles are assumed identical. Thus, the cooling is not modeled, nor is the thrust chamber's mass.
- The cycle's main thrust chamber performance (equivalent velocity) is modeled using CEA.
- The mass estimation of "power" components, i.e. turbine, pump, inverter, electric motor, and battery, is based on a specific power. Thus a linear relation between their power and mass is assumed.
- The mass estimation of the tanks and gas generator is found from thin walled pressure vessel theory.
- The pressure difference over each pump is given as a factor of the combustion chamber pressure.
- The battery in the electric pump cycle is cooled by a recirculating fuel flow.
- The battery heat loss, which determines its coolant flow, is based on the battery's (in)efficiency, which is based on discharge time, i.e. burn time.
- The engine's propellants are RP-1 and Liquid Oxygen

Combining the above assumptions leads to a flow schematic for these cycles as shown in fig. 3.1. With the note that the thrust chamber is only modeled through a performance estimate from CEA.

The initial mass of each cycle is calculated as sum of all components listed above, while the final mass is simply the initial mass minus the propellant mass. Subsequently, the mass ratio is simply calculated as the ratio of these two.

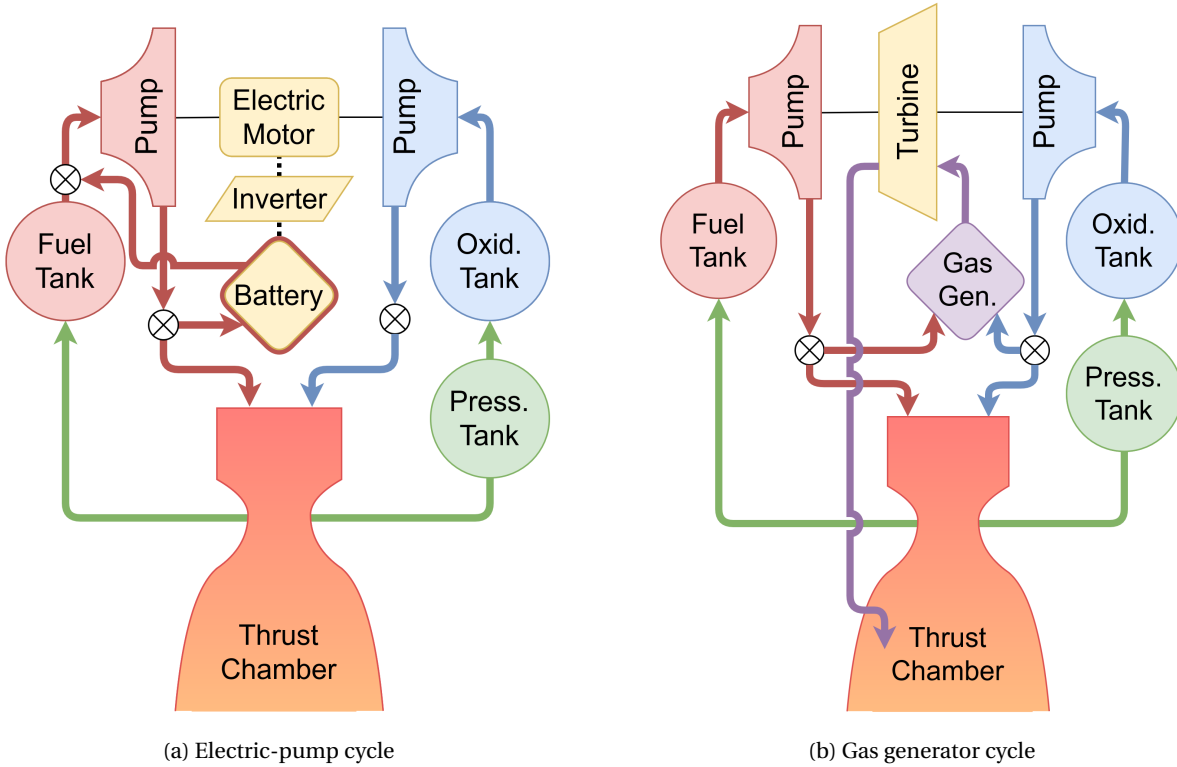


Figure 3.1: Schematic overview of the cycles as defined above

### 3.2. Replication Model

Based on Kwak's model a replication model was built using the aforementioned main assumptions and the detailed theory provided in Kwak's paper [34]. In addition some implementation choices were also made whenever the approach taken in the paper was not explicitly clear. These choices concern mostly minor details and are discussed in appendix A.2. The results from this replication model are compared with the original data in table 3.1. This table only considers the cycles with a burn time of 300 seconds. The burn time is of interest due to the battery efficiency being dependent on it as well as the trade-off between specific energy and specific power for the battery. The complete tables, which also consider 390 and 1200 seconds burn times, are given in appendix A.3. This appendix section also explains how the values were rounded in accordance with Kwak's data. The total propellant mass is split between combustion chamber (CC) and gas generator (GG).

	<i>Electric Pump</i>			<i>Gas Generator</i>		
	<b>Kwak</b>	<b>Repl.</b>	<b>Diff. [%]</b>	<b>Kwak</b>	<b>Repl.</b>	<b>Diff. [%]</b>
CC Propellants [kg]	8350	8350	0.00	8318	8267	-0.61
GG Propellants [kg]	-	-	-	505	508	0.59
Battery Pack [kg]	415	426	2.65	-	-	-
Feed System [kg]	151	155	2.65	43	43	0.00
Tanks [kg]	207	207	0.00	219	217	-0.91
Helium [kg]	33	33	0.00	35	35	0.00
Total [kg]	9156	9171	0.16	9120	9070	-0.55
Mass Ratio [-]	0.0880	0.0895	1.70	0.0326	0.0325	-0.31
Specific Impulse [s]	370.0	370.0	0.00	348.6	352.1	1.00
Velocity Change [m/s]	8817	8756	-0.69	11707	11829	1.04

Table 3.1: Comparison of replication model and data from Kwak et al. [34]

( $t_b = 300$  s,  $F_T = 100$  kN,  $p_{cc} = 10$  MPa)

Looking at the data in table 3.1 it is clear that the replication quite closely matches the data presented by Kwak et al. with some deviations. For the electric pump cycle there seems to be a difference that affects both the battery and all other feed system components, but nothing else. This indicates a difference in the battery coolant flow, as this increases the power needed by the pumps without affecting the total propellant mass consumed. For the gas generator cycle differences are found in the propellants and tanks, indicating potential differences in the gas generator and/or chamber mass flow.

Although the differences are small, they are still unexpected as the theory given in the paper was followed to the letter. Consequently, a further investigation into these differences was made. This investigation brought to light several differences between the theory and results as presented in Kwak's paper. The following section discuss these differences.

### 3.3. Detailed Analysis of Kwak's approach

Several inconsistencies in the results of Kwak et al [34] have been found and are listed below. They are discussed one by one and the difference between the approach given in the paper and the apparent approach that created the results are investigated. Many of the conclusions drawn, concerning these approaches, were drawn due to the availability of a more detailed data sheet, which was made available by Kwak himself [33]. Kwak requested this data remain private, which is why substantiation of the modeling is done using data of the original paper wherever possible.

- Gas generator cycle:
  1. Gas-generator mass flow is determined oddly
  2. Specific impulse calculations neglect the exhaust thrust contribution
  3. Propellant masses calculated inconsistently
- Electric-pump cycle:
  1. Electric-pump cycle battery coolant mass flow is determined with 100% efficiency

Each of the following subsections discusses one of the four inconsistencies listed above. Each subsection consists of four parts. First, the modeling of this part is discussed. Here the equations as stated in Kwak's paper [34] are given. This is followed by the actually applied approach, as deduced from the paper's data and detailed data sheet [33]. Secondly, it is clarified how this approach leads to inconsistencies in the model. Thirdly, it is shown that the data of the paper indeed contains these inconsistencies. And, lastly, the fix to this inconsistent approach is discussed. The equations are not discussed in detail as the reader is expected to be familiar with the original work by Kwak et al.[34] and thus is also referred there for further clarification.

#### 3.3.1. Gas-generator mass flow

To model the gas generator mass flow, Kwak provides the relations as given in eqs. (3.1) to (3.3).

$$P_{tu} = P_{pu} = P_{op} + P_{fp} = \frac{\Delta p_{op} \dot{m}_{op}}{\rho_{ox} \eta_{op}} + \frac{\Delta p_{fp} \dot{m}_{fp}}{\rho_{fu} \eta_{fp}} \quad (3.1)$$

$$\dot{m}_{gg,req} = P_{tu} \left( \eta_{tu} c_{p,gg} T_{tu,in} \left( 1 - \left( \frac{p_{tu,in}}{p_{tu,out}} \right)^{\frac{1-\gamma_{gg}}{\gamma_{gg}}} \right) \right)^{-1} \quad (3.2)$$

$$\dot{m}_{op} = \dot{m}_{gg,ox} + \dot{m}_{cc,ox} \quad (3.3a)$$

$$\dot{m}_{fp} = \dot{m}_{gg,fu} + \dot{m}_{cc,fu} \quad (3.3b)$$

With  $P$  denoting power [W],  $p$  pressure [Pa],  $\dot{m}$  mass flow [kg/s],  $\eta$  efficiency [-],  $\rho$  density [kg/m<sup>3</sup>],  $T$  temperature [K],  $c_p$  specific heat capacity J/(mol K), and  $\gamma$  the heat capacity ratio. As for the subscript:  $tu$  turbine,  $op$  oxidizer pump,  $fp$  fuel pump,  $ox$  oxidizer,  $fu$  fuel,  $gg$  gas generator,  $req$  required, and  $cc$  combustion chamber.

The above equations combined with the oxidizer-to-fuel ratios for both the chamber and gas generator can be solved to find the required gas generator mass flow. The resulting equation is implicit, thus is solved iteratively. However, from the detailed data sheet [33] it is deduced that, instead of consistent iteration, the following approach has been taken:

1. The initial chamber mass flow is calculated from the thrust and CEA equivalent velocity, while the gas generator mass flow is initially zero, this leads to an initial turbine power required and consequently a required mass flow through the gas generator

$$\dot{m}_{gg,0} = 0 \quad (3.4a)$$

$$\dot{m}_{cc,0} = \frac{F_T}{c^* C_F} \quad (3.4b)$$

$$\rightarrow P_{tu,0} \rightarrow \dot{m}_{gg,req,0} \quad (3.4c)$$

With  $F_T$  the thrust [N],  $c^*$  the characteristic velocity [m/s], and  $C_F$  the thrust factor [–]

2. The gas generator mass flow is now set equal to the required mass flow found in the previous step, which leads to a higher total mass flow and the process of the previous step is repeated

$$\dot{m}_{gg,1} = \dot{m}_{gg,req,0} \quad (3.5a)$$

$$\dot{m}_{cc,1} = \dot{m}_{cc,0} \quad (3.5b)$$

$$\rightarrow P_{tu,1} \rightarrow \dot{m}_{gg,req,1} \quad (3.5c)$$

3. In the final step the gas generator mass flow is updated as in the previous step, but additionally the chamber flow is reduced such that the total flow through the pumps remains the same as the previous step. The chamber flow is reduced for the oxidizer and fuel separately. Since the total flow remains the same, so do the turbine power and gas generator mass flow required.

$$\dot{m}_{gg,2} = \dot{m}_{gg,req,1} \quad (3.6a)$$

$$\dot{m}_{cc,2,ox} = \dot{m}_{op,1} - \dot{m}_{gg,req,1,ox} \quad (3.6b)$$

$$\dot{m}_{cc,2,fu} = \dot{m}_{fp,1} - \dot{m}_{gg,req,1,fu} \quad (3.6c)$$

$$\rightarrow P_{tu,2} = P_{tu,1} \rightarrow \dot{m}_{gg,req,2} = \dot{m}_{gg,req,1} \quad (3.6d)$$

By reducing the chamber flow in this last step, the thrust provided by the chamber is reduced. This could be seen as accounting for the turbine exhaust thrust contribution, but leads to an arbitrary value for this thrust contribution instead of the 1% of the total thrust stated in the paper. Additionally, reducing the fuel and oxidizer flow separately leads to an  $o/f$ -ratio for the combustion chamber which is slightly higher than originally intended (assuming the gas generator burns fuel rich).

Cycle	Parameter	Unit	Engine 1	Engine 2	Engine 3
Both	<i>Burn Time</i>	<i>s</i>	<i>1200</i>	<i>390</i>	<i>300</i>
EP	<i>CC Propellants</i>	<i>kg</i>	<i>33402</i>	<i>10856</i>	<i>8350</i>
EP	CC Mass Flow	kg/s	27.559	27.560	27.558
EP	Equivalent Velocity	m/s	3628.5	3628.4	3628.7
GG	<i>CC Propellants</i>	<i>kg</i>	<i>33273</i>	<i>10812</i>	<i>8318</i>
GG	CC Mass Flow	kg/s	27.453	27.449	27.452
GG	CC Thrust	kN	99.61	99.60	99.61

Table 3.2: Data shows the GG-cycle thrust is not consistent with the 1% thrust contribution. (Data from paper [34] in italics)

From the data provided in the paper it can be found that indeed the thrust provided by the gas generator cycle engine's chamber isn't consistent with either a 1% or 0% thrust reduction. This is shown in table 3.2. First,

the overall equivalent velocity for the electric-pump cycle engines is determined using the data provided in the table in combination with a thrust of 100 kN and a propellant margin factor of 1.01. The found equivalent velocities are consistent with the one found from CEA (3628.55  $m/s$ ). Subsequently, the chamber thrust is calculated for the gas generator cycle engines with this equivalent velocity. This shows that they indeed do not match either 99 kN nor 100 kN. Since no individual oxidizer and fuel data for the gas generator cycle engines is available in the paper, the  $o/f$ -ratio shift cannot be shown.

To fix this inconsistency the first 2 steps of the process should be repeated until acceptable convergence.

### 3.3.2. Gas-generator specific impulse

Kwak does not explicitly state how the total specific impulse is calculated. From the specific impulse graph and data (see appendix A.1) it is inferred that the specific impulse has been calculated using eq. (3.7).

$$I_{sp,tot} = \frac{\dot{m}_{cc} \cdot I_{sp,cc}}{\dot{m}_{cc} + \dot{m}_{gg}} \quad (3.7)$$

With  $I_{sp}$  denoting the specific impulse [s] and  $_{tot}$  denoting total.

This equation is correct if the gas generator mass flow does not contribute to the thrust. However, the paper states that a thrust contribution of 1% is assumed. Additionally, even if the gas generator mass flow is assumed to not contribute to the thrust, eq. (3.7) still leads to a lower specific impulse than expected since the chamber mass flow has been reduced during the calculation of the gas generator mass flow, as discussed above. Either way, the specific impulse is lower.

Parameter	Unit	Engine 1	Engine 2	Engine 3
Burn Time	s	<i>1200</i>	<i>390</i>	<i>300</i>
CC Propellants	kg	<i>33273</i>	<i>10812</i>	<i>8318</i>
GG Propellants	kg	<i>2021</i>	<i>656</i>	<i>505</i>
Total Mass Flow	kg/s	29.137	29.131	29.135
Specific Impulse	s	349.97	350.05	349.99

Table 3.3: Data shows the GG-cycle specific impulse to be around 350s (Data for 100 kN engines, original data in italics)

It is clear that use of eq. (3.7) leads to inconsistencies when comparing the propellant mass data and the specific impulse graph of Kwak's paper. The mass data is shown in table 3.3 and the specific impulse found from the graph is 348.6 s (see appendix A.1). From the data of Kwak's paper the total mass flow and subsequently the specific impulse are calculated using eqs. (3.8a) and (3.8b), with  $\kappa_p = 1.01$  and  $F_T = 100$  kN, which is consistent with the equations provided by Kwak. From table 3.3 it is clear that the specific impulses found from the mass data are around 350.0 s, which does not match with the 348.6 s found from the graph. Conversely, for the electric-pump cycle the specific impulses from the mass data and graph are in agreement.

$$\dot{m}_{tot} = \frac{m_{p,cc} + m_{p,gg}}{\kappa_p t_b} \quad (3.8a)$$

$$I_{sp,tot} = \frac{F_T}{\dot{m}_{tot} g_0} \quad (3.8b)$$

With  $\dot{m}_{tot}$  the total mass flow,  $m_{p,cc}/m_{p,gg}$  the combustion chamber/gas generator propellants mass,  $\kappa_p$  the propellant margin factor,  $t_b$  the burn time,  $I_{sp,tot}$  the total specific impulse, and  $F_T$  the thrust.

To fix this inconsistency eq. (3.9) should be used instead.

$$I_{sp,tot} = \frac{F_T}{g_0 \cdot (\dot{m}_{cc} + \dot{m}_{gg})} \quad (3.9)$$

### 3.3.3. Gas generator propellant masses

The propellant masses are calculated using eq. (3.10) according to the original paper [34].

$$m_p = \dot{m} \cdot t_b \cdot \kappa_p \quad (3.10)$$

With  $m_p$  the propellant mass,  $\dot{m}$  the propellant mass flow,  $t_b$  the burn time, and  $\kappa_p$  the propellant margin factor.

However, for the gas generator cycle, the propellant margin factor seems to have not been applied to the gas generator propellant and the chamber propellant has been calculated as the "rest" instead. For example consider a case with 900 and 100 kg of chamber and gas generator propellant, respectively. After application of the propellant margin of 1% their masses have become 910 and 100, instead of the 909 and 101 expected. Thus, this leads to a lower gg propellant mass and higher cc propellant mass, but their sum remains equal to the correct total propellant mass (which is why this inconsistency does not influence the adjusted specific impulses found in table 3.3). Conversely, the factor seems to have been applied correctly to the total fuel and oxidizer masses. This is summarized in eqs. (3.11a) to (3.11d).

$$m_{fu} = \dot{m}_{fu} \cdot t_b \cdot \kappa_p \quad (3.11a)$$

$$m_{ox} = \dot{m}_{ox} \cdot t_b \cdot \kappa_p \quad (3.11b)$$

$$m_{p,gg} = \dot{m}_{gg} \cdot t_b \quad (3.11c)$$

$$m_{p,cc} = m_{p,tot} - m_{p,gg} = m_{fu} + m_{ox} - m_{p,gg} \quad (3.11d)$$

With  $m$  the mass [kg],  $\kappa_p$  the propellant margin [-], and  $t_b$  the burn time.

Since the chamber mass flow nor the gas generator mass flow is given in the original paper this inconsistency cannot be shown from its data.

To fix this inconsistency eq. (3.10) should be applied correctly for both the combustion chamber and gas generator propellant masses.

### 3.3.4. Electric-pump battery coolant flow

According to the paper [34], eq. (3.12) is used to determine the battery coolant mass flow. However, from the data it can be deduced that the equation has been used without applying the efficiencies (85% for the inverter, 95% for the electric motor and 86-99% for the battery for 300-1200 s burn time). With these inputs this leads to 25-43% less battery coolant mass flow. Note that for the calculation of the battery mass, the efficiencies seem to have been applied correctly.

$$\dot{m}_{bat,cl} = \frac{(1 - \eta_E)(P_{fp} + P_{op})}{c_{p,fu} \Delta T_{cl}} \cdot \frac{1}{\eta_{inv} \eta_{em} \eta_E} \quad (3.12)$$

This inconsistency is easily verified with the private detailed data [33], but less so with the public data of the paper. Comparing with the graphical data available was deemed the best option, although not completely satisfactory. The paper's figure, fig. 3.2, has been replicated with and without taking into account the efficiencies when calculating the battery coolant flow, shown in fig. 3.3. Figure 3.3a matches very closely with the original, while fig. 3.3b does not.

To fix this inconsistency the efficiencies should simply be taken into account for the coolant flow calculation.

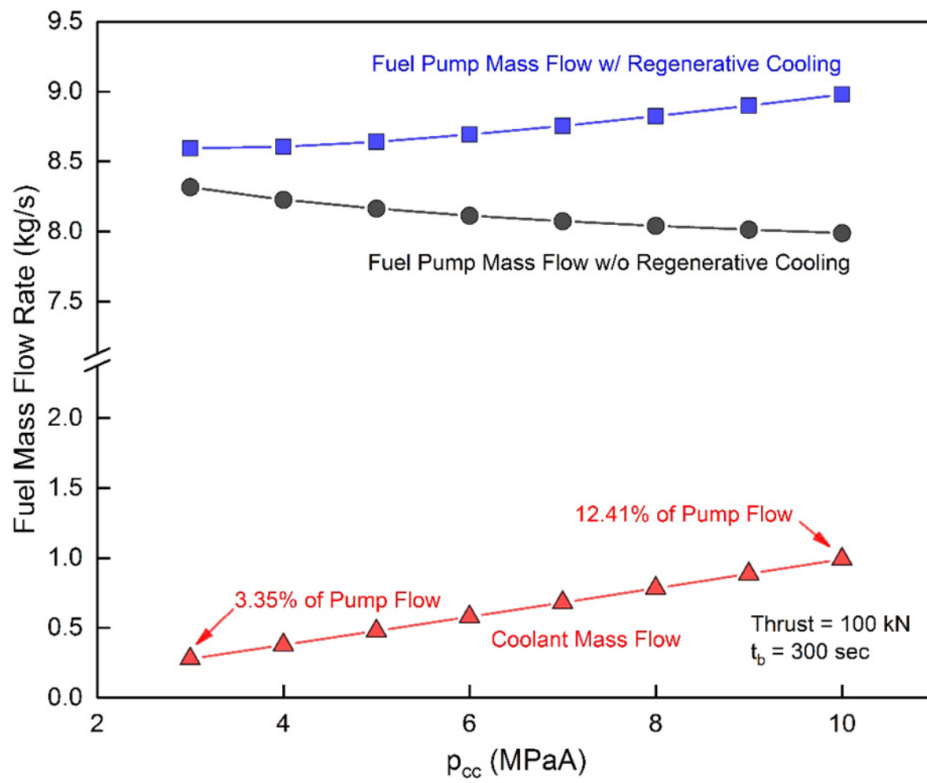


Figure 3.2: Original graph showing battery coolant flow for a 100 kN, 300 s EP-cycle engine [34]

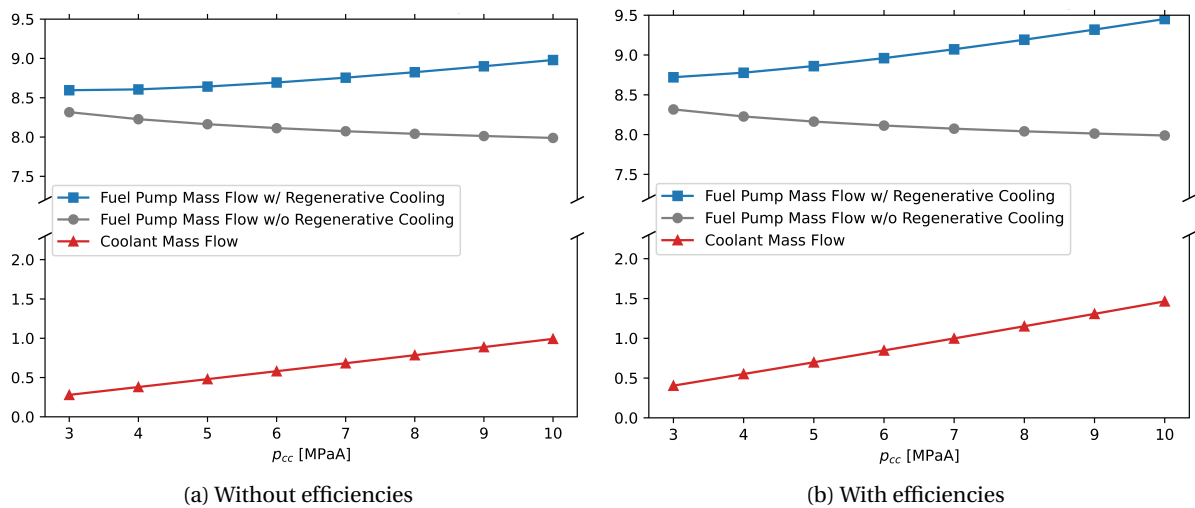


Figure 3.3: Replications of fig. 3.2

### 3.4. Adjusted Replication Model

In the previous section several inconsistencies have been discussed. The modeling approaches that have been deduced from these inconsistencies have been implemented in a copy of the replication model to produce a new model, "the adjusted model". This adjusted model replicates the values as presented by Kwak without any (rounded) difference in the case of 300 seconds burn time. A table full of identical numbers is not very interesting, but can be found in appendix A.4 where the adjusted model is compared to that of Kwak for every burn time. Instead the 390 s burn time case is given below in table 3.4, which is the case where the adjusted model and Kwak's data differ most. Adjusted model values that do not match with Kwak values are highlighted in bold. It can be seen that individual components only differ by at most 2 kg and the total by at most 3 kg. Although it does not match perfectly it is deemed more than accurate enough to verify the adjusted model.

	<i>Electric Pump</i>		<i>Gas Generator</i>	
	<b>Kwak</b>	<b>Adjusted</b>	<b>Kwak</b>	<b>Adjusted</b>
CC Propellants [kg]	10856	10856	10812	<b>10814</b>
GG Propellants [kg]	-	-	656	<b>657</b>
Battery Pack [kg]	521	<b>520</b>	-	-
Feed System [kg]	150	150	43	43
Tanks [kg]	272	272	287	287
Helium [kg]	44	<b>43</b>	46	46
Total [kg]	11843	<b>11841</b>	11844	<b>11847</b>
Mass Ratio [-]	0.0832	0.0832	0.0317	0.0317
Specific Impulse [s]	370.0	370.0	348.6	348.6
Velocity Change [m/s]	9023	<b>9016</b>	11795	<b>11794</b>

Table 3.4: Comparison of adjusted model and data from Kwak et al. [34]  
( $t_b = 390$  s,  $F_T = 100$  kN,  $p_{cc} = 10$  MPa)

The mass data given in Kwak's paper all concern the same chamber pressure and thrust. So to show the adjusted model also matches Kwak's model for varying pressure and thrust many of the figures presented in the original paper [34] have been replicated and are shown in appendix A.5. Additionally, with the clear justification of the differences between the replication model and adjusted model the replication model is also deemed verified. Consequently, the replication model can confidently serve as foundation for RoCAT.

# 4

## Engine Cycles

In this chapter the cycles implemented in RoCAT are discussed. Their general lay-out is given as well as a selection of the components that are modeled. The exact implementation of each cycle and the corresponding theory is given in chapter 6, after the discussion of the individual component models in the next chapter.

The cycles to be modeled are the electric-pump cycle, gas generator cycle, and open expander cycle. The gas generator is modeled to be able to compare to previous research, while the open expander cycle is modeled to extend this research. As mentioned in the introduction & chapter 2, previous research found the electric-pump cycle to perform generally worse than the gas generator cycle, while being close at certain operating points. Since it is expected that the open expander cycle's performance is somewhat lower than that of the gas generator, its comparison to the electric-pump cycle should be even closer.

For each cycle a simplified schematic representation is discussed. Real engine cycles are generally much more complicated and often have many additional components, e.g. feed lines, valves, bleed-lines, booster pumps, multiple turbines, gearing and other added complexities. Many of these details are not shown: the focus is on first order approximation and calculation needs to be limited. Additionally, the possible configurations of each cycle are vast and can have a significant effect on (simulated) performance. Nonetheless, the configuration for each cycle, as presented in this chapter, is deemed the best general representation of that cycle.

First the components to be modeled are selected, this is followed by a discussion of the configuration choices that are applicable to all cycles. Finally, each cycle configuration is discussed individually.

#	Component	Electric-Pump	Gas Generator	Open Expander
1	Fuel Tank	X	X	X
2	Oxidizer Tank	X	X	X
3	Fuel Pump	X	X	X
4	Oxidizer Pump	X	X	X
5	Turbine		X	X
6	Heat Exchanger	X	X	X
7	Thrust Chamber	X	X	X
8	Injector	X	X	X
9	Splitter/Merger	X	X	X
10	Turbine Exhaust		X	X
11	Gas Generator		X	
12	Electric Motor	X		
13	Inverter	X		
14	Battery	X		
15	Battery Cooler	X		
16	Pressurant Tank	X	X	X
17	Pressurant	X	X	X
18	Fuel	X	X	X
19	Oxidizer	X	X	X

Table 4.1: Overview of components and in which cycles they are present. The components are referred to by number in most schematics in this report.

## 4.1. Modeled Components

Table 4.1 shows all components relevant to the cycle configuration schematics shown in fig. 4.2 (at the end of this chapter) and discussed in the next sections. The last four components, i.e. pressurant tank, pressurant, fuel, and oxidizer, have been excluded from the flow schematics for the sake of clarity but are present in every cycle. With respect to Kwak the following components have been added: thrust chamber, heat exchanger, and secondary nozzle. As discussed previously the thrust chamber is added to get a more realistic mass ratio as well as model slight differences in chamber conditions. The heat exchanger is also modeled which makes it possible to check if the thrust chamber can be cooled, but most importantly it is a necessary component to model expander cycles since they use the coolant to power the turbine. Lastly, the secondary nozzle is added such that the thrust contribution of the open cycles can be estimated. This would be an improvement as Kwak simply assumed this contribution to be 1% of the total thrust, irrespective of the combustion chamber, gas generator, and ambient conditions. Some of the existing components have also been changed, which is made clear for each component individually in the next chapter. A complete list of differences between Kwak's model and RoCAT is given at the end of chapter 6.

## 4.2. General Configuration

All cycles are configured with only one "power source", i.e. turbine or electric motor, that powers both pumps for simplicity sake with the exception of engines modeled for the verification & validation. Additionally, all cycles are configured to have a high pressure inert gas pressurant to pressurize the propellant tanks. The tank for this pressurant is submerged in the oxidizer tank. The pressurization choice is made for simplicity relative to other pressurization options, i.e. autogenous pressurization. The submersion choice is made such that results are as comparable to Kwak's research [34] as possible. Other than that the choice is arbitrary and RoCAT can model the pressurant tank submerged in either propellant tank or outside it. Each configuration assumes fuel to be the main coolant as this is generally most common, since handling hot oxidizer requires very specialized metals/materials especially if it is used to power the turbine. For the open cycles the turbine exhaust gas is vented overboard through a secondary nozzle. This choice was made mainly to simplify the calculation of the exhaust gas thrust contribution. Finally, the cooling of the thrust chamber is assumed to be one loop. In real engines the cooling is sometimes split into multiple sections; generally one loop cooling the chamber with another cooling the nozzle. Although the heat exchanger component has been built to be modular and two section cooling has been implemented for verification purposes, the main cycle configurations implement a single heat exchanger.

## 4.3. Individual Cycle Configuration

### 4.3.1. Electric Pump Cycle

In fig. 4.2a (end of chapter) the detailed schematic configuration of the electric pump cycle is shown. It powers the pumps through an electric motor, which itself gets its power from a battery with an inverter in between. As discussed in the introduction, it is important to keep the battery at optimal temperature. Consequently a cooling loop has been added to the basic design of the electric-pump cycle, which is in line with the work of Kwak whose configuration was shown in fig. 3.1a. The complete chamber fuel flow is used to cool the engine, while a recirculating loop of fuel is used to cool the battery. The inverter is not cooled, while the electric motor is assumed to be cooled by oxygen leakage. Not cooling the electric motor, beyond the inherent oxidizer leakage, has been found to be acceptable up to 100 kN for a single motor from a first order analysis by Kwak [34], i.e. 200 kN for a double motor configuration. For higher thrusts than 200 kN, the electric motor component does a simple check to estimate if oxidizer leakage cooling is sufficient, as is discussed in more detail in chapter 5.

### 4.3.2. Gas Generator Cycle

In fig. 4.2b (end of chapter) the detailed schematic configuration of the gas generator cycle is shown. This configuration follows quite directly from the simplified configuration shown in fig. 1.1a. The gas generator cycle combusts a fraction of both the fuel and oxidizer flow to create enough hot gas to drive a turbine and power the pumps. For the configuration in this report only fuel rich gas generators have been considered and although RoCAT should be perfectly capable of handling oxidizer rich combustion, this has not been tested. Additionally, it is assumed the turbine exhaust gas is dumped overboard at ambient pressure.

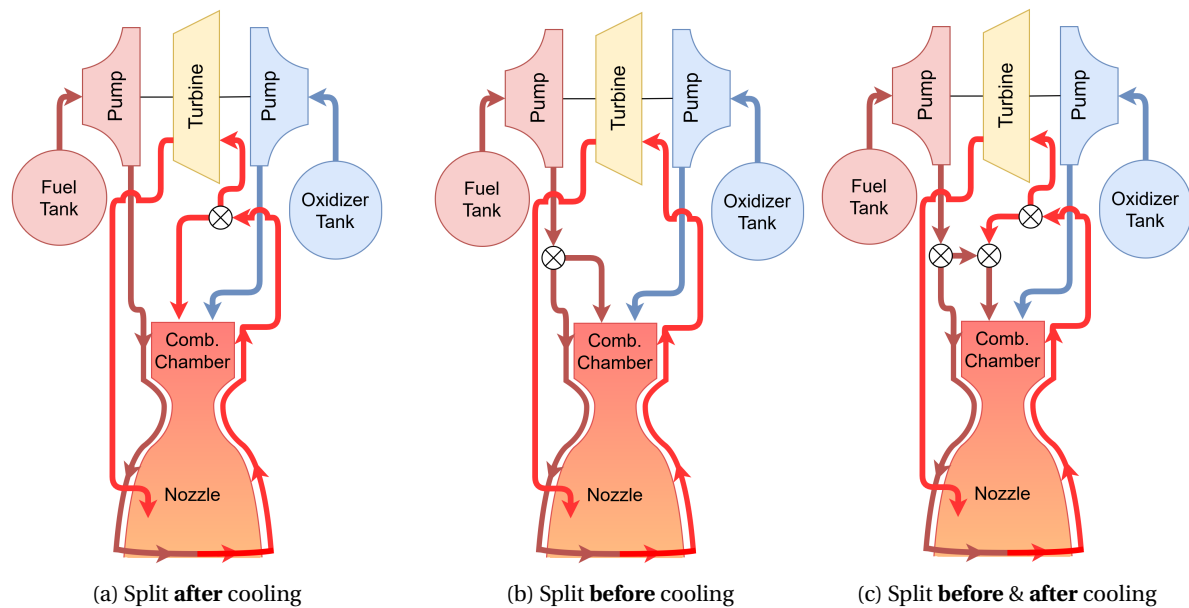


Figure 4.1: Possible open expander cycle configurations based on location of turbine flow split

### 4.3.3. Expander Differentiation

For the expander cycles three configurations are considered, which needs some clarification. In fig. 4.1a the open expander cycle configuration can be seen. For the expander cycle part of the heated fuel flow is used to drive the turbine and power the pumps. Note that the flow that ends up at the turbine is split from the main flow after the heat exchanger. Alternatively, fig. 4.1b shows a configuration in which this split occurs before the heat exchanger. Let the former temporarily be called (a)-cycle and the latter (b)-cycle. Both configurations have some clear inefficiency. Comparing these two cycles Herbertz et al. say the following: "... *analysis showed however, that [(a)-cycle] is severely inefficient, since the heat transferred to the coolant is distributed among a higher mass flow ... and therefore substantially more fluid is needed to drive the turbine.*"[26]. In addition the (a)-cycle needs a higher (fuel) pump outlet pressure, although this is partially compensated by a higher pressure ratio over the turbine. Herbertz clearly favors the (b)-cycle, but it also has a clear drawback. If the mass flow required for cooling is higher than the mass flow required for the turbine, more propellant is expelled at low specific impulse than necessary. Although this additional waste of propellant for (b)-cycle is dependent on parameters like the total heat transfer and maximum turbine temperature, it cannot happen in any condition in the (a)-cycle. The solution is to combine both cycles with the addition of a secondary pump, which is shown in fig. 4.1c. Now the turbine flow is as hot as possible and no extra propellant is expelled at low specific impulse.

In the rest of this report the term open expander cycle (OE-cycle) is used exclusively to denote the configuration as shown in fig. 4.1c, while the term coolant bleed cycle (CB-cycle) is used exclusively to denote the configuration as shown in fig. 4.1a. The main analysis will only focus on the OE-cycle.

### 4.3.4. Coolant Bleed Cycle

The coolant bleed cycle configuration can be seen in fig. 4.2c (end of chapter). It is the simplest configuration. The full fuel flow flows through the heat exchanger, after which the turbine flow is split off, while the main flow flows directly to the chamber. Once again the turbine flow is assumed to exit at ambient pressure, i.e. as shown in fig. 4.2c, but not in fig. 4.1. Additionally, it is assumed that both the chamber and (part of) the nozzle are cooled.

### 4.3.5. Open Expander Cycle

Figure 4.2d (end of chapter) shows the open expander cycle configuration, which splits the fuel flow before the heat exchanger into a cooling flow and a chamber flow. After the heat exchanger the flow is once again split in a turbine flow and an additional chamber flow. For this cycle a minimum required coolant flow is calculated,

which depends on either the turbine inlet temperature or the maximum thrust chamber wall temperature, whichever is lower. If the required turbine flow is larger than the minimum coolant flow, the split after the heat exchanger is unnecessary and the additional chamber flow is zero. This reduces this configuration to the configuration shown in fig. 4.1b, but never happens in any case discussed in this report.

Now that all cycle have been discussed and their configurations are known, the equations used to model the performance and mass of each component can be discussed, which will be done in the next chapter.

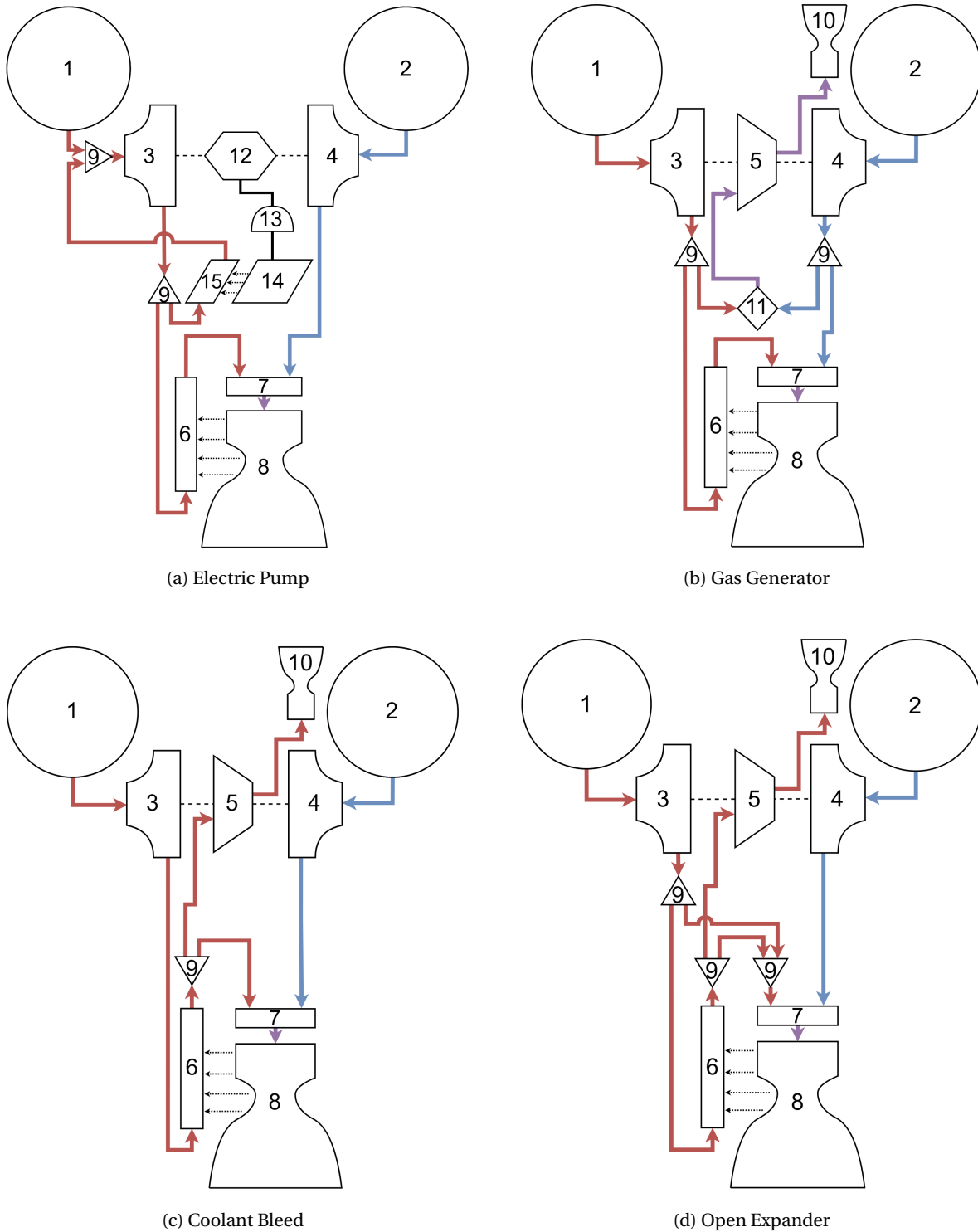


Figure 4.2: Schematic overview of cycle configurations

# Engine Components

This chapter discusses the components of all cycles as implemented in RoCAT and listed in section 4.1. The theory used to model the various components is specified as well as the empirical relations that were used and the main aspects of their implementation. Additionally, the most important inputs and outputs of each component are given. Note that these are not exhaustive and for a full list of in- and output the reader is referred to the code and documentation, both of which are available on GitHub at:

<https://github.com/RubenvdBerg/RoCAT>

Most components inherit from (abstract) base classes. These base classes simply encapsulate the functionality that various components share. These base classes are discussed first, after which the main components are discussed that are present in all cycles. These are followed by a section on the components required for the open cycles (gas generator and open expander cycle) and a section on components that are unique to each individual cycle. This is followed by an example schematic of how these components would be connected in an electric-pump cycle. The chapter is concluded by a list of main input values as used in this report. For a complete overview of inputs used, see appendix B.

## 5.1. Base Classes

Quite a few components share some form of functionality. For example several components' masses are estimated based on an internal pressure and a yield strength. Consequently, these components inherit from a base class called Pressure Structure, which contains the functionality for this mass calculation and requires a pressure, yield strength, and safety factor. This grouping of shared functionality follows the principles of object oriented programming and makes it easier to adjust or improve these relations later on. This section discusses the base classes, which is followed by the main component classes.

### 5.1.1. Flow State

#### Main input:

- temperature
- pressure
- propellant name
- type
- mass flow

#### Main output:

- specific gas constant
- molar mass
- heat capacity ratio
- specific heat capacity
- density
- conductivity
- prandtl number
- mass specific enthalpy

This class deals with the various flows of propellant, e.g. fuel, oxidizer, coolant, combustion gas, that flow from one component to the other and provides info on the flow properties dependent on its specie, temperature, and pressure. These properties are provided by the CoolProp-package [5]. Additionally, it also keeps track of the mass flow.

CoolProp is limited to 122 pure components and mixtures thereof. This means that RP-1 cannot be modeled directly, since it is a complex mix of various carbohydrates. n-Dodecane has been selected as an acceptable surrogate as its structure is close to the average of the types of carbohydrate chains found in RP-1. More

complex surrogate mixtures for RP-1 were considered, e.g. Huber[27] and Han[23], but were found to be too complex and contained components not available in CoolProp. For the density of RP-1 a small correction is made to the values provided by CoolProp for n-Dodecane, based on the RP-1 density data provided by Magee et al. [39]. Additionally, a replacement of the specific heat capacity data of n-Dodecane with known experimental data from Abdulagatov [1] was initiated, but abandoned since it only gave marginal improvement while greatly complicating the calculation of flow properties. A more streamlined implementation of RP-1 property estimation remains for future work.

### Manual Flow State

CoolProp is very flexible and versatile when dealing with pure species, but less applicable for combustion products. Thus, for flows of combustion products (after the combustion chamber or gas generator) a Manual Flow State is used. The same properties are available, but are calculated once using CEA and given to a Manual Flow State instead of being calculated by CoolProp. This means that the flow properties are constant and are not affected by any temperature or pressure changes downstream of initial combustion. This has some further ramifications that are discussed in section 6.2

### 5.1.2. Flow Component

#### Main input:

- inlet flow state

#### Main output:

- outlet flow state

Besides requiring flow properties, most components have an inlet flow, which they have an effect on, and subsequently produce an outlet flow. This basic behavior is encapsulated in the base class Flow Component, which requires an inlet Flow State and gives the ability to provide a change in temperature, pressure, and mass flow. Subsequently an adjusted copy of the inlet flow is provided as the new outlet flow. Almost all other components inherit from this class.

### 5.1.3. Material

#### Main input:

- yield strength
- density
- thermal conductivity
- poisson ratio

#### Main output:

- -

This component only serves as a container to group the properties of a single material, making them easier to pass along.

### 5.1.4. Pressure Structure

#### Main input:

- structure material
- safety factor
- volume
- max pressure
- geometry factor

#### Main output:

- mass

The Pressure Structure base class encapsulated mass estimation for cylindrical/spherical thin walled pressure vessels, which is why Tank, Gas Generator, Pressurant Tank, and Combustion Chamber all inherit from this class. The mass estimation of these components assumes the components to be thin walled pressure vessels.

The elementary equations for various pressure vessels have been rewritten to use tank volume and a geometry factor, which leads to the general equation shown in eq. (5.1) and geometry factors as listed below.

$$m = \kappa_{sf} \kappa_g \frac{\rho V p_{max}}{\sigma} \quad (5.1)$$

Where  $\kappa_{sf}$  is the structural safety factor,  $\kappa_g$  is a geometry factor,  $\rho$  is the density of the shell material,  $V$  is the internal volume of the shell component,  $p_{max}$  is the maximum expected operating pressure, and  $\sigma$  is the yield strength of the shell material.

Geometry factors (with  $r$  the radius and  $l$  the length of the cylinder):

- $\kappa_g = \frac{3}{2}$  for a sphere
- $\kappa_g = 2$  for a cylinder without caps
- $\kappa_g = 2 + \frac{2r}{l}$  for a cylinder with flat end caps
- $\kappa_g = 3 - \frac{\pi l r^2}{V}$  for a cylinder with hemispherical end caps

## 5.2. Main Components

With the base classes explained, the following subsections discuss the individual components as implemented in RoCAT.

### 5.2.1. Propellant

#### Main input:

- main flow state
- burn time
- margin factor

#### Main output:

- mass
- volume

The main function of the Propellant-component is to calculate the total mass of the fuel or oxidizer using eq. (5.2c), and subsequently the volume using eq. (5.2d). This component receives a flow state even though it is not a flow component. This flow state contains the initial temperature, initial pressure, and specie of the propellant (i.e. fuel or oxidizer). Initial in this case refers to the state in propellant tank. Additionally, the flow state contains the main mass flow rate of the propellant, which is the mass flow rate at the tank exit.

$$m_{fu} = \kappa_p \cdot \dot{m}_{fu} \cdot t_b \quad (5.2a)$$

$$m_{ox} = \kappa_p \cdot \dot{m}_{ox} \cdot t_b \quad (5.2b)$$

$$m_p = m_{fu} + m_{ox} \quad (5.2c)$$

$$V_p = m_{fu} \cdot \rho_{fu} + m_{ox} \cdot \rho_{ox} \quad (5.2d)$$

With  $\kappa_p$  the propellant margin factor,  $\dot{m}_{fu/ox}$  the fuel/oxidizer mass flow (at tank outlet),  $m_{p/fu/ox}$  the propellant/fuel/oxidizer mass,  $t_b$  the burn time, and  $\rho_{fu/ox}$  the fuel/oxidizer density (in the tank).

### 5.2.2. Tank

#### Main input:

- max acceleration
- propellant volume
- ullage factor
- pressurant tank volume
- inlet flow state

#### Main output:

- mass
- outlet flow state

The Tank-component is mainly used to model the mass of the propellant tanks and it inherits from Pressure Structure. The tank is seen as the starting point of the flow process, which is why it is also modeled as a flow component. However, it does not physically have an inlet flow. Nonetheless it is given the main flow state, described in the Propellant section above, as inlet flow and simply returns it unaltered as outlet flow. This is somewhat odd physically, but assures all components are derived from flow component.

Its model is based on that of Kwak et al. [34], which assumes spherical tanks with the pressurant tank submerged in the oxidizer tank. The equations with these assumptions are given here. However, the program also allows for cylindrical tanks with hemispherical caps and an external pressurant tank or one that is submerged in the fuel tank. The tank volumes are as follows:

$$V_{ft} = \kappa_{ull} \cdot V_{fu} \quad (5.3a)$$

$$V_{ot} = \kappa_{ull} \cdot V_{ox} + V_{pt} \quad (5.3b)$$

Where  $V_{ft}$  is the fuel tank volume,  $\kappa_{ull}$  the ullage factor, and  $V_{fu}$  is the fuel volume. The terms for the oxidizer tank volume are identical with the addition of  $V_{pt}$ , the pressurant tank volume.

The mass of each tank is found by combining the tank volume with thin walled theory as seen in eq. (5.1) and selecting the appropriate geometry-factor. The maximum pressure accounts for the acceleration of the rocket as shown for the fuel tank in eq. (5.4) and taken from Kwak[34].

$$p_{ft, lower} = p_{ft, i} + \rho_{fu} a_{max} H_{fu,0} \quad (5.4a)$$

$$p_{ft, upper} = p_{ft, i} + \rho_{fu} a_{max} (H_{fu,0} - r_{ft}) \quad (5.4b)$$

$$p_{ft} = \frac{(p_{ft, lower} + p_{ft, upper})}{2} \quad (5.4c)$$

With  $p_{ft, i}$  the initial fuel tank pressure,  $\rho_{fu}$  the initial fuel density,  $a_{max}$  the maximum acceleration,  $H_{fu,0}$  the initial fuel height in the tank, and  $r_{ft}$  the fuel tank radius.

The initial propellant fluid height is determined from the two equations shown in eq. (5.5) for a spherical fuel tank.

$$V_{ft} - V_{fu} = \pi * H_{ft, cap}^2 \cdot \left( r_{ft} - \frac{1}{3} H_{ft, cap} \right) \quad (5.5a)$$

$$H_{fu,0} = 2r_{ft} - H_{ft, cap} \quad (5.5b)$$

With  $H_{ft, cap}$  the height of the empty volume in the sphere.

### 5.2.3. Pressurant

#### Main input:

- initial fluid state
- final pressure
- propellant tanks ullage factor
- oxidizer volume
- oxidizer tank initial pressure
- fuel volume
- fuel tank initial pressure
- tanks ullage factor
- margin factor

#### Main output:

- mass
- volume

The Pressurant-component is solely used to estimate the pressurant mass and volume. Note that the pressurant margin factor is not the same as the propellant margin factor. The initial fluid state contains the name, initial pressure, and initial temperature of the pressurant. The pressurant mass is calculated using Sutton's approximation for adiabatic expansion of the pressurant gas as given in eq. (5.6) [58]:

$$m_{pr} = \frac{p_p V_p}{R_{pr} T_{pr,0}} \left( \frac{\gamma_{pr}}{1 - p_{pr,1}/p_{pr,0}} \right) \quad (5.6)$$

With  $m_{pr}$  the pressurant mass,  $p_p$  the propellant tank pressure,  $V_p$  the propellant tank volume (filled with pressurant),  $R_{pr}$  the pressurant specific gas constant,  $T_{pr,0}$  the initial pressurant temperature,  $\gamma_{pr}$  the pressurant heat capacity ratio, and  $p_{pr,0}/p_{pr,1}$  the initial and final pressurant pressures.

With the addition of margin factors and expanding this becomes:

$$m_{pr} = \kappa_{pr} \kappa_{ull} \frac{\gamma_{pr}}{R_{pr} T_{pr,0}} \left( \frac{p_{ot} V_{ox} + p_{ft} V_{fu}}{1 - p_{pr,1}/p_{pr,0}} \right) \quad (5.7)$$

With  $\kappa_{pr}$  the pressurant margin factor,  $\kappa_{ull}$  the ullage factor, and  $p_{ft}/p_{ot}$  the fuel and oxidizer tank pressure respectively.

The pressurant volume is found using the ideal gas law as can be seen below.

$$V_{pr,0} = \frac{m_{pr} R_{pr} T_{pr,0}}{p_{pr,0}} \quad (5.8)$$

### 5.2.4. Pressurant Tank

#### Main input:

- pressurant volume
- pressurant initial pressure

#### Main output:

- mass

The Pressurant Tank-component serves to calculate its own mass and it inherits from Pressure Structure. Consequently, it uses eq. (5.1) in combination with the pressurant volume and initial pressure to calculate this mass.

### 5.2.5. Pump

#### Main input:

- inlet flow state
- expected outlet pressure
- efficiency
- specific power

#### Main output:

- power required
- mass
- outlet flow state

The Pump-component calculates the power required to deliver the expected pressure increase, which is done using eq. (5.9), the same as Kwak [34].

$$P_{pu,req} = \frac{\dot{m}_{pu} \Delta p_{pu}}{\rho_p \eta_{pu}} \quad (5.9)$$

With  $\dot{m}_{pu}$  the mass flow through the pump,  $\Delta p_{pu}$  the pressure increase over the pump,  $\rho_p$  the propellant density, and  $\eta_{pu}$  the pump efficiency.

Additionally, the outlet flow state must be determined. The change in pressure is trivial, but the change in temperature must be calculated. This is done using eq. (5.10) by Gulich [22], which is solved implicitly, since the inlet conditions as well as the outlet pressure are known. CoolProp is used to find the enthalpy from temperature and pressure.

$$h_{out} = h_{in} + \frac{P_{pu}}{\dot{m}_{pu}} \quad \rightarrow \quad f(T_{out}, p_{out}) = f(T_{in}, p_{in}) + \frac{P_{pu}}{\dot{m}_{pu}} \quad (5.10)$$

with  $h$  the mass specific enthalpy,  $p$  the pressure,  $T$  the temperature, and  $P_{pu}$  the pump power.

Lastly, the mass of the pumps is determined by assuming a linear relation with the required power. The resulting equation is shown in eq. (5.11).

$$m_{pu} = \frac{P_{pu,req}}{\delta_{p,pu}} \quad (5.11)$$

With  $m_{pu}$  the pump mass [kg], and  $\delta_{p,pu}$  the pump specific power [W/kg]

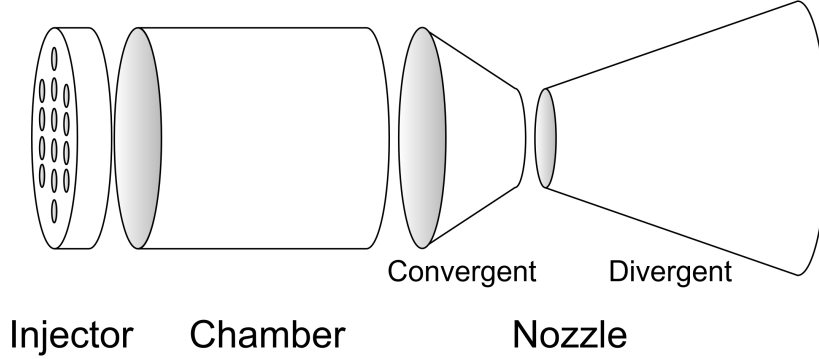


Figure 5.1: Schematic overview of the thrust chamber and injector shell components

### 5.2.6. Injector

#### Main input:

- inlet flow states
- pressure drop
- combustion chamber area

#### Main output:

- mass
- outlet flow state

The injector combines the oxidizer and fuel flows. A pressure drop over the injector can be manually given or is calculated using a linear relation between the drop and chamber pressure as shown in eq. (5.12). The pressure drop factor assumed for the injector is 0.15 in accordance with Humble [28], but can be manually given as well.

$$\Delta p = \kappa_{\Delta p} \cdot p_{cc} \quad (5.12)$$

With  $\Delta p$  the pressure drop over the component,  $\kappa_{\Delta p}$  the pressure drop factor, and  $p_{cc}$  the chamber pressure.

The mass of the injector is modeled as two uniformly loaded circular plates with fixed edges, both of which need to withstand the chamber pressure (at start up). Combining Roark's stress for such a plate [9] and the shell mass equation, eq. (5.13), leads to the injector mass as given by eq. (5.14).

$$m = S \cdot \rho \cdot t \quad (5.13)$$

Where  $S$  is the surface area of the component,  $\rho$  the density of the component's material, and  $t$  the thickness of the component.

$$m_{inj} = 2 \left( \kappa_{inj} \rho_{inj,m} A_{cc} \sqrt{(1 + \nu_{inj,m}) \frac{3 p_{cc} r_{cc}^2}{4 \sigma_{inj,m}}} \right) \quad (5.14)$$

Where  $\kappa_{inj}$  is the injector safety factor,  $\rho_{inj,m}$  the injector material density,  $r_{cc}$  the chamber area,  $r_{cc}$  the chamber radius,  $\nu_{inj,m}$  the injector material Poisson's ratio,  $p_{cc}$  the chamber pressure, and  $\sigma_{inj}$  the injector material yield strength.

### 5.2.7. Thrust Chamber

#### Main input:

- nozzle
- chamber

#### Main output:

- mass
- length
- surface area
- get radius()
- get mach()

The Thrust Chamber-component acts as a container that integrates the nozzle, and combustion chamber components. Mainly such that a total surface area and combined mass can be calculated. Additionally, the mach number and cross sectional radius can be found for any distance from the throat within the thrust chamber. Both of these functions are required to calculate the heat transfer, as is discussed in section 5.2.11. Its mass is simply a sum of its constituent masses, as shown in eq. (5.15).

$$m_{tc} = m_{inj} + m_{noz} + m_{cc} \quad (5.15)$$

### 5.2.8. Combustion Chamber

#### Main input:

- throat area
- characteristic length
- combustion chamber pressure
- area ratio chamber throat
- inlet flow state

#### Main output:

- mass
- volume
- area
- surface area
- outlet flow state

The Combustion Chamber-component sizes its volume and area, through eq. (5.16a) and eq. (5.16b) respectively. The combustion chamber mass is found with eq. (5.1) as inherited from Pressure Structure. Its geometry factor is set to 2 as its assumed to be a cylinder without end caps, which is also shown in fig. 5.1. Table 5.1 shows the assumed characteristic lengths for each propellant combination, while eq. (5.16c) shows the equation to estimate the chamber throat area ratio, both are taken from Humble [28].

$$V_{cc} = L^* \cdot A_{th} \quad (5.16a)$$

$$A_{cc} = \left( \frac{A_{cc}}{A_{th}} \right) A_{th} \quad (5.16b)$$

$$\left( \frac{A_{cc}}{A_{th}} \right) = 0.469479 \cdot A_{th}^{-0.3} + 1.25 \quad (5.16c)$$

With  $L^*$  the characteristic length,  $A_{th}$  the throat area, and  $\left( \frac{A_{cc}}{A_{th}} \right)$  the chamber-throat area ratio.

Propellants	$L^*$ [m]
RP-1/LOX	1.145
LH2/LOX	0.890
LCH4/LOX	1.450

Table 5.1: Data from Humble [28]

## 5.2.9. Nozzle

### Main input:

- throat area
- expansion ratio
- chamber pressure
- divergent throat half angle
- convergent throat half angle
- area ratio chamber throat
- inlet flow state

### Main output:

- get radius()
- mass
- surface area
- exit area
- length
- outlet flow state

The Nozzle-component models the nozzle contour, which gives the radius at any distance from the throat, the surface area, and the length of the nozzle. The first two are required for modeling the convective and radiative heat transfer respectively, while the last is needed for general sizing. The contour structure is shown in fig. 5.2 with  $r_{l,1-3}$  the longitudinal radii of various bends,  $\theta$  the divergence half angles,  $r$  the radii of the chamber, throat, and exit, and  $l$  the lengths of the convergent and divergent section.

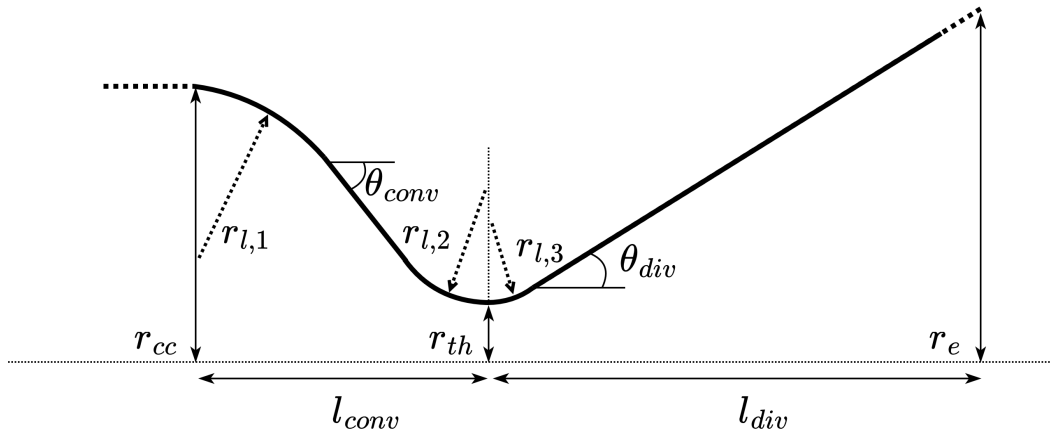


Figure 5.2: Schematic overview of nozzle longitudinal cross-section

The longitudinal radii are found relative to the chamber or throat radius as shown in eq. (5.17), if  $\kappa_{rl,1-3}$  are not provided manually they are assumed to be 1.0, 0.8, and 0.328 as suggested by Huzel&Huang [29].

$$r_{l,1} = \kappa_{rl,1} \cdot r_{cc} \quad (5.17a)$$

$$r_{l,2} = \kappa_{rl,2} \cdot r_{th} \quad (5.17b)$$

$$r_{l,3} = \kappa_{rl,3} \cdot r_{th} \quad (5.17c)$$

The mass of the nozzle is determined as a shell component, see eq. (5.13). Both the divergent and convergent parts of the nozzle are simplified as a frustum for determination of the surface area, as shown in fig. 5.1. For simplicity the thickness is set equal to the chamber thickness, as suggested by Humble [28]. This leads to eq. (5.18) for the mass of the complete nozzle.

$$m_{noz} = \rho_{noz,m} \cdot \pi \left( (r_{cc} + r_{th}) l_{con} + (r_e + r_{th}) l_{div} \right) \cdot \frac{p_{cc} r_{cc}}{\sigma_{cc,m}} \quad (5.18)$$

With  $\rho_{noz}$  the nozzle material density,  $r_{cc}/r_{th}/r_e$  the radius of the combustion chamber/throat/nozzle exit,  $l_{con}/l_{div}$  the length of the convergent/divergent nozzle section,  $p_{cc}$  the combustion chamber pressure,  $\sigma_{cc}$  the combustion chamber material yield strength.

### 5.2.10. Heat Exchanger

#### Main input:

- inlet flow state
- heat flow rate
- max outlet temperature
- pressure drop

#### Main output:

- outlet flow state
- mass

The Heat Exchanger-component serves mainly to calculate the increase in temperature over the cooling channels. If the pressure drop is not given manually, it is calculated assuming a linear relation between the pressure drop and chamber pressure, synonymous to eq. (5.12). The outlet temperature is found from eq. (5.19), in a similar manor as described for the Pump-component. The heat flow rate itself is found by the Heat Transfer Section-component using eq. (5.25), which is explained below.

$$h_{\text{out}} = h_{\text{in}} + \frac{\dot{Q}}{\dot{m}} \quad \rightarrow \quad f(T_{\text{out}}, p_{\text{out}}) = f(T_{\text{in}}, p_{\text{in}}) + \frac{\dot{Q}}{\dot{m}} \quad (5.19)$$

With  $\dot{m}$  the coolant mass flow [kg/s],  $\dot{Q}$  the heat flow rate through the wall [W],  $h$  the specific enthalpy of the coolant [J/kg],  $T$  the temperature of the coolant [K],  $p$  the pressure of the coolant [Pa], and  $_{\text{in/out}}$  denoting the inlet and outlet conditions.

The estimation of the mass of the Heat Exchanger-component has not been implemented.

### 5.2.11. Heat Transfer Section

#### Main input:

- thrust chamber
- chamber flow state
- hot gas emissivity
- wall emissivity
- wall temperature
- min distance
- max distance/max area ratio

#### Main output:

- heat flow rate

The Heat Transfer Section-component has as sole purpose to calculate the total, i.e. convective and radiative, heat flow rate for a section of the thrust chamber wall. The section to be cooled can be indicated using a min/max distance (measured from the throat in direction of the nozzle exit) or area ratio, e.g. cooling up to an area ratio of 5 in the nozzle. Multiple Heat Transfer Sections and Heat Exchangers can be created to model engines with more than one coolant loop, however this report only discusses single cooling loop configurations.

#### Convective Heat Transfer

To estimate the convective heat flux eq. (5.20) is used. The wall temperature is assumed to be constant, while the heat transfer coefficient and reference temperature are evaluated locally in the one-dimensional thrust chamber.

$$q_{\alpha} = h_{\alpha} (T_{\text{ref}} - T_w) \quad (5.20)$$

With  $q_{\alpha}$  the convective heat flux [ $W/m^2$ ],  $h_{\alpha}$  the convective heat transfer coefficient [ $W/(Km^2)$ ],  $T_{\text{ref}}$  the reference temperature of the hot gas inside the thrust chamber,  $T_w$  the temperature of the thrust chamber wall.

The local adiabatic wall temperature is taken as the reference temp, shown in eq. (5.21a). If the recovery factor is not given manually it is estimated from the Prandtl-number as shown in eq. (5.21b). The local static temperature is estimated using isentropic flow relations and it is assumed the stagnation temperature is equal

to the combustion temperature, as shown in eq. (5.21c). The local Mach number is found implicitly from another isentropic flow relation, shown in eq. (5.21d).

$$(T_w)_{ad} = T \cdot \left( 1 + r \frac{\gamma - 1}{2} M^2 \right) \quad (5.21a)$$

$$r = Pr^{1/3} \quad (5.21b)$$

$$T_{hg} = T_{hg,0} \left( 1 + \frac{\gamma - 1}{2} M^2 \right)^{-1} \quad (5.21c)$$

$$\frac{A}{A_*} = \frac{1}{M} \left( \frac{\frac{\gamma + 1}{2}}{1 + \frac{\gamma - 1}{2} M^2} \right)^{\frac{\gamma + 1}{2(1 - \gamma)}} \quad (5.21d)$$

With  $T_{hg}$  the local static temperature of the hot gas [K],  $T_{hg,0}$  the (constant) hot gas stagnation temperature [K],  $\gamma$  the heat capacity ratio [-],  $M$  the local Mach number [-],  $(T_w)_{ad}$  the local adiabatic wall temperature [K],  $r$  the recovery factor [-], and  $Pr$  the Prandtl-number[-].

The heat transfer coefficient in eq. (5.20) can be estimated using various methods. The standard Bartz, modified Bartz, and Cornelisse methods [3, 17] have all be implemented in RoCAT, but the modified Bartz method has been used throughout this report. The general equation for both the Modified Bartz and Cornelisse method is shown eq. (5.22a) and their coefficients in table 5.2. The film temperature has been assumed to be a combination of the wall, static, and reference temperature, as was done by Ziebland [65] and shown in eq. (5.22b).

$$h_\alpha = 1.213a \frac{m^{0.8} \mu^{0.2} c_p}{D^{1.8} Pr^b} \left( \frac{T_{hg,0}}{T_{film}} \right)^c \quad (5.22a)$$

$$T_{film} = 0.5T_w + 0.22(T_w)_{ad} + 0.28T_{hg} \quad (5.22b)$$

With  $a, b, c$  coefficients shown in table 5.2[-],  $m$  the mass flow,  $\mu$  the dynamic viscosity of the hot gas [ $Pa \cdot s$ ],  $c_p$  the specific heat capacity of the hot gas [ $J/kg$ ],  $D$  the local diameter of the thrust chamber, [ $kg/s$ ]  $T_{film}$  the film temperature [K], and  $T_w$  the wall temperature [K].

Method	a	b	c
Modified Bartz [3]	0.026	0.6	0.86
Cornelisse et al. [17]	0.023	2/3	0

Table 5.2: Coefficients for the calculation of the convective heat transfer coefficient for two methods.

In eq. (5.22a) the mass flow is constant, the temperatures and diameter are known locally, and ideally the transport properties (viscosity, Prandtl-number, and specific heat capacity) would be known locally as well. They can be estimated by CEA at various points in the thrust chamber, but this was too computationally intensive and thus they are taken to be constant and equal to the value in the chamber.

Combining these assumptions and eqs. (5.20) to (5.22) the convective heat flux becomes a function of the local diameter i.e. the local radius.

$$\dot{Q}_\alpha = \int_{x_{min}}^{x_{max}} q_\alpha \cdot 2\pi r dx \quad (5.23)$$

With  $\dot{Q}_\alpha$  the convective heat flow rate [W],  $x$  the distance from the throat [m],  $q_\alpha(x)$  the local heat flux [ $W/m^2$ ], and  $r(x)$  the local cross sectional radius of the thrust chamber [m].

### Radiative Heat Transfer

The radiative heat flux is estimated assuming the thrust chamber surface to be a grey body and the hot gas to be a grey medium. This leads to eq. (5.24) as given by Bejan [4]. Similar to the convective heat flux, the radiative heat flux is a function of the local radius.

$$q_r = \frac{\bar{\sigma} \cdot (T_{hg}^4 - T_w^4)}{\frac{1}{\epsilon_{hg}} + \frac{1}{\epsilon_w} - 1} \quad (5.24)$$

With  $q_r$  the radiative heat flux [ $W/m^2$ ],  $\bar{\sigma}$  the Stefan-Boltzmann constant [ $W/(m^2K^4)$ ],  $T_{hg}$  the local static temperature of the hot gas [ $K$ ],  $T_w$  the wall temperature [ $K$ ],  $\epsilon_{hg}$  the hot gas emissivity [-], and  $\epsilon_w$  the wall emissivity [-].

### Total Heat Transfer

With both the convective and radiative heat flux defined, they can be combined and integrated over (the section of) the thrust chamber. They are both functions of the local radius, which in turn is a function of the distance from the throat (positive towards the exit) defined by the Thrust Chamber-component. Consequently, the total heat flow rate can be found with eq. (5.25) in which both heat fluxes and the radius are functions of the distance from the throat.

$$\dot{Q} = \int_{x_{min}}^{x_{max}} 2\pi r (q_\alpha + q_r) dx \quad (5.25)$$

With  $\dot{Q}$  the total heat flow rate [ $W$ ],  $x$  the distance from the throat [ $m$ ],  $q_\alpha/q_r$  the local convective/radiative heat flux [ $W/m^2$ ], and  $r$  the local cross sectional radius of the thrust chamber [ $m$ ].

#### 5.2.12. Splitter

##### Main input:

- inlet flow state
- req mass flows

##### Main output:

- outlet flow states

The Splitter-component has as singular function to split the inlet flow state into multiple outlet flow states with the same state, but different mass flows. In this report it is only ever used to split it into two flows, thus this case is shown eq. (5.26).

$$\dot{m}_{out,1} = \dot{m}_{out,req} \quad (5.26a)$$

$$\dot{m}_{out,2} = \dot{m}_{in} - \dot{m}_{out,req} \quad (5.26b)$$

#### 5.2.13. Merger

##### Main input:

- inlet flow states

- outlet flow state

##### Main output:

The Merger-component merges multiple flows. It is assumed the inlet flow states have the same heat capacity, such that the outlet temperature are the mass average of the inlet temperatures. The outlet pressure is equal to the inlet pressures, which are required to all be equal. Additionally, it can be made to throw an error if the inlet flows are not the same propellant and/or pressure.

## 5.3. Open Cycle Components

This section discusses the turbine and turbine exhaust, which are both present in any of the open cycles, i.e. gas generator and open expander cycles.

### 5.3.1. Turbine

#### Main input:

- inlet flow state
- power required
- efficiency
- specific power
- pressure ratio
- outlet pressure

#### Main output:

- mass flow required
- mass
- outlet flow state

The Turbine-component main function is to calculate the mass flow required to provide the power to drive the pumps, for which eq. (5.27) is used.

$$\dot{m}_{tu} = \frac{P_{tu,req}}{\eta_{tu} c_p T_{in,0} \left( 1 - \left( \frac{p_{out}}{p_{in,0}} \right)^{\frac{\gamma-1}{\gamma}} \right)} \quad (5.27)$$

With  $\dot{m}_{tu}$  the turbine mass flow required [kg/s],  $P_{tu,req}$  the power required from the turbine [W],  $\eta_{tu}$  the turbine efficiency,  $c_p$  the specific heat capacity of the flow [J/kg],  $T_{in}$  the inlet stagnation temperature [K],  $p_{out}$  the outlet static pressure,  $p_{in,0}$  the inlet stagnation pressure.

The mass of the turbine is calculated using the specific power, similar to the pumps, as shown in eq. (5.28).

$$m_{tu} = \frac{P_{tu,req}}{\delta_{p,tu}} \quad (5.28)$$

With  $m_{tu}$  the turbine mass [kg], and  $\delta_{p,tu}$  the turbine specific power [W/kg]

### 5.3.2. Turbine Exhaust

#### Main input:

- inlet flow state
- expansion ratio
- exit pressure
- ambient pressure

#### Main output:

- thrust
- mass
- outlet flow state

The Secondary Exhaust-component calculates the thrust provided by the turbine exhaust gasses that are dumped overboard. To do so it uses general Ideal Rocket Theory equations where the inlet conditions are equated to chamber conditions. Either the expansion ratio or exit pressure can be provided with the other being found from eq. (5.29). The thrust is subsequently found from eq. (5.31). If no ambient pressure is provided ideal expansion is assumed, i.e.  $p_e = p_a$ . No correction/quality factors for the turbine exhaust are used automatically in RoCAT, since no data on very fuel-rich combustion was found for multiple propellants. However, a single combined quality factor can be given manually.

$$\varepsilon_{exh} = \frac{\Gamma}{\sqrt{\frac{2\gamma}{\gamma-1} \cdot \left( \frac{p_e}{p_{in}} \right)^{\frac{2}{\gamma}} \left( 1 - \left( \frac{p_e}{p_{in}} \right)^{\frac{\gamma-1}{\gamma}} \right)}} \quad (5.29)$$

$$\Gamma = \sqrt{\gamma} \cdot \left( \frac{2}{\gamma+1} \right)^{\frac{\gamma+1}{2(\gamma-1)}} \quad (5.30)$$

$$C_{F,exh} = \Gamma \cdot \sqrt{\frac{2\gamma}{\gamma-1} \cdot \left( 1 - \left( \frac{p_e}{p_{in}} \right)^{\frac{\gamma-1}{\gamma}} \right)} + \left[ \frac{p_e}{p_{in}} - \frac{p_a}{p_{in}} \right] \cdot \varepsilon \quad (5.31a)$$

$$c_{exh}^* = \frac{1}{\Gamma} \cdot \sqrt{R \cdot T_{in}} \quad (5.31b)$$

$$F_{T,exh} = \dot{m}_{exh} C_{F,exh} c_{exh}^* \quad (5.31c)$$

With  $\varepsilon_{exh}$  the expansion/area ratio of the turbine exhaust [-],  $\Gamma$  the "Vandenkerckhove"-function [-],  $\gamma$  the heat capacity ratio of the flow [-],  $p_e/p_{in}$  the exit/inlet pressure of the turbine exhaust [Pa],  $C_{F,exh}$  the thrust coefficient of the turbine exhaust [-],  $p_a$  the ambient pressure [Pa],  $c_{exh}^*$  the characteristic velocity of the turbine exhaust [m/s],  $R$  the specific gas constant of the flow [J/(kgK)],  $T_{in}$  the inlet temperature of the flow [K],  $F_{T,exh}$  the thrust of the exhaust [N], and  $\dot{m}_{exh}$  the mass flow through the exhaust [kg/s].

The mass of the secondary exhaust is found from similar relations as the Nozzle-components, see eq. (5.18) (inputs for mass calculation not shown at the start of this subsection).

## 5.4. Class Specific Components

### 5.4.1. Gas Generator

#### Main input:

- fuel inlet flow state
- oxidizer inlet flow state
- gas generator chamber pressure
- maximum outlet temperature
- stay time

#### Main output:

- outlet flow state
- mass

The gas generator component combines a fuel and oxidizer flow and calculates the combusted outlet flow in which their combination results. In addition the mass is calculated using a volume estimate based on the stay time.

The gas generator is modeled generally the same as was done by Kwak [34], but with some clear differences. Kwak's approach as well as the differences are discussed in the following paragraphs.

In Kwak's approach the outlet temperature of the gas generator is assumed to be equal to the maximum turbine temperature, which is given as an input as well as the flow properties inside the gas generator. Therefore, the combustion modeling was not required in Kwak's model. However, Kwak also provided the gas generator  $^{o/F}$ -ratio manually, while the gas generator combustion temperature is directly dependent on it. This makes it possible for values that do not match to be provided simultaneously. To fix this RoCAT uses CEA to find the  $^{o/F}$ -ratio that matches the given maximum turbine temperature. Additionally, by using CEA, various other properties of the gas leaving the gas generator can now be found automatically as well, instead of being required as inputs, e.g. the gas density required to calculate the gas generator volume in eq. (5.33) (given later in this section) and the specific heat capacity and heat capacity ratio, which are both required to calculate the turbine power in eq. (5.27).

This method works well for most propellants, however, it was found that CEA is not very accurate when calculating highly fuel-rich RP-1/LOX combustion temperatures. This was found to be the case for all fuels containing long organic compounds by Kauffmann [32] and Mota [43]. Solutions for adapting CEA to counteract this inaccuracy are suggested by Kauffmann [32] as well as Cho [15]. However, for RoCAT a simple linear relation was applied, as given by Choi [16] and shown in eq. (5.32).

$$(^{o/F})_{gg} = \frac{T_{gg}}{1550.3} - 409.3 \quad (5.32)$$

Based on the data points given by Choi [16] this relation is accurate for  $^{o/F}$ -ratios between 0.25-0.45. Consequently, the relation only replaces CEA when an  $^{o/F}$ -ratio below 0.45 is found and warns the user if the relation results in an  $^{o/F}$ -ratio below 0.25. Figure 5.3 shows that this relation matches much better with gas generator data of known engines as well as the design point chosen by Kwak [34]. The gas generator pressures of the

engines shown in fig. 5.3 are given in table 5.3. Note that the relation is independent of this gas generator pressure, while it ideally would also account for it.

Of course the option to give the mixture ratio manually is also still present. If it is given manually it is up to the user to ensure the gas generator combustion temperature (i.e. maximum turbine temperature) and gas generator mixture ratio are compatible.

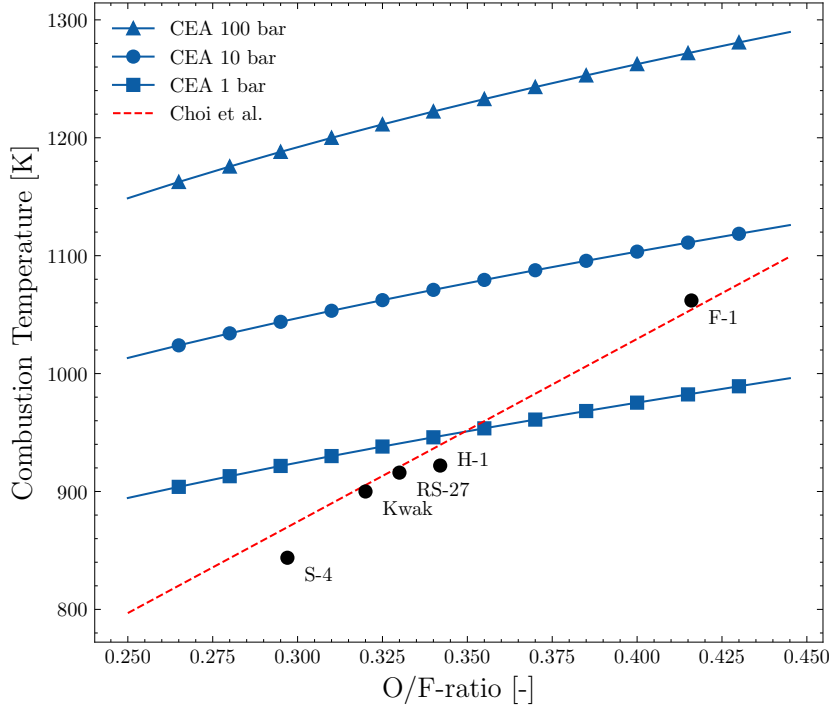


Figure 5.3: Fuel-rich RP-1/LOX Combustion Temperature (Engine Data from McHugh [41])

Engine	F-1	H-1	RS-27	Kwak	S-4
GG Pressure [bar]	77.6	41.3	48.7	30-100	46.0

Table 5.3: Gas generator pressures for engines shown in fig. 5.3

The gas generator is assumed to be a spherical pressure vessel, thus eq. (5.1) is used. The volume is found from eq. (5.33), which was also used by Kwak [34] and can be found in many other works, e.g. by NASA [45], Rachov [48], Moroz [42], and Huzel&Huang[29]. Additionally, all use similar values of around 10 ms for the stay time. However, the volumes found through this relation were intuitively deemed quite low. Unfortunately, no gas generator volume or mass data could be found to substantiate this suspicion further. A characteristic length based sizing method for the gas generator as given by Ernst [20] was tried instead. Both methods were compared, but the latter was found to generally result in even smaller volumes. Thus, eq. (5.33) was ultimately used for RoCAT.

$$V_{gg} = \frac{t_s \dot{m}_{gg}}{\rho_{gg}} \quad (5.33)$$

With  $t_s$  the gas generator stay time,  $\dot{m}_{gg}$  the gas generator mass flow, and  $\rho_{gg}$  the density of the gas generator gas.

### 5.4.2. Electrical Component

#### Main input:

- output power
- electric efficiency
- specific power

#### Main output:

- input power
- mass

The Electrical Component is an abstract base class that serves as the basis for Electric Motor, Inverter, and Battery. All of them consequently calculate their input power and mass using eq. (5.34) and eq. (5.35) respectively. Thus a linear relation between the mass of these components and their power is assumed.

$$P_{in} = P_{out}/\eta \quad (5.34)$$

$$m = \frac{P_{out}}{\delta_P} \quad (5.35)$$

With  $P_{out}$  the output power,  $\eta$  the electric efficiency, and  $\delta_P$  the specific power.

### 5.4.3. Electric Motor

#### Main input:

- output power
- electric efficiency
- specific power
- electric heat loss factor
- magnet temp limit
- oxidizer leak factor
- oxidizer pump inlet flow state

#### Main output:

- input power
- mass

The Electric Motor-component inherits from Electrical Component and thus calculates an input power and mass. Additionally, the electric motor warns the user if the expected cooling of electric motor through oxidizer leakage is insufficient, which might demagnetize the permanent magnets inside the electric motor. The warning condition is shown in eq. (5.36).

$$\frac{P_{em,out}\kappa_{em,loss}}{c_{p,ox}(T_{mag} - T_{ox})} > (\dot{m}_{op} \cdot \kappa_{ox,leak}) \quad (5.36)$$

With  $P_{em,out}$  the electric motor output power [W],  $\kappa_{em,loss}$  the electric heat loss factor [-],  $c_{p,ox}$  the oxidizer specific heat capacity [J/kg],  $T_{mag}$  the magnet temperature limit [K],  $T_{ox}$  the oxidizer pump inlet temperature [K],  $\dot{m}_{op}$  the oxidizer pump mass flow [kg/s], and  $\kappa_{ox,leak}$  the oxidizer leak factor [-].

### 5.4.4. Inverter

#### Main input:

- output power
- electric efficiency
- specific power

#### Main output:

- input power
- mass

The Inverter-component inherits from the Electrical Component and makes no other calculations than made by Electrical Component (mass and input power).

### 5.4.5. Battery

#### Main input:

- output power
- specific power
- specific energy
- battery packing factor
- burn time

#### Main output:

- input power
- mass
- power heat loss

The Battery-component inherits from Electrical Component, but differs in quite a few ways. Firstly, it does not require an electric efficiency. This efficiency is calculated instead using the empirical relation as given by Kwak [34], which is shown in eq. (5.37). The discharge time is assumed to be equal to the burn time.

$$\eta_{bat} = 0.093 \cdot \ln(t_d) + 0.3301 \quad (5.37)$$

With  $\eta_{bat}$  the electric (energy) efficiency of the battery [-], and  $t_d$  the discharge time of the battery [s].

The power heat loss is required to calculate the cooling flow in the Battery Cooler and is given by eq. (5.38), which assumes that all of the energy inefficiency of the battery is dissipated into heat.

$$\dot{Q}_{bat,loss} = P_{bat,in} \cdot (1 - \eta_{bat}) \quad (5.38)$$

With  $\dot{Q}_{bat,loss}$  the battery heat loss flow rate [W], and  $P_{bat,in}$  the battery "input" power [W].

The mass of the battery is calculated using the equations shown in eq. (5.39) and can be either limited in energy or power with the larger of the two determining the actual battery mass.

$$m_{bat,P} = \kappa_{bat} \frac{P_{bat,out}}{\delta_{P,bat}} \quad (5.39a)$$

$$m_{bat,E} = \kappa_{bat} \frac{P_{bat,out} \cdot t_d}{\eta_{bat} \cdot \delta_{E,bat}} \quad (5.39b)$$

$$m_{bat} = \text{MAX}(m_{bat,E}, m_{bat,P}) \quad (5.39c)$$

With  $m_{bat,P}/m_{bat,E}$  the power/energy limited battery mass [kg],  $\kappa_{bat}$  the battery packing factor [-],  $\delta_{P,bat}$  the battery specific power [W/kg],  $\delta_{E,bat}$  the battery specific energy [J/kg], and  $P_{bat,out}$  the battery output power [W].

### 5.4.6. Battery Cooler

#### Main input:

- inlet flow state
- power heat loss
- coolant temp change

#### Main output:

- outlet flow state
- mass

The Battery Cooler-component calculates the coolant mass flow required to cool the battery. This is done using eq. (5.40) with a maximum change in coolant temperature required as input. This is the same as used by Kwak [34] except that the coolant specific heat is calculated through CoolProp by the flow state instead of being given directly as input.

$$\dot{m}_{bat,cl} = \frac{\dot{Q}_{bat,loss}}{c_{p,cl} \Delta T_{cl}} = \frac{P_{bat} (1 - \eta_{bat})}{c_{p,cl} \Delta T_{cl}} \quad (5.40)$$

With  $c_{p,cl}$  the specific heat at constant pressure of the coolant (i.e. fuel),  $\dot{m}_{cl}$  the coolant mass flow, and  $\Delta T_{cl}$  the maximum temperature increase of the coolant.

The mass estimation of the battery cooler has not been implemented.

### 5.5. Component Connection

In fig. 5.4 an example simplified schematic of the electric-pump cycle can be seen. It gives an indication as to how the components are interconnected. Only the most crucial inputs and outputs are shown. If components are connected by a double line the flow state is given to the downstream component (i.e. specie, temperature, pressure, and mass flow). A more detailed discussion of cycle configurations is given in the next chapter.

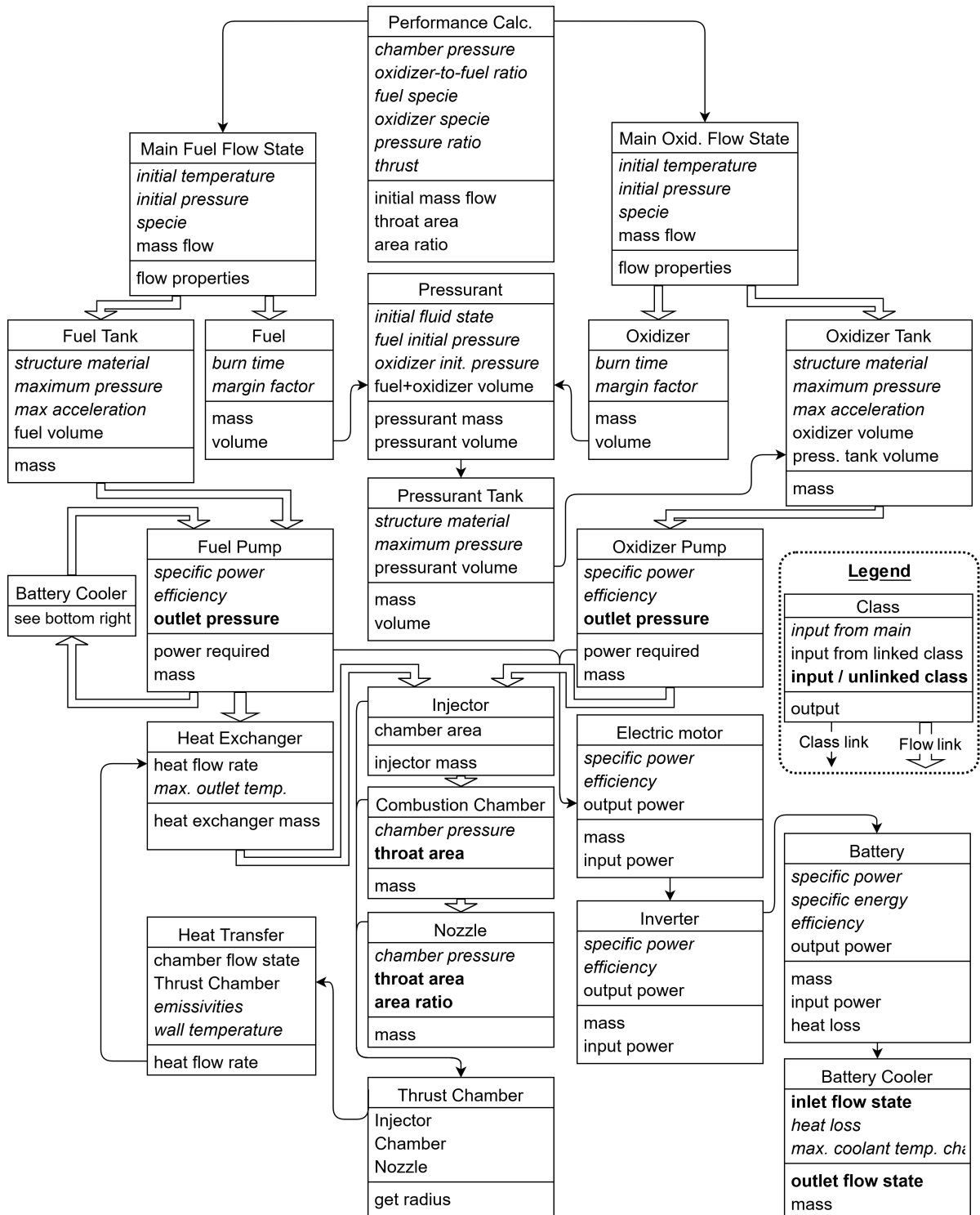


Figure 5.4: Schematic overview of electric-pump cycle component connections

## Input values

This section gives the default input values. Generally, values have been taken from Kwak et al. [34] wherever possible. Table 5.4 gives the default inputs values that are used for all engines in this report unless specified otherwise. Values that are not taken from Kwak are the bend ratios and throat half angles. Both are taken from Huzel and Huang [29] with the former suggested and the latter being the mean of suggested ranges. The pressure drop factors are taken from Humble [28], while the emissivities are suggested by Zandbergen [64]. Table 5.5 gives several default inputs that are propellant or propellant mixture dependent. Initial temperatures are taken such that CoolProp density is roughly equal to the densities provided by Kwak. Characteristic lengths and oxidizer-to-fuel ratios are suggested by Humble [28]. The quality factors have been determined from several engines, most of which are discussed in chapter 7. These are only used if CEA is set to calculate frozen flow. If shifting equilibrium is used a quality factor of 0.9028 is used instead, as calculated by Ernst [20]. Lastly, if no ambient pressure is provided, it is assumed to be equal to the exit pressure, i.e. ideal expansion is assumed.

Parameter	Symbol	Unit	Value
max acceleration	$a_{max}$	[g <sub>0</sub> ]	4.5
oxidizer tank pressure	$p_{ot}$	bar	4.0
fuel tank pressure	$p_{ft}$	bar	2.5
oxidizer tank temperature	$T_{ot}$	K	90.19
pressurant initial temperature	$T_{pr,0}$	K	100
pressurant initial pressure	$p_{pr,0}$	bar	270
pressurant final pressure	$p_{pr,f}$	bar	50
pressurant margin factor	$\kappa_{pr}$	-	1.1
pressurant tank safety factor	$\kappa_{prt,sf}$	-	1.2
propellant margin factor	$\kappa_p$	-	1.01
tanks structural factor	$\kappa_{t,st}$	-	2.5
ullage volume factor	$\kappa_{ull}$	-	1.08
combustion chamber safety factor	$\kappa_{cc,sf}$	-	1.5
injector safety factor	$\kappa_{inj,sf}$	-	1.5
nozzle safety factor	$\kappa_{noz,sf}$	-	1.5
convergent throat bend ratio	$\kappa_{rl,1}$	-	0.8
convergent chamber bend ratio	$\kappa_{rl,2}$	-	1
divergent bend ratio	$\kappa_{rl,3}$	-	0.328
divergent throat half angle	$\theta_{div}$	°	15
convergent half angle	$\theta_{conv}$	°	30
injector pressure drop factor	$\kappa_{inj,\Delta p}$	-	0.15
cooling pressure drop factor	$\kappa_{cs,\Delta p}$	-	0.4
maximum wall temperature	$T_{w,max}$	K	850
thrust chamber wall emissivity	$\epsilon_w$	-	0.8
hot gas emissivity	$\epsilon_{hg}$	-	0.1
shaft mechanical efficiency	$\eta_{shaft}$	-	0.95
fuel pump efficiency	$\eta_{fp}$	-	0.61
oxidizer pump efficiency	$\eta_{op}$	-	0.66
fuel pump specific power	$\delta_{p,fp}$	kW/kg	15.0
oxidizer pump specific power	$\delta_{p,op}$	kW/kg	20.0
ambient pressure	$p_a$	bar	$p_e$

Table 5.4: Default input values

Propellant	$o/F$ -ratio	Quality Factor [-]	Characteristic Length [m]	Initial Temperature [K]
LH2(/LOX)	5.60	0.98	0.89	20.25
RP1(/LOX)	2.45	0.95	1.145	263.60
LCH4(/LOX)	3.60	0.97	1.45	111.00
LOX	-	-	-	90.19

Table 5.5: Default inputs based on propellant or propellant mixture.

Table 5.6 gives the default fluids and materials, which are largely self explanatory. The properties of the materials are given in appendix B and the numbered materials refer to materials defined by the inputs of Kwak [34].

Parameter	Value
oxidizer	Liquid Oxygen
pressurant	Helium
fuel tank material	Material1
oxidizer tank material	Material1
pressurant tank material	Material2
combustion chamber material	NarloyZ
injector material	NarloyZ
nozzle material	Inconel600

Table 5.6: Default materials and fluids.

Lastly, the cycles have unique parameters that also have default values, which are given in table 5.7 for the electric-pump cycle and in table 5.8 for the gas generator and open expander cycle. All parameters in the latter table are present in both cycles except for the parameters which contain the text "gas generator", which are only present in the gas generator cycle. All inputs in both tables are equal to those provided by Kwak [34].

Parameter	Symbol	Unit	Value
electric motor specific power	$\delta_{P,em}$	kW/kg	5.3
inverter specific power	$\delta_{P,inv}$	kW/kg	60.0
battery specific power	$\delta_{P,batt}$	kW/kg	6.95
battery specific energy	$\delta_{E,batt}$	kJ/kg	712.8
electric motor efficiency	$\eta_{em}$	-	0.95
inverter efficiency	$\eta_{inv}$	-	0.85
battery structural factor	$\kappa_{bat,st}$	-	1.2
battery coolant temperature change	$\Delta T_{bat,cl}$	K	40
electric motor magnet temp limit	$T_{mag,max}$	K	400
electric motor heat loss factor	$\kappa_{em,loss}$	-	0.015
electric motor ox leak factor	$\kappa_{ox,leak}$	-	0.005

Table 5.7: Default inputs for the electric-pump cycle.

Parameter	Symbol	Unit	Value
turbine pressure ratio	$p_{tu,in}/p_{tu,out}$	-	27
turbine efficiency	$\eta_{tu}$	-	0.52
turbine maximum temperature	$T_{tu,max}$	K	900
turbopump specific power	$\delta_{P,tp}$	kW/kg	13.5
turbine exhaust expansion ratio	$\epsilon_{exh}$	-	20
turbine exhaust material	-	-	Inconel600
turbine exhaust safety factor	$\kappa_{tu,sf}$	-	1.5
gas generator stay time	$t_{s,gg}$	K	0.01
gas generator structural factor	$\kappa_{gg,st}$	K	2.5
gas generator material	-	-	Material3

Table 5.8: Default input for the gas generator cycle and open expander cycle



# 6

## Engine Cycle Implementation

This chapter combines the information from chapter 4 and chapter 5 and provides the theory necessary to integrate the component models into a complete cycle model. In the implementation of the cycles a modular approach has been taken, just like for the components, and the principles of object-oriented programming have been applied. Shared functionality and components of the cycles are therefore grouped in two abstract base classes as shown in fig. 6.1. These base classes are first discussed and are then followed by the individual cycles. Lastly, the implemented cycle variants are discussed. For the component numbering used in this chapter see table 4.1.

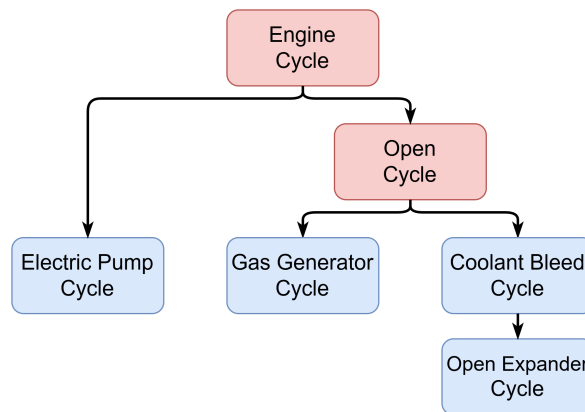


Figure 6.1: Overview of main (blue) cycles' dependence on the abstract (red) base classes.

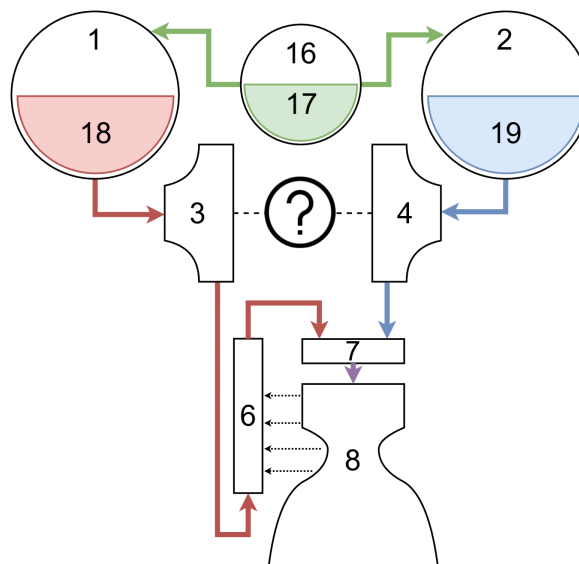


Figure 6.2: Cycle schematic of the abstract base class "Engine Cycle"

## 6.1. Engine Cycle

The first abstract base class is the Engine Cycle. This is the main cycle on which all the others are built. Consequently, it groups the components and functionality that all the cycles share. This leads to the simplified cycle schematic as shown in fig. 6.2. As can be seen most of the components are already implemented and the missing components are those that are responsible for driving the pumps. These components are added in the lower level classes.

Generally speaking this cycle has three purposes: component integration, remaining parameter calculation, and mass aggregation. The first two of these are discussed in the following subsections, specifically for the base engine cycle, while the mass aggregation is discussed later for all cycles at once in section 6.8.1.

### 6.1.1. Component Integration

The class' first purpose is to properly integrate the components, assigning the right outputs to the right inputs. Most importantly, the flow components are connected such that each inlet flow state is equal to the outlet flow state of its upstream component. Additionally, required component inputs are connected to the matching outputs of other components, e.g. the Propellant output, volume, is given as input to the Pressurant component. Although this sounds rather trivial it is quite easy to create self reference where the output of one component is required to create its own input. This is a disadvantage of the modular/OOP implementation approach relative to a more sequential approach.

### 6.1.2. Parameter Calculation

The second purpose is to calculate any other parameters required by the components, which are not calculated by the components themselves. Additionally, it should calculate the performance parameters of the engine. These purposes overlap and are thus discussed together. The main parameters that need to be calculated for the cycle are the chamber flow state, main thrust chamber performance and pump outlet pressures. The first two are found using CEA (if not manually provided). CEA requires the following inputs: propellant names, mixture ratio, pressure ratio, and chamber pressure. Propellant names and chamber pressure are required inputs, while a reasonable mixture ratio can also be assumed based on the propellant choice. Instead of the pressure ratio, the expansion ratio or exit pressure can also be given, which is then used to find the pressure ratio using eq. (6.1). Note that in RoCAT the expansion ratio and pressure ratio are thus related through ideal rocket theory, which is different from their relation through CEA. Consequently, providing the expansion ratio directly to CEA would give slightly different results.

$$\varepsilon = \frac{A_e}{A_{th}} = \frac{\Gamma}{\sqrt{\frac{2\gamma}{\gamma-1} \cdot \left(\frac{p_e}{p_{cc}}\right)^{\frac{2}{\gamma}} \left(1 - \left(\frac{p_e}{p_{cc}}\right)^{\frac{\gamma-1}{\gamma}}\right)}} \quad (6.1)$$

With  $\varepsilon$  the expansion ratio [-],  $A_e$  the exit area [ $m^2$ ],  $A_{th}$  the throat area [ $m^2$ ],  $\Gamma$  the Vandekerckhove-function [-] (see eq. (5.30)),  $\gamma$  the heat capacity ratio [-],  $p_e$  the exit pressure [ $Pa$ ], and  $p_{cc}$  the chamber pressure [ $Pa$ ].

From CEA the following variables are found:

#### Performance parameters:

- $c^*$ , characteristic velocity [ $m/s$ ]
- $C_F^o$ , the characteristic thrust coefficient [-]
- $T_c$ , combustion temperature [ $K$ ]

#### Hot gas properties inside the chamber:

- $\gamma_{cc}$ , heat capacity ratio [-]
- $\mathfrak{M}_{cc}$ , molar mass [ $kg/mol$ ]
- $\mu_{cc}$ , dynamic viscosity [ $Pa \cdot s$ ]
- $c_{p,cc}$ , specific heat [ $J/(kg \cdot K)$ ]
- $Pr_{cc}$ , Prandtl number [-]

The hot gas properties are combined with the combustion temperature and pressure and are bundled in a ManualFlowState. This flow state corresponds to the state in the combustion chamber and these constant

flow properties are used to model the heat flow, as previously discussed in section 5.2.11. With all of these values from CEA the actual thrust coefficient, main specific impulse, mass flow, and throat area are found using ideal rocket theory as shown in eqs. (6.2a) to (6.2d).

$$C_F = C_F^o + \left( \frac{p_e}{p_{cc}} - \frac{p_a}{p_{cc}} \right) \frac{A_e}{A_{th}} \quad (6.2a)$$

$$I_{sp,cc} = \eta_{isp} \cdot \frac{C_F c^*}{g_0} \quad (6.2b)$$

$$\dot{m} = \frac{F_T}{I_{sp} \cdot g_0} \quad (6.2c)$$

$$A_{th} = \frac{\dot{m} \sqrt{R \cdot T_c}}{\Gamma p_{cc}} \quad (6.2d)$$

With  $\eta_{isp}$  the specific impulse quality factor [-],  $F_T$  the thrust force [N], and  $R$  the specific gas constant [ $J/(kg K)$ ].

Using the mixture ratio, the total mass flow is split into an oxidizer and fuel mass flow. Subsequently, the outlet mass flows of the oxidizer and fuel tank are set equal to these mass flows. Combined with the temperature and pressure for both tanks as inputs, the starting flow states for both propellant streams are created. With this state as starting point each component is provided with an inlet flow state, from which it can get its properties, and produces an outlet flow state to pass along to the next component. With the required inputs for the model, and the parameters found in this section all component inputs are known with the single exception of the pump expected outlet pressures. An initial guess is made using eqs. (6.3a) and (6.3b), which is corrected to the exact value using eqs. (6.4a) and (6.4b) afterwards, which need to be adapted depending on the configuration. If the latter equations are used directly there would be self reference, since any component downstream of the pump requires the pump outlet pressure to be known.

$$p_{fp,out} = \kappa_{fp} \cdot p_{cc} \quad (6.3a)$$

$$p_{op,out} = \kappa_{op} \cdot p_{cc} \quad (6.3b)$$

$$p_{fp,out} = p_{cc} - \Delta p_{inj} - \Delta p_{cs} \quad (6.4a)$$

$$p_{op,out} = p_{cc} - \Delta p_{inj} \quad (6.4b)$$

With  $p_{fp/op,out}$  the fuel/oxidizer pump outlet pressure [Pa],  $\kappa_{fp/op}$  the fuel/oxidizer pump pressure factor [-], and  $\Delta p_{inj/cs}$  the change in temperature over the injector/cooling section [Pa].

Finally, the cycle makes a small adjustment to the total power required from the power source, i.e. the electric motor or turbine. This adjustment accounts for the mechanical efficiency of the shaft driving the pumps as shown in eq. (6.5). Note that although this input value for the power source is calculated, the power source itself is not yet modeled in the main engine cycle.

$$P_{req} = \eta_{shaft} \cdot (P_{fp} + P_{op}) \quad (6.5)$$

With  $P_{req}$  the power required from the power source [W],  $\eta_{shaft}$  the shaft mechanical efficiency [-], and  $P_{fp}/P_{op}$  the power required by the fuel/oxidizer pump [W].

### 6.1.3. Checks

Besides the above calculated parameters, the cycle makes some additional calculations, which check the validity of inputs. The inputs should not lead to impossible engine designs or conditions that do not match assumptions.

Concerning the pressure ratio (either given or calculated) it is checked whether it fulfills the choked flow condition, as given in eq. (6.6a). If that is not the case the program exits and indicates the exit pressure is too high. Additionally, if an ambient pressure is provided, the pressure ratio is checked to exceed the Summerfield

criterion at which flow separation inside the nozzle occurs, as shown in eq. (6.6b). If this is not the case the program warns the user. Note that the Summerfield criterion can be overly conservative.

$$\frac{p_e}{p_{cc}} < \left( \frac{2}{\gamma+1} \right)^{\frac{\gamma}{\gamma-1}} \quad (6.6a)$$

$$\frac{p_e}{p_a} < .45 \quad (6.6b)$$

With  $p_e/p_{cc}/p_a$  the exit/chamber/ambient pressure [ $Pa$ ], and  $\gamma$  the heat capacity ratio [-].

Finally, the cycle also calculates the minimum required mass flow through the cooling section using eq. (6.7). For this a maximum outlet temperature of the cooling section is required. If it is not provided manually it is assumed to be equal to the wall temperature. If the main fuel flow is less than this required coolant flow, the program exits and indicates that no cooling solution could be found.

$$\dot{m}_{cs,min} = \frac{\dot{Q}_{tot}}{h(T_{max,cs,out}, p_{out}) - h(T_{in}, p_{in})} \quad (6.7)$$

With  $\dot{m}_{cs,min}$  the minimum required mass flow through the cooling section [ $kg/s$ ],  $\dot{Q}_{tot}$  the total heat flow rate [ $W$ ],  $h(T, p)$  the specific enthalpy of the coolant for a given temperature and pressure [ $J/kg$ ], and  $T_{max,cs,out}$  the maximum outlet temperature of the cooling section [ $K$ ].

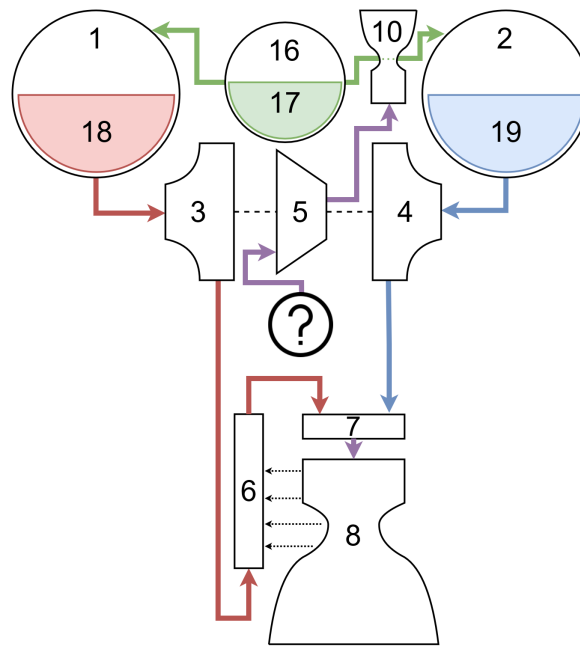


Figure 6.3: Cycle schematic of the abstract base class "Open Cycle"

## 6.2. Open Cycle

The second abstract base class is the Open Cycle. This cycle inherits from the EngineCycle class and adds the components that the gas-generator and open expander cycle share, i.e. the turbine and turbine exhaust (#5 and #10). This leads to the simplified cycle schematic as shown in fig. 6.3. It shows that a component which provides the turbine inlet flow is still missing. This is added in the final cycles.

Just like the Engine Cycle the components are integrated and given their required inputs. With the addition of the turbine and turbine exhaust two additional effects need to be taken into account; the turbine exhaust thrust and the turbine mass flow. Firstly, part of the propellant does not exit through the main thrust chamber,

but through the turbine exhaust. This turbine exhaust flow contributes to the thrust, but substantially less than the chamber flow. Consequently, eq. (6.2c) needs to be adjusted to account for this additional thrust, which leads to eq. (6.8). Secondly, the turbine mass flow leads to an increase in total mass flow through the pumps, which is shown in eq. (6.9).

$$\dot{m}_{cc} = \frac{F_{T,cc}}{I_{sp,cc} \cdot g_0} = \frac{F_{T,tot} - F_{T,exh}}{I_{sp,cc} \cdot g_0} \quad (6.8)$$

With  $\dot{m}_{cc}$  the mass flow through the combustion chamber [kg/s],  $F_{T,cc}$  the thrust produced by the main thrust chamber [N],  $I_{sp,cc}$  the specific impulse of the main thrust chamber [s],  $F_{T,tot}$  the total thrust of the engine [N], and  $F_{T,exh}$  the thrust produced by the turbine exhaust [N] (given by eq. (5.31c)).

$$\dot{m}_{pu} = \dot{m}_{cc} + \dot{m}_{tu} \quad (6.9)$$

With  $\dot{m}_{pu}$  the mass flow through the pumps [kg/s],  $\dot{m}_{cc}$  the mass flow through the chamber [kg/s], and  $\dot{m}_{tu}$  the mass flow through the turbine [kg/s].

### 6.2.1. Iteration

Both the turbine mass flow and turbine exhaust thrust need to be calculated iteratively since they are dependent on themselves and each other; the required turbine mass flow is calculated from the power of the pumps, which depends on the total mass flow, which depends on the chamber mass flow, which depends on the turbine exhaust thrust, which depends on the turbine mass flow, etc.. This interconnected circular dependence is illustrated in fig. 6.4. To solve this the iteration is started with an assumed turbine mass flow of 0 and iterated until a certain relative error between iterations is reached. If not given manually, a relative error of 1E-3 is chosen. This value was selected since higher iteration has very little effect as table 6.1 shows. Even setting the relative error to 1E-14 (smaller values lead to floating point errors, which mess with convergence) leads to very little change in several key outputs of all engine cycles. Consequently, 1E-3 as relative error gives enough accuracy.

Cycle Type	Initial Mass	Final Mass	Ideal Velocity Change
Electric-Pump	-2.117E-5 %	-2.808E-4 %	1.004E-4 %
Gas Generator	-4.011E-4 %	-4.126E-4 %	4.040E-4 %
Open Expander	-1.626E-3 %	-1.574E-3 %	1.613E-3 %

Table 6.1: Relative difference for key outputs for engines iterated to 1E-3 relative error and iterated to 1E-14 relative error.

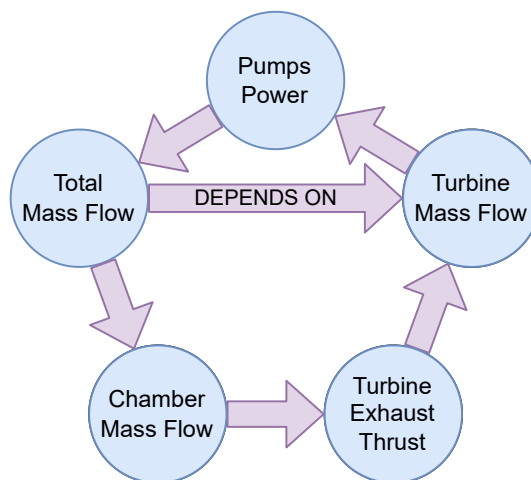


Figure 6.4: Circular dependence for the turbine mass flow and turbine exhaust thrust in an open cycle.

This iteration is shown mathematically in eqs. (6.10a) to (6.10e).

$$(\dot{m}_{cc})_i = \frac{F_{T,tot} - (F_{T,exh})_i}{I_{sp,cc} \cdot g_0} \quad (6.10a)$$

$$(\dot{m}_{fp})_{i+1} = (\dot{m}_{f,cc})_i + (\dot{m}_{f,tu})_i \quad (6.10b)$$

$$(\dot{m}_{op})_{i+1} = (\dot{m}_{o,cc})_i + (\dot{m}_{o,tu})_i \quad (6.10c)$$

$$(\dot{m}_{tu})_{i+1} = f[(\dot{m}_{fp})_{i+1}, (\dot{m}_{op})_{i+1}] \quad (6.10d)$$

$$(F_{T,exh})_{i+1} = f[(\dot{m}_{tu})_{i+1}] \quad (6.10e)$$

With  $\dot{m}_{fp}/\dot{m}_{op}$  the mass flow through the fuel/oxidizer pump [kg/s],  $\dot{m}_{f,cc}/\dot{m}_{o,cc}$  the fuel/oxidizer mass flow through the chamber [kg/s], and  $\dot{m}_{f,tu}/\dot{m}_{o,tu}$  the fuel/oxidizer mass flow through the turbine [kg/s]. subscript  $i$  denotes the  $i$ th iteration and  $f[x]$  denotes a function of  $x$ .

### 6.2.2. Parameter Calculation

In addition to setting up the iteration process for any open cycle engine, the open cycle class also splits the total propellant mass,  $m_p$  into a turbine propellant mass, given in eq. (6.11a), and a chamber propellant mass, given in eq. (6.11b).

$$m_{p,tu} = \kappa_p \cdot \dot{m}_{tu} \cdot t_b \quad (6.11a)$$

$$m_{p,cc} = \kappa_p \cdot \dot{m}_{cc} \cdot t_b \quad (6.11b)$$

With  $m_{p,tu}/m_{p,cc}$  the turbine/chamber propellant mass [kg],  $\kappa_p$  the propellant margin factor [-] (same as in eq. (5.2c)),  $\dot{m}_{tu}/\dot{m}_{cc}$  the turbine/chamber mass flow [kg/s], and  $t_b$  the burn time [s].

The open cycle also calculates a new overall specific impulse as shown in eq. (6.12a). Additionally, the total thrust is also adjusted and given by eq. (6.12b).

$$I_{sp,tot} = \frac{F_{T,tot}}{(\dot{m}_{tu} + \dot{m}_{cc}) g_0} \quad (6.12a)$$

$$F_{T,tot} = F_{T,exh} + F_{T,cc} = I_{sp,exh} \dot{m}_{tu} + I_{sp,cc} \dot{m}_{cc} \quad (6.12b)$$

With  $F_T$  the thrust force [N],  $I_{sp}$  the specific impulse [s],  $\dot{m}$  the mass flow [kg/s], and with subscripts  $tot/cc/exh/tu$  denoting properties of the total, chamber, turbine exhaust, and turbine.

### 6.3. Electric Pump Cycle

The electric-pump cycle directly inherits from the Engine Cycle and adds the electric motor, inverter, and battery (#13, #14, and #15 respectively) to provide the power to drive the pumps, as shown in fig. 6.5. This leads to a very straightforward design: the pumps power required, as defined in eq. (6.5), is passed along to the electric motor and the rest follows quite trivially. Unfortunately, it is also necessary to cool the battery with a battery cooler (#16), which complicates the design of this cycle. The fuel pump (#3) as well as the cooling section (#6) now have a different inlet flow, while the rest of the design remains the same. Additionally, iteration is required, since the battery coolant mass flow depends on itself, as shown in fig. 6.6a. Similar to the turbine mass flow for the open cycle, the battery coolant mass flow is set to 0, which leads to a required battery coolant mass flow, which is then added to the fuel pump flow, which leads to a new battery coolant mass flow required, etc.. The iteration is continued until the relative error between iterations reaches a value smaller than 1E-3 just like the for the open cycle iteration.

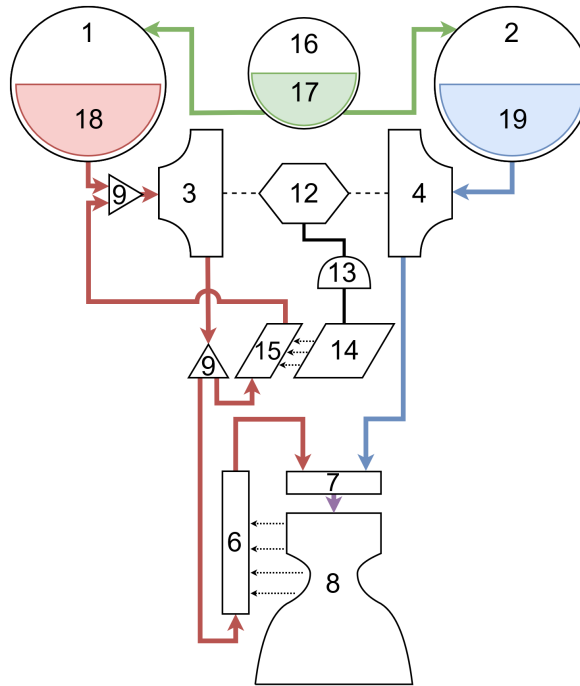
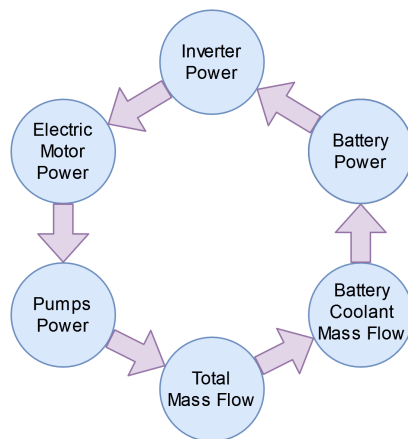
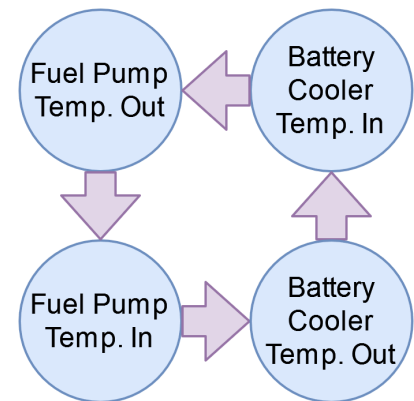


Figure 6.5: Cycle schematic of the main class "Electric-Pump Cycle"



(a) For the battery coolant mass flow



(b) For the battery coolant temperature

Figure 6.6: Circular dependence in the electric-pump cycle. (Purple arrows indicate dependence)

### 6.3.1. Check

The addition of the battery cooler does not only make the battery mass flow circularly dependent, but also the temperatures between the fuel pump and battery cooler, as shown in fig. 6.6b.

Fortunately the way the program is set-up the iteration of these temperatures happens as a consequence of the iteration of the mass flow. However, the amount of iterations required to reach an acceptable error (see section 6.2.1) is not necessarily the same for both iterations. Luckily the circular temperature dependence is quite simple as well as the relevant equations, which means they can be solved analytically to check the final temperatures once the mass flow is known. This equation is shown in eq. (6.13f) and its derivation in eqs. (6.13a) to (6.13e). After the battery cooler mass flow iteration the battery cooler outlet temperature is set to the value obtained from eq. (6.13f), after which the other temperatures also follow.

$$x = \Delta T_{merge} = T_{fp,in} - T_{ft}, \quad a = \frac{\dot{m}_{bc}}{\dot{m}_{fp}}, \quad b = \Delta T_{bc} + \Delta T_{fp} \quad (6.13a)$$

$$x_{i+1} = a(x_i + b) \text{ with } x_0 = 0 \rightarrow x_i = \frac{ab(1-a^i)}{1-a} \quad (6.13b)$$

$$\lim_{i \rightarrow \infty} \frac{ab(1-a^i)}{1-a} \text{ with } a < 1 = \frac{ab}{1-a} \quad (6.13c)$$

$$\Delta T_{merge} = \frac{\frac{\dot{m}_{bc}}{\dot{m}_{fp}} (\Delta T_{bc} + \Delta T_{fp})}{1 - \frac{\dot{m}_{bc}}{\dot{m}_{fp}}} \quad (6.13d)$$

$$T_{bc,out} = T_{ft,out} + \Delta T_{merge} \cdot \frac{\dot{m}_{fp}}{\dot{m}_{bc}} \quad (6.13e)$$

$$T_{bc,out} = T_{ft,out} + \frac{\Delta T_{bc} + \Delta T_{fp}}{1 - \frac{\dot{m}_{bc}}{\dot{m}_{fp}}} \quad (6.13f)$$

With  $T_{fp,in}$  the fuel pump inlet temperature,  $T_{ft}$  the fuel tank temperature,  $\Delta T_{merge}$  the temperature difference between the fuel tank outlet and fuel pump inlet,  $\Delta T_{bc}$  the (given) temperature change over the battery cooler,  $T_{bc,out}$  the battery cooler outlet temperature, and  $\frac{\dot{m}_{bc}}{\dot{m}_{fp}}$  the fraction of the coolant mass flow relative to the total fuel pump mass flow [-].

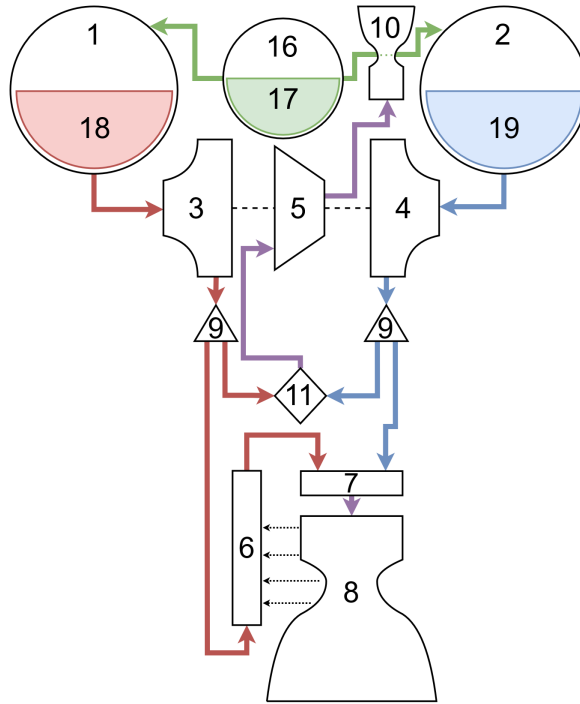


Figure 6.7: Cycle schematic of the main class "Gas Generator Cycle"

## 6.4. Gas Generator Cycle

The gas generator cycle inherits from the open cycle and adds the gas generator (#11), as shown in fig. 6.7. With most of the calculations and iterations already defined in the open cycle, the gas generator cycle only needs to add two splitters (#9) and redefine the inlet flow states to complete the cycle. Additionally, it must define the division of the turbine mass flow, see eqs. (6.10b) and (6.10c). This is done below in eq. (6.14).

$$\dot{m}_{f,tu} = \dot{m}_{f,gg} = \dot{m}_{tu} \cdot \frac{1}{(O/F)_{gg} + 1} \quad (6.14a)$$

$$\dot{m}_{o,tu} = \dot{m}_{o,gg} = \dot{m}_{tu} \cdot \frac{(^{o/f})_{gg}}{(^{o/f})_{gg} + 1} \quad (6.14b)$$

With  $\dot{m}_{f,tu}/\dot{m}_{o,tu}$  the turbine fuel/oxidizer mass flow [kg/s],  $\dot{m}_{f,gg}/\dot{m}_{o,gg}$  the gas generator fuel/oxidizer mass flow [kg/s],  $\dot{m}_{tu}$  the turbine mass flow [kg/s], and  $(^{o/f})_{gg}$  the oxidizer-to-fuel ratio of the gas generator [-].

Note that the gas generator oxidizer-to-fuel ratio is found from the maximum turbine temperature, see section 5.4.1, and the (total) turbine mass flow,  $\dot{m}_{tu}$ , is found from the power required, see section 5.3.1. Also note that, in case of the gas generator cycle, the only flow through the turbine is a combined combusted flow, so the concepts of oxidizer/fuel turbine flow are somewhat implicit, but they enable a direct comparison between any engine derived from the open cycle. With the turbine flow defined the gas generator cycle is completed, all else is already handled by the open cycle.

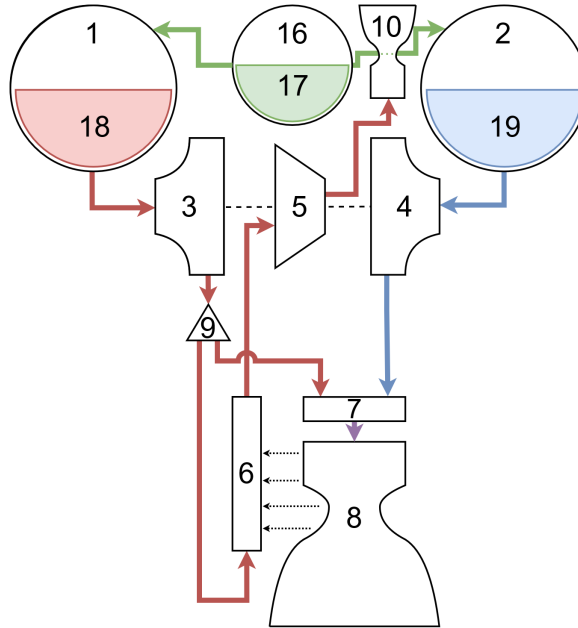


Figure 6.8: Cycle schematic of the main class "Coolant Bleed Cycle"

## 6.5. Coolant Bleed Cycle

The coolant bleed cycle inherits from the open cycle and adds no main components, but rearranges the flow as shown in fig. 6.8. Similar to the gas generator, very little functionality needs to be added on top of the open cycle. The inlet flow states of the cooling section and injector now come from the splitter after the fuel pump and the turbine inlet comes directly from the cooling section outlet. Additionally, the division of the turbine mass flow is very straightforward, as shown in eq. (6.15).

$$\dot{m}_{f,tu} = \dot{m}_{tu} \quad (6.15a)$$

$$\dot{m}_{o,tu} = 0 \quad (6.15b)$$

Finally, a change needs to be made to the minimum required coolant mass flow from eq. (6.7). Since the turbine is now connected to the cooling section outlet, the maximum cooling outlet temperature should be at most equal to the maximum turbine temperature. Consequently, the default maximum cooling outlet temperature is redefined as shown in eq. (6.16) (but can still also be set manually).

$$T_{max,cs,out} = \text{MIN}(T_w, T_{max,tu}) \quad (6.16)$$

With  $T_{max,cs,out}$  the maximum cooling section outlet temperature [K], the  $T_w$  the wall temperature [K], and  $T_{max,tu}$  the maximum turbine temperature [K].

With the above additions the coolant bleed cycle is complete as all else is already handled by the open cycle.

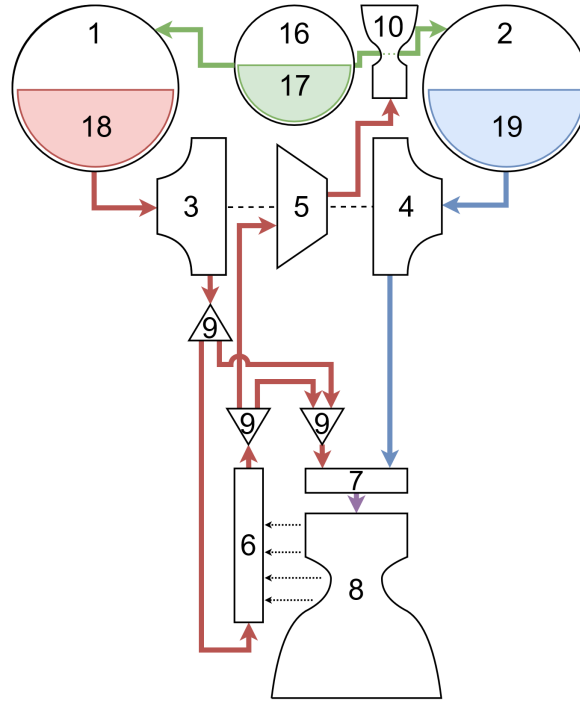


Figure 6.9: Cycle schematic of the main class "Open Expander Cycle"

## 6.6. Open Expander Cycle

The open expander cycle inherits from the coolant bleed cycle and only rearranges the flow as shown in fig. 6.9. Due to the added splitters and merger the flows have become more complex, which warrants some clarification. Let's distinguish the two splitters: let the splitter directly down stream of the fuel pump be called the "pre splitter", as it splits the flow before the cooling section, and let's call the splitter directly down stream of the cooling section the "post splitter". Note that the underlying assumption for this cycle is that more coolant mass flow is required for minimum cooling than is needed for powering the turbine, i.e.  $\dot{m}_{tu} < \dot{m}_{min,cs}$ , otherwise there is no need for the "post splitter" and the cycle becomes identical to the coolant bleed cycle, as previously discussed in section 4.3.3. The program for the open expander cycle checks if this condition is met, and if it is not it warns the user that they should probably use a coolant bleed cycle.

With this assumption in mind, the following mass flows can be defined. Combining eq. (6.10b) from the open cycle, and eq. (6.15a) from the coolant bleed cycle, we get eq. (6.17a). From the mentioned assumption, we get eq. (6.17b) and we know the mass flow through the turbine,  $\dot{m}_{tu}$ , from eq. (5.27). For both splitters the inlet flow and one of the outlet mass flows is now known, thus it is trivial to determine the other outlet mass flow, which can be seen for both splitters combined in eq. (6.17c), which simplifies back to eq. (6.17a) as it should.

$$\dot{m}_{fp} = \dot{m}_{f,cc} + \dot{m}_{tu} \quad (6.17a)$$

$$\dot{m}_{cs} = \dot{m}_{cs,min} \quad (6.17b)$$

$$\dot{m}_{f,cc} = (\dot{m}_{fp} - \dot{m}_{cs}) + (\dot{m}_{cs} - \dot{m}_{tu}) \quad (6.17c)$$

With  $\dot{m}_x$  the mass flow through component x [kg/s], with the subscripts  $_{fp}$  the fuel pump,  $_{f,cc}$  the chamber fuel,  $_{tu}$  the turbine, and  $_{cs/min,cs}$  the (minimum) cooling section.

With the above mass flows clarified the open expander is complete with all other aspects of the cycle already handled by the coolant bleed cycle or open cycle.

## 6.7. Additional Cycle Configuration

Above, all the cycles which have been implemented in RoCAT have been discussed. However, only their simplest or default configuration have been considered. Due to the modular approach further configuration of the cycles is relatively simple, but still requires adjusting the code. Therefore several common configuration options have already been implemented in RoCAT. These configurations are mostly of concern in the verification and validation chapter, chapter 7, where the configuration of other engines are copied as exactly as possible. Consequently, for examples of complete engines that use these non-standard configurations the reader is referred to this chapter. This section quickly touches upon the individual configurations implemented in RoCAT.

### 6.7.1. Double Fuel Pumps

Many real engines have multiple pumps for a single propellant stream. This can help with preventing cavitation as well as lowering the total power needed by the pumps. The latter can be done by rerouting a large part of the flow directly to the injector and only part of the flow going through the second pump and cooling section. The additional pressure needed to overcome the cooling section is thus only provided to the necessary flow. Since in this report the fuel has been assumed to be the coolant, as explained in section 4.2, this configuration addition only makes sense for the fuel pumps. Consequently, this is what has been added for all cycles and is shown in fig. 6.10. The flow after the first fuel pump is split into a flow that goes directly to the injector and a flow that goes through the second pump to the cooling section. For a complete example of a double fuel pump see fig. 7.5 in chapter 7.

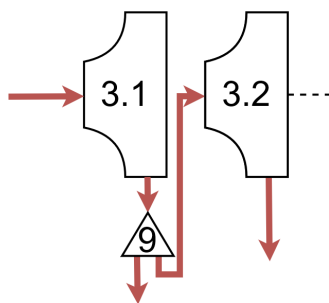


Figure 6.10: Detail schematic overview of double fuel pump configuration

### 6.7.2. Parallel Double Turbines

In conventional cycle engines different turbines are sometimes used to drive the fuel and oxidizer pump(s) individually. This is in part due to the different ideal rotational speeds for different density propellants or simply being more practical to place two smaller turbopump assemblies around the engine than one big one, as noted by Sutton[58]. Although the current tool does not model the effects of rotational speeds in the pumps or turbines, individual turbines still give the possibility to have different efficiencies and pressure ratios. Thus the turbine configuration as shown in fig. 6.11 has been implemented for all open cycles. In a parallel configuration this also leads to separate turbine exhausts than can have different inlet flows and properties. For a complete example of a parallel double turbines configuration see fig. C.1 in appendix C.

### 6.7.3. Series Double Turbines

Another possibility with double turbines is to have the flow through the turbines in series. This leads to only one turbine exhaust. Additionally, this requires some manual care in the pressure ratio or exit pressure inputs for the turbines, otherwise the second turbine is not able to deliver enough power. A double turbines in series configuration has been implemented for all open cycles with the flow going through the fuel side first, as shown in fig. 6.12. For a complete example of a series double turbines configuration see fig. C.2 in appendix C.

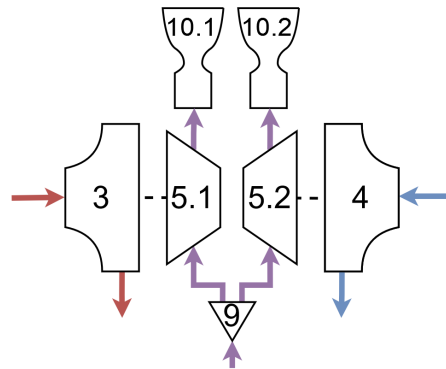


Figure 6.11: Detail schematic overview of parallel double turbine configuration

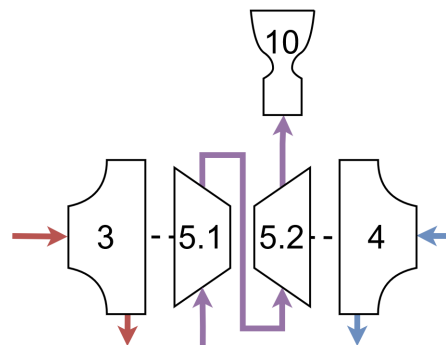


Figure 6.12: Detail schematic overview of series double turbine configuration

#### 6.7.4. Double Electric Motor

Lastly, a double electric motor configuration has been implemented for the electric-pump cycle. This gives the option to have different specific powers and efficiencies for each motor. The configuration chosen only has one inverter and battery as shown in fig. 6.13.

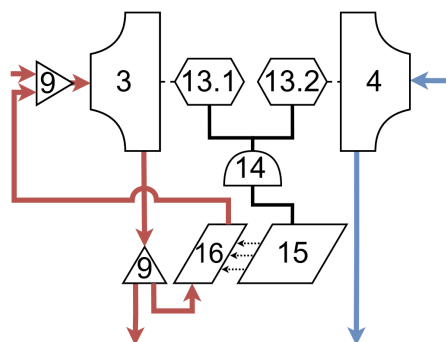


Figure 6.13: Detail schematic overview of double motor configuration

## 6.8. Other Parameters

### 6.8.1. Mass Aggregation

Several aggregate masses are also defined in RoCAT, which are listed below. An overview of these aggregate masses for all cycles and their constituent masses is shown in fig. 6.14. The colors/levels indicate groupings, with each lower level/color grouping all components above it. For example, the initial mass consists of the

propellants masses and final mass, the final mass in turn consists of the pressurant, payload and dry mass, etc.. Also note that the masses are only accounted for if the engine (cycle) actually contains these components, e.g. an EP-cycle engine's feed system mass does not include a turbine mass nor does the propellants mass contain turbine (flow) propellant masses. The list below also shows the symbols for some of these mass groupings. The mass ratio is defined as  $\Lambda = m_0/m_f$ .

- $m_0$ : Initial Mass
- $m_f$ : Final Mass
- $m_{dry}$ : Dry Mass
- $m_{engine}$ : Engine Dry Mass
- $m_{fs}$ : Feed System Mass
- $m_p$ : Propellants Mass
- $m_{p,cc}$ : Chamber Props. Mass
- $m_{p,tu}$ : Turbine Props. Mass
- $m_u$ : Payload Mass

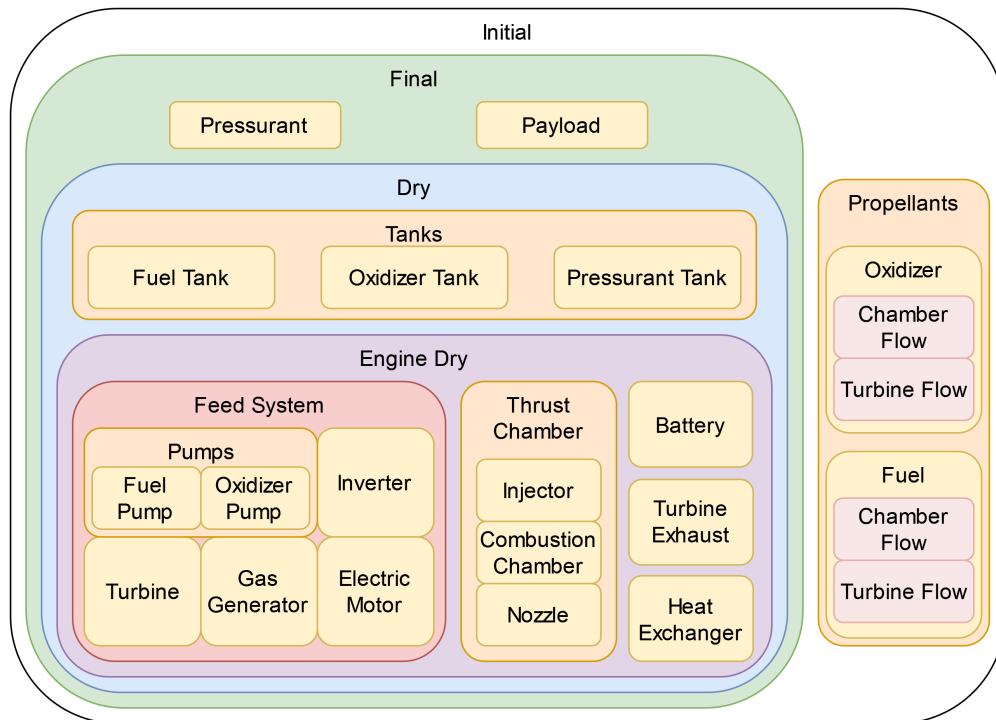


Figure 6.14: Overview of mass aggregations

### 6.8.2. Mass Factor

Since RoCAT only calculates the masses of certain components the mass ratio that is defined above does not match with a real rocket stage. To compensate for this, several mass factors have been calculated from mass break down data of the Centaur-D upper stage, see appendix D. The relevant factors have been calculated by assuming that the initial mass without payload from RoCAT (as defined in the above section) is roughly equal to the sum of body, propulsion group, pressurization group, total propellants, and total helium as defined in the Centaur-D data set table D.1. How the adjusted mass ratio is calculated is shown in the list of assumptions, list of averages, and equations below.

Assumptions:

- Residual Propellants are not taken into account (assumed to be expelled)
- Report Mass = Body + Propulsion Group + Pressurization Group + Total Propellants + Total Helium
- Rest Expendables = Total Jettisonable Hardware + Expandable H2O2 + Expandable Ice
- Final Mass = Total Tanked Weight - Total Jettisonable Hardware - Total Expendables

Averages of the Centaur-D:

- (Ground Weight - Payload) / Report Mass = 1.1459
- (Final Mass - Payload) / (Report Mass - Total Propellants) = 1.9188

Combining the above leads to the new adjusted values for the initial mass, final mass, and mass ratio as shown below.

$$(m_0)_{adj} = \kappa_{m_0} (m_0 - m_u) + m_u \quad (6.18a)$$

$$(m_f)_{adj} = \kappa_{m_f} (m_f - m_u) + m_u \quad (6.18b)$$

$$\Lambda_{adj} = \frac{(m_0)_{adj}}{(m_f)_{adj}} \quad (6.18c)$$

With  $\kappa_{m_0} = 1.1459$  and  $\kappa_{m_f} = 1.9188$

Despite this adjustment giving more realistic values it should still be taken with a grain of salt as the Centaur-D is not necessarily representative. For example it has jettisonable hydrogen insulation panels, which are not used on almost any other second stage. Additionally, the calculated component masses are not always fully identical to their equivalent listed masses or it is at least unclear. Nonetheless, it certainly gives a more realistic value than without adjustment.

### 6.8.3. Change in velocity

In addition to the parameters already calculated by each cycle the change in velocity is also calculated, as shown in eq. (6.19a), as well as an adjusted version, which is found from the adjust mass ratio discussed above, as shown in eq. (6.19b).

$$\Delta V = I_{sp,tot} g_0 \ln(\Lambda) \quad (6.19a)$$

$$\Delta V_{adj} = I_{sp,tot} g_0 \ln(\Lambda_{adj}) \quad (6.19b)$$

With  $\Delta V$  the change in velocity [ $m/s$ ],  $I_{sp,tot}$  the total specific impulse [ $s$ ],  $\Lambda$  the mass ratio [-], and  $_{adj}$  denoting the adjusted version of a parameter.

With these final parameters defined the description of the cycle implementation is concluded and RoCAT has been complete described. A list of assumptions as well as a list of differences w.r.t. Kwak are given in appendix E. This chapter has described the implementation of each individual cycle. It touched upon the abstract cycles from which they inherit, their optional configurations, and the parameters they calculate, both internal and external. Combining this information with that of the previous chapter RoCAT has been fully described. It still requires verification and validation, which is done in the next chapter.

# Verification&Validation

This chapter contrasts the various cycles modeled in RoCAT with data from existing engines and compares them to the results from other engine models. The aim is to showcase the accuracy of the model and to highlight the outputs that need to be viewed with some skepticism. The performance models of RoCAT are investigated first, followed by an examination of the mass models.

## 7.1. Performance

The focus of this section is on performance and flow parameters, i.e. mainly the specific impulse but also the pressures at various in- and outlets as well as the mass flows to the chamber and either the turbine or battery cooler. The choice to focus on comparing to other models, here called verification, was made because data from existing rocket engines was only found to a limited extent in literature. However, it is done whenever possible.

Each subsection starts by introducing the model, engine, and inputs that are used to compare results. The results are presented in two ways: firstly, a detailed performance schematics and secondly, a table of main output parameters, which is discussed in-depth. After the performance verification of each individual cycle, the performance is also validated, although to a lesser extent, due to the lack of data from existing engines.

### 7.1.1. Performance Schematics

Before starting the verification, this paragraph quickly explains the set-up of the performance schematics of which the first example can be seen in fig. 7.1. Each schematic shows the total specific impulse at the top as well as the input total thrust. Furthermore, it shows the flow state in between each component and consequently how each component influences the pressure, temperature, and mass flow. The splitters and mergers (9) do not affect the former two properties, so for their downstream flows only the mass flow is given. The numbers refer to the components as defined in table 4.1. From these schematics it becomes clear which exit streams contributes how much to the total thrust (for the open cycles) and which streams contribute to the pump power requirement. All values presented are output values, unless underlined. Generally the only input values are the expansion ratios,  $\varepsilon$ , the total thrust,  $F_{T,tot}$ , the efficiencies,  $\eta$ , and the mixture ratio of the thrust chamber,  $MR$ .

### 7.1.2. Electric-Pump Verification

For the verification of the electric-pump cycle, the results need to be compared with those of another model for electric-pump cycle engines. The best model to compare with would be the model of Kwak [34]. This has actually already been done at the start of this report in chapter 3, where several implementation inconsistencies were found. They were corrected for and this model was used as basis for RoCAT, which means one could say RoCAT has already been verified with the model of Kwak too the highest extent possible. However, it is still interesting to see how the different models compare and if large differences can be explained.

Since Kwak's model is not available and the paper's data is limited, RoCAT is compared to the Adjusted Replication model instead. This model very accurately replicates the data in the paper, as discussed in section 3.4, and thus should accurately show the difference between Kwak's model and RoCAT. Note that this is not the model from which RoCAT was built as that is the Replication model discussed in section 3.2.

Performance parameters were calculated for an electric-pump cycle engine with a thrust, chamber pressure, and burn time of 100 kN, 10 MPa, and 300 s, respectively, using both models. These values are selected since they led to the largest differences between the initial replication and Kwak's model in section 3.2 and consequently are likely to lead to the clearest differences once again. Detailed schematic overviews of these parameters for both models are presented in figs. 7.1 and 7.2. An overview of selected parameters is provided in table 7.1.

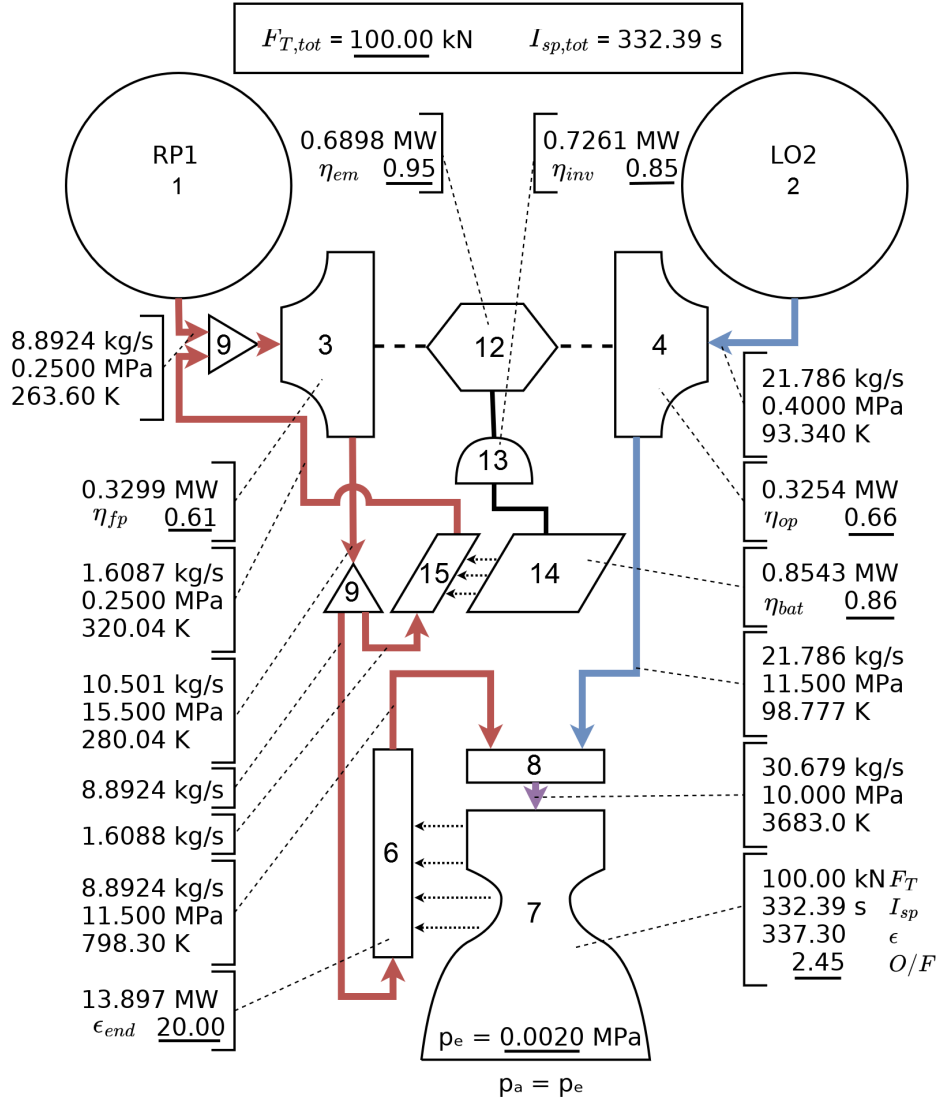


Figure 7.1: Schematic overview of performance and flow parameters for an electric-pump cycle engine ( $F_T=100\text{kN}$ ,  $p_{cc}=10\text{MPa}$ ,  $t_b=300\text{s}$ ) as simulated with RoCAT

	Unit	Adjusted Replication	RoCAT	Diff [%]
<b>Specific Impulse</b>	[s]	370.0	332.4	10.17
<b>Oxidizer Pump Outlet Pressure</b>	[bar]	115.0	115.0	0.0
<b>Fuel Pump Outlet Pressure</b>	[bar]	155.0	155.0	0.00
<b>Battery Coolant Mass Flow</b>	[kg/s]	0.9916	1.609	-62.24
<b>Chamber Oxidizer Mass Flow</b>	[kg/s]	19.57	21.79	-11.32
<b>Chamber Fuel Mass Flow</b>	[kg/s]	7.988	8.892	-11.32
<b>Electric Motor Power</b>	[kW]	571.40	689.8	-20.72
<b>Turbine Oxidizer Power</b>	[kW]	3130	2660	15.01
<b>Turbine Fuel Power</b>	[kW]	12054	13139	-9.00

Table 7.1: Comparison of performance parameters for an electric-pump cycle engine ( $F_T=100\text{kN}$ ,  $p_{cc}=10\text{MPa}$ ,  $t_b=300\text{s}$ ) as produced by RoCAT and by a replication of Kwak's model [43]

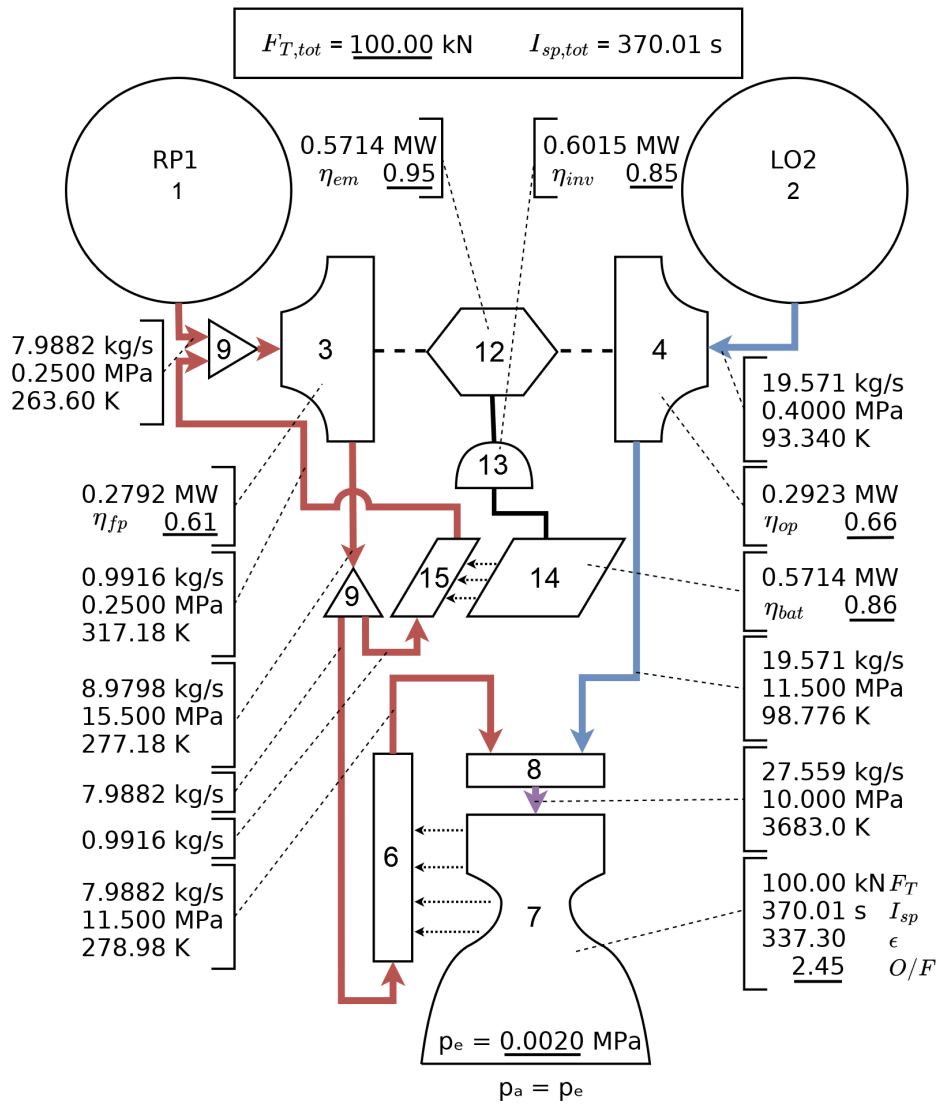


Figure 7.2: Schematic overview of performance and flow parameters for an electric-pump cycle engine ( $F_T=100\text{kN}$ ,  $p_{cc}=10\text{MPa}$ ,  $t_b=300\text{s}$ ) as simulated with Adjusted Replication of Kwak's model [34]

From table 7.1 it becomes clear that there are quite a few differences between both models. The differences are not very large, which is to be expected since the foundation of RoCAT is based on the model by Kwak. The difference in specific impulse can be largely explained by switching from "shifting equilibrium" to "frozen at throat" assumptions for the CEA calculation. Additionally quality factors were added as well as a mechanical shaft efficiency that all lead to slightly more propellant flow being required in the RoCAT model. Although the combined effect of frozen settings, quality factors, and shaft efficiency is substantial, it leads to much more realistic specific impulse values than those posed by Kwak, see for example the 343 s specific impulse reported for the vacuum-optimized Rutherford engine [49]. Additionally, the thrust chamber and regenerative cooling heat flow rate were not modeled in Kwak's model, leading to no temperature increase over the heat exchanger in fig. 7.2, contrary to RoCAT where the temperature jumps about 520 K as seen in fig. 7.1. Finally, the largest difference can be found in the battery coolant mass flow, which is also expected. Kwak's model underestimates the heat flow rate from the battery as was discussed in section 3.3.4. The pump outlet pressures are the same although the method has changes somewhat. Kwak assumed the pump outlet pressure to be 1.15/1.55 times the chamber pressure directly, while RoCAT calculates the outlet pressure based on the pressure drop over the heat exchanger and injector. However, if no pressure drops are manually supplied these pressure drops are assumed to be 0.4 and 0.15 times the chamber pressure. With the fuel flowing through both and the oxidizer only through the injector this leads to exactly the same pump outlet pressures. To summarize: the differences found between the two models are considerable, but can largely be attributed to implementation choices that have been consciously made and have been explained previously in chapter 3 and chapter 5.

### 7.1.3. Gas Generator Verification

To verify the performance model for the gas generator cycle it is compared to the model given by Mota et al.[43]. Both models analyze the Vulcain (or HM60) engine, for which the inputs were taken from Mota et al. and McHugh [41, 43] and can be found in appendix B.3.2. It is a liquid hydrogen/liquid oxygen engine with 1025 kN of thrust using a parallel turbine configuration and an oxidizer-to-fuel ratio of 5.1. Note that despite being a first stage engine, the specific impulse calculated by Mota is clearly for a vacuum. Consequently, the ambient pressure has been set to 0. The detailed schematic overview of the results from RoCAT and Mota can be found in fig. 7.3 and fig. 7.4 respectively. Table 7.2 shows the comparison of important parameters from both models.

	Unit	Mota et al.	RoCAT	Diff [%]
<b>Specific Impulse</b>	[s]	433.3	435.3	-0.46
<b>Oxidizer Pump Outlet Pressure</b>	[bar]	130.0	115.0	11.5
<b>Fuel Pump Outlet Pressure</b>	[bar]	158.0	155.0	1.90
<b>Turbine Oxidizer Mass Flow</b>	[kg/s]	4.086	4.066	0.48
<b>Turbine Fuel Mass Flow</b>	[kg/s]	4.540	4.590	-1.10
<b>Chamber Oxidizer Mass Flow</b>	[kg/s]	206.3	193.5	6.18
<b>Chamber Fuel Mass Flow</b>	[kg/s]	35.42	37.94	-7.13
<b>Turbine Oxidizer Power</b>	[kW]	3130	2660	15.01
<b>Turbine Fuel Power</b>	[kW]	12054	13139	-9.00

Table 7.2: Comparison of performance parameters for the Vulcain (HM60) engine as produced by RoCAT and Mota's model [43]

It is clear that RoCAT closely matches with Mota's model with the exception of the oxidizer pump outlet pressure and as a direct result the power required for the oxidizer pump. As mentioned in the previous subsection, the outlet pressure is determined rather simplistic. It seems the model could be improved by looking at Mota's modeling of the pump, but unfortunately the description in the paper is insufficient. Part of the formula to estimate the pump exit pressure drop remains unexplained and consequently cannot be replicated. Additionally, it could also be possible pressure drops were manually provided, although no values are provided by Mota [43]. Nonetheless, the values match well enough to be considered satisfactory.

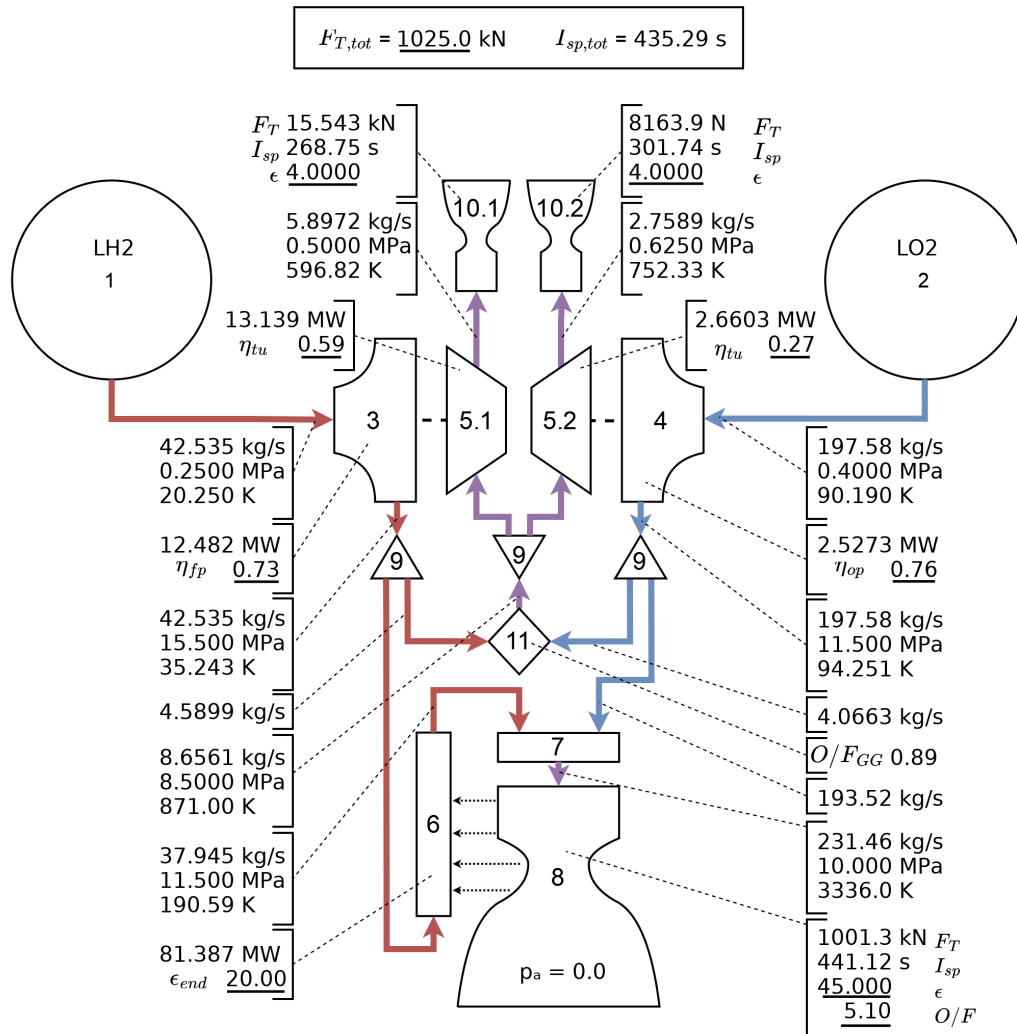


Figure 7.3: Schematic overview of performance parameters and flow parameters for the Vulcain as simulated with RoCAT

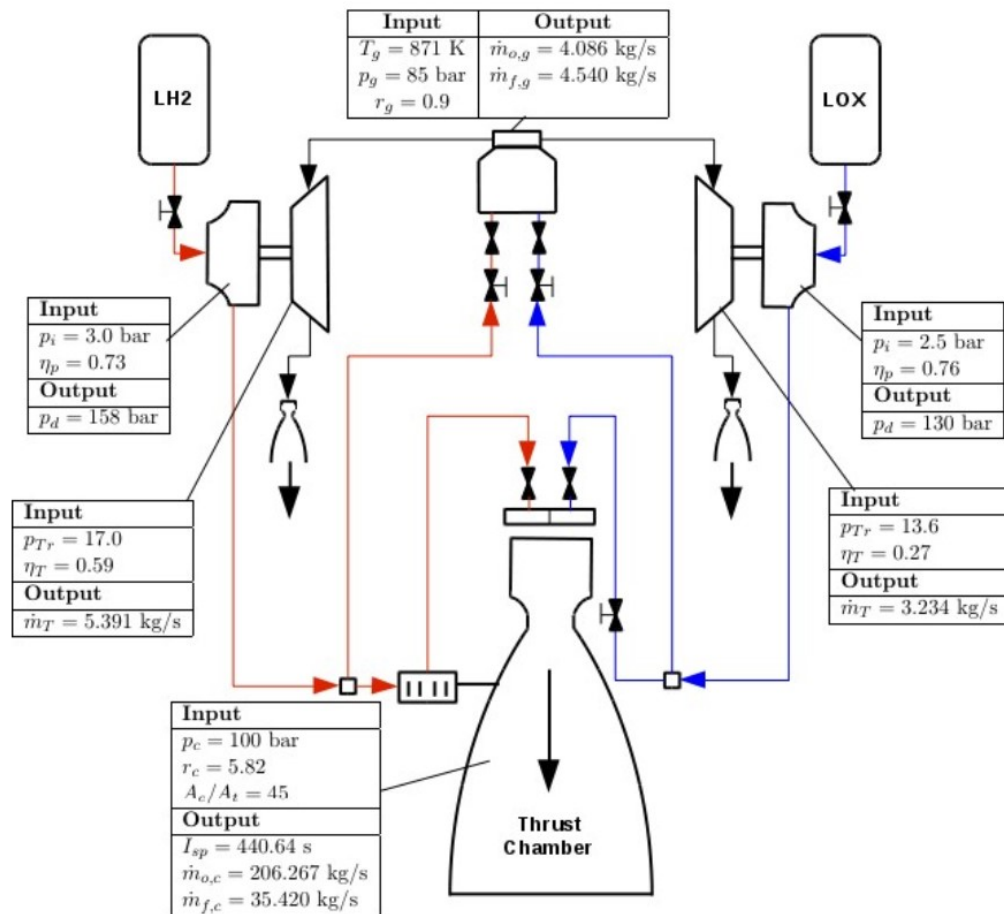


Figure 7.4: Schematic overview of performance parameters and flow parameters for the Vulcain as simulated by Mota [43]

### 7.1.4. Gas Generator Validation

For several existing gas generator engines performance data was available. Most data is from a paper by McHugh [41] and concerns the HM7B, H-1, RS-27, F-1, HM60 (Vulcain), and J-2 engines. All of these engines have been modeled and analyzed. Their performance schematics can be found in appendix C and a detailed comparison between McHugh's data and RoCAT output can be found in appendix F. A summary of the differences for performance parameters is given in table 7.3.

	HM7B	H-1	RS-27	F-1	HM60	J-2	Abs.Avg.
GG Mass Flow [kg/s]	-4.7	-54.8	-47.5	-30.7	3.0	11.7	25.4
GG Mixture Ratio [-]	0.49	-3.3	-1.0	1.2	-1.6	0.03	1.3
Fuel Mass Flow [kg/s]	2.4	0.30	-0.08	2.1	7.1	2.4	2.4
Oxidizer Mass Flow [kg/s]	-1.3	-3.4	-3.6	-1.5	-2.4	-2.5	2.5
Fuel Pump Outlet Pressure [MPa]	0.54	-10.1	6.5	-7.5	-1.9	-2.9	4.9
Oxidizer Pump Outlet Pressure [MPa]	-17.5	-24.8	-22.8	-18.9	-11.5	-18.7	19.0
(Fuel) Turbine Power [kW]	-0.9	-16.1	-11.0	-10.4	17.3	0.45	9.4
Oxidizer Turbine Power [kW]					-11.3	-19.4	15.4
Specific Impulse [s]	0.41	0.14	-0.43	0.46	0.41	-0.15	0.34

Table 7.3: Differences between performance data from McHugh and RoCAT for selected engines as well as average of absolute differences

The table above shows that there is good agreement between the data of the existing engines and their simulation by RoCAT. The oxidizer pump outlet pressure is an exception and does not agree very well. That is in line with results from the verification where pump outlet pressures also deviated. It is of interest to note that it is consistently overestimated, which means it could be adjusted for relatively easily with a correction factor. Alternatively, the feed lines could be modeled and its pressure drop could at least partly compensate for the underestimation.

The gas generator mass flow has the biggest deviation and is generally an underestimation by RoCAT. Upon closer inspection it seems that a distinction must be made based on propellant choice, since the average deviation for liquid hydrogen based engines (HM7B, HM60, J-2) is only 6.5%, while for the RP-1 engines (H-1, RS-27, F-1) the deviation is 50.7%. It is clear this inaccuracy is only present for RP-1 engines. This singles out a likely cause. As previously discussed in section 5.4.1, CEA does not properly handle very fuel-rich combustion of long organic compounds [32]. An alternative empirical formula was applied to compensate, but this only corrected the relation between combustion temperature and mixture ratio in the gas generator. Which is why the gas generator mixture ratio is not inaccurate for the RP-1 engines. However, no corrections for the other flow properties were applied. On closer examination this seems to be the main cause, as the specific heat capacity found by CEA(frozen) is around 4.2 kJ/kg/K, while Huzel and Huang [29] give around 2.7 kJ/kg/K for fuel-rich RP-1/LOX combustion ( $o/f$ -ratio around 0.35). Note that if CEA is used assuming equilibrium condition even more inaccurate specific heat capacities are found of around 10 kJ/kg/K. Unfortunately, no satisfactory work around could be implemented in time for this research.

### 7.1.5. Open Expander Verification

To verify the performance model for the open expander cycle it is compared to the results of Sippel [53], which simulated a ~2000 kN LH2/LOX open expander engine, named SE21D. The schematic overview of the flow and performance parameters are shown at the end of this section. Figure 7.5 shows the new data as produced with RoCAT, while fig. 7.6 shows the original data from Sippel [53]. The inputs used were directly taken from Sippel's paper and are listed in appendix B.3.3. Since Sippel's schematic is just as detailed as the one produced by RoCAT almost all parameters can be compared and there is good agreement between the two schematics. To more accurately compare the results, the most important parameters have been listed in table 7.4.

The first columns of interest are the columns labeled *Sippel*, *RoCAT*, and *Diff.*. These show the difference between the two models, the columns denoted with a 2 are discussed later. The Expected Heat Flow Rate in the *Sippel*-column is highlighted in bold, because it has been calculated from Sippel's data instead of being taken directly from the paper. The differences found in this comparison are mainly found in three areas: Firstly, the

pressure rises over the pumps are not very accurate, which in turn affect the required power. Secondly, the heat flow rate is quite severely overestimated, which also directly affects the coolant flow. And, finally, the difference in the throat radius carries on to most of the sizing of the thrust chamber. Notice that the secondary fuel pump's pressure increase is underestimated, while the coolant flow passing through it is overestimated, which almost cancel each other out in the secondary fuel pump power required. For the heat flow rate, there

Name	Unit	Sippel	RoCAT	Diff. [%]	RoCAT 2	Diff. 2 [%]
<b>Chamber Sp. Impulse</b>	[s]	365.085	368.80	1.02	368.80	1.02
<b>Exhaust Sp. Impulse Fu.</b>	[s]	158.933	155.13	2.39	154.41	2.84
<b>Exhaust Sp. Impulse Ox.</b>	[s]	153.064	155.13	1.35	154.42	0.88
<b>Overall Sp. Impulse</b>	[s]	360.985	365.14	1.15	364.68	1.02
$\Delta P$ Oxid. Pump	[MPa]	8.249	7.1463	13.37	8.2490	0.00
$\Delta P$ Fuel Pump	[MPa]	8.449	7.3463	13.05	8.4490	0.00
$\Delta P$ Fuel Pump 2	[MPa]	3.36	2.6596	20.85	3.3600	0.00
<b>Fuel Pump Power Req.</b>	[MW]	15.443	13.649	11.62	15.882	2.84
<b>Fuel Pump 2 Power Req.</b>	[MW]	1.01	1.0335	2.33	1.0182	0.81
<b>Oxid. Pump Power Req.</b>	[MW]	4.315	3.7203	13.78	4.2906	0.57
<b>Total Pump Power Req.</b>	[MW]	20.768	18.589	10.49	21.405	3.07
<b>Heat Flow Rate</b>	[MW]	<b>111.037</b>	140.12	26.19	111.04	0.00
<b>Turb. Mass Flow</b>	[kg/s]	10.174	9.3034	8.56	10.448	2.69
<b>Cool. Mass Flow</b>	[kg/s]	16.394	20.596	25.63	16.327	0.41
<b>Main Fuel Flow</b>	[kg/s]	93.677	91.524	2.30	92.598	1.15
<b>Main Oxid. Flow</b>	[kg/s]	456.323	452.22	0.90	451.83	0.99
<b>Chamber Diameter</b>	[m]	0.985	.84159	14.56	.98500	0.00
<b>Chamber Volume</b>	[m <sup>3</sup> ]	1.029	.75037	27.08	1.0279	0.11
<b>Subs. Length</b>	[m]	1.582	1.5187	4.00	1.5476	2.17
<b>Throat Radius</b>	[m]	0.286	.24436	14.56	.28600	0.00
<b>Nozzle Length</b>	[m]	2.548	2.3310	8.52	2.7282	7.07

Table 7.4: Comparison between SE21D performance values as expected from the Sippel paper [53], estimated by RoCAT, and estimated with several extra inputs

are several factors that can lead to deviations in the output of the model as compared to the data. A possible factor is the uncertainty of the area ratio for regenerative cooling cut-off, which was taken from a previous study and seems to be used in Sippel's simulation, but is not explicitly clear [54]. Evidently, a larger cooled area would directly influence the heat flow rate. Additionally, the heat transfer model makes many simplifying assumptions, i.e. constant wall temperature and constant hot gas properties. Improving the model to work without some of these simplifying assumptions will likely improve the heat transfer estimate.

For the pump outlet pressures, the cause is almost certainly the simple relations used to estimate the pressure drop over the injector and cooling section. This also seems in line with previous research as Ernst, who used similar relations, found a RSE of 19.6% for the outlet pressures while comparing with similar engines [20]. As already suggested in the gas generator section, addition of a feed line component will likely increase the accuracy of the pump outlet pressure.

For the throat radius it is not clear what causes the deviation, but temperature, pressure, and mass flow in the combustion chamber all deviate less than 2%. These properties should determine the throat area according to ideal rocket theory in combination with the heat capacity ratio and molar mass of the gas in the combustion chamber. Consequently, it can be concluded that Sippel sizes the throat differently from ideal rocket theory or his chamber gas properties deviate from CEA. The former seems more likely.

To ensure these 3 differences are the main ones the simulation was run again, but this time with the throat radius, heat transfer, and pressure rises given as inputs. As can be seen from the 2nd-columns, with these additional inputs the remaining parameters match up very well. The small exception is the nozzle length, which makes sense as Sippel did not provide detailed information on the divergent nozzle section, thus a 15° conical divergent was assumed instead of a bell nozzle. The latter is longer than the former and thus this is a likely reason for the difference.

Exit Conditions	Sippel	CEA	Diff [%]
Mach Number [-]	3.411	3.354	-1.67
Temperature [K]	1579	1569.68	-0.59
Pressure [kPa]	60	72.432	20.7

Table 7.5: Exit conditions of the SE21D as found by Sippel and from CEA

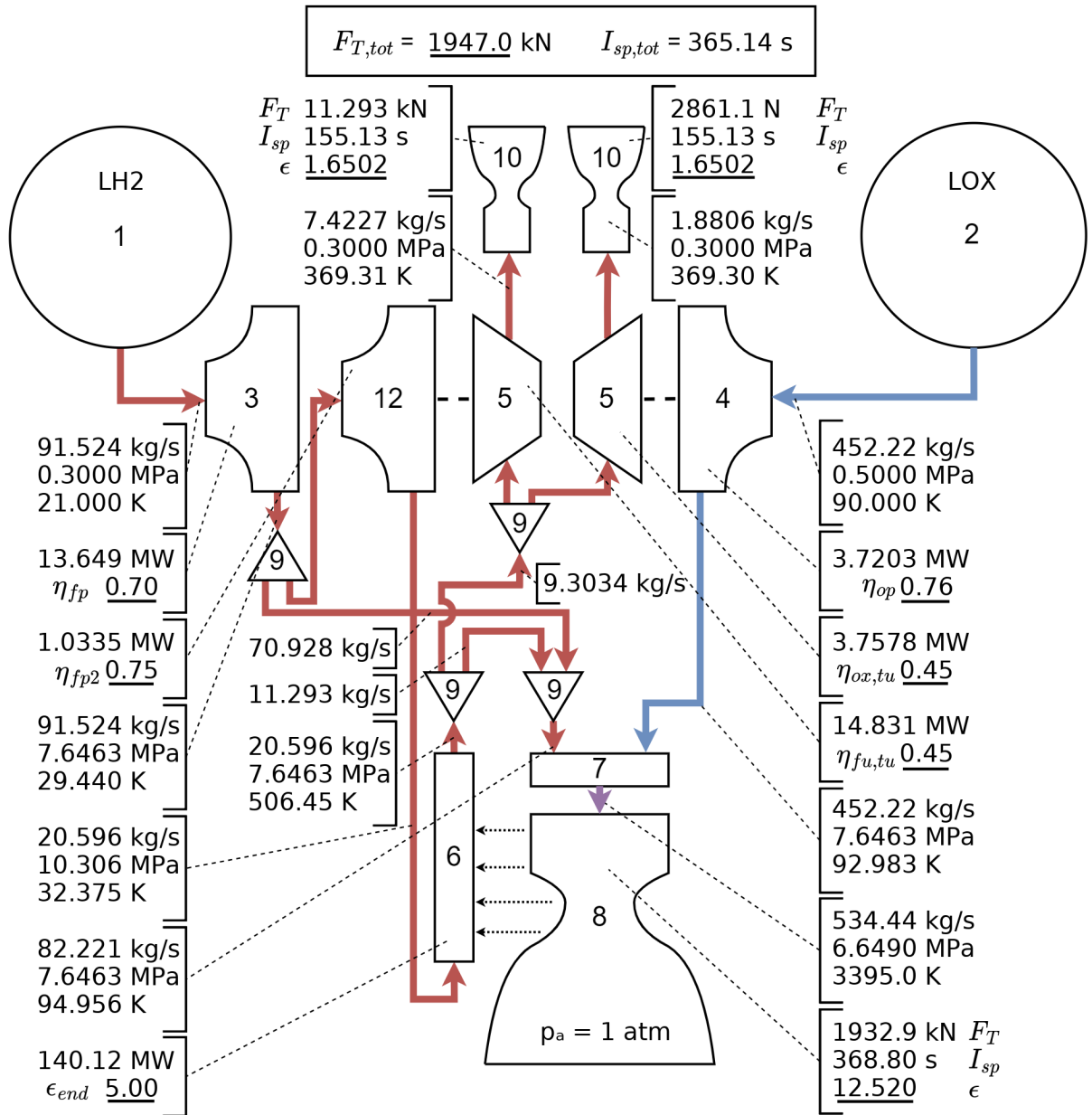


Figure 7.5: Schematic overview of performance parameters and flow parameters for the SE21D as simulated by RoCAT

Some differences in the specific impulses remain as well. Although not a large difference, the main specific impulse difference is quite important and a 1% difference has a considerable effect on performance. A possible reason is heat loss due to regenerative cooling, which is not accounted for in the modeling. The latter reason was also identified by Ernst [20], who also compared his simulation with Sippel's SE21D data, but that seems not very likely in this case as exit temperature and mach number are lower as found by CEA than given by Sippel as can be seen in table 7.5. A final aspect to be considered is that the decomposition of RP-1 due to a high temperature after the cooling section is not accounted for, which might lead to reduced specific impulse. This aspect is discussed in more detail in section 8.1.3.

Overall it is clear that there is room from improvement in the heat transfer model and pump outlet pressure calculation, but otherwise the models agree nicely.

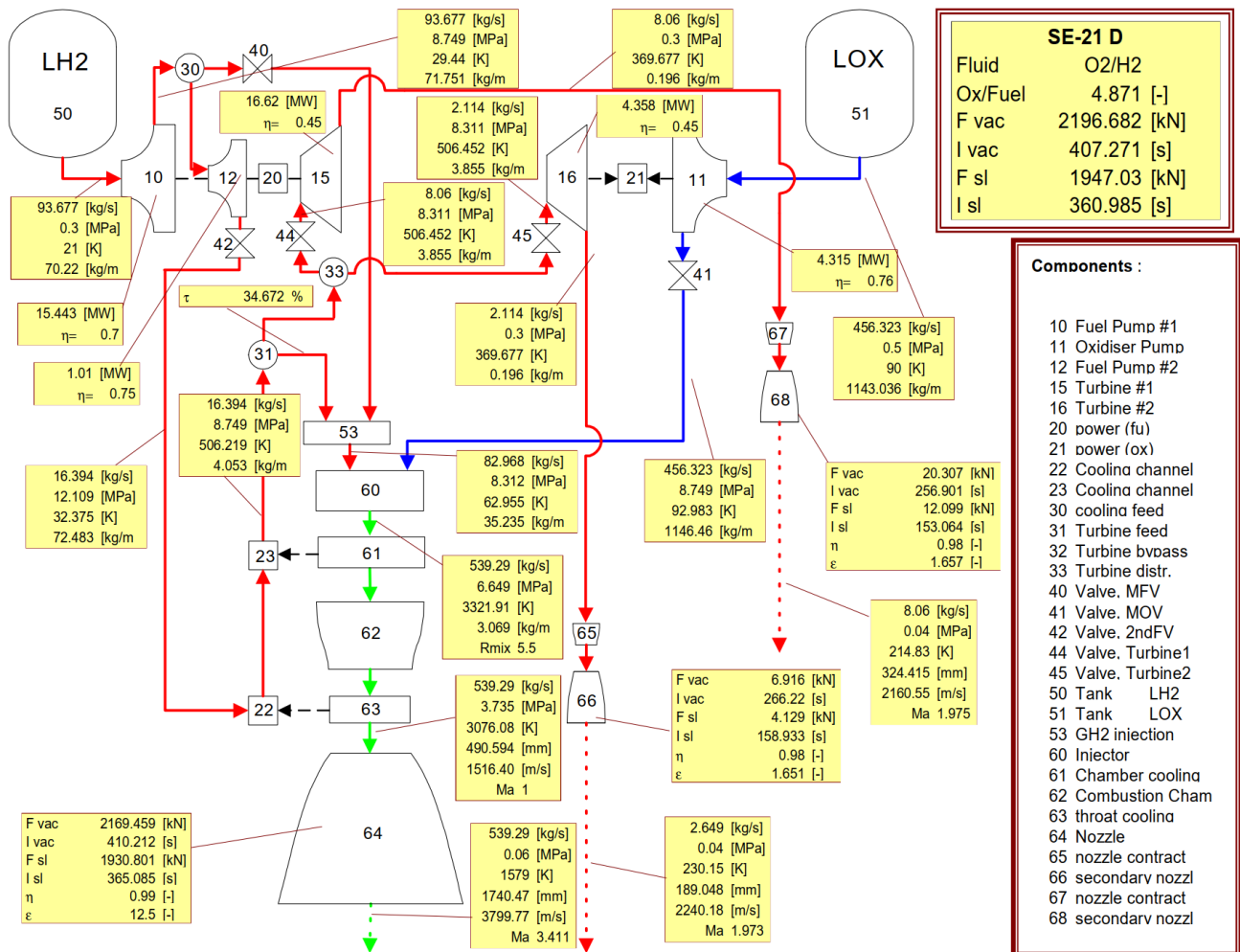


Figure 7.6: Schematic overview of performance parameters and flow parameters for the SE21D as simulated by Sippel [53]

### 7.1.6. Open Expander Validation

Real world data is limited for the open expander cycle as very few engines of this type have been made, the closed expander cycle is more common. More specifically, the LE-5A and B engines are the only production engines with this cycle [37] (more recently joined by the LE-9). The LE-5A has complex split cooling, while the LE-5B's configuration is more in line with most open expander cycle configurations discussed in this report. As a consequence the LE-5B is used in the comparison. The specific configuration of the LE-5B is an open expander with single pumps and double turbine in series.

Unfortunately, data on the LE-5B is limited and sometimes intermixed with data from the LE-5 engine, which is a gas generator and not an open expander, e.g. in the work of Ernst [20]. Almost all required inputs were found with the exception of four parameters: the efficiencies of both pumps, and the efficiencies of the turbines. Therefore, these have been assumed to be equal to the values given for the SE21D discussed previously. Since these are quite crucial parameters this brings some added uncertainty to the RoCAT outputs, but differences are expected to be small enough for the comparison to still be relevant. The complete set of inputs can be found in appendix B and the comparison between output values is shown in table 7.6 below.

	LE-5B [2]	RoCAT	Abs. Diff. [%]
<b>Exit Diameter [m]</b>	1.65	1.67	0.94
<b>Vacuum Specific Impulse [s]</b>	447	451.0	0.90
<b>Length [m]</b>	2.75	3.16	15.08
<b>Engine Dry Mass [kg]</b>	285	104.5	63.33
<b>Heat Transfer [MW]</b>	8.30	11.86	42.81
<b>Fuel Side</b>			
<b>Pump Outlet Pressure [bar]</b>	68.6	56.1	18.21
<b>Pump Mass Flow [kg/s]</b>	5.20	5.72	10.00
<b>Shaft Power [kW]</b>	805.7	593.3	26.36
<b>Turbine Inlet Pressure [bar]</b>	36.9	41.6	12.82
<b>Turbine Inlet Temperature [K]</b>	409	409	-
<b>Turbine Outlet Pressure [bar]</b>	7.20	8.12	12.82
<b>Turbine Mass Flow [kg/s]</b>	0.66	0.67	1.33
<b>Oxidizer Side</b>			
<b>Pump Outlet Pressure [bar]</b>	53.0	41.6	21.45
<b>Pump Mass Flow [kg/s]</b>	26.9	25.3	6.11
<b>Shaft Power [kW]</b>	182.0	115.3	36.66
<b>Turbine Inlet Pressure [bar]</b>	6.30	8.12	28.94
<b>Turbine Inlet Temperature [K]</b>	329	348	5.77
<b>Turbine Outlet Pressure [bar]</b>	2.90	3.74	28.96
<b>Turbine Mass Flow [kg/s]</b>	0.49	0.29	41.22

Table 7.6: Comparison between real data and RoCAT output for LE-5B open expander engine

From table 7.6 it can be seen that there is decent agreement overall, but serious differences for several parameters. Some chaining effects can be seen, for both propellant sides the pump outlet pressure is significantly underestimated, which leads to reduced shaft power. On the contrary the turbine inlet and outlet pressures are too high. Oddly enough the combination of high turbine pressure and reduced shaft power leads to a very accurate turbine mass flow for the fuel side. For the oxidizer side the turbine mass flow is reduced, which is more in line with expectations, especially considering the somewhat higher inlet temperature. Lastly, it is important to note that the heat transfer is overestimated by about 43%, which likely means RoCAT calculates more cooling flow than is the case in reality.

### 7.1.7. Performance Conclusions

In this section the RoCAT model has been compared to another model for every cycle type. In general there seems to be good agreement between models on the overall specific impulse and most other parameters of interest. The parameters that deviate consistently are the regenerative heat transfer and pump outlet pressures. For the former this deviation is deemed acceptable as first order heat transfer estimation is notoriously difficult and very simplifying assumptions have been made. Additionally, any improvement to this part of the model would most likely cost quite some time while also greatly increasing the calculation time of each analysis run. The outlet pressures deviation with respect to the other models is more concerning and would most likely be easier to fix. The current estimation accounts for the pressure drop over each individual component, but the individual component pressure drops are all calculated as a simple linear factor of the chamber pressure. The performance verification and validation have identified this as a clear weak point of the model.

## 7.2. Mass

This section focuses on the validation of the mass models for RoCAT. Similar to the previous section each cycle is discussed in turn, which is followed by overarching conclusions. In contrast to the previous section, only validation is discussed as no enough data is available from similar models to do verification.

### 7.2.1. Electric-Pump

For the electric-pump cycle no real world mass data is available. Only the Electron has flown with this cycle and Rocket Lab has not published any well defined mass data. Consequently, comparison is only possible with simulated data from literature. Although a handful of models for the electric-pump cycle have been presented in previous research, only two give absolute mass data; Kwak et al. [34] and Lee et al. [35]. Since the former has been the foundation for RoCAT there is good agreement between RoCAT and Kwak's results as has been established in section 3.2. Therefore, the comparison is made with data from Lee's paper as an addition. The mass comparison is made for the electric-pump cycle engine discussed in that paper for which the RoCAT inputs can be found in appendix B.3.1. The main inputs are listed below:

- Thrust: 500 N
- Chamber Pressure: 20 bar
- Burn Time: 600 sec
- O/F-ratio: 2.45
- Fuel: RP-1
- Oxidizer: LOX

The results of this comparison can be seen in table 7.7. "Power" in this table refers to the sum of the battery, inverter, electric motor and pumps. From table 7.7 one can see that there is varying agreement between

Component	Lee	RoCAT	Abs. Diff. [%]
Tanks	0.598	0.650	8.82
Feed line	2.474	-	-
Power*	2.585	2.179	15.73
Thrust Chamber	5.138	0.254	95.05
Propellant	97.788	106.241	8.64
Total**	106.110	109.324	3.03

Table 7.7: Comparison of RoCAT and Lee et al.[35] masses for an electric-pump cycle engine

\* Battery, Inverter, Electric Motor, and Pumps - \*\*Total mass without Feed line mass

the mass parameters for both models. The mass values for the tanks, propellant, and total match acceptably (<10%), while for the combination of all power components the agreement is somewhat less and for the thrust chamber the difference is more than an order of magnitude. Upon further inspection a likely explanation for the smaller differences is a difference in specific impulse, which is somewhat expected as Lee uses CEA with shifting equilibrium settings, while RoCAT uses frozen settings. This explains the higher propellant mass and consequently higher tank mass. However, a higher propellant mass would also indicate a higher mass flow, which would cause higher mass for all power components, while the opposite seems the case. Most likely this is caused by a difference in pump exit pressures, as Lee used more detailed methods to estimate them. Finally, the thrust chamber values do not agree at all. This seems to be the case for all cycles and configurations, as shown in the following subsections, and this is discussed further in the general conclusions at the end of this chapter.

### 7.2.2. Gas Generator

For the gas generator cycle mass data from McHugh is used [41] just as was done in the performance section. The deviation of RoCAT output from the data from McHugh is shown in table 7.8.

	HM7B	H-1	RS-27	F-1	HM60	J-2	Abs.Avg.
Engine Dry Mass [%]	-67.03	-58.72	-62.28	-28.52	-12.16	-52.09	46.80
Chamber Mass [%]	-66.38	-41.58	-46.95	-	-12.17	-43.72	42.16

Table 7.8: Differences between mass data from McHugh [41] and RoCAT for selected GG engines

It is evident from the data in the table that the estimated mass of the engine is vastly underestimated for most of the engines. Some underestimation is expected, as not all components are modeled. Additionally, the components that are modeled only include the essentials while neglecting peripherals such as connections,

sensors, and support structures. However, it is concerning that the engine's dry mass is not even half of what was expected.

The deviation for these same engines is small for the performance parameters, as previously shown in section 7.1.4. Consequently, it can be deduced that the issues lies with the mass models. More specifically, the modeling of the thrust chamber (injector, chamber, and nozzle) is shown to be a main problem in table 7.8. Unfortunately, it is not clear from this limited data how the mass of the other components that make up the engine's dry mass compare to the real masses.

### 7.2.3. Open Expander

Almost no real world data could be found for open expander engines with the single exception of the LE-5B engine dry mass. Other open expanders were or are under development like the M10 for the Vega-E, BE-7 for the New Glenn, and LE-9 for the HIII. However, for none enough data could be gathered to simulate them, despite their (expected) dry masses being available. Consequently, for the open expander cycle mass model the LE-5B's dry mass is the only validation point. It was already given in table 7.6, but for convenience is repeated below table 7.9:

	LE-5B [2]	RoCAT	Diff [%]
Engine Dry Mass [kg]	285	104.5	-63.33

Table 7.9: Comparison between RoCAT and real data for LE-5B engine dry mass

Some deviation is likely due to uncertainty in assumed inputs, as discussed in section 7.1.6. Nonetheless, the engine dry mass is severely underestimated, which is in line with the findings in the previous sections.

### 7.2.4. Mass Conclusions

Combining the discussion from the previous subsections, it becomes apparent that the mass models are quite inaccurate and severely underestimate the engine dry mass. Although detailed mass data per component is lacking, it seems that this is mostly due to the thrust chamber (injector, chamber, and nozzle) mass. This is most likely due to limited modeling which only accounts for a shell mass. Additionally, some components that have not been modeled in RoCAT contribute significantly to the total engine dry mass, i.e. feed lines and valves. Furthermore, the mass of the heat exchanger has also not been modeled. The lack of these components exacerbates the underestimation of the engine dry mass.

Several options are available to improve the mass modeling, but none of them have been applied in this research. Since the primary objective of this study is comparative, accurate absolute values are of lesser concern. Although the models' accuracy may be limited, they remain reasonably consistent over a wide range of thrusts and cycles, and are therefore still useful for comparing individual cycles. Nevertheless, it is essential to note the inaccuracy of the mass models, and ideally, they should be improved. Some options for improvement include:

- Adding (mass) models for the feed lines, valves, and cooling jacket
- Improving the thrust chamber mass model through more detailed modeling
- Adding correction factors based on existing data
- Switching from physical modeling to empirical models

Each of these has some drawbacks, but the empirical factors are probably the easiest improvement. As an example a correction factor of about 1.44 for the thrust chamber mass could have been found from table 7.8. This also matches reasonably with the correction factor found by Ernst [20] of 1.51, which used similar mass models and also applies such a correction factor. However, the mass data is quite limited and adding correction factors to match this data somewhat invalidates their use in validation.

In this chapter the models of RoCAT have been verified and validated. It can be concluded that the performance and flow parameters are all generally modeled within acceptable margins ( $<30\%$ ), while this is not the case for the mass models. Especially the thrust chamber mass is severely underestimated. Outputs that see considerable, but acceptable deviation are the pump outlet pressures and the regenerative heat flow rate. With the models of RoCAT validated and verified and its limitations identified, it can be used to compare the various cycles in the next chapter.

## Results & Discussion

In this chapter the electric-pump cycle is compared to the gas generator cycle and open expander cycle. First for the same input chamber pressure and mixture ratio and secondly with the same inputs individually optimized. Four aspects are considered: initial mass, mass ratio, total specific impulse and velocity change. This is followed by an analysis of future development of the electric-pump cycle. A detailed definition of the performance aspects is given in fig. 6.14 for the initial mass, section 6.8.1 for the mass ratio, eqs. (6.2b) and (6.12a) for the total specific impulse, and eq. (6.19a) for the velocity change.

As already mentioned in the introduction, the performance of the engine cycles is of interest, which is why these parameters were chosen. Initial mass largely determines acceleration, places a lower limit on the initial thrust, and largely determines the payload mass of its lower stage if applied as upper stage. The velocity change directly shows what payload can be taken to which altitude or orbit. The mass ratio itself is mostly of interest as determining parameter of the velocity change. The same is true for the specific impulse, while it also shows how efficiently the engine uses propellant. Finally, the mass ratio itself is also of interest, since it will clearly show the difference between the expelled turbine drive gas and the battery which is carried along.

### 8.1. Direct Cycle Comparison

The models in RoCAT are used to compare the electric pump, gas generator, and open expander cycle. In this section this is done directly, i.e. each cycle is compared to another at the same input chamber pressure, burn time, and thrust, assuming RP-1 as fuel. All other inputs are taken as default, see tables 5.4, 5.5, 5.7 and 5.8 for these default values. There are two exceptions:

- End of cooling expansion ratio: 10
- Exit pressure: 0.02 bar

The cooling of the nozzle needed to be limited because otherwise the required coolant flow would be greater than the main fuel flow for large sections of the design space, which lead to invalid designs and which RoCAT consequently does not accept. This does not limit the energy supplied to the turbine in the open expander cycle since the minimum required coolant flow was higher than the required turbine flow in almost all cases, i.e. the temperature of the turbine inlet was almost always maximum in the open expander cycle. This is also what one would expect from the double split open expander cycle, as previously discussed in section 4.3.3. The exit pressure was selected to stay in concordance with the work of Kwak et al. [34].

To give some more detailed insight into the cycles their performance schematics are first provided in figs. 8.1 to 8.3 for each cycle. This is only a single engine in the middle of the considered ranges, i.e. a burn time of 750 and a chamber pressure of 50 bar. The schematics give insight in the differences between the cycles. It is interesting to note that the electric-pump and gas generator cycle have almost the same fuel flow, despite the clear difference in recirculating battery coolant and additional flow for the gas generator. Furthermore, it also clearly shows that the turbine exhaust contributes less to the thrust in the case of the open expander cycle than for the gas generator cycle, despite the former having a higher turbine mass flow. These quirks will be discussed further in the specific impulse subsection.

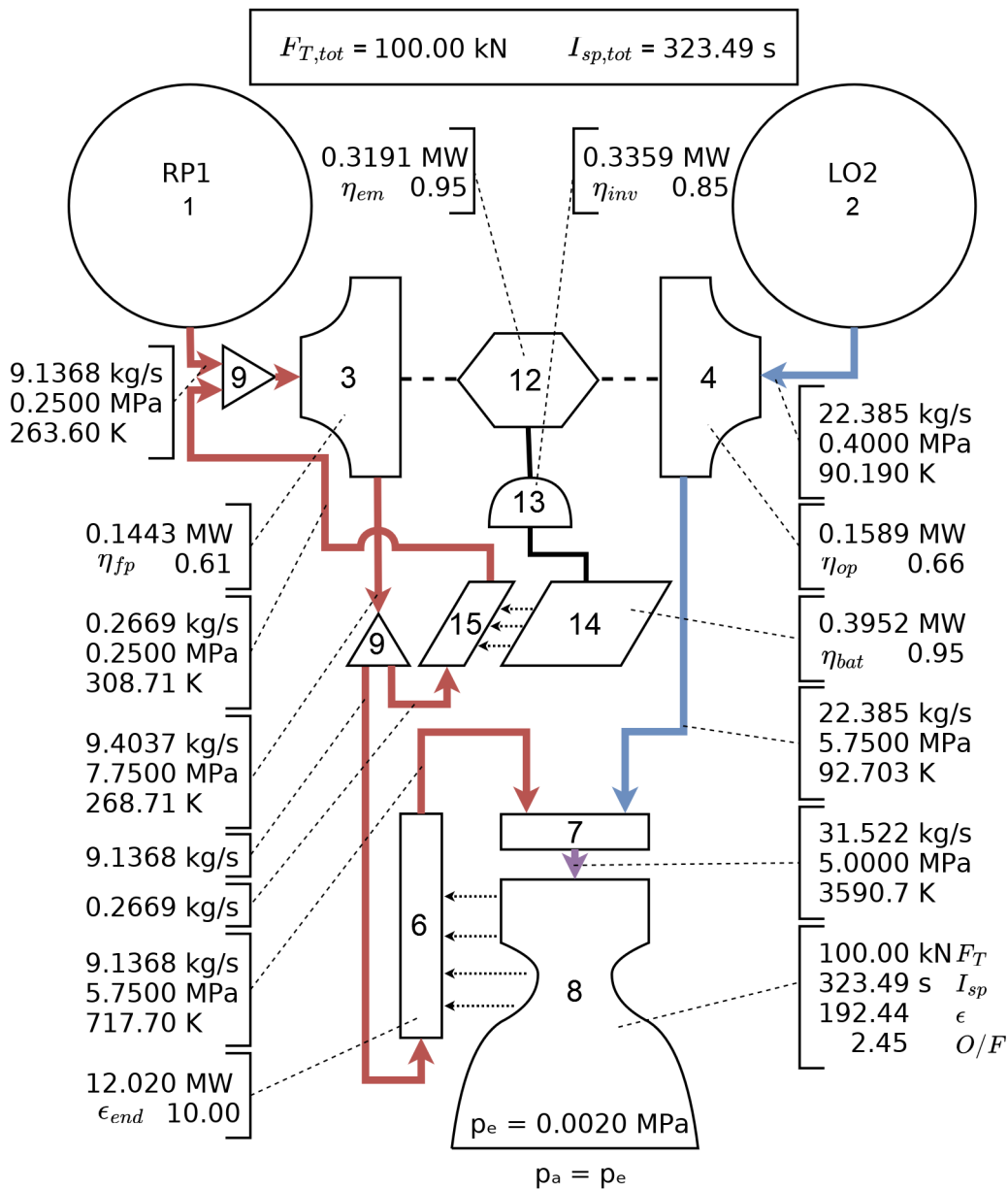


Figure 8.1: Performance schematic of an electric-pump cycle engine with  $F_T=100\text{kN}$ ,  $t_b=500\text{s}$ ,  $p_{cc}=50\text{bar}$

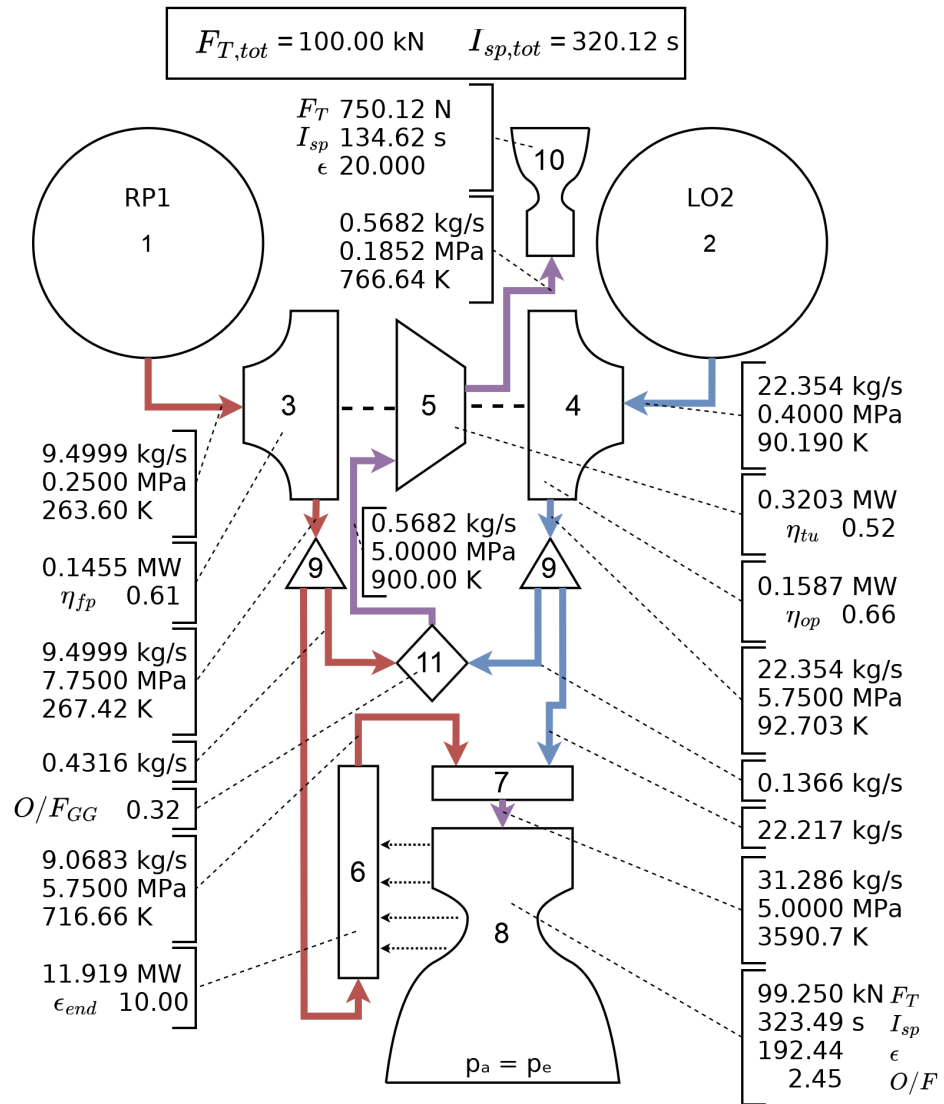


Figure 8.2: Performance schematic of a gas generator cycle engine with  $F_T=100\text{kN}$ ,  $t_b=500\text{s}$ ,  $p_{cc}=50\text{bar}$

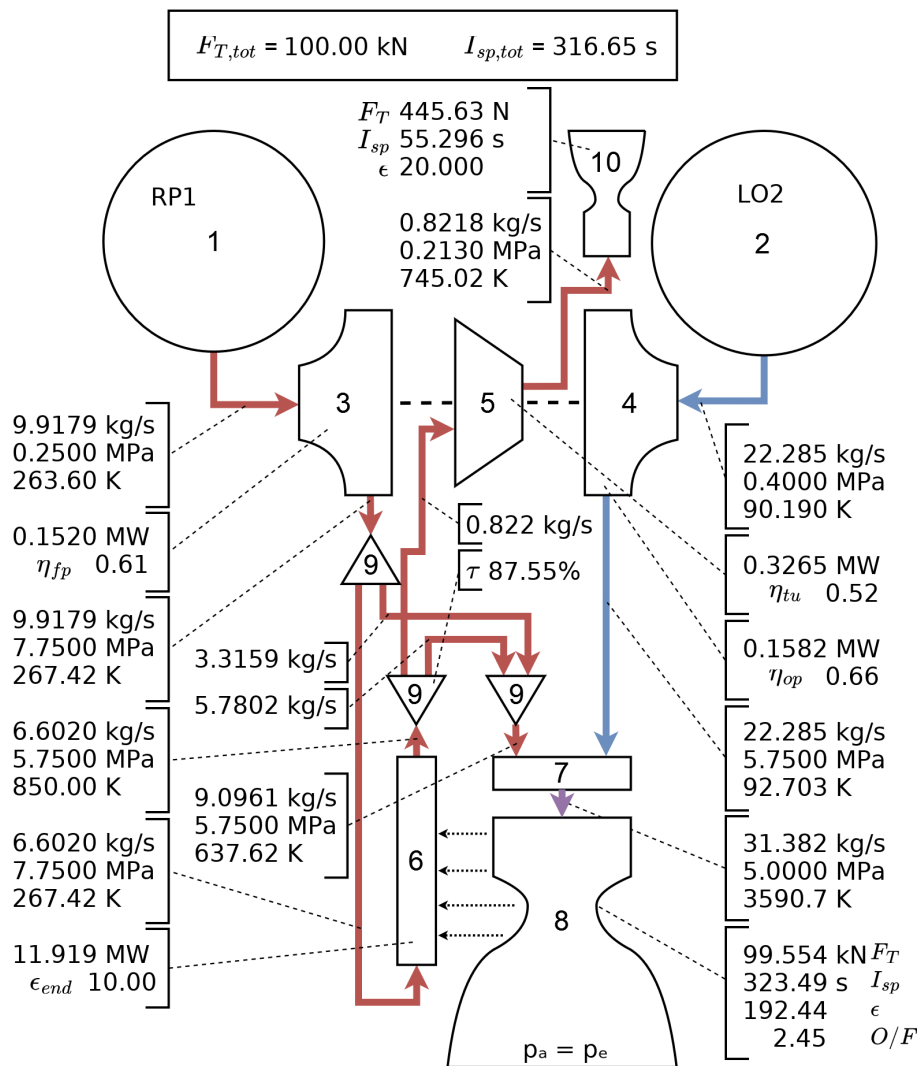


Figure 8.3: Performance schematic of an open expander cycle engine with  $F_T=100\text{kN}$ ,  $t_b=500\text{s}$ ,  $p_{cc}=50\text{bar}$

With some initial insight from the schematics, it is now time to compare the cycles over the whole considered ranges. The electric-pump cycle is compared to the gas generator cycle and open expander cycle on the four parameters mentioned at the start of this chapter. This direct comparison is made for engines with 100 kN thrust for which the chamber pressure and burn time are varied. Only a single thrust is selected since it was observed that thrust has very little effect on the relative differences although it greatly influences the absolute values, which is in line with Kwak's findings [34].

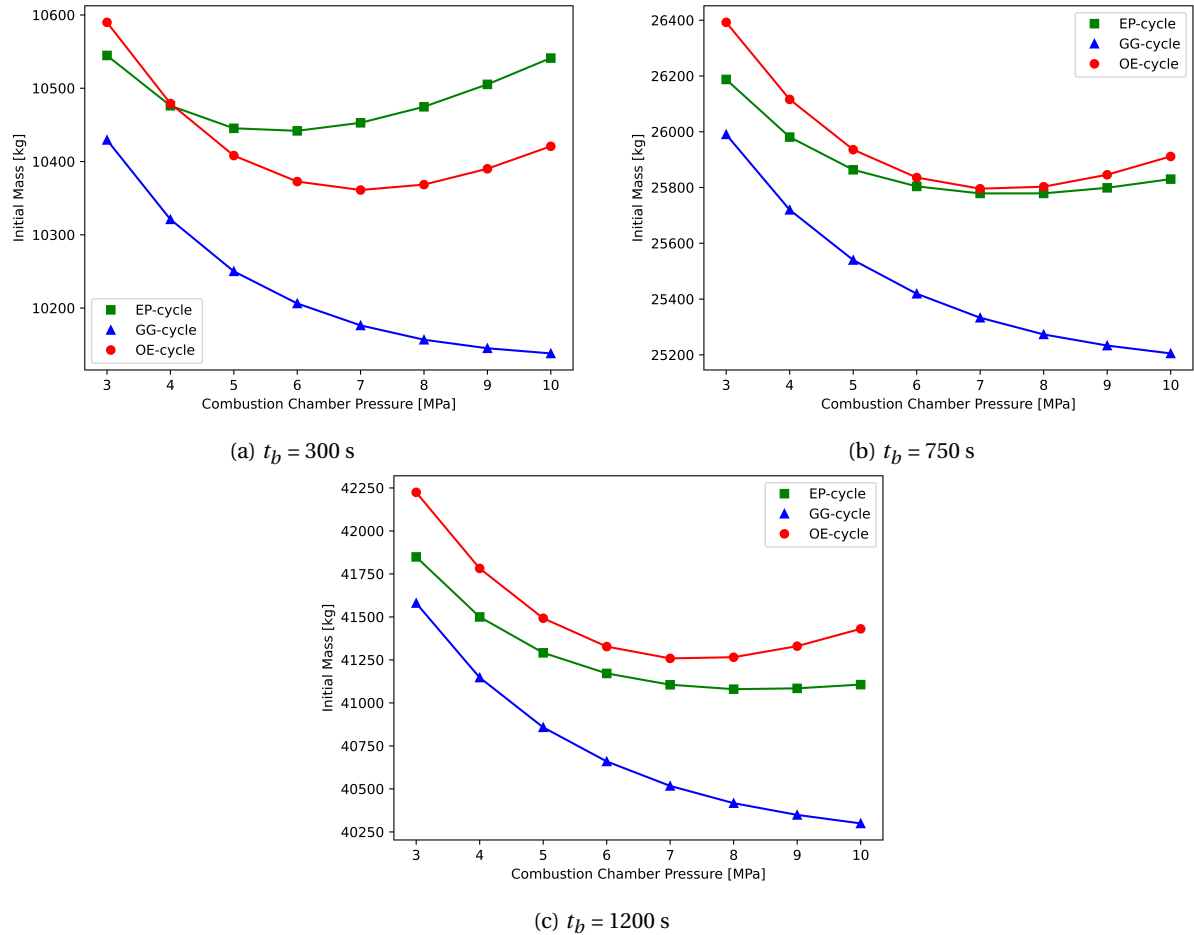


Figure 8.4: Comparison of initial mass between EP-, GG-, and OE-cycle

### 8.1.1. Initial Mass

As can be seen in fig. 8.4 the initial mass of the electric-pump cycle engine is larger than that of the gas generator cycle over the whole range of chamber pressures and for all burn times. This is different from previous research, most notably Kwak et al [34], which found the initial mass of the electric-pump cycle to be lower than the gas generator cycle's initial mass for burn times above 390 seconds with the same inputs. Additionally, the open expander cycle is quite a bit heavier than the gas generator cycle for all considered inputs. Further discussion as to why the open expander performs worse than the gas generator is discussed in a subsequent part of this chapter.

In the three graphs all cycles have an optimal chamber pressure at which they have the lowest initial mass, although that of the gas generator is slightly outside the considered range (10.5 and 13.0 MPa for burn times of 300 and 1200 sec respectively). Additionally, for both conventional cycles this optimum moves marginally for different burn times, while burn time has a large effect on the optimum for the electric-pump cycle. Both the effects of chamber pressure and burn time are considered in more detail.

Group	Components	$p_{cc}$	$t_b$
Energy Source	Turbine Propellant, Battery	↑↑	↑↑
Feed System	Pumps, Turbine, Gas Generator, Electric Motor, Inverter	↑↑	-
CC Prop. Group	Chamber Propellant, Pressurant, Tanks	↓	↑↑
Thrust Chamber	Injector, Combustion Chamber, Nozzle	?	-

Table 8.1: Expected effect of an increase in chamber pressure and burn time on component masses

To do so the components are divided in four groups as is shown in table 8.1. This table also shows the theoretical effect that increases in burn time and chamber pressure are expected to have. Firstly, the feed system components' masses are expected to roughly increase linearly with chamber pressure as this directly increases the power required by the pumps on which the mass estimation of these components is based. Burn time, however, is not expected to have any effect on these components.

This is in contrast to the energy source group, which is also dependent on the pump power, but should scale roughly linearly with burn time as longer operation leads to more turbine propellant mass and a heavier battery. An important caveat for the battery is that the battery should be energy limited for it to scale with burn time. This is true for all considered burn times as the selected battery has an optimal discharge time of only 100 sec.

For the third group, it is a core principle of engine design that chamber propellant is expected to decrease with increasing pressure due to specific impulse gains and subsequent decrease in chamber propellant flow. The effect of burn time on this group is expected to be positive and roughly linear. Additionally, the tanks and pressurant scale with total propellant volume, but can be assumed to scale the same as the chamber propellant, since this makes up at least 94% of the total propellant volume in all considered cases.

Finally, for the thrust chamber the effect of an increase in chamber pressure is less clear as it increases the thickness of the components, but reduces their size through a reduced throat area (also through reduced mass flow). Additionally, the area ratio is changed since the exit pressure is given, while the chamber pressure is varied. This also has an effect on the size of the nozzle. Changes in burn time are expected to not have any effect on the thrust chamber mass.

### Detailed Pressure Effects

Above the expected behavior of these groups has been predicted, while figs. 8.5 and 8.6 show the actual behavior of these mass groups with changing chamber pressure with a burn time of 300 sec. In fig. 8.5 it can be seen that feed system mass indeed grows with chamber pressure and the electric-pump cycle's feed system mass is heavier and grows much faster than that of the two conventional cycles for which the difference is barely noticeable on this scale. The thrust chamber mass develops similarly for all cycles, with the electric-pump cycle's being slightly heavier. This can be explained due to a slightly higher chamber mass flow. The sudden kink in the graph line for thrust chamber mass is due to the minimum material thickness, i.e. for pressures lower than 5 MPa the thickness is decided by this minimum and increases in pressure lead to a smaller throat area, which ultimately leads to a lower mass. Above 5 MPa the thickness is determined by the chamber pressure and increases in pressure still lead to a reduced throat area, but the effect of increased thickness is larger and leads to a heavier thrust chamber.

The masses of the energy source and chamber propellant group are plotted in fig. 8.6, which directly shows that the former increases with increasing pressure, while the latter decreases. In this graph both y-axes cover a range of 700 kg, thus visual differences for both mass groups translate to equal absolute numerical differences and can be compared more intuitively. The differences between the cycles for the energy source masses are larger than those between the cc prop group. Additionally, energy source mass growth rate is constant or increases for all cycles. This in contrast to the CC propellant group mass, whose decrease levels off with increasing pressure. These two effects combined explain the optimum chamber pressures for initial mass that were found in fig. 8.4. The growth of the feed system and thrust chamber mass also contribute, but for the conventional cycles they comprise at most 1.2% of initial mass, while for the EP-cycle this is 2.4%. This only becomes less with increasing burn times, so their effect is limited.

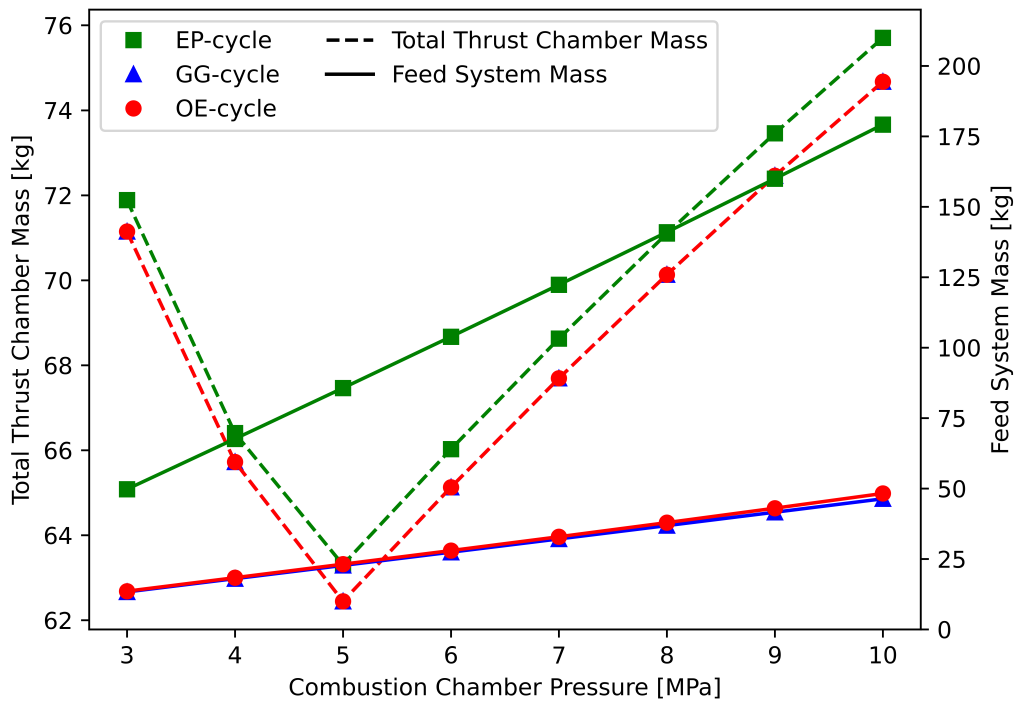


Figure 8.5: Development of thrust chamber mass and feed system mass with chamber pressure

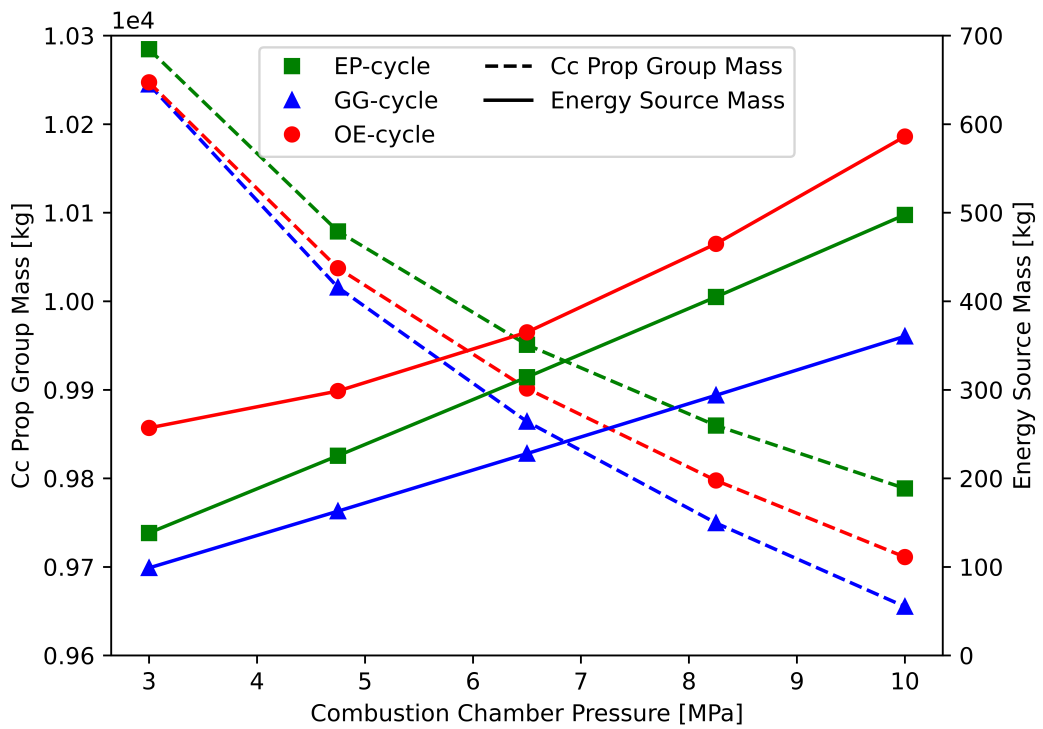


Figure 8.6: Development of energy source mass and cc prop. group mass with chamber pressure

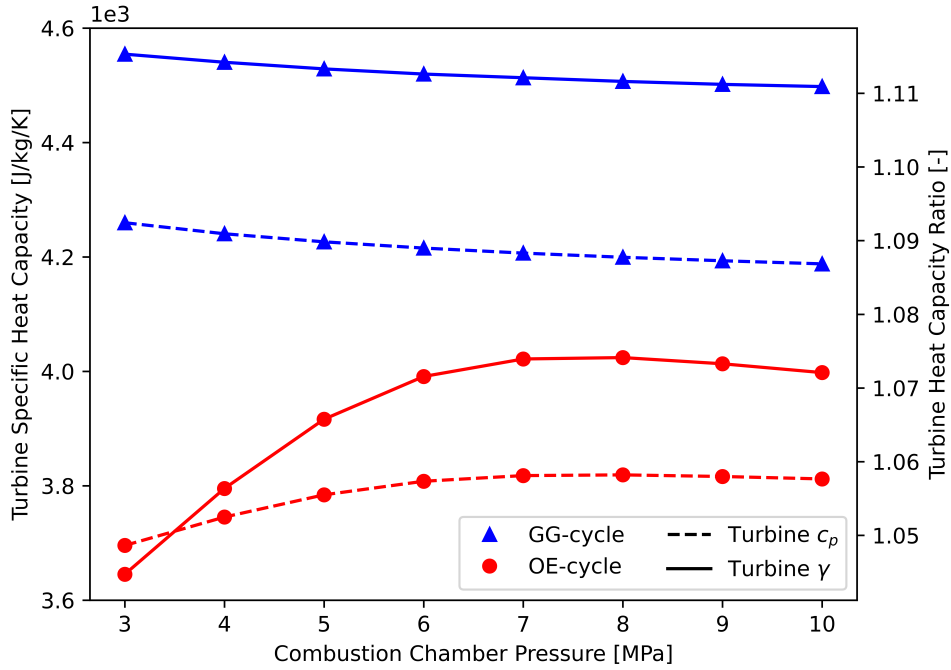


Figure 8.7: Turbine inlet properties versus chamber pressure for the GG- and OE-cycle

A last thing to be discussed from fig. 8.6 is the fact that the energy source mass for the EP- and GG-cycle is nearly linear with chamber pressure, while for the OE-cycle the growth rate increases. Upon closer inspection this is caused by the turbine inlet properties relation to chamber pressure. Figure 8.7 show their development. It becomes clear that the turbine inlet properties develop differently for the gas generator and open expander cycle. Since the mass flow required by the turbine,  $\dot{m}_{tu}$ , is proportional to the specific heat capacity,  $c_p$ , and heat capacity ratio,  $\gamma$ , as given below in eq. (8.1).

$$\dot{m}_{tu} \propto \left( c_p \left( 1 - \left( \frac{p_{in}}{p_{out}} \right)^{\left( \frac{1}{\gamma} - 1 \right)} \right) \right)^{-1} \quad (8.1)$$

From the above equation it can be concluded that with increasing  $\gamma$  and  $c_p$  the required turbine mass flow decreases, consequently a decreasing growth rate of these properties results in an increasing growth rate of the turbine mass flow and subsequent turbine propellant mass as was found in fig. 8.6. Therefore, the property deviation explains why the turbine propellant mass does not grow linearly with pressure for the open expander, but does for the gas generator. It is important to note that the open expander and gas generator have different driving gasses for the turbine: heated fuel and fuel-rich combustion gasses respectively. Additionally, different models calculate the properties of these turbine drive gasses. For the OE-cycle they are determined through CoolProp, while for the GG-cycle they are determined through an empirical relation or CEA as discussed in section 5.4.1. Additional ramifications of this difference are discussed below in section 8.1.3.

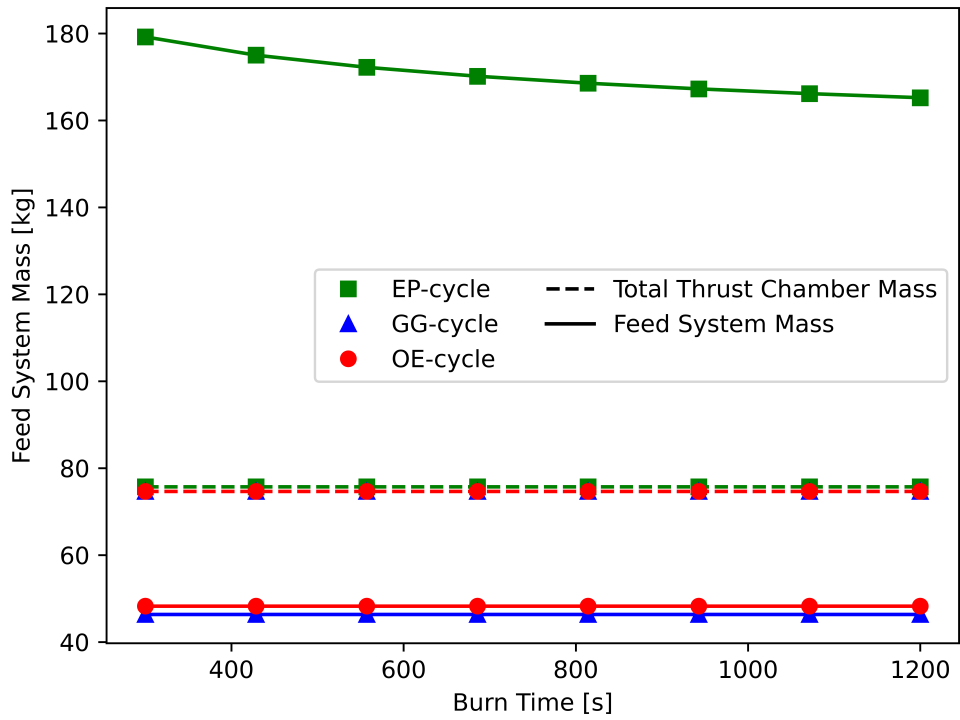


Figure 8.8: Development of feed system mass and thrust chamber mass with burn time

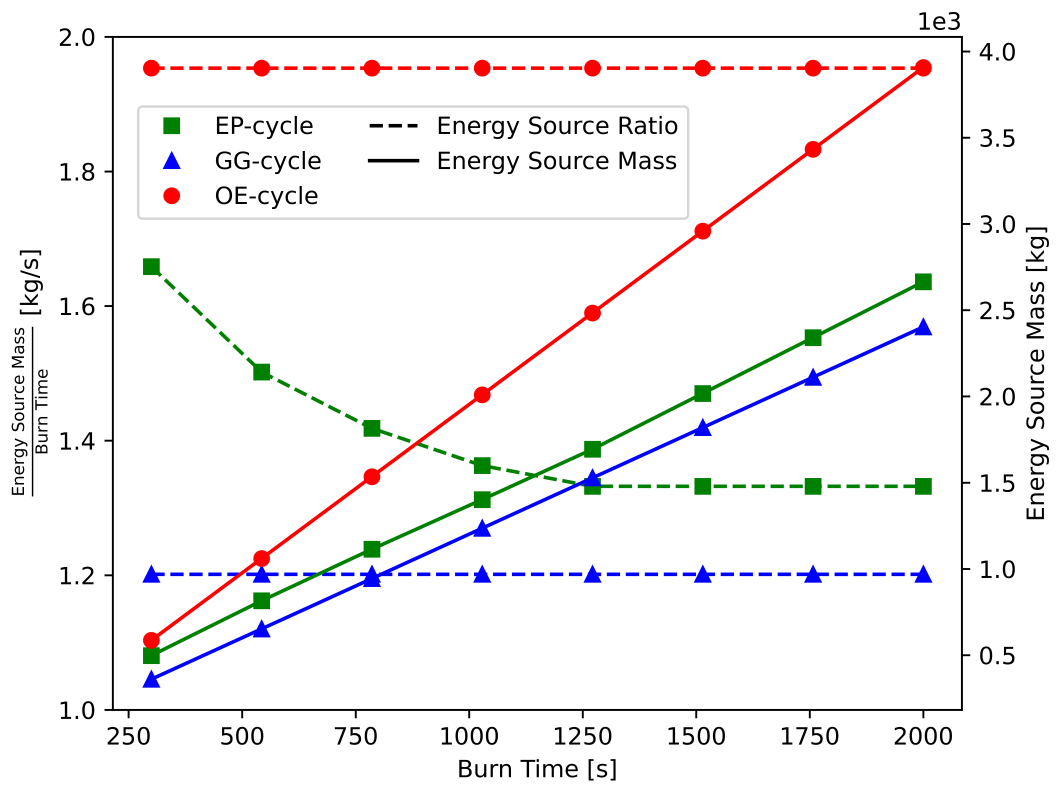


Figure 8.9: Development of energy source mass with burn time

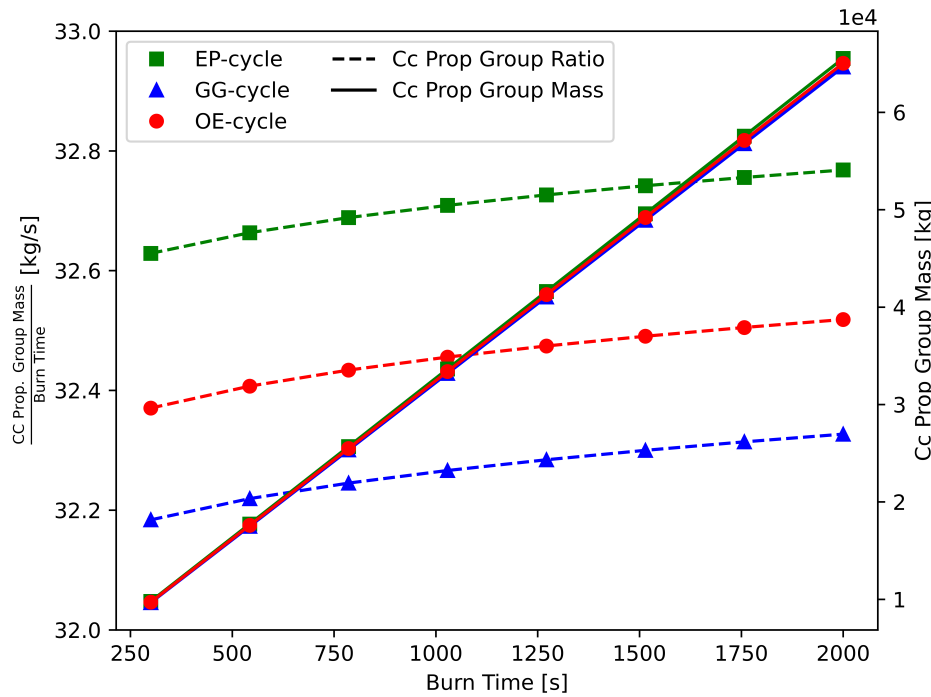


Figure 8.10: Development of chamber propellant group mass with burn time

### Detailed Burn Time Effects

In this paragraph the effect of changes in burn time on the the previously defined four groups are analyzed. The mass groups are plotted against burn time for engines with a chamber pressure of 10 MPa. Figure 8.8 shows the feed system mass and thrust chamber mass. For both it was predicted that burn time would have no influence and that is the case with the clear exception of the EP-cycle feed system mass, which decreases with burn time. This decrease is due to the battery efficiency being dependent on discharge time, i.e. burn time; with higher burn times the battery is more efficient, produces less heat and less battery coolant is required, which leads to lower pump power and ultimately a lighter feed system. This is in line with the findings made by Kwak et al. [34].

The effect burn time has on the energy source mass and chamber propellant group mass are shown in figs. 8.9 and 8.10. In addition to the absolute mass values a burn time ratio is shown to clearer visualize the effects of burn time on the different cycles. Therefore, in fig. 8.9 the straight horizontal lines for the OE- and GG-cycle energy source ratio indicate a linear relation with burn time. For the EP-cycle the energy source mass grows with burn time, but from the burn time ratio it becomes clear that the growth rate declines until it hits a minimum. This coincides with the battery hitting a discharge efficiency of 100% at  $\pm 1344$  seconds. With the current assumptions no battery cooling would be required from this point onwards. This limit was not considered in previous research, but is important to consider since it means that further burn time increases do not improve the relative performance of the EP-cycle to conventional cycles. Additionally, the battery heating model is probably not adequate for these burn times as discharging batteries heat up, even at 100% discharge efficiency and above. It however essentially shows the performance of an electric-pump cycle that does not need cooling.

Figure 8.10 shows the difference between the chamber propellant group mass. Its growth with burn time is the same for all cycles. Since it is visually not very clear: the Chamber propellant mass of the open expander cycle is consistently 0.8% less than that of the electric-pump cycle, while that of the gas generator cycle is consistently 1.4% less. The development of this mass group is as expected and the relative differences between the cycles are independent of burn time for this group.

### 8.1.2. Mass Ratio

In the previous section the initial mass has been divided into four groups and the effect of chamber pressure and burn time on each of these groups has been discussed. The mass ratio is derived from these groups and defined as initial mass divided by final mass. For all cycles the feed system and thrust chamber groups are part of the final mass. The chamber propellant group should be split, since the tanks and pressurant are part of the final mass, but the chamber propellant is not.

Lastly, the energy source group should be considered. This is where the main difference between the cycles is found; the turbine propellant is expelled during flight for the conventional cycles, while the battery is kept on board for the electric-pump cycle.

This leads to the mass ratio developing as shown in fig. 8.11 for various burn times and chamber pressures.

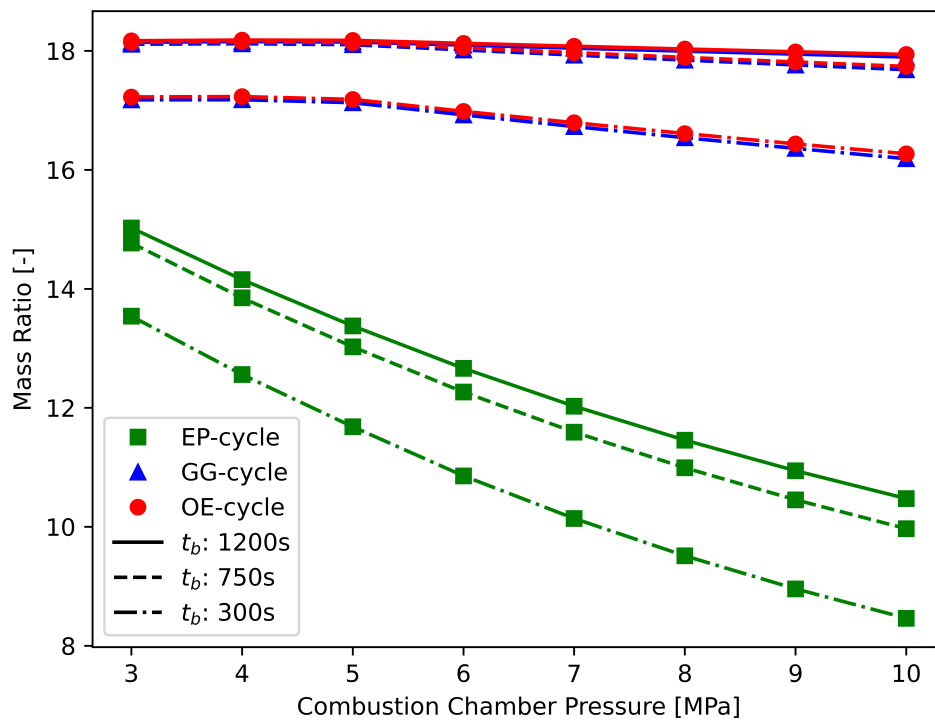


Figure 8.11: Comparison of mass ratio between EP-, GG-, and OE-cycle

In fig. 8.11 the differences between the conventional cycles are barely visible compared to the difference with the electric-pump cycle. The main cause of this large difference is the battery mass. However, even if the battery mass would be "expelled", fig. 8.5 already showed that the feed system of the electric-pump cycle is heavier than that of the other cycles over the considered pressure range. Additionally, it is clear that all cycles have higher mass ratios for longer burn times. This is to be expected as the increase in required propellant dominates all other effects of increased burn time. The graph also shows a decrease in mass ratio with chamber pressure for all cycles. This is also as expected. For example, for the electric-pump cycle, the total propellant decreases about 6% when increasing the chamber pressure from 3 MPa to 10 MPa. Conversely, the feed system mass more than triples. So the final mass increases, while the initial mass decreases leading to decreased mass ratios. Although previously it was found that the mass of the tanks and pressurant decreases with increasing pressure as well as the mass of the thrust chamber (below 5 MPa), this effect is not large enough to offset the large increase in feed system mass. E.g. Increasing the pressure from 3 to 5 MPa for the EP-cycle reduces the thrust chamber mass by 9 kg and the tanks&pressurant by 13 kg, while the feed system mass increases by 35 kg.

### 8.1.3. Specific Impulse

In fig. 8.12 the development of overall specific impulse with chamber pressure is shown for all three cycles. It is clear that both conventional cycles perform worse than the electric-pump cycle. This is as expected since the propellant used to power the turbine is expelled at a significantly lower specific impulse than the propellant going through the main chamber. Since all propellant goes through the main chamber for the electric-pump cycle the other two cycles have a lower overall specific impulse.

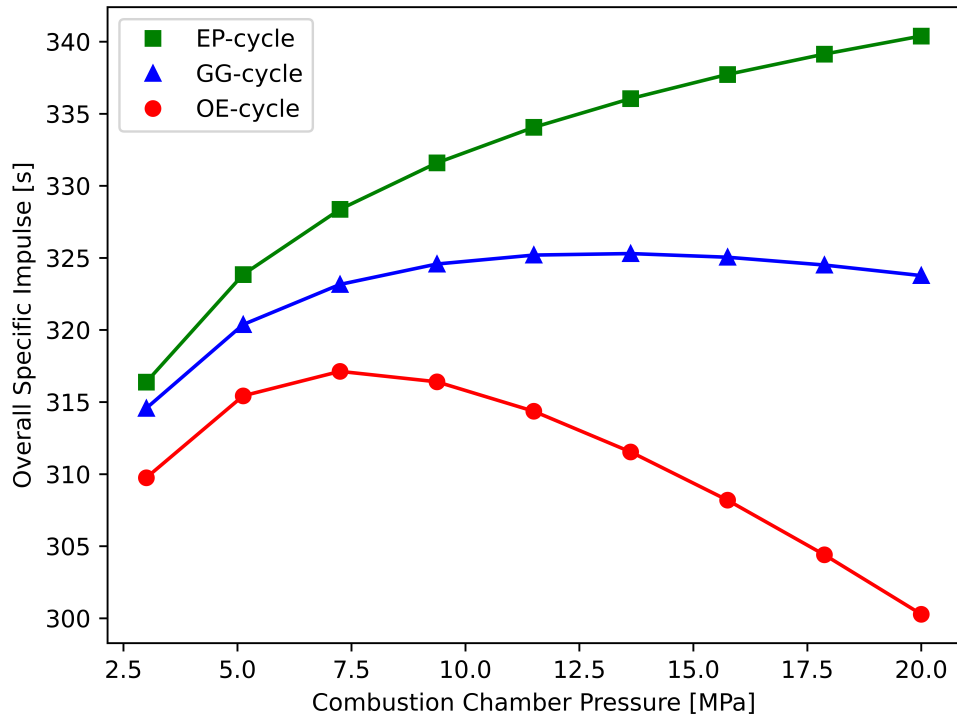


Figure 8.12: Comparison of specific impulse between EP-, GG-, and OE-cycle

Additionally, the conventional cycles have an optimum chamber pressure while this is not the case for the electric-pump cycle. This optimum is found at 13.2 and 7.4 MPa for the gas generator and open expander cycle respectively. For these cycles there are two opposing effects at work; an increase in chamber pressure leads to improved combustion in the chamber and thus higher specific impulse for the chamber flow. Conversely, increased chamber pressure leads to more pump work and, consequently, a larger percentage of the total flow is required to power the turbine. This flow is expelled at a low specific impulse and thus negatively affects the overall specific impulse. A slight compensation is that this turbine flow still marginally contributes to the thrust thus reducing the required chamber flow, which also has been modeled.

With diminishing improvements in chamber specific impulse for ever increasing chamber pressure this leads to the optima as found in fig. 8.12 for the conventional cycles. Since the electric-pump cycle does not use a turbine there is no negative effect of increasing pressure and overall specific impulse keeps increasing.

#### Gas generator vs Open Expander

So far the trends found in fig. 8.12 are as expected, but there is one aspect of the graph that still was to be explained: namely that the open expander cycle has a worse specific impulse than the gas generator over the whole considered range.

Generally, the expander cycle is seen as more efficient than the gas generator, but there are explanations for this unexpected result. The main one being the propellant choice. In these results only engines with RP-1/LOX as propellant combination have been considered. However, in literature and within existing engines

no expander cycles are found that use this propellant combination. Most designs use liquid hydrogen and oxygen instead. There are practical reasons why not to use RP-1, i.e. coking of hydrocarbon fuels at high temperatures [38], but one of the main reasons is the relatively low specific heat capacity of RP-1:  $\pm 2$  kJ/kg. Compare this to the specific heat capacity of hydrogen,  $\pm 14$  kJ/kg, and it becomes clear that RP-1 is a worse coolant and can carry less heat from the thrust chamber to the turbine.

This also means that regenerative cooling with RP-1 is actually quite limited. At a thrust of 25 kN the nozzle is small enough that cooling becomes almost impossible for all cycles. Cooling beyond an area ratio of 6 after the throat requires more RP-1 than is needed for the main combustion.

Besides these inferior cooling properties, RP-1 has a high (average) molecular mass, which means the turbine exhaust contributes less to the thrust than if a propellant would be used with a lower molecular mass, i.e. hydrogen. In comparison to the gas generator cycle the difference in molecular mass is even more pronounced. For hydrolox the gas generator combustion products are heavier than the pure hydrogen used in the open expander cycle, while for RP-1/LOX the combustion products are considerably lighter than pure RP-1. This further reduces the performance of the open expander cycle relative to the gas generator cycle when RP-1 is used as fuel. An alternative would be to compare the cycles with hydrolox as fuel instead. However, the chosen electric-pump cycle configuration does not allow for this currently. The configuration chosen in this report feeds the hot battery coolant back into the main fuel pump. With RP-1 this is possible, but with cryogenic propellants this would quickly lead to cavitation issues in the fuel pump. Hence, the comparison has been made for RP-1 engines despite its unsuitability for the open expander cycle.

### RP-1 properties estimation

The previous paragraph has given a theoretical explanation for the low specific impulse of the open expander relative to the gas generator. However, besides the theoretical explanation there is a further cause that is mostly due to RoCAT's implementation. As previously discussed in section 5.1.1 CoolProp is used to handle pure substances, while CEA is used to handle combustion products. Consequently, the properties of the flow entering the turbine are determined differently for the open expander cycle and gas generator cycle.

For RP-1 (i.e. n-Dodecane in CoolProp) both methods are not in line with real world data. CEA overestimates the decomposition of hydrocarbons and ends up with mostly atomic carbon for both combustion or thermal decomposition [32], while CoolProp does not model thermal decomposition at all. As a result the specific heat capacity, heat capacity ratio, and molar mass differ significantly.

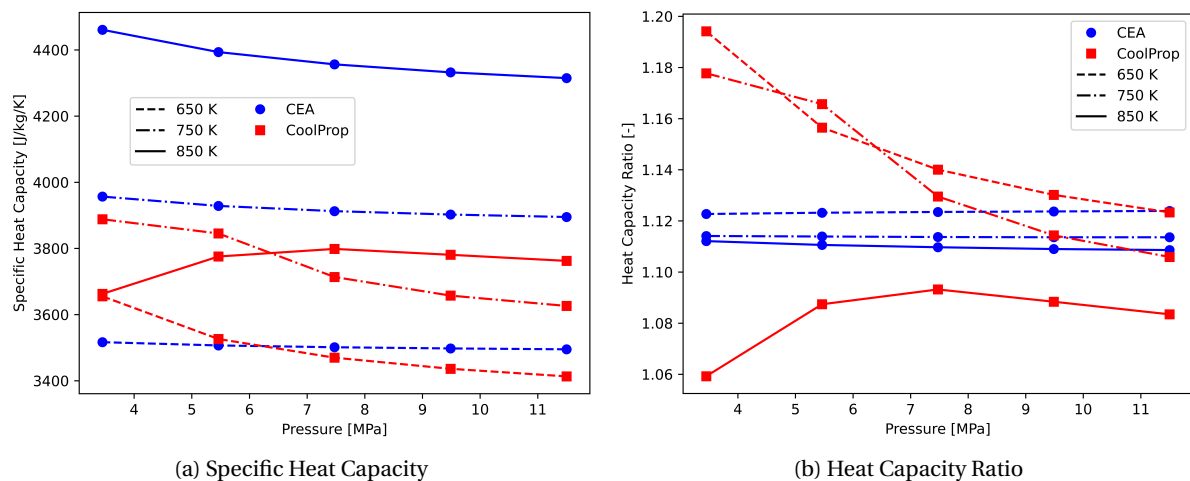


Figure 8.13: Properties of (Decomposed) RP-1 according to CEA and CoolProp

The graphs shown in fig. 8.13 show the specific heat capacity and heat capacity ratio as found by CEA and CoolProp for pure RP-1, or its near equivalent n-Dodecane. When found with CEA the specific heat capacity changes quite a bit more with changes in temperature and/or pressure than when CoolProp is used. The opposite is true for the heat capacity ratio, which is more sensitive when estimated with CoolProp. It is also clear that the general trends of both properties are more predictable for CEA; the specific heat capacity increases

with increasing temperature and decreasing pressure. For CoolProp the trends are less clear. Regardless, there are clear differences between these two models and the resulting differences in the flow properties effect how much mass is required to run the turbine. In addition to the two properties shown in fig. 8.13 there is also a large difference in molar mass. CEA predicts a molar mass of 12.66 - 13.75 g/mol depending on temperature and pressure, while CoolProp predicts 170.33 g/mol irrespective of the temperate and pressure. The molar mass does not influence the turbine mass flow directly, but alters the turbine exhaust thrust contribution. The more than 10 times decrease in molar mass leads to more than 3.5 times higher thrust contribution, thus substantially reducing the required main flow, which eventually also lead to a reduction in the turbine mass flow.

The combined effect of these differences has also been calculated for an open expander cycle engine with a thrust of 100 kN, chamber pressure of 10 MPa, and turbine inlet temperature of 850 K. Switching from CoolProp's property estimation to CEA, gives a 3.1% increase in overall specific impulse. Note that although the relative difference in specific heat capacity is largest at lower pressure, more turbine propellant is required at higher chamber pressure, thus the difference between CEA and CoolProp grows as chamber pressure increases. A 3% difference in specific impulse is considerable and would put the open expander's specific impulse slightly above that of the gas generator cycle if CEA's properties are used. However, as previously stated, CEA leads to an overestimation of the overall specific impulse, while CoolProp leads to an underestimation. The true value will be in between both estimates, but it is important to note that currently RoCAT underestimates the overall specific impulse of the open expander cycle if RP-1 is used as turbine drive gas.

#### 8.1.4. Change in Velocity

In the previous subsections the engine cycles have been compared on mass ratio and overall specific impulse. Both are important for the velocity change the rocket can impart to its payload, which is the final measure of the performance for a cycle. In fig. 8.14 one can see this change in velocity for each cycle for various burn times. Note that the mass ratio only accounts for the modeled components and a mass compensation factor (see section 6.8.2) has not been applied. This leads to an overestimation of the change in velocity. Consequently, the absolute values should be taken with a grain of salt and the focus should be on the relative performance of the cycles.

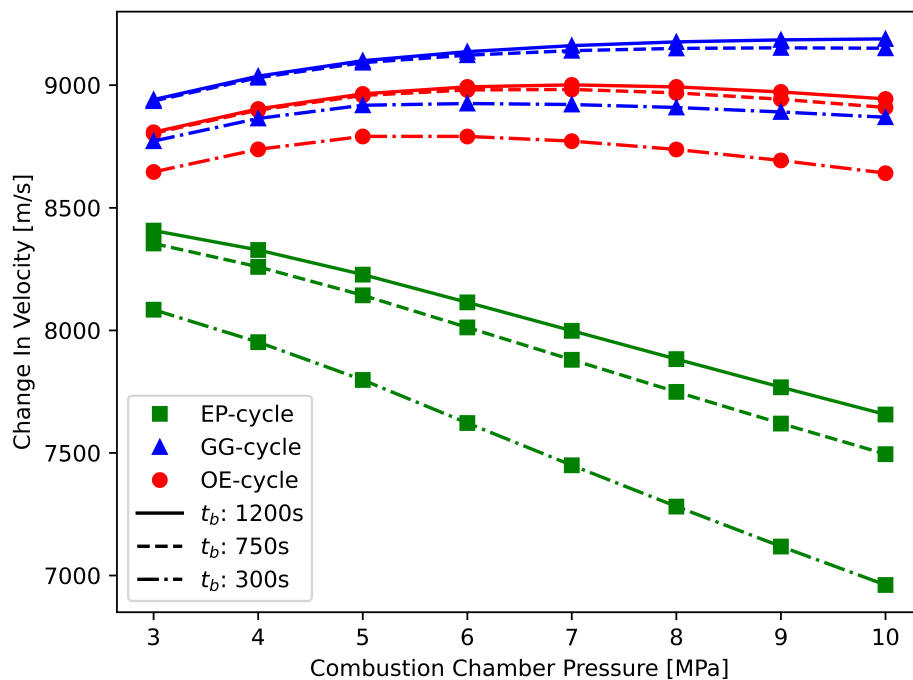


Figure 8.14: Comparison of idealized velocity change between EP-, GG-, and OE-cycle

Figure 8.14 is a clear combination of the previous graphs displaying the mass ratio and specific impulse (figs. 8.11 and 8.12). The effect of the mass ratio still dominates and the electric-pump cycle performs worse than both cycles over the whole range of considered inputs. Additionally, the relative difference between the electric-pump cycle and the others is smaller for higher burn times and greater for higher chamber pressures. This is in line with the observations for the mass ratio. The difference is somewhat lessened by the higher specific impulse, but only marginally so.

In effect it can be concluded that the electric-pump cycle performs worse than the conventional cycles for the same burn time and chamber pressure. The electric-pump cycle compares worst against the gas generator cycle at 300 s burn time and 10 MPa chamber pressure where it has a velocity change that is 26.6% lower. Conversely, the difference is only 8.9% when compared at 1200 s and 3 MPa. Compared to the open expander cycle the largest and smallest relative difference are 24.7% and 7.5% respectively. These relative differences for idealized velocity change for the gas generator are similar to those found by Kwak et al. (8 and 25 %), but slightly worse. This is as expected since the differences in modeling between RoCAT and Kwak were expected to slightly improve the gas generator performance, e.g. more complete consideration of turbine exhaust thrust contribution (see section 6.2), while decreasing the performance of the electric-pump cycle, e.g. accounting for efficiencies in battery coolant flow (see section 3.3.4).

All in all this section has shown that in direct comparison the electric-pump cycle performs worse than conventional cycles on all aspects considered, i.e. initial mass, mass ratio, specific impulse, and velocity change. Despite the higher specific impulse of the electric-pump cycle with respect to the conventional cycles, the difference is far too small to compensate for the great reduction in mass ratio as a result of carrying the battery the whole flight. The relative difference in the performance parameters between the gas generator cycle and electric-pump cycle are in line with previous research, but RoCAT predicts slightly worse relative performance of the electric-pump cycle. Furthermore, there is one clear exception: the initial mass. No combination of burn time and chamber pressure were found where the initial mass was lower for the electric-pump cycle, while previous research did find these points at burn times above 390 seconds [34].

Additionally, it was found that the open expander cycle also performs worse than the gas generator cycle. The main cause for this was found to be the propellant selection. RP-1 seems to be ill suited for use in an open expander cycle engine, mainly due to its inferior cooling capabilities. In addition, the chosen implementation of propellant property estimation does not model the thermal decomposition of hydrocarbon fuels, which exacerbates the lower performance results for the open expander cycle.

## 8.2. Optimized Cycle Comparison

In the previous section the cycles have been compared for the same input chamber pressure, and burn time. However, the different cycles clearly operate optimally at different chamber pressures. Furthermore, previous research found that the electric-pump cycle might operate better at slightly leaner mixture ratios [63] (for methane engines). Consequently, an optimization routine was written to compare the engine cycles while optimizing for chamber pressure and chamber mixture ratio. The goal is to find the highest velocity change achievable for a given total impulse (i.e. burn time and thrust). Visualization of the complete design space and optimal points for all cycles can be seen in figs. 8.15 and 8.16 for a burn time of 300 and 1200 seconds respectively. Both sets of 3D graphs are made for a thrust of 100 kN.

From fig. 8.15 it is clear that the conventional cycles have very similar optimal pressure and chamber O/F-ratio for a burn time of 300 sec; 5.01 MPa and 2.33 for the GG-cycle and 4.94 MPa, 2.32 for the OE-cycle. The EP-cycle's optimal point is however found at a much lower pressure and somewhat fuel-richer O/F-ratio; 1.42 MPa and 2.23. In addition to the different optimal inputs the  $\Delta V$  achieved is also different. Similar to the direct comparison the gas-generator still performs best with the open expander a close second and the electric-pump having the lowest. The EP-cycle has a 9.9% and 8.6% lower velocity change than the GG- and OE-cycle respectively. This is still a clear gap, but much better than if the cycles are compared for the same high chamber pressure, which lead to differences upwards of 20%. The difference in O/F-ratio between the cycles are explained later in this section.

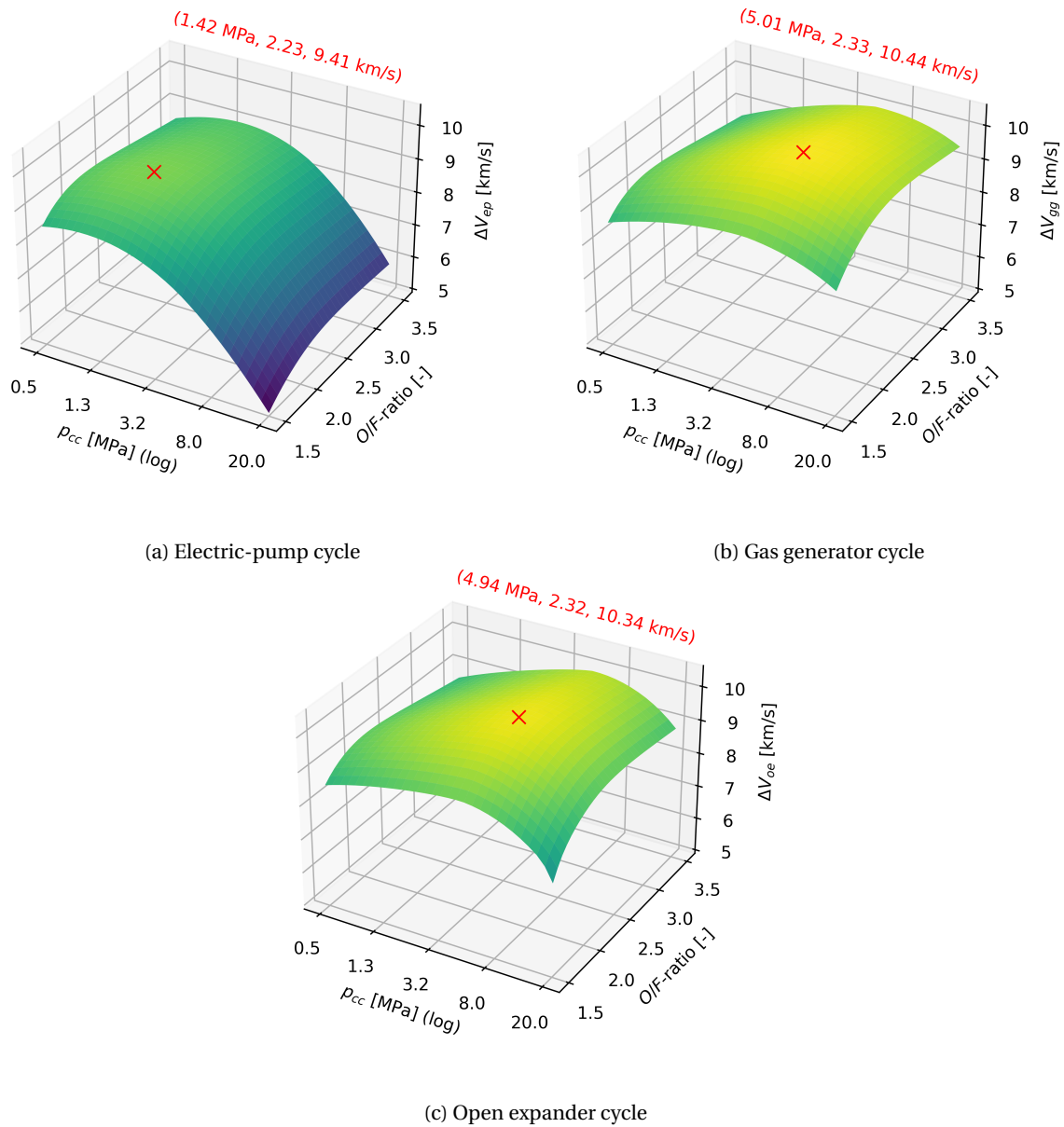
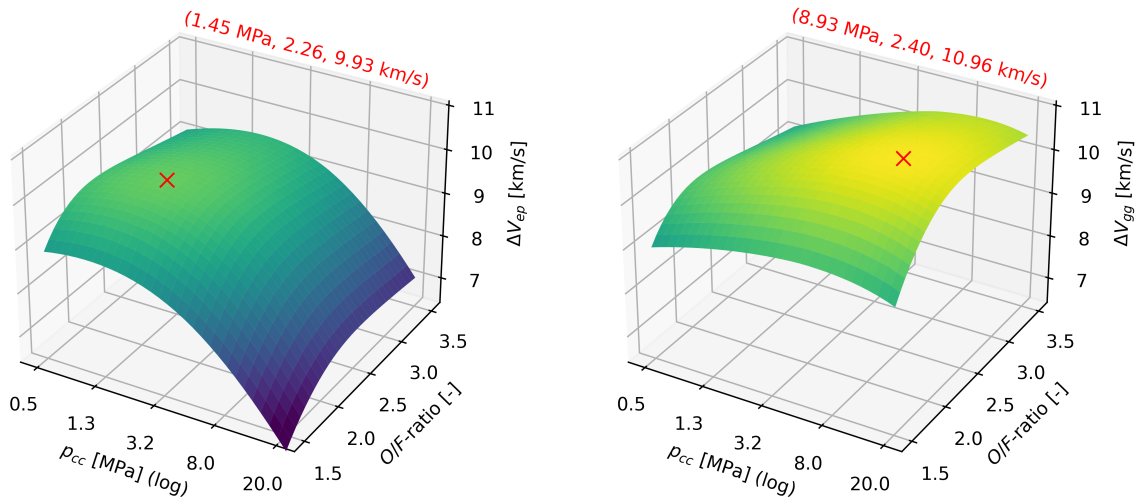
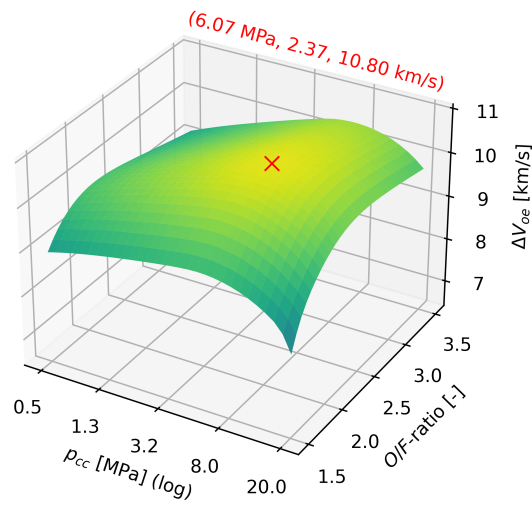


Figure 8.15: Optimization space for velocity change with  $F_T=100\text{kN}$ ,  $t_b=300\text{s}$



(a) Electric-pump cycle

(b) Gas generator cycle



(c) Open expander cycle

Figure 8.16: Optimization space for velocity change with  $F_T=100\text{kN}$ ,  $t_b=1200\text{s}$

Now looking at fig. 8.16 the relative differences in maximum change in velocity between the cycles have changed for this higher burn time of 1200 sec. As was seen previously, the improvement in battery efficiency for longer burn times is a boon to the EP-cycle that the other cycles do not have. Consequently, the electric-pump cycle now performs only 9.4% and 7.7% worse than the GG- and OE-cycle respectively.

Besides this relative improvement of the EP-cycle, it is clear that the optimal points have shifted as well. For all cycles both the chamber pressure and O/F-ratio have increased. However, the increase in chamber pressure is very small for the EP-cycle. It still operates at a relatively low pressure; 1.45 MPa. Conversely, the optimal pressure for the other cycles have increased to 8.93 MPa and 6.53 MPa for the GG- and OE-cycle respectively.

This difference in increased optimal chamber pressure can be explained by what was observed for the mass ratio in fig. 8.11; higher chamber pressure leads to lower mass ratios, but this effect is less pronounced for higher burn times (for the conventional cycles). In contrast the development of chamber specific impulse with chamber pressure is not affected by burn time. Consequently, at higher burn times an increase in chamber pressure becomes worth the gain in specific impulse relative to the loss in mass ratio. For the electric-pump cycle however the mass ratio trend is barely influenced by the burn time and consequently the optimal chamber pressure also barely changes with burn time. The effect of burn time on this mass ratio trend can be explained using the groups from table 8.1. The energy source and chamber propellant groups both increase in mass with burn time. For the conventional cycles both these groups are only in the numerator of the mass ratio, while the for the electric-pump cycle the energy source mass is also in the denominator, reducing the effect of its changes.

The previous paragraphs have mainly discussed the reasons for differences in optimal chamber pressure between cycles and for different burn times, yet the O/F-ratio also is different in each of these cases. Originally, it was thought that a difference in cycle could explain these differences. Especially for the electric-pump cycle burning more fuel-rich would mean a lower relative effect of the battery coolant on the main fuel pump inlet flow, leading to a lower temperature and higher density. This higher density, in turn, would lead to relatively lower fuel-pump power required, which, in combination with the absolutely lower oxidizer-pump power (due to the reduced O/F-ratio), could potentially lead to reduced overall pump power and consequently be worth a slight reduction in specific impulse. However, this is not the case. Although the fuel pump inlet density increases with a decrease in O/F-ratio this does not lead to a reduction in total pump power.

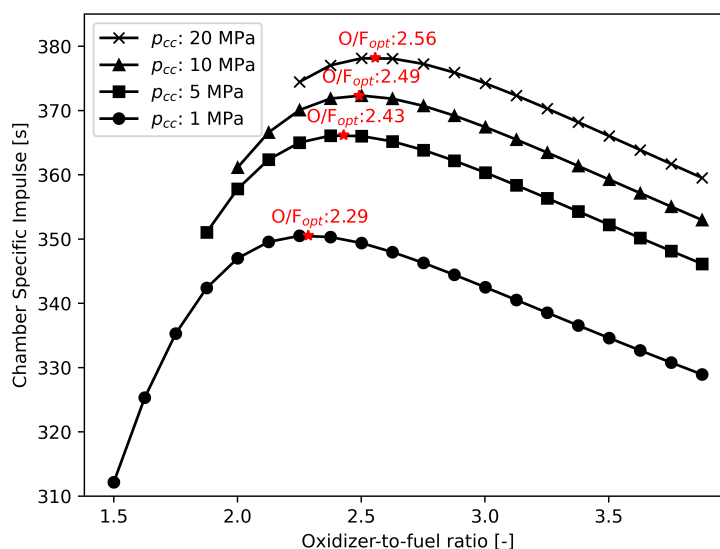


Figure 8.17: Effect of chamber pressure on optimal O/F-ratio for specific impulse ( $p_e = .002$  MPa Found from CEA with "frozen at throat" assumption)

Consequently, another explanation for the differing O/F-ratios is required. Upon further inspection this explanation is quite straightforward: the optimal O/F-ratio is simply determined by the chamber pressure. The effect of the chamber O/F-ratio on the mass ratio is actually quite small for all cycles, while it naturally has a large effect on the chamber specific impulse. Additionally, the optimal O/F-ratio for specific impulse is influenced by chamber pressure as is shown in fig. 8.17.

This effect is the main reason for the differences in optimal O/F-ratio between the cycles and different burn times. Additionally, the mass ratios are even slightly better when burning slightly fuel-rich for all cycles. Therefore, it can be concluded that there is no benefit of burning slightly lean for the EP-cycle, in contrast to the research by Yu et al. [63]. It should however be noted that Yu et al. investigated engines with 30 kN of thrust and that used methane as fuel. Thus, it could be possible this effect is dependent on these inputs, especially the fuel selection, and ideally a more equal comparison should be made. However no methane engines have been verified nor validated for the RoCAT tool, which could be a goal for future research. Furthermore, Yu et al. did not account for regenerative cooling of the battery using the fuel, but simply ignored the cooling. It would be interesting to see if this is a potential cause for the different conclusions.

All taken together this section has shown the differences in the optimal operating points for the different cycles. It was found that the effect of O/F-ratio on mass ratio is limited and mostly influences specific impulse. Consequently, the optimal O/F-ratio is almost completely dependent on the chamber pressure with higher chamber pressures leading to higher optimal O/F-ratios.

The optimal chamber pressures for the electric-pump cycle can be found around 1.44 MPa and is only slightly dependent on burn time, while an increase in burn time leads to considerable increases in optimal chamber pressure for both conventional cycles, especially for the gas generator cycle, whose optimal chamber pressures range from 4.94 MPa to 8.93 MPa.

Finally, the difference in velocity change for the electric-pump cycle compared to the conventional cycles at their respective optimal points is between 9.9% - 7.7% depending on burn time and cycle choice. This gap is still considerable, which is highlighted by the fact that the optimal electric-pump cycle design at 1200 seconds still performs worse than that of the open expander cycle at 300 seconds.

### 8.3. Future of Electric-Pump Cycle

As has been discussed in the literature study and in the introduction of this report, an important advantage of the electric-pump cycle is that its main technologies have constantly been improving and this trend is projected to continue. Any improvements in the efficiencies, specific powers, or specific energies of the electric motor, inverter, and battery would lead to improvements in performance of the electric-pump cycle. However, the battery is the heaviest component and has seen the most improvement. Additionally, the specific power is generally irrelevant as in all cases previously considered the battery was energy limited, so its mass was determined by the specific energy. Therefore, this section focuses on the specific energy of the battery. The discharge efficiency is burn time dependent and thus literature is less clear about what gains have been made here. Consequently, it is of interest to see how the performance of the electric-pump cycle improves with higher specific energy for the battery. This is done in this section.

To get a fair comparison the engines have been individually optimized as done in the previous section, i.e. their chamber pressure and mixture ratio have been selected for highest velocity change. Plotting this optimized velocity change for all cycles and various burn times lead to the graph as shown in fig. 8.18. It clearly shows the improvement of the performance of the electric-pump cycle relative to that of the gas generator and open expander cycles. Once again it is clear that the relative difference between the conventional cycles and electric-pump cycle is smallest for high burn times. However, even for the highest burn time and highest specific energy considered the velocity change is still lower than that of the conventional cycles for the same burn time. This is the case despite this highest specific energy being 10 times the value used in previous calculations of 713 kJ/kg, which was deemed reasonable for modern batteries. Another aspect to this is the fact that the electric-pump lines for 300 and 500 seconds of burn time flatten at 2.7 MJ/kg and 3.8 MJ/kg respectively. This is due to hitting the specific power limit. For these lower burn times the specific energy becomes high enough that it is no longer the limiting factor, but instead the specific power becomes the limiting factor.

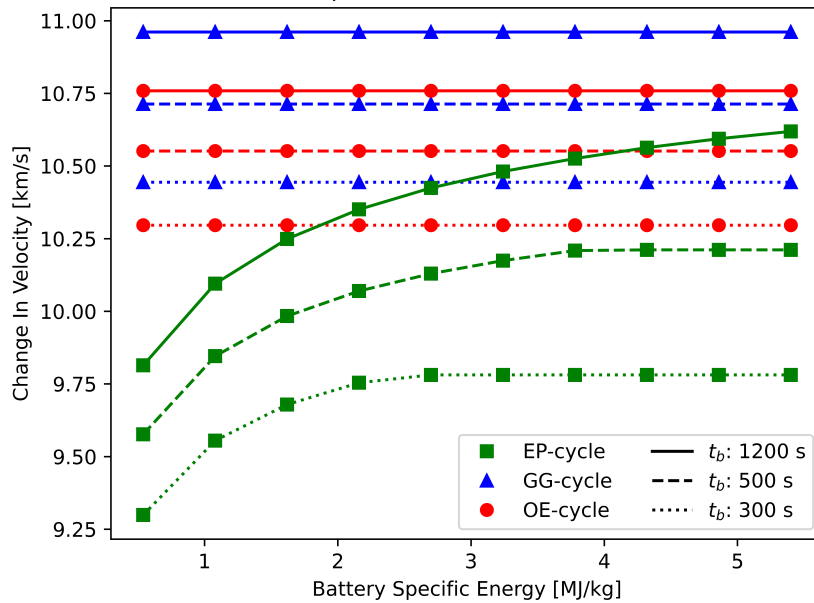


Figure 8.18: Effect of battery specific energy on performance of electric-pump cycle

If the 1200 seconds EP-cycle case would be extended this specific power limit is also reached at around 8 MJ/kg and reaches a  $\Delta V$  of 10.70 km/s, slightly less than that of the 1200s OE-cycle case 10.76 km/s. Even at a burn time for maximum discharge efficiency (1344 sec) the EP-cycle still ends up just lower than the OE-cycle at 10.75 km/s. It seems that without improvement in battery specific power there is no possibility for the electric-pump cycle to reach a higher velocity change than the conventional cycles regardless of the battery specific energy. Luckily, in reality this is likely not a problem as specific energy and specific power of the battery are intrinsically linked. Any future improvements in specific energy would lead to enough improvements in specific power to prevent this, although it is important to keep in mind either of these parameters could be limiting in the performance of the electric-pump cycle.

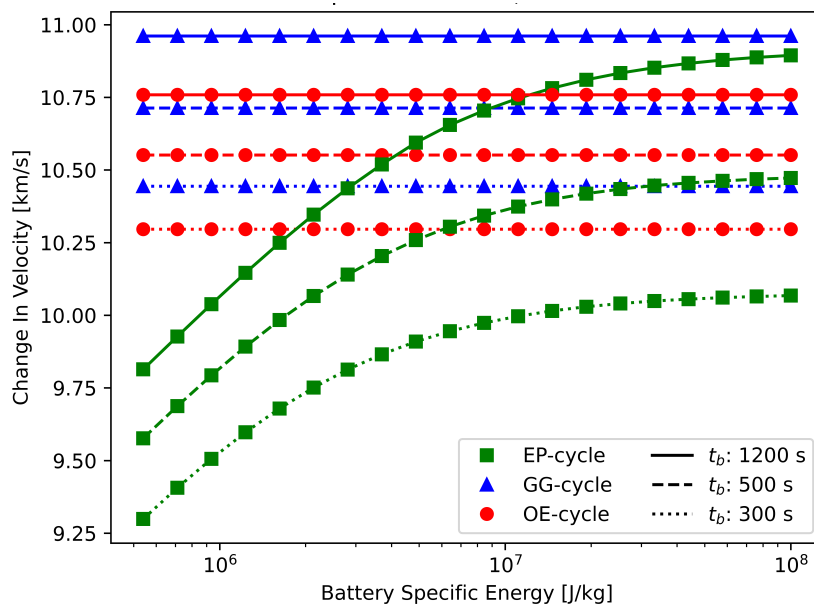


Figure 8.19: Effect of battery specific energy without specific power limit

Consequently, if the specific power limit is ignored, the graph as shown in fig. 8.19 is produced. Note that the ranges of battery specific energy is much wider than previously considered. From this graph one can see that the electric-pump cycle performs equal to the open expander cycle at  $\pm 11$  MJ/kg for a 1200 s case. However, it still never reaches the performance of the gas generator. For the lower burn times cases the performance of neither conventional engine cycle is achieved for the electric-pump cycle. This can be easily understood if one breaks down the initial masses. This has been done for the 500 seconds burn time case of fig. 8.19 at the extremely high specific energy of 100 MJ/kg and is shown in table 8.2.

<b>(Optimal) Input</b>	<b>EP</b>	<b>GG</b>	<b>OE</b>
<b>Chamber Pressure [MPa]</b>	4.88	6.13	5.42
<b>O/F-Ratio [-]</b>	2.345	2.363	2.354
<b>Battery Specific Energy [MJ/kg]</b>	100	-	-
<b>Mass [kg]</b>			
<b>Chamber Propellant</b>	15925.2	15633.7	15762.7
<b>Turbine Propellant</b>	-	358.8	536.3
<b>Pressurant</b>	61.9	62.1	63.2
<b>Fuel Tank</b>	81.5	84.4	90.1
<b>Oxidizer Tank</b>	224.2	222.3	222.3
<b>Pressurant Tank</b>	93.2	93.5	95.1
<b>Fuel (Turbo)Pump</b>	9.9	13.6	12.8
<b>Oxidizer (Turbo)Pump</b>	7.6	14.3	12.6
<b>Injector</b>	6.4	5.3	5.8
<b>Combustion Chamber</b>	4.5	4.5	4.5
<b>Nozzle</b>	51.3	54.9	52.5
<b>Electric Motor</b>	59.7	-	-
<b>Inverter</b>	5.6	-	-
<b>Battery</b>	2.6	-	-
<b>Secondary Exhaust</b>	-	1.1	0.7
<b>Gas Generator</b>	-	0.1	
<b>Output</b>			
<b>Mass Ratio [-]</b>	27.2	29.7	30.1
<b>Overall Specific Impulse [s]</b>	323.4	322.0	315.9
<b>Velocity Change [m/s]</b>	10472.4	10713.5	10551.7

Table 8.2: Detailed initial mass composition of all cycles with optimized chamber pressure and O/F-ratio. For  $t_b=500$ s.

Looking at table 8.2 it becomes obvious that at such a high battery specific energy the mass of the battery becomes inconsequential. At 2.6 kg it now weighs less than the inverter. Nonetheless, the mass ratio of the electric-pump cycle is still considerably lower than that of the gas generator cycle, 27.2 versus 29.7. The components responsible for this can be found in the feed system: The feed system of the gas generator is 28.1 kg, while that of the electric-pump cycle is 82.8. Clearly, only an improvement in battery is not sufficient. The effect of carrying unwanted extra mass to the end of flight seems to be so extreme that even the added mass of the electric motor and inverter alone reduce the performance of the electric-pump cycle below that of the conventional cycles for these burn times. Consequently, for shorter burn times it seems essential that not only the battery specific energy must improve, but also the specific power of the electric motor and inverter.

Upon further inspection of table 8.2 the electric motor's mass is much larger than that of the inverter, which is why only improvements for the electric motor are considered for now. Luckily, the specific power of electric motors has also made great progress in the past decades, similar to the specific energy of batteries. Consequently, both parameters are related to a historic trend, such that future development of the EP-cycle can be estimated.

Sakama et al. state that brushless DC electric motors have a 10 times higher specific power than 20 years ago [50]. However, the same research states that increases in specific power for electric motors in general has stagnated in the last decade. Nonetheless, a simple linear trend is assumed. This is likely overoptimistic, but gives a maximum boundary as to EP-cycle future performance.

For the historic development of the battery specific energy the trend as defined by Tiede et al. is used [59]. Note that this concerns the battery cells with maximum specific energy, which often have relatively poor specific power. Consequently, neglecting the specific power limit, as was done previously, is most likely not realistic with these values. However, this is done anyway in the following analysis, but at the end of this section the specific power limit is reconsidered.

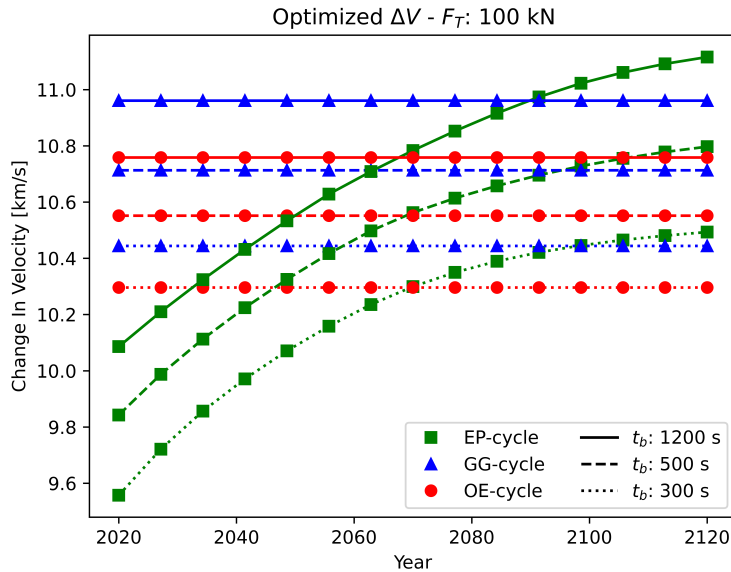


Figure 8.20: Projected development of EP-cycle in the future

In fig. 8.20 the projected development of the EP-cycle is shown, assuming the electric motor and battery technologies develop as given by Sakama and Tiede. Additionally, the specific power is assumed to not limit the battery mass and the conventional cycles are assumed to not improve in the future. As is clear from the graph even with these optimistic trends and assumptions it still is projected that the EP-cycle will take more than half a century to become equal in performance to the open expander cycles and even longer to equate the gas generator cycles. For clarity, table 8.3 gives the years at which the EP-cycle has an equal change in velocity to the other cycles.

Burn Time [s]	GG [year]	OE [year]
300	75.1	46.6
500	72.3	45.8
1200	66.8	44.7

Table 8.3: Number of years after 2023 at which EP-cycle overtakes the performance of the other cycles

It becomes clear that the EP-cycle does not surpass either conventional cycle in the near future. Furthermore, it is quite dubious if these predictions are even realistic as the trends by Tiede and Sakama are not meant to be extrapolated multiple decades into the future. Additionally, theoretical limits of battery and electric motor performance might be reached much sooner. Thus, an analysis of the actual performance values is in order. Table 8.4 shows the values predicted by Tiede and Sakama at the cross over years as well as the corresponding minimum required specific power for the battery. The values are given for the first and latest surpassing of the conventional cycles as well as current state of the art.

Case	[Unit]	OE @1200s	GG @300s	Current State of the Art
<i>When does EP reach this performance</i>	[Year]	2067	2098	2023
<i>Battery Specific Energy [Wh/kg]</i>	[Wh/kg]	1492	4258	636[46] (@75 W/kg)
<i>Electric Motor Specific Power [kW/kg]</i>	[kW/kg]	1440	47900	10 [24]
<i>Battery Specific Power [kW/kg]</i>	[kW/kg]			20 [21] (@150 Wh/kg)
<i>Required <math>\delta_{p,batt}</math> @300 s [kW/kg]</i>	[kW/kg]	15.4	44.0	
<i>Required <math>\delta_{p,batt}</math> @500 s [kW/kg]</i>	[kW/kg]	9.76	27.8	
<i>Required <math>\delta_{p,batt}</math> @1200 s [kW/kg]</i>	[kW/kg]	4.43	12.6	

Table 8.4: Specific powers and energy as expected at surpassing of conventional cycles

Comparing the values from table 8.4 it becomes clear that the required jump in specific power is much lower than the required jump in the battery specific energy and electric motor specific power. It seems reasonable that the limitations of the battery specific power have been ignored in the previous paragraphs. However it should be noted that battery specific power and energy are always a trade-off: the highest achieved specific power and highest achieved specific energy are not found in the same battery. Nonetheless, based on the values in table 8.4 it seems reasonable to focus on the battery specific energy as the limiting factor for the battery mass.

Before the data from table 8.4 is analyzed further it should be noted that it is unlikely that the trends by Tiede and derived from Sakama's data hold so far into the future. The theoretical limits of these technologies will be approached and will pose severe hurdles in further improvements. For example, the theoretical maximum specific energy of current commercial lithium-ion battery chemistries is around 885 Wh/kg [44]. This is clearly lower than the required 4258 Wh/kg to get similar performance as the gas generator for low burn times. Thus, even if the theoretical maximum of this current technology is reached, it would not be enough. Nonetheless, several new battery technologies have theoretical maximum specific energies that surpass even that very high requirement (e.g. Li-O<sub>2</sub> with a theoretical maximum of 5217 Wh/kg [11]), but most of these technologies are very far from commercialization and possible breakthroughs in these technologies are not modeled by historic trends.

In table 8.4 it becomes clear that both the battery specific energy needs to increase by an order of magnitude and the electric motor specific power several orders of magnitude before the EP-cycle performs equal to the conventional cycles. Consequently, it can be concluded that the EP-cycle will stay a cycle that performs worse than the conventional cycles without any major breakthrough in both battery and electric motor technologies. This leaves this cycle as one that should be selected for its other benefits at the cost of this performance reduction. A performance reduction which decreases relative to the conventional cycles over the years, but remains substantial in the near future.

An unmentioned positive for the electric-pump cycle is that this section has solely focused on specific power and energy, but has not considered the efficiencies. However, improvements in the efficiency of the electric motor, inverter, and battery are to be expected in the future. Especially gains in battery efficiency will improve the performance as less battery cooling is required as a consequence. Additionally, batteries whose efficiency is less dependent on discharge time could lead to improved performance at lower burn times. Consequently, gains are most likely to be made through the battery efficiency, even moreso because the electric motor and inverter efficiencies are already quite high currently (assumed 95% and 85% respectively for the analysis in this chapter).

A final note is that as that is battery specific energy increases, so does the optimal chamber pressure of the EP-cycle. This makes intuitive sense as the gain in specific impulse with chamber pressure comes at a increasingly lower cost in added battery mass as the battery specific energy increases, leading to higher optimal chamber pressures. That the operating chamber pressure of the EP-cycle shifts with battery specific energy should be kept in mind when viewing fig. 8.18 and is shown in fig. 8.21. The lack of smoothness in the graph is due to a combination of CEA's limited precision and a relatively large tolerance required for the optimization routine.

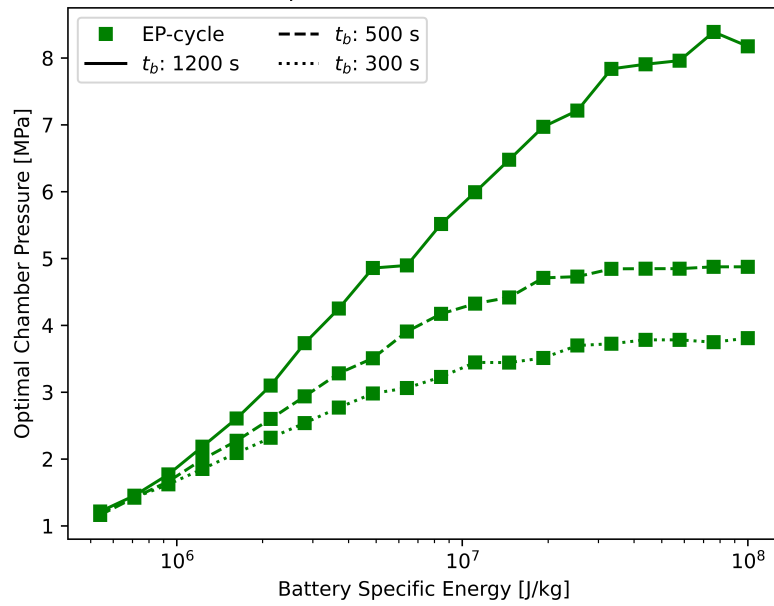


Figure 8.21: Effect of battery specific energy on electric-pump cycle optimal chamber pressure

So, to conclude, this chapter has compared the electric-pump cycle, gas generator cycle and open expander cycle for various cases, directly and optimized, for current and for future performance. It can be concluded that in all cases the electric-pump cycle has a clear disadvantage in terms of performance relative to the conventional cycles. Furthermore, multiple components of the electric-pump cycle will need to see improvements of at least an order of magnitude before this disadvantage can be completely overcome. This will require breakthroughs in the technologies of batteries, electric motors, and inverters, which are hard to predict. However, if historic trends are an indication, this will take at least several decades.

# Conclusion

## 9.1. Conclusions

This research set out to quantify the performance of the electric-pump cycle relative to that of conventional cycles and its development in the future. For this purpose a tool was built, RoCAT, which can analyze various cycle configurations of the gas generator and open expander cycle in addition to that of the electric-pump cycle. It is based on several previous studies, e.g. that of Ernst, Mota, and Rachov [20, 43, 48], but most importantly on the work of Kwak [34]. It extends the last mentioned by the addition of a thrust chamber model, including regenerative cooling, and the capacity for analyzing open expander cycle engines. It also models the flow and its properties at every component inlet and outlet using CoolProp and CEA. Furthermore, it takes a modular approach by being programmed according to the object oriented approach in Python. Additionally, RoCAT has the ability to optimize a cycle for velocity change ( $\Delta V$ ) and return the optimal mixture ratio and chamber pressure.

The results of RoCAT were compared to those of several engines and engine designs and matched quite well with several exceptions. Known trends are followed by RoCAT and both intermediate and final performance values coincide with previous research and actual rocket data. When considering the performance parameters noteworthy differences were found in the required pressure change over the pumps and heat flow rate. With differences around 15% for the former and 20% for the latter. The inaccuracy of the pump pressure change is somewhat expected since the pressure drops for individual components were calculated as linearly dependent on chamber pressure, which is only a rough estimate. Similarly, the model used for the heat transfer has been kept consciously simple to reduce complexity and calculation time. Consequently, a lower accuracy was deemed acceptable. Looking at the mass estimation it was found that the engine dry mass is severely underestimated, on average around 50%. This is partly caused by the limited amount of components that are modeled, but also due to underestimation of the mass of several components, most notably the thrust chamber. Despite this being an unacceptable error for determining absolute values, it was accepted as the analysis of this research is solely comparative.

With this verified and validated tool in hand the electric-pump cycle with regenerative battery cooling was compared to two conventional cycles. In a direct comparison the electric-pump cycle was found to deliver 7.5% to 26.7% less  $\Delta V$  than the conventional cycles, with the smaller difference found at low chamber pressures and high burn times and vice versa. When optimizing for chamber pressure and mixture ratio for each cycle before comparing  $\Delta V$ , the difference with the gas generator cycle was 9.4 - 9.9% and with the open expander cycle was 7.7 - 8.6%. Smaller differences are found at higher burn times. Thus, in both direct and optimized comparison the electric-pump cycle performed worse than the conventional cycles.

The main driving factor for the lower performance is due to the difference in "energy source"; a battery which needs to be carried the whole flight, unlike the turbine propellant used for the conventional cycles. The higher specific impulse of the electric-pump cycle only marginally compensates for this significant drawback as was concluded in the results. Furthermore, the feed system was found to be much heavier than that of the conventional cycles as well, which was in line with expectations and previous research.

Differences with previous research were also found, more specifically the conclusions of Kwak et al. [34]. Most notably it was found that the electric-pump cycle has a higher initial mass than the gas generator cycle over the complete considered range of chamber pressure and burn time, while Kwak found lower initial mass for the electric-pump cycles for burn times above 390 seconds. This difference can be explained by two main factors:

Firstly, during initial replication of Kwak's results there were found to be several calculations steps that did not match the description within the paper. Foremost of these were the omission of efficiencies in the calculation of the battery coolant flow and the odd iteration of the gas generator mass flow. Correcting the former leads to a heavier electric-pump cycle, while correcting the latter leads to a lighter gas generator cycle.

Secondly, several aspects of the cycles have consciously been modeled differently in RoCAT than has been done by Kwak. Most importantly the modeling of flow properties and the calculation of turbine exhaust thrust contribution. The former leads to slightly "better" properties of the turbine flow than the values given by Kwak and the latter was also found to be beneficial relative to the 1% thrust contribution assumed by Kwak. Consequently, both approaches lead to a lower initial mass for the gas generator.

During the analysis of the three cycles it was discovered that the chosen electric-pump cycle configuration did not work with cryogenic propellants. The combination of increased temperature and low pressure which occurs when feeding the battery coolant back into the main fuel pump stream leads to risk of cavitation or simply pumping gaseous fuel. Consequently, only analysis using RP-1 was possible.

On the contrary, the open expander cycle performed worse than expected when using RP-1 as fuel. The cause for this is twofold. Firstly, RP-1 was found to simply not to be a good fuel choice for the open expander cycle due to its low specific heat capacity and high molecular mass. Secondly, RoCAT does not model thermal decomposition of uncombusted flow, which leads to overestimation of the already high molecular mass and leads to errors in the flow properties. These issues are of much less concern when using other fuels, e.g. liquid hydrogen. This meant that the comparison between the open expander cycle and electric-pump cycle using RP-1 is somewhat uninformative. Nonetheless, these conclusions show the value of RoCAT as a design tool.

The future of the electric-pump cycle was considered by focusing on two aspects: Firstly, the battery specific energy, since it was assumed that the battery was restricted more by energy than power, which was also confirmed. Secondly, the electric motor specific power, since its mass dominated the feed system mass. It was found that if battery specific energy would increase by one order of magnitude and electric motor specific power by two, the electric-pump cycle performs better than the conventional cycles. Following historic trends it was found this will take at least multiple decades.

Consequently, it can be concluded that in the foreseeable future the electric-pump cycle is a rocket engine cycle that performs worse than the conventional cycles. It comes with a list of potential advantages, as given in the introduction, but this cycle will need to be selected despite its performance, not because of it.

## 9.2. Recommendations

RoCAT has been designed such that it is capable of handling various propellants, cycles, and configurations. Consequently, it could be used to analyze many more aspect of preliminary rocket design in general and the electric-pump cycle in specific. Several cases would be of interest:

An interesting case would be to add an electric-pump cycle configuration that allows the use of cryogenic propellants. This would allow for fairer comparison with the open expander cycle, since it was found to under perform with kerosene, while also showing if another propellant works for the electric-pump cycle. Since verification and validation for several liquid hydrogen engines has already been done, this would be the most logical choice, but some initial tests with liquid methane for RoCAT have also been performed.

Another case that would require very little adjustment of RoCAT, would be a study into expander cycle configurations. As discussed in section 4.3.3 the work of Herberitz et al. [25] compares three possible configurations all of which split the flow before the cooling section. All of these configurations are already present in the RoCAT tool as well as configurations that split the flow after the cooling section and splits both before and after. Verifying the work of Herberitz and extending it by quantifying the difference in performance for all these configurations and for several propellants could be of great value to future open expander design.

A last case of interest is the effect of dropping the battery mid flight, which was ultimately not considered in this report. However, this case should require only a minimal adjustment of the mass ratio calculation by RoCAT make a first estimate, but much more work if considered in detail. Ideally some simple flight dynamics would be added to consider the effect of dropping, e.g. half the battery midway or dropping in thirds, etc..

However, before non-comparative cases can be researched with the help of RoCAT some improvements are recommended or careful consideration of its limitations. As mentioned in chapter 7, several inaccuracies were found in the RoCAT model. Most importantly concerning the pump pressure, heat flow rate, and engine dry mass. Ideally, improvements would be made for these estimates before continuing with future work. Concerning the required pump pressure it is recommended that the pressure drop models for the injector and cooling channels be improved. For the latter an improved component was already coded, but has not been implemented due to time constraints. If this is not sufficient to get more accurate pump outlet pressure estimates the addition of a pressure drop for the merger and splitter components could be introduced as well as new components like feed lines and valves. These relatively straightforward additions should be more than adequate to get a more accurate pump outlet pressures.

Concerning the heat flow rate the recommendation is to simply accept this error. Accurate but simple heat transfer estimation is notoriously hard to find. Additionally, a more complex models was built for the heat transfer and heat exchanger, but led to many additional inputs being required and greater instability of the tool as a whole. If the heat flow rate error is truly deemed unacceptable these complex components could prove a good starting point and can be found in the source code.

Lastly, the engine dry mass could also be improved by the addition of several minor compents like feed lines and valves and accompanying mass estimates. Suggestions for both pressure drop and mass models for these components can be found in the literature study of this research [6]. More importantly the thrust chamber mass estimation should be improved, the shell mass method simply seems inadequate. An empirical factor of around 2.27 can be deduced from the data presented in chapter 7, although this factor is found from only 6 data points and ideally should be strengthened with additional data. Alternatively, the empirical method presented by Schlingloff [51] and also used by Mota [43] could be used instead. A final recommendation is to look at the gas generator mass model, which is based on stay time. This method is ubiquitous in past research (e.g. [34, 36, 45, 48]), but leads to very low estimates for the gas generator mass. Unfortunately, no mass values from existing engines could be found to confirm this suspicion.

All in all there is both room for improvement and extension, but much research can be envisioned with the RoCAT tool. In this research it has been used to place the electric-pump cycle more firmly in the context of existing rocket cycles, to confirm trends of previous research, and to show that despite continuous improvements its relatively low  $\Delta V$  will remain in the near future. But in general RoCAT offers analysis of a broad scope of rocket engines with various cycles, propellants, and configurations as well as modularity to easily adjust the model of any individual component. This makes it a formidable tool, for future research as well as preliminary design.



# Bibliography

- [1] Abdulagatov, I. and Azizov, N. (2011). Heat capacity of rocket propellant (RP-1 fuel) at high temperatures and high pressures. *Fuel*, 90(2):563–567.
- [2] Aoki, H. (2001). Turbopumps for LE-5B Rocket Engine. *Turbomachinery*, 29(3):168–175.
- [3] Bartz, D. R. (1965). Turbulent Boundary-Layer Heat Transfer from Rapidly Accelerating Flow of Rocket Combustion Gases and of Heated Air. In Hartnett, J. P. and Irvine, T. F., editors, *Advances in Heat Transfer*, volume 2, pages 1–108. Elsevier.
- [4] Bejan, A. (1993). *Heat transfer*. John Wiley & Sons, Inc, New York.
- [5] Bell, I. H., Wronski, J., Quoilin, S., and Lemort, V. (2014). Pure and Pseudo-pure Fluid Thermophysical Property Evaluation and the Open-Source Thermophysical Property Library CoolProp. *Industrial & Engineering Chemistry Research*, 53(6):2498–2508.
- [6] Berg, van den, R. J. F. (2021). *Electric-Pump Rocket Engines*. Literature Study, Delft University of Technology, Delft.
- [7] Berry, W. and Sundén, R. (1985). An electric pump feed system for apogee propulsion of geostationary spacecraft. In *Proceedings of the 36th Congress of the International Astronautical Federation*, Stockholm. IAF.
- [8] Bradford, J., Charania, A., and St. Germain, B. (2004). REDTOP-2: Rocket Engine Design Tool Featuring Engine Performance, Weight, Cost, and Reliability. In *40th AIAA/ASME/SAE/ASEE Joint Propulsion Conference and Exhibit*, Fort Lauderdale, Florida. American Institute of Aeronautics and Astronautics.
- [9] Budynas, R. G. and Sadegh, A. M. (2020). *Roark's formulas for stress and strain*. McGraw-Hill Education, New York, ninth edition.
- [10] Burcham, R. E. (1978). *Liquid rocket engine turbopump rotating-shaft seals*, volume 8121. National Aeronautics and Space Administration.
- [11] Cao, W., Zhang, J., and Li, H. (2020). Batteries with high theoretical energy densities. *Energy Storage Materials*, 26:46–55.
- [12] Casalino, L. and Pastrone, D. (2010). Optimization of a Hybrid Rocket Upper Stage with Electric Pump Feed System. In *46th AIAA/ASME/SAE/ASEE Joint Propulsion Conference & Exhibit*, Nashville, TN. American Institute of Aeronautics and Astronautics.
- [13] Chazen, M. L. (1984). Pump-Fed Satellite Delivery Stage Engine Technology. In *Aerospace Congress and Exposition*, page 841528.
- [14] Chernyshov, M. V., Lekanov, A. V., Razhikov, V. N., and Kholopov, S. A. (2018). Study of the Radial Vibrations of a Rotor of a Leak-Proof Electric Pump Engine. *Russian Aeronautics*, 61(4):593–598.
- [15] Cho, W. K. and Kim, C. I. (2019). System Analysis of a Gas Generator Cycle Rocket Engine. *International Journal of Aerospace System Engineering*, 6(2):11–16.
- [16] Choi, H.-S., Seo, S.-H., Kim, Y.-M., and Cho, G.-R. (2009). Development of 30-Ton<sub>f</sub> LOx/Kerosene Rocket Engine Combustion Devices(II) - Gas Generator. *Journal of the Korean Society for Aeronautical & Space Sciences*, 37(10):1038–1047.
- [17] Cornelisse, J. W., Schöyer, H. F. R., and Wakker, K. F. (1979). *Rocket propulsion and spaceflight dynamics*. Pitman, London ; San Francisco.
- [18] Crierie, R. (2012). Centaur Mass Breakdowns and Ground Ignition Weights.

- [19] Debrock, S. C. and Rudey, C. J. (1974). Agena Primary and Integrated Secondary Propulsion Systems. *Journal of Spacecraft and Rockets*, 11(11):769–777.
- [20] Ernst, R. R. L. (2014). Liquid Rocket Analysis (LiRA): Development of a Liquid Bi-Propellant Rocket Engine Design, Analysis and Optimization Tool. Master's thesis, University of Technology Delft.
- [21] Futscher, M. H., Brinkman, L., Müller, A., Casella, J., Aribia, A., and Romanyuk, Y. E. (2023). Monolithically-stacked thin-film solid-state batteries. *Communications Chemistry*, 6(1):1–7. Number: 1 Publisher: Nature Publishing Group.
- [22] Gülich, J. F. (2010). *Centrifugal pumps*. Springer, Berlin, 2nd edition.
- [23] Han, S., Li, X., Zheng, M., and Guo, L. (2018). Initial reactivity differences between a 3-component surrogate model and a 24-component model for RP-1 fuel pyrolysis evaluated by ReaxFF MD. *Fuel*, 222:753–765.
- [24] Hemmati, R., Vahid, S., and EL-Refaie, A. (2020). A Novel Design for a High Specific Power Interior Permanent Magnet Machine for Aerospace Applications. In *2020 IEEE Energy Conversion Congress and Exposition (ECCE)*, pages 1735–1742. ISSN: 2329-3748.
- [25] Herbertz, A. (2016). Component Modeling for Rocket Engine Cycle Analysis. *Transactions of the Japan Society for Aeronautical and Space Sciences, Aerospace Technology Japan*, 14(30):119–127.
- [26] Herbertz, A., Kauffmann, J., and Sippel, M. (2001). Systems analysis of a future semi-reusable launcher, based on a high thrust bleed cycle rocket engine. In *37th Joint Propulsion Conference and Exhibit*, Salt Lake City, UT. American Institute of Aeronautics and Astronautics.
- [27] Huber, M. L., Lemmon, E. W., Ott, L. S., and Bruno, T. J. (2009). Preliminary Surrogate Mixture Models for the Thermophysical Properties of Rocket Propellants RP-1 and RP-2. *Energy & Fuels*, 23(6):3083–3088.
- [28] Humble, R. W. (1995). *Space propulsion analysis and design*. McGraw-Hill, New York, 1st edition.
- [29] Huzel, D. K. and Huang, D. H. (1992). *Modern Engineering for Design of Liquid-Propellant Rocket Engines*. American Institute of Aeronautics and Astronautics, Reston.
- [30] Johnsson, G. and Bigert, M. (1990). Development of small centrifugal pumps for an electric propellant pump system. *Acta Astronautica*, 21(6):429–438.
- [31] Kakuma, Y., Yasui, M., Onga, T., Sekita, R., and Warashina, S. (2000). LE-5B engine development. In *36th AIAA/ASME/SAE/ASEE Joint Propulsion Conference and Exhibit*, Las Vegas, NV, U.S.A. American Institute of Aeronautics and Astronautics.
- [32] Kauffmann, J., Herbertz, A., and Sippel, M. (2001). Systems Analysis of a High Thrust, Low-Cost Rocket Engine. In *Fourth International Conference on Green Propellants for Space Propulsion*, Noordwijk.
- [33] Kwak, H.-D. (2021). Complementary detailed dataset to 2018 paper on electric-pump cycle engine (personal correspondence).
- [34] Kwak, H.-D., Kwon, S., and Choi, C.-H. (2018). Performance assessment of electrically driven pump-fed LOX/kerosene cycle rocket engine: Comparison with gas generator cycle. *Aerospace Science and Technology*, 77:67–82.
- [35] Lee, H. J., Lee, J., Roh, T.-S., and Huh, H. (2020). Performance Analysis and Mass Estimation of a Small-Sized Liquid Rocket Engine with Electric-Pump Cycle. *International Journal of Aeronautical and Space Sciences*.
- [36] Lentini, D., Rachov, P. A., and Tacca, H. (2013). Electric Feed Systems for Liquid-Propellant Rockets. *Journal of Propulsion and Power*, 29(5):1171–1180.
- [37] Leonardi, M., Nasuti, F., and Onofri, M. (2017). Basic Analysis of a LOX/Methane Expander Bleed Engine. In *Proceedings of the 7th European Conference for Aeronautics and Space Sciences*, Milano.
- [38] MacDonald, M. E. (2012). *Decomposition kinetics of the rocket propellant rp-1 and its chemical kinetic surrogates*. Stanford University.

- [39] Magee, J. W., Bruno, T. J., Friend, D. G., Huber, M. L., Laesecke, A., Lemmon, E. W., McLinden, M. O., Perkins, R. A., Baranski, J., and Widegren, J. A. (2007). Thermophysical properties measurements and models for rocket propellant RP-1: phase I. Technical Report NIST IR 6646, National Institute of Standards and Technology, Gaithersburg, MD.
- [40] McBride, B. J. and Gordon, S. (1994). Computer Program for Calculation of Complex Chemical Equilibrium Compositions and Applications I. Analysis. Technical report, NASA.
- [41] McHugh, B. (1995). Numerical analysis of existing liquid rocket engines as a design process starter. In *31st Joint Propulsion Conference and Exhibit*, Joint Propulsion Conferences. American Institute of Aeronautics and Astronautics.
- [42] Moroz, L., Burlaka, M., and Barannik, V. (2019). Development of Highly Competitive Liquid Rocket Engines in Time of Space Gold Rush. In *35th Space Symposium*, page 11, Colorado Springs, CO.
- [43] Mota, F. A., Hinckel, J. N., Rocco, E. M., and Schlingloff, H. (2018). Modeling and Analysis of a LOX/Ethanol Liquid Rocket Engine. *Journal of Aerospace Technology and Management*, 10.
- [44] M. Thackeray, M., Wolverton, C., and D. Isaacs, E. (2012). Electrical energy storage for transportation—approaching the limits of, and going beyond, lithium-ion batteries. *Energy & Environmental Science*, 5(7):7854–7863. Publisher: Royal Society of Chemistry.
- [45] NASA (1972). Liquid Propellant Gas Generators. Technical Report SP-8081, NASA, Cleveland, Ohio.
- [46] Pierre Mwizerwa, J., Liu, C., Xu, K., Zhao, N., Li, Y., Ndagijimana, P., Chen, Z., and Shen, J. (2022). Activated carbon/reduced graphene oxide wrapped LiFePO<sub>4</sub> cathode for Li-ion batteries with ultrahigh capacities and high specific energy density. *FlatChem*, 34:100393.
- [47] Ponomarenko, A. (2010). RPA: Tool for Liquid Propellant Rocket Engine Analysis C++ Implementation.
- [48] Rachov, P. (2010). Electric Feed Systems for Liquid Propellant Rocket Engines. Research Report, University of Buenos Aires, Buenos Aires.
- [49] Rocket Lab (2020). Electron Payload User Guide. Technical Report v6.6, Rocket Lab USA.
- [50] Sakama, S., Tanaka, Y., and Kamimura, A. (2022). Characteristics of Hydraulic and Electric Servo Motors. *Actuators*, 11(1):11. Number: 1 Publisher: Multidisciplinary Digital Publishing Institute.
- [51] Schlingloff, H. and Ruppe, H. O. (2005). *Aeronautical engineering: an introduction to the technology of spaceflight*. Schlingloff Publications, Bad Abbach.
- [52] Schneider, S., Veres, J., Hah, C., Nerone, A., Cunningham, C., Kraft, T., Tavernelli, P., and Fraser, B. (2005). Satellite Propellant Pump Research. In *41st AIAA/ASME/SAE/ASEE Joint Propulsion Conference & Exhibit*, Tucson, Arizona. American Institute of Aeronautics and Astronautics.
- [53] Sippel, M., Herbertz, A., Burkhardt, H., Imoto, T., Haeseler, D., and Götz, A. (2003). Studies on Expander Bleed Cycle Engines for Launchers. In *39th AIAA/ASME/SAE/ASEE Joint Propulsion Conference and Exhibit*, Huntsville, Alabama. American Institute of Aeronautics and Astronautics.
- [54] Sippel, M., Herbertz, A., Haeseler, D., and Götz, A. (2002). Feasibility of high thrust bleed cycle engines for reusable booster applications. In *4th International Conference on Launcher Technology "Space Launcher Liquid Propulsion"*.
- [55] Sokolowski, J. A. and Banks, C. M. (2009). *Principles of Modeling and Simulation: A Multidisciplinary Approach*. John Wiley & Sons.
- [56] Solda, N. and Lentini, D. (2008). Opportunities for a Liquid Rocket Feed System Based on Electric Pumps. *Journal of Propulsion and Power*, 24(6):1340–1346.
- [57] Spiller, D., Stabile, A., and Lentini, D. (2013). Design and Testing of a Demonstrator Electric—Pump Feed System for Liquid Propellant Rocket Engines. *Aerotecnica Missili & Spazio*, 92(3):123–130.

- [58] Sutton, G. P. and Biblarz, O. (2017). *Rocket propulsion elements*. John Wiley & Sons Inc, Hoboken, New Jersey, 9th edition.
- [59] Tiede, B., O'Meara, C., and Jansen, R. (2022). Battery Key Performance Projections based on Historical Trends and Chemistries. In *2022 IEEE Transportation Electrification Conference & Expo (ITEC)*, pages 754–759, Anaheim, CA, USA. IEEE.
- [60] Vilja, J., Briley, G., and Murphy, T. (1993). J-2S rocket engine. In *29th Joint Propulsion Conference and Exhibit*, Monterey, CA, U.S.A. American Institute of Aeronautics and Astronautics.
- [61] Waxenegger-Wilfing, G., Hahn, R. H. S., and Deeken, J. (2018). Studies on Electric Pump-fed Liquid Rocket Engines for Micro-launchers. In *Proceedings of the 6th Space Propulsion Conference*, page 8, Sevilla.
- [62] Wu, J. (2005). Liquid-propellant rocket engines health-monitoring—a survey. *Acta Astronautica*, 56(3):347–356.
- [63] Yu, B., Kwak, H.-D., and Kim, H. J. (2020). Effects of the O/F Ratio on the Performance of a Low Thrust LOX/Methane Rocket Engine with an ElecPump-fed Cycle. *International Journal of Aeronautical and Space Sciences*, 21(4):1037–1046.
- [64] Zandbergen, B. (2022). *Course AE4S01 - Thermal Rocket Propulsion - Lecture Notes*. University of Technology Delft.
- [65] Ziebland, H. and Parkinson, R. C. (1971). Heat Transfer in Rocket Engines. Technical report, Advisory Group for Aerospace Research and Development Paris.

# Detailed Data for Kwak Replication Model

In this appendix several data points from the paper by Kwak et al. [34] are extracted and it lists some minor assumptions made in the replication of that paper's model. Additionally, detailed data sets are provided that show the differences between the initial replication model and Kwak's model, as well as between the adjusted replication model and Kwak's model. Finally, several figures from the paper have been replicated with the adjusted replication model to show that these match perfectly or at least as perfect as possible by visual inspection.

## A.1. Specific Impulse

To determine the specific impulses calculated by Kwak et al. [34] the only source was the figure as shown in fig. A.1. This figure was digitized and the data points estimated, which leads to the data as shown in table A.1.

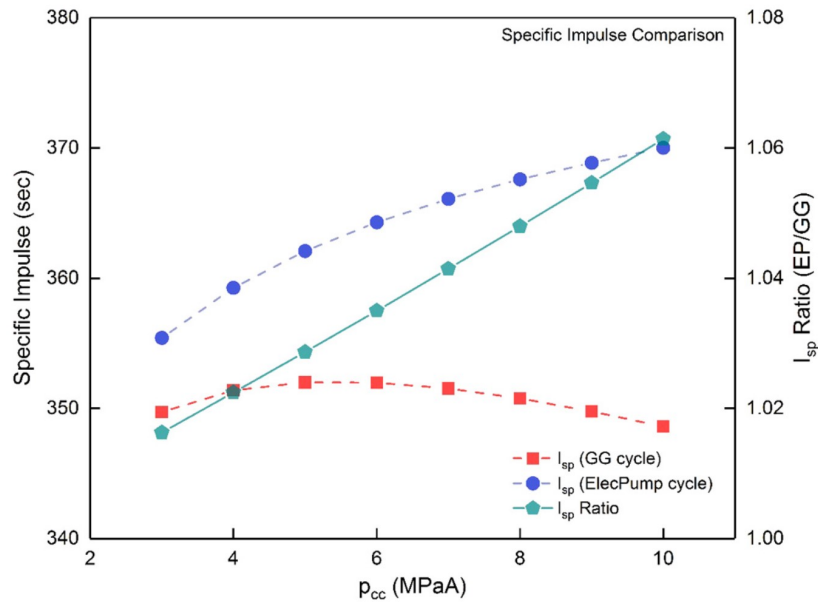


Figure A.1: Specific impulse graph taken from Fig.10 in reference [34]

Chamber Pressure [MPa]	Specific Impulse [s]	
	EP	GG
3.0	355.4	349.7
4.0	359.3	351.4
5.0	362.1	352.0
6.0	364.3	352.0
7.0	366.1	351.5
8.0	367.6	350.8
9.0	368.9	349.8
10.0	370.0	348.6

Table A.1: Specific impulses extracted from fig. A.1

## A.2. Minor modeling details

Other minor details had to be figured out as best matching Kwak's modeling approach. Most of these are elementary and have mostly been included to be as thorough as possible, facilitating replication of the results of Kwak and this paper. These are given in the list below.

- CEA is set to shifting equilibrium and no correction factors are applied
- CEA is used with the pressure ratio as input (Equivalent IRT area ratio gives different results)
- The values found from CEA are rounded to five significant figures
- The CEA propellants which have been used are the NASA standards for RP-1 and Liquid Oxygen seen below
- CEA propellants are: RP-1,  $-5907.672 \text{ cal/mol}$ ,  $298.150 \text{ K}$  - O<sub>2</sub>(L),  $-3102.055 \text{ cal/mol}$ ,  $90.170 \text{ K}$
- Thrust and specific impulse denote ideally expanded thrust and specific impulse unless specified otherwise

## A.3. Replication Model Comparison

In this section the data from Kwak et al. [34] is compared to the replication model. Tables A.2 to A.4 show the mass, specific impulse, and change in velocity values as calculated by the replication model and presented in Kwak et al.. The next paragraph clarifies how the data in these tables was exactly produced or where it was taken from.

For these tables, the mass and mass ratio data in the "Kwak"-columns is directly taken from Fig.10 in Kwak et al. [34], while the specific impulse was extracted from Fig.11 in the paper (see appendix A.1). For the replication-columns partial masses are rounded to the nearest kilogram and the total is the sum of these rounded values. Additionally, the mass ratio is calculated using eq. (A.1a). This choice of rounding and mass ratio calculation are done in correspondence with the original data. No intermediate rounding is applied for any other data shown in this report. For both the Kwak and replication data the velocity change is calculated using eq. (A.1b) without intermediate rounding of the mass ratio. Furthermore, the Feed System is defined as shown in eq. (A.1c). Finally, it should be noted that the mass ratio, MR, as used by Kwak and in these tables is not the same as the mass ratio,  $\Lambda$ , as used throughout the rest of the report, but roughly the inverse.

$$MR = (\text{Total} - \text{CC Propellants} - \text{GG Propellants}) / \text{Total} \quad (\text{A.1a})$$

$$\Delta V = I_{sp} g_0 \ln(MR^{-1}) \quad (\text{A.1b})$$

$$\text{Feed System} = \text{Fuel Pump} + \text{Oxidizer Pump} + (\text{Gas Generator OR (Inverter + Electric Motor)}) \quad (\text{A.1c})$$

With  $\Delta V$  the change in velocity,  $I_{sp}$  the specific impulse, and  $MR$  the mass ratio as defined in eq. (A.1a).

	<i>Electric Pump</i>			<i>Gas Generator</i>		
	<b>Kwak</b>	<b>Repl.</b>	<b>Diff. [%]</b>	<b>Kwak</b>	<b>Repl.</b>	<b>Diff. [%]</b>
CC Propellants [kg]	8350	8350	0.00	8318	8267	-0.61
GG Propellants [kg]	-	-	-	505	508	0.59
Battery Pack [kg]	415	426	2.65	-	-	-
Feed System [kg]	151	155	2.65	43	43	0.00
Tanks [kg]	207	207	0.00	219	217	-0.91
Helium [kg]	33	33	0.00	35	35	0.00
Total [kg]	9156	9171	0.16	9120	9070	-0.55
MR [-]	0.0880	0.0895	1.70	0.0326	0.0325	-0.31
Specific Impulse [s]	370.0	370.0	0.00	348.6	352.1	1.00
Velocity Change [m/s]	8817	8756	-0.69	11707	11829	1.04

Table A.2: Comparison of replication model and data from Kwak et al. [34]  
( $t_b = 300 \text{ s}$ ,  $F_T = 100 \text{ kN}$ ,  $p_{cc} = 10 \text{ MPa}$ )

	<i>Electric Pump</i>			<i>Gas Generator</i>		
	<b>Kwak</b>	<b>Repl.</b>	<b>Diff. [%]</b>	<b>Kwak</b>	<b>Repl.</b>	<b>Diff. [%]</b>
CC Propellants [kg]	10856	10856	0.00	10812	10747	-0.60
GG Propellants [kg]	-	-	-	656	661	0.76
Battery Pack [kg]	521	530	1.73	-	-	-
Feed System [kg]	150	152	1.33	43	43	0.00
Tanks [kg]	272	272	0.00	287	285	-0.70
Helium [kg]	44	43	-2.27	46	45	-2.17
Total [kg]	11843	11853	0.08	11844	11781	-0.53
MR [-]	0.0832	0.0841	1.08	0.0317	0.0317	0.00
Specific Impulse [s]	370.0	370.0	0.00	348.6	352.1	1.00
Velocity Change [m/s]	9016	8983	-0.37	11794	11922	1.09

Table A.3: Comparison of replication model and data from Kwak et al. [34]  
( $t_b = 390$  s,  $F_T = 100$  kN,  $p_{cc} = 10$  MPa)

	<i>Electric Pump</i>			<i>Gas Generator</i>		
	<b>Kwak</b>	<b>Repl.</b>	<b>Diff. [%]</b>	<b>Kwak</b>	<b>Repl.</b>	<b>Diff. [%]</b>
CC Propellants [kg]	33402	33402	0.00	33273	33068	-0.62
GG Propellants [kg]	-	-	-	2021	2034	0.64
Battery Pack [kg]	1373	1374	0.07	-	-	-
Feed System [kg]	143	143	0.00	43	43	0.00
Tanks [kg]	878	878	0.00	927	921	-0.65
Helium [kg]	134	134	0.00	141	140	-0.71
Total [kg]	35930	35931	0.00	36405	36206	-0.55
MR [-]	0.070	0.070	0.57	0.0305	0.03	-1.64
Specific Impulse [s]	370.0	370.0	0.00	348.6	352.1	1.00
Velocity Change [m/s]	9630	9629	-0.01	11929	12052	1.03

Table A.4: Comparison of replication model and data from Kwak et al. [34]  
( $t_b = 1200$  s,  $F_T = 100$  kN,  $p_{cc} = 10$  MPa)

## A.4. Adjusted Model Comparison

In this section the data from Kwak et al. [34] is compared to the adjusted replication model. This model was made to show that if certain models were changed w.r.t. the original replication model the data of Kwak could be almost exactly replicated. Consequently, the tables mostly contain the same values for both models, but differences have been highlighted in bold. The same considerations concerning the sources and calculations of the parameters as in appendix A.3 need to be considered.

	<i>Electric Pump</i>		<i>Gas Generator</i>	
	<b>Kwak</b>	<b>Adjusted</b>	<b>Kwak</b>	<b>Adjusted</b>
CC Propellants [kg]	8350	8350	8318	8318
GG Propellants [kg]	-	-	505	505
Battery Pack [kg]	415	415	-	-
Feed System [kg]	151	151	43	43
Tanks [kg]	207	207	219	219
Helium [kg]	33	33	35	35
Total [kg]	9156	9156	9120	9120
MR [-]	0.0880	0.0880	0.0326	0.0326
Specific Impulse [s]	370.0	370.0	348.6	348.6
Velocity Change [m/s]	8817	8817	11707	11707

Table A.5: Comparison of adjusted model and data from Kwak et al. [34]  
( $t_b = 300$  s,  $F_T = 100$  kN,  $p_{cc} = 10$  MPa)

	Electric Pump		Gas Generator	
	Kwak	Adjusted	Kwak	Adjusted
CC Propellants [kg]	10856	10856	10812	<b>10814</b>
GG Propellants [kg]	-	-	656	<b>657</b>
Battery Pack [kg]	521	<b>520</b>	-	-
Feed System [kg]	150	150	43	43
Tanks [kg]	272	272	287	287
Helium [kg]	44	<b>43</b>	46	46
Total [kg]	11843	<b>11841</b>	11844	<b>11847</b>
MR [-]	0.0832	0.0832	0.0317	0.0317
Specific Impulse [s]	370.0	370.0	348.6	348.6
Velocity Change [m/s]	9023	<b>9016</b>	11795	<b>11794</b>

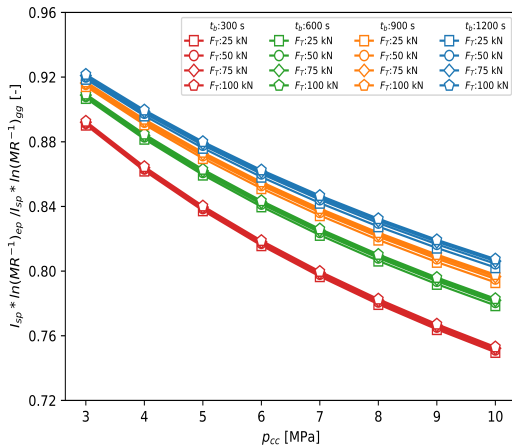
Table A.6: Comparison of adjusted model and data from Kwak et al. [34]  
 ( $t_b = 390$  s,  $F_T = 100$  kN,  $p_{cc} = 10$  MPa)

	Electric Pump		Gas Generator	
	Kwak	Adjusted	Kwak	Adjusted
CC Propellants [kg]	33402	33402	33273	33273
GG Propellants [kg]	-	-	2021	2021
Battery Pack [kg]	1373	<b>1372</b>	-	-
Feed System [kg]	143	143	43	43
Tanks [kg]	878	878	927	927
Helium [kg]	134	134	141	141
Total [kg]	35930	<b>35929</b>	36405	36405
MR [-]	0.0700	0.0700	0.0305	0.0305
Specific Impulse [s]	370.0	370.0	348.6	348.6
Velocity Change [m/s]	9632	<b>9630</b>	11929	11929

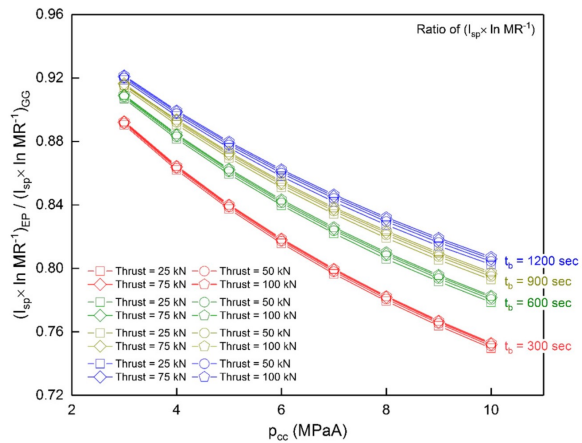
Table A.7: Comparison of adjusted model and data from Kwak et al. [34]  
 ( $t_b = 1200$  s,  $F_T = 100$  kN,  $p_{cc} = 10$  MPa)

### A.5. Adjusted Model Figures

In this section the figures from Kwak’s paper[34] are reproduced using the adjusted model. As already stated in chapter 3, the data produced by the adjusted model very closely matched that of Kwak’s paper. This is also the case for the graphs shown below.

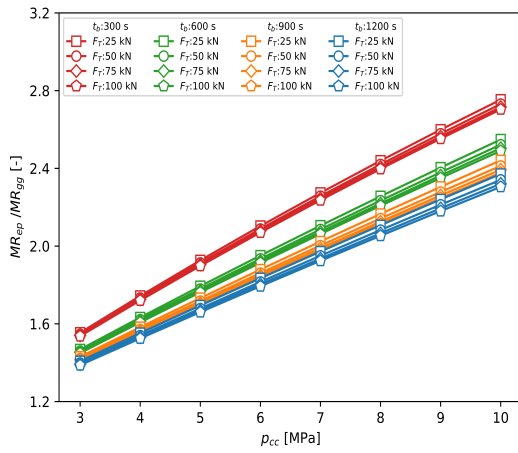


(a) Adjusted Model

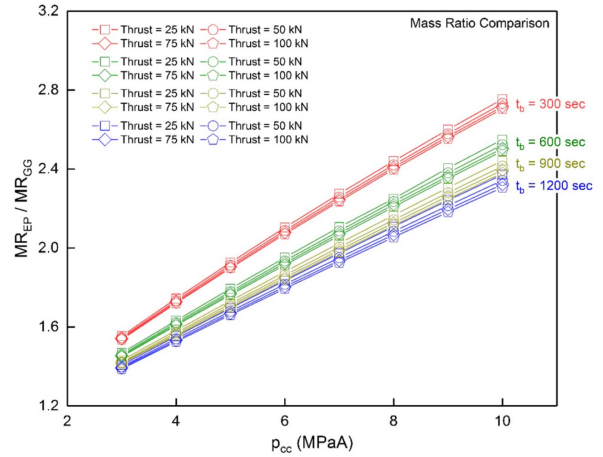


(b) Original Kwak Figure [34]

Figure A.2: Comparison between EP- and GG-cycle for idealized change in velocity

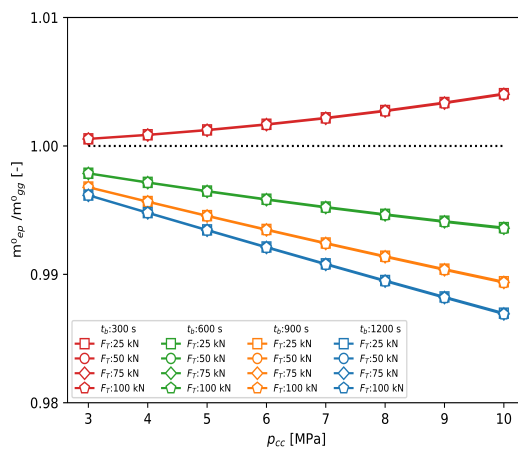


(a) Adjusted Model

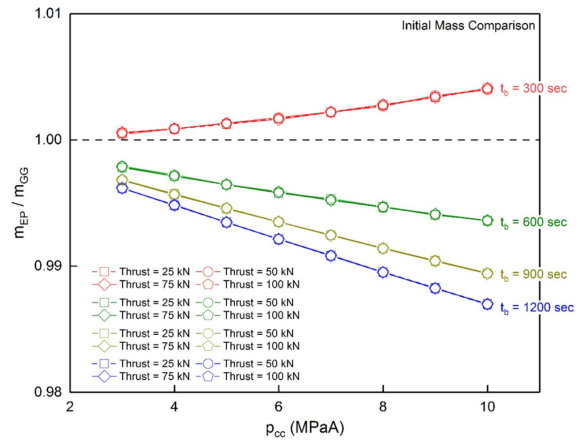


(b) Original Kwak Figure [34]

Figure A.3: Comparison between EP- and GG-cycle for mass ratio

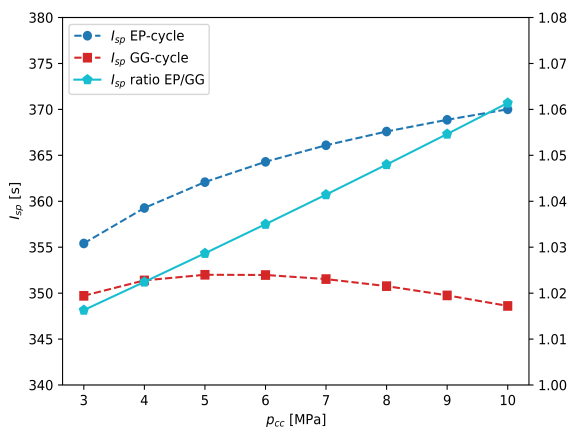


(a) Adjusted Model

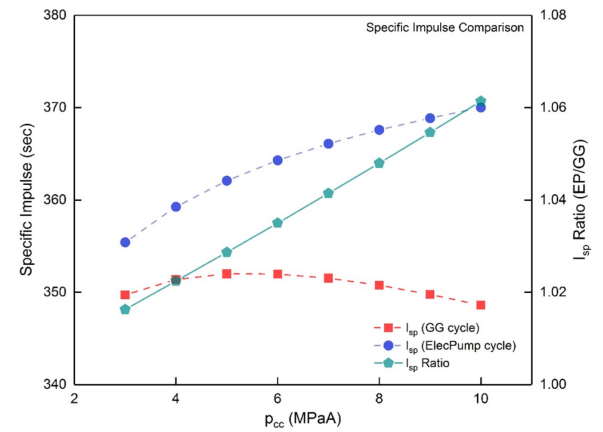


(b) Original Kwak Figure [34]

Figure A.4: Comparison between EP- and GG-cycle for initial mass



(a) Adjusted Model



(b) Original Kwak Figure [34]

Figure A.5: Comparison between EP- and GG-cycle for specific impulse



# B

## Inputs

This appendix contains the input values used to produce the results as presented in this report. They are presented with parameter symbol, value, and unit. See the nomenclature for clarification on the symbols and subscripts or section 5.5 for a table that contains both names and symbols. Additionally, most inputs, and their use in the model, are discussed in more detail in chapter 5. First, the inputs used by Kwak are given, followed by the properties of the materials used in RoCAT. Lastly, the non-default inputs are listed for all engines simulated in this report.

### B.1. Kwak Replication Inputs

Table B.1 shows all inputs used in the replication of Kwak's model. This is essentially a copy of Table 3 from Kwak's paper [34] with the addition of several inputs only mentioned in the text, e.g. the battery coolant change in temperature,  $\Delta T_{bat,cl}$ .

Parameter	Value	Unit	Parameter	Value	Unit
$c_{p,f}$	2009	J/kg-K	$a_{max}$	4.5	$g_0$
$c_{p,gg}$	2024.7	J/kg-K	$\eta_{fp}$	0.61	-
$(O/F)_{cc}$	2.45	-	$\eta_{op}$	0.66	-
$(O/F)_{gg}$	0.32	-	$\eta_{tu}$	0.52	-
$\gamma_{pr}$	1.667	-	$\eta_{em}$	0.95	-
$\gamma_{gg}$	1.16	-	$\eta_{inv}$	0.85	-
$p_e$	0.002	MPa	$\kappa_{fp}$	1.55	-
$p_{pr,0}$	27	MPa	$\kappa_{op}$	1.15	-
$p_{pr,f}^1$	5	MPa	$\kappa_t$	2.5	-
$p_{ft}$	0.25	MPa	$\kappa_{gg}$	2.5	-
$p_{ot}$	0.4	MPa	$\kappa_{prt}$	1.2	-
$p_{tu,in}/p_{tu,out}$	27	-	$\kappa_u$	1.08	-
$R_{pr}$	2080	J/kg-K	$\kappa_{pr}$	1.1	-
$R_{gg}$	274.1	J/kg-K	$\kappa_p$	1.01	-
$\Delta T_{bat,cl}$	40	K	$\kappa_{bat}$	1.2	-
$T_{pr,0}$	100	K	$\rho_{ox}$	1126.1	kg/m <sup>3</sup>
$T_{tu,in}$	900	K	$\rho_{fu}$	804.2	kg/m <sup>3</sup>
$t_{gg,s}$	10	ms	$\rho_{ft,m}$	2850	kg/m <sup>3</sup>
$\delta_{tp}$	13.5	kW/kg	$\rho_{ot,m}$	2850	kg/m <sup>3</sup>
$\delta_{op}$	20	kW/kg	$\rho_{prt,m}$	4430	kg/m <sup>3</sup>
$\delta_{fp}$	15	kW/kg	$\rho_{gg,m}$	8220	kg/m <sup>3</sup>
$\delta_{em}$	5.3	kW/kg	$\sigma_{ft,m}$	250	MPa
$\delta_{inv}$	60	kW/kg	$\sigma_{ot,m}$	250	MPa
$\delta_{bat,P}$	6.95	kW/kg	$\sigma_{prt,m}$	1100	MPa
$\delta_{bat,E}$	198	Wh/kg	$\sigma_{gg,m}$	550	MPa

Table B.1: Inputs used in the replication of Kwak's model [34]

## B.2. Predefined Materials

RoCAT defines several materials and their properties, all of which are given in table B.2 below. The numbered materials refer to the properties given by Kwak [34] with Material1 being used for the propellant tanks, Material2 for the pressurant tank, and Material3 for the gas generator.

Material	Yield Strength [MPa]	Density [kg/m3]	Poisson Ratio [-]	Therm. Cond. [W/(Km)]
Inconel600	1035	8470	0.31	21
Ti6Al4V	1170	4330	0.31	6.7
Al2219	414	2840	0.33	120
NarloyZ	315	9130	0.34	350
Al7075T6	570	2810	0.33	130
Steel301 (Annealed)	275	7830	0.27	16.3
Steel301 (Full Hard)	965	7830	0.27	16.3
Al6061T6	276	2700	0.33	167
Material1	250	2850	-	-
Material2	1100	4430	-	-
Material3	550	8220	-	-

Table B.2: Predefined materials in RoCAT and their properties

## B.3. Non-Default Inputs for Engines

In the following subsections the inputs are listed for each engine simulated in this report and their sources. Only inputs that are different from the default inputs, given in section 5.5, are shown.

### B.3.1. Electric-pump

Inputs for the electric-pump cycle engines.

#### Lee's engine

Below the inputs are given for the electric-pump cycle described by Lee et al. [35], which was compared with RoCAT outputs in section 7.2.1. Besides the listed values below the material for the propellant tanks is Al6061T6 and for the combustion chamber and nozzle the material is Steel301 (Annealed). The engine uses RP-1 as fuel.

Parameter	Value	Unit	Parameter	Value	Unit
$F_T$	0.5	kN	$a_{max}$	0	m/s <sup>2</sup>
$t_b$	600	s	$\kappa_p$	1.1	-
$p_{cc}$	2	MPa	$\kappa_t$	1.0	-
$p_{amb}$	1028	Pa	$\kappa_{ull}$	1.2	-
$p_e$	1028	Pa	$\kappa_{cc,sf}$	2.0	-
$p_{ft}$	0.379	MPa	$\kappa_{inj,sf}$	2.0	-
$p_{ot}$	0.310	MPa	$\kappa_{noz,sf}$	2.0	-
$L^*$	1.145	m	$\delta_{P,em}$	875	W/kg
$(O/F)_{cc}$	2.45	-	$\delta_{P,bat}$	650	W/kg
$\eta_{isp}$	1.0	-	$\delta_{E,bat}$	325	Wh/kg
$\eta_{em}$	0.87	-			

Table B.3: D

### B.3.2. Gas Generator

The inputs for the gas generator cycle engines are given here. The discussion of their simulation can be found in section 7.1.4. For all these engines a turbine exhaust expansion ratio of 4 has been assumed. Despite all being first stage engines, except for the HM7B, vacuum ambient pressure has been assumed, since McHugh gives vacuum thrust and specific impulse only.

**F-1**

Table B.4 shows the inputs that were used to simulate the F-1 gas generator engine. All data is taken from McHugh [41] and Ernst [20]. The F-1 uses RP-1 as fuel and has a 0.416 gas generator oxidizer-to-fuel ratio (which is not used as input).

Parameter	Value	Unit	Parameter	Value	Unit
$F_T$	7775.5	kN	$p_{tu,in}/p_{tu,out}$	16.3	-
$t_b$	161	s	$(O/F)_{cc}$	2.27	-
$p_{cc}$	7.76	MPa	$\eta_{fp}$	0.764	-
$p_{amb}$	0	MPa	$\eta_{op}$	0.714	-
$p_{gg}$	6.76	MPa	$\eta_{tu}$	0.605	-
$T_{tu,in}$	1062	K	$\varepsilon$	16	-
$L^*$	1.22	m	$\varepsilon_{exh}$	4	-

Table B.4: inputs used for simulating the F-1 engine

**H-1**

Table B.5 shows the inputs that were used to simulate the H-1 gas generator engine. All data is taken from McHugh [41] and Ernst [20]. The H-1 uses RP-1 as fuel and has a 0.342 gas generator oxidizer-to-fuel ratio (which is not used as input).

Parameter	Value	Unit	Parameter	Value	Unit
$F_T$	945.4	kN	$p_{tu,in}/p_{tu,out}$	18.21	-
$t_b$	150	s	$(O/F)_{cc}$	2.26	-
$p_{cc}$	4.15	MPa	$\eta_{fp}$	0.75	-
$p_{amb}$	0	MPa	$\eta_{op}$	0.71	-
$p_{gg}$	4.22	MPa	$\eta_{tu}$	0.66	-
$T_{tu,in}$	922	K	$\varepsilon$	8	-
$L^*$	0.983	m	$\varepsilon_{exh}$	4	-
$\left(\frac{A_{cc}}{A_{th}}\right)$	1.67	-			

Table B.5: inputs used for simulating the H-1 engine

**HM60**

Table B.6 shows the inputs that were used to simulate the HM60 gas generator engine. All data is taken from Mota et al. [43] and McHugh [41]. The HM60 uses liquid hydrogen as fuel and has a 0.9 gas generator oxidizer-to-fuel ratio (which is not used as input).

Parameter	Value	Unit	Parameter	Value	Unit
$F_T$	1025	kN	$(p_{tu,in}/p_{tu,out})_{fu}$	17.0	-
$t_b$	605	s	$(p_{tu,in}/p_{tu,out})_{ox}$	13.6	-
$p_{cc}$	10.0	MPa	$(O/F)_{cc}$	5.1	-
$p_{amb}$	0	MPa	$\eta_{fp}$	0.76	-
$p_{gg}$	8.5	MPa	$\eta_{op}$	0.73	-
$T_{tu,in}$	871	K	$\eta_{tu,fu}$	0.59	-
$L^*$	0.84	m	$\eta_{tu,ox}$	0.27	-
$\left(\frac{A_{cc}}{A_{th}}\right)$	2.99	-	$\varepsilon$	45	-
			$\varepsilon_{exh}$	4	-

Table B.6: inputs used for simulating the HM60 engine

**HM7B**

Table B.7 shows the inputs that were used to simulate the HM7B gas generator engine. All data is taken from [43] with the exception of the exhaust gas expansion ratio,  $\varepsilon_{exh}$ , which was broadly estimated from HM7B schematics. The HM7B uses liquid hydrogen as fuel and has a 0.87 oxidizer-to-fuel ratio for the gas generator (which is not used as input).

Parameter	Value	Unit	Parameter	Value	Unit
$F_T$	62.6	kN	$p_{tu,in}/p_{tu,out}$	16.7	-
$t_b$	731	s	$(O/F)_{cc}$	4.565	-
$p_{cc}$	3.6	MPa	$\eta_{fp}$	0.73	-
$p_{amb}$	0	MPa	$\eta_{op}$	0.60	-
$p_{ft}$	0.2	MPa	$\eta_{tu}$	0.45	-
$p_{ot}$	0.3	MPa	$\varepsilon$	82.9	-
$p_{gg}$	2.3	MPa	$\varepsilon_{exh}$	4	-
$T_{tu,in}$	860	K	$\left(\frac{A_{cc}}{A_{th}}\right)$	2.78	-
$L^*$	0.68	m			

Table B.7: inputs used for simulating the HM7B engine

**J-2**

Table B.8 shows the inputs that were used to simulate the J2 gas generator engine. All data is taken from McHugh [41] and Vilja et al.[60]. The J-2 uses liquid hydrogen as fuel and has a 0.94 gas generator oxidizer-to-fuel ratio (which is not used as input).

Parameter	Value	Unit	Parameter	Value	Unit
$F_T$	1023	kN	$(p_{tu,in}/p_{tu,out})_{fu}$	7.20	-
$t_b$	475	s	$(p_{tu,in}/p_{tu,out})_{ox}$	2.65	-
$p_{cc}$	5.4	MPa	$(O/F)_{cc}$	5.5	-
$p_{amb}$	0	MPa	$\eta_{fp}$	0.80	-
$p_{gg}$	4.7	MPa	$\eta_{op}$	0.73	-
$T_{tu,in}$	922	K	$\eta_{tu,fu}$	0.60	-
$L^*$	0.62	m	$\eta_{tu,ox}$	0.47	-
$\left(\frac{A_{cc}}{A_{th}}\right)$	1.58	-	$\varepsilon$	27.5	-
			$\varepsilon_{exh}$	4	-

Table B.8: inputs used for simulating the J-2 engine

**RS-27**

Table B.9 shows the inputs that were used to simulate the RS-27 gas generator engine. All data is taken from McHugh [41] and Ernst [20]. The RS-27 uses RP-1 as fuel and has a 0.33 gas generator oxidizer-to-fuel ratio (which is not used as input).

Parameter	Value	Unit	Parameter	Value	Unit
$F_T$	1043	kN	$p_{tu,in}/p_{tu,out}$	22.0	-
$t_b$	274	s	$(O/F)_{cc}$	2.245	-
$p_{cc}$	4.87	MPa	$\eta_{fp}$	0.779	-
$p_{amb}$	0	MPa	$\eta_{op}$	0.718	-
$p_{gg}$	4.7	MPa	$\eta_{tu}$	0.589	-
$T_{tu,in}$	916	K	$\varepsilon$	12	-
$L^*$	0.99	m	$\varepsilon_{exh}$	4	-
$\left(\frac{A_{cc}}{A_{th}}\right)$	1.62	-			

Table B.9: inputs used for simulating the RS-27 engine

### B.3.3. Open Expander

Inputs for the open expander cycle engines.

#### LE-5B

Table B.10 shows the inputs that were used to simulate the LE-5B open expander engine for validation in section 7.1.6. Most of the inputs are taken from Aoki et al. [2]. The chamber to throat area ratio is assumed to be the same as the LE-5, whose value is taken from McHugh [41]. The expansion ratio at which the cooling ends has been visually estimated from a schematic in Kakuma et al.[31]. The efficiencies of the propellant pumps and turbines have been assumed to be the same as those of the SE21D provided below.

Parameter	Value	Unit	Parameter	Value	Unit
$F_T$	137	kN	$(p_{tu,in}/p_{tu,out})_{fu}$	5.125	-
$t_b$	534	s	$(p_{tu,in}/p_{tu,out})_{ox}$	2.172	-
$(O/F)_{cc}$	5.0	-	$\left(\frac{A_{cc}}{A_{th}}\right)$	3.11	-
$\varepsilon$	110	-	$\varepsilon_{cl,end}$	6	-
$p_{cc}$	3.62	MPa	$T_{ft}$	21	K
$p_{amb}$	0	MPa	$T_{ot}$	90	K
$p_{ft}$	0.2	MPa	$T_{tu,in}$	409	K
$p_{ot}$	0.4	MPa	$L^*$	1.145	m

Table B.10: Inputs used for simulating the LE-5B engine

#### SE21D

Table B.11 shows the inputs that were used to simulate the SE21D open expander engine for verification in section 7.1.5. The SE21D is a LH2/LOX-engine and is simulated for sea level conditions. All inputs are taken from Sippel's paper[53].  $\varepsilon_{exh}$  has been taken as the mass based average of both secondary exhausts.

Parameter	Value	Unit	Parameter	Value	Unit
$F_T$	1947.03	kN	$\kappa_{isp}$	0.99	-
$p_{cc}$	6.649	MPa	$\kappa_{exh,isp}$	0.98	-
$p_{amb}$	0.101325	MPa	$(O/F)_{cc}$	5.5	-
$p_{ft}$	0.3	MPa	$\eta_{fp}$	0.7	-
$p_{ot}$	0.5	MPa	$\eta_{op}$	0.76	-
$p_{tu,out}$	0.3	MPa	$\eta_{tu}$	0.45	-
$p_{exh,e}$	0.04	MPa	$\eta_{fp2}$	0.75	-
$T_{tu,in}$	506.452	K	$\varepsilon$	12.52	-
$T_{ft}$	21	K	$\varepsilon_{exh}$	1.6502	-
$T_{ot}$	90	K	$\varepsilon_{end,cl}$	5	-
$L^*_{cc}$	4	m	$A_{cc}/A_{th}$	2.9654	-

Table B.11: inputs used for simulating the SE21D engine



# Gas Generator Performance Schematics

In this appendix the performance schematics are provided for all gas generators which have been modeled to validate RoCAT in section 7.1.4. For the readers convenience the component numbering is repeated below in table C.1. Each schematic shows the total specific impulse at the top as well as the input total thrust. Furthermore, it shows the flow state in between each component and consequently how each component influences the pressure, temperature, and mass flow. The splitters and mergers do not affect the former two properties, so for their downstream flows only the mass flow is given. From these schematics it becomes clear which exit stream contributes how much to the total thrust and with which individual specific impulse. All values presented are output values with the exception of the expansion ratio,  $\varepsilon$ , of the thrust chamber and turbine exhaust(s), the total thrust,  $F_{T,tot}$ , the efficiencies,  $\eta$ , and the mixture ratio,  $MR$ , of the thrust chamber.

#	Component	Electric-Pump	Gas Generator	Open Expander
1	Fuel Tank	X	X	X
2	Oxidizer Tank	X	X	X
3	Fuel Pump	X	X	X
4	Oxidizer Pump	X	X	X
5	Turbine		X	X
6	Heat Exchanger	X	X	X
7	Injector	X	X	X
8	Thrust Chamber	X	X	X
9	Splitter/Merger	X	X	X
10	Turbine Exhaust		X	X
11	Gas Generator		X	
12	Electric Motor	X		
13	Inverter	X		
14	Battery	X		
15	Battery Cooler	X		
16	Pressurant Tank	X	X	X
17	Pressurant	X	X	X
18	Fuel	X	X	X
19	Oxidizer	X	X	X

Table C.1: Overview of components and in which cycles they are present. The components are referred to by number in most schematics in this report.

C.1. HM60

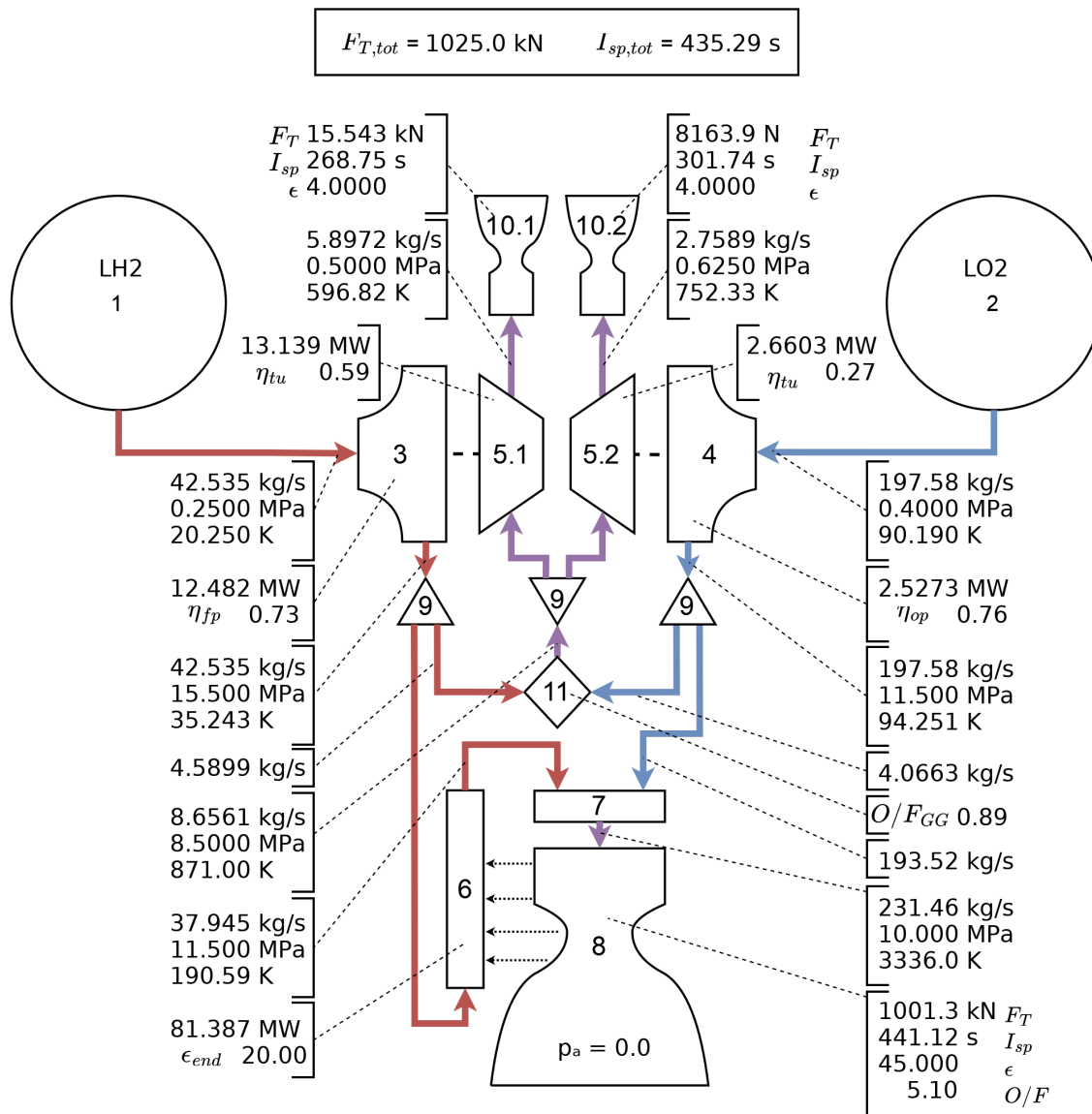


Figure C.1: Schematic overview of performance parameters and flow state of the HM60 engine as simulated by RoCAT

C.2. J-2

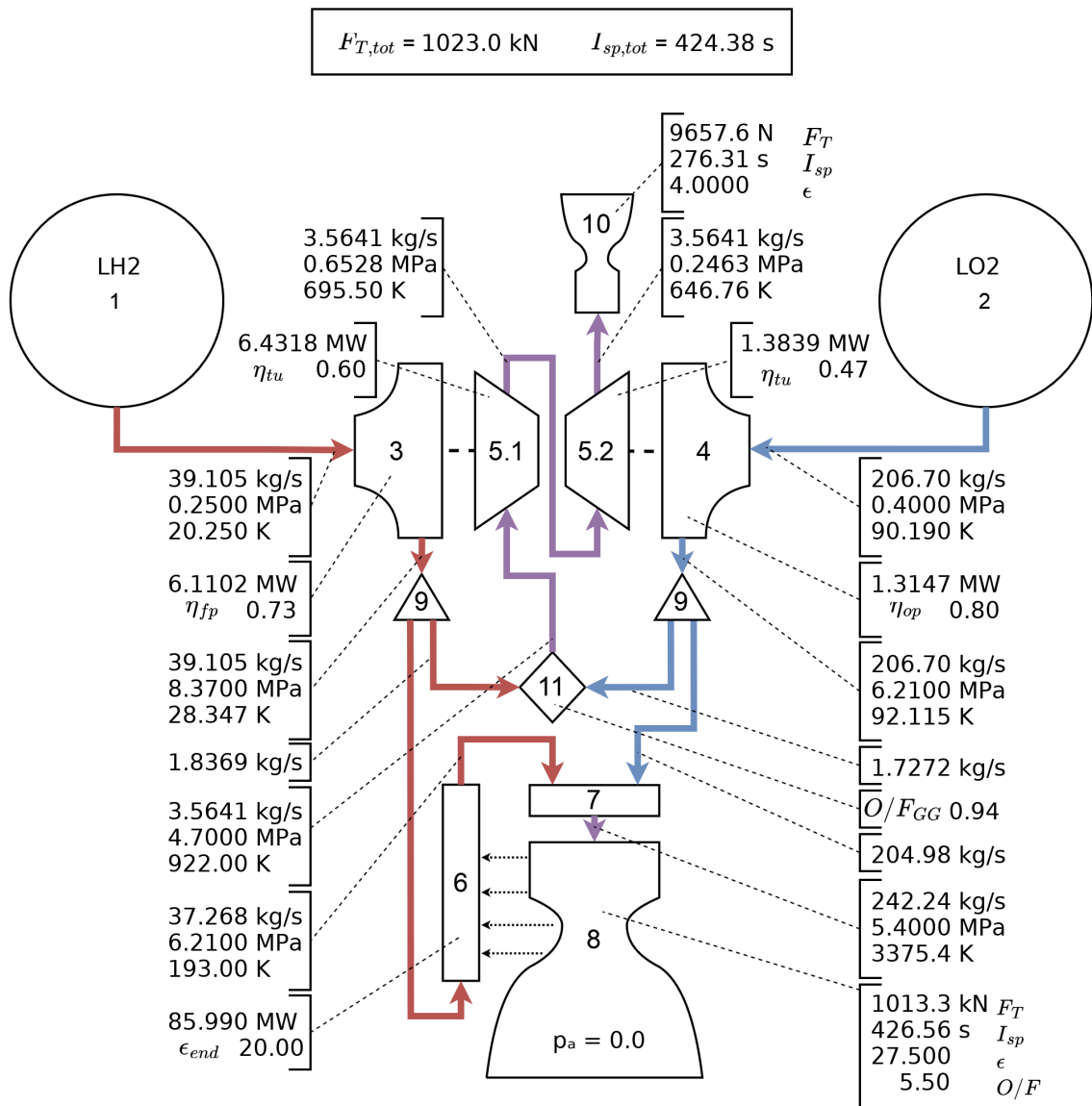


Figure C.2: Schematic overview of performance parameters and flow state of the J-2 engine as simulated by RoCAT

### C.3. HM7B

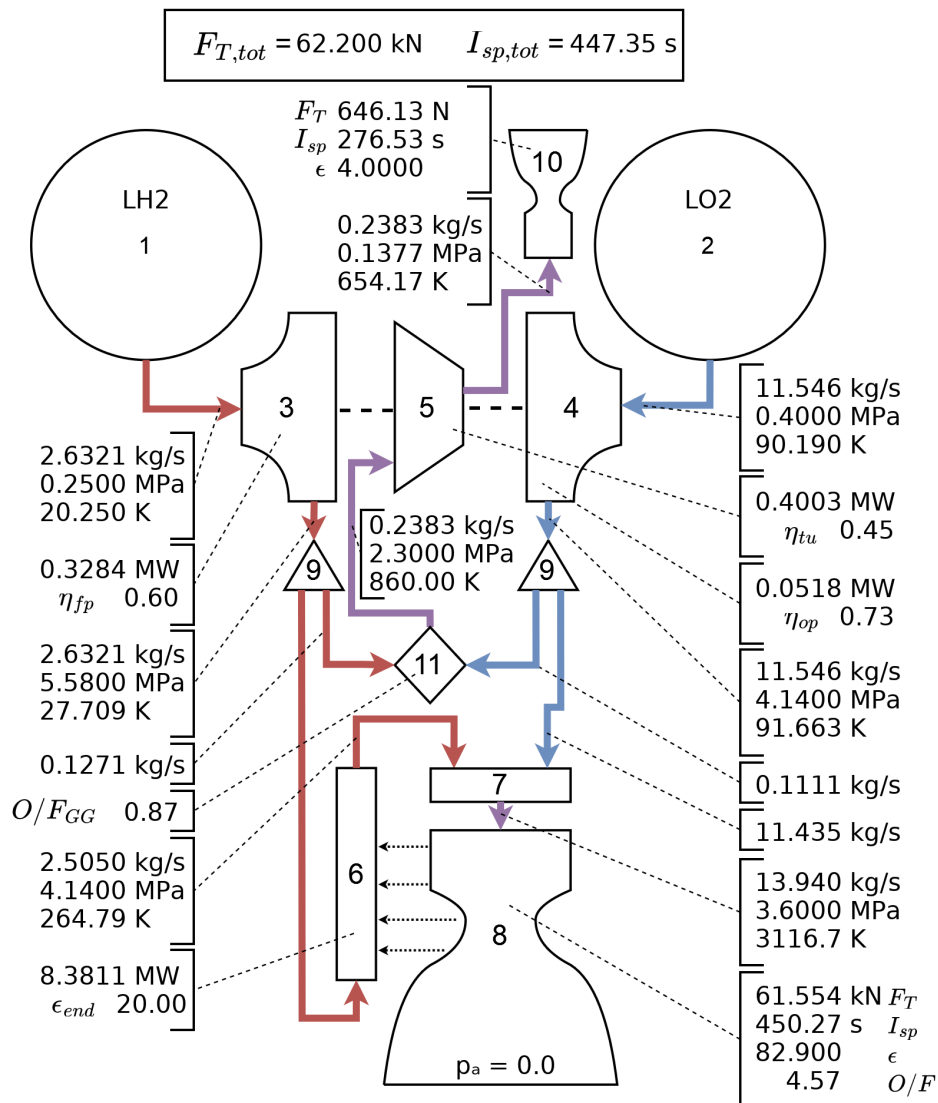


Figure C.3: Schematic overview of performance parameters and flow state of the HM7B engine as simulated by RoCAT

C.4. RS-27

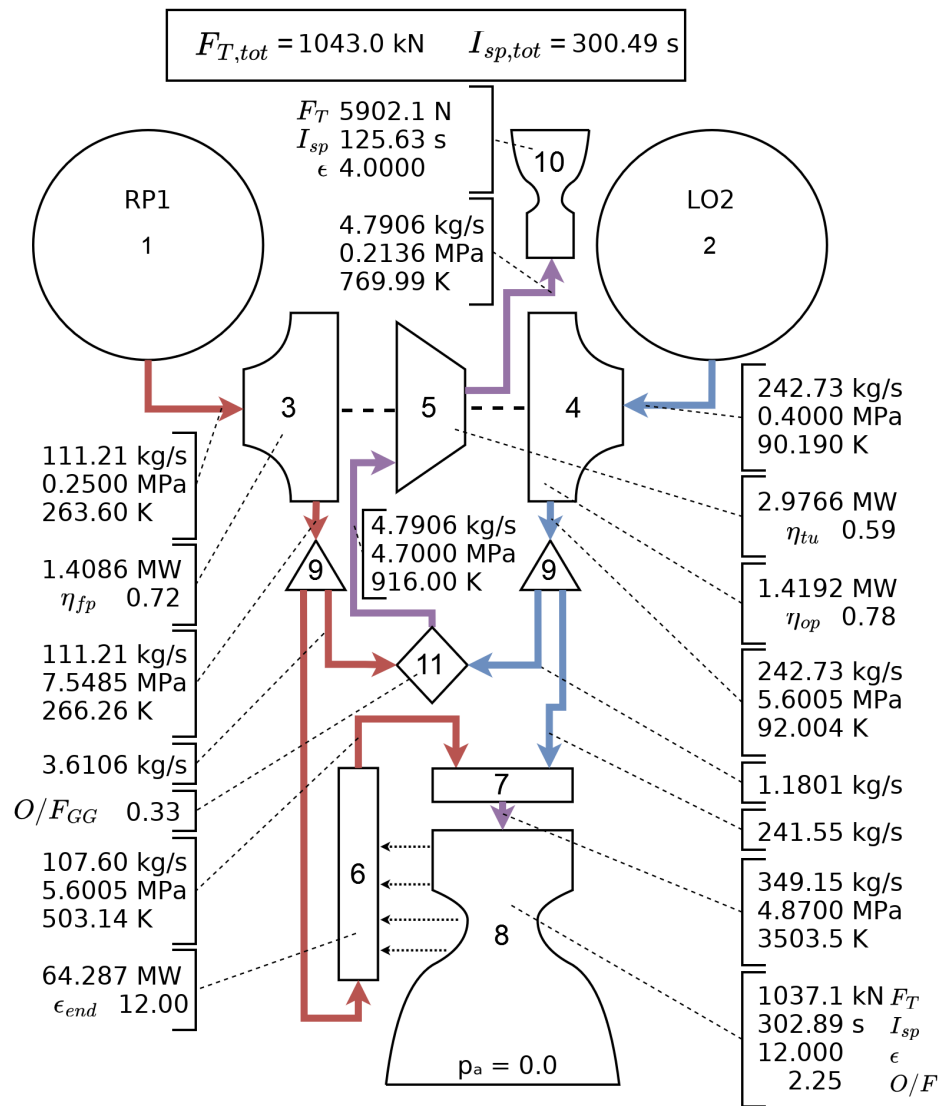


Figure C.4: Schematic overview of performance parameters and flow state of the RS-27 engine as simulated by RoCAT

C.5. H-1

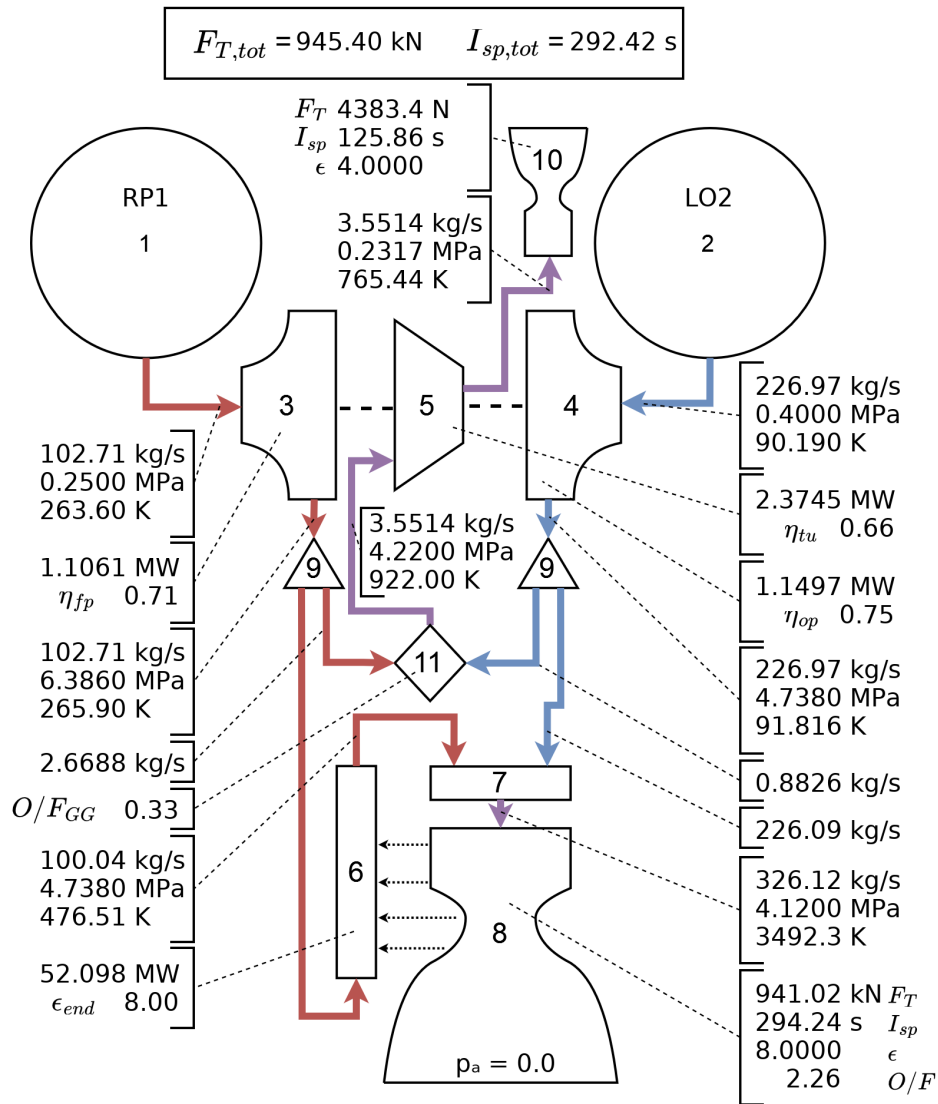


Figure C.5: Schematic overview of performance parameters and flow state of the H-1 engine as simulated by RoCAT

C.6. F-1

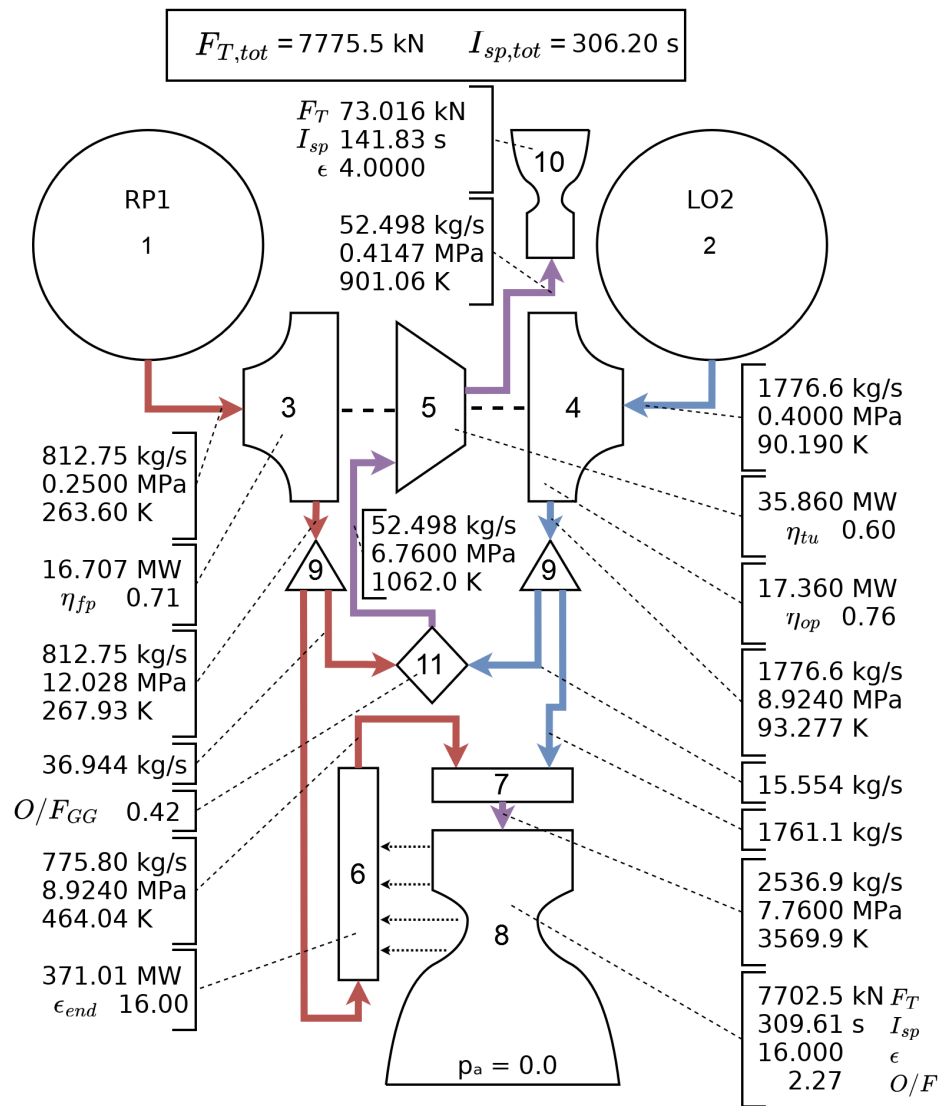


Figure C.6: Schematic overview of performance parameters and flow state of the F-1 engine as simulated by RoCAT



# D

## Centaur Mass Data

This appendix contains the mass break down of the Centaur-D as taken from reference [18], followed by ratios calculated from this data in table D.3. Note that the data given in tables D.1 and D.2 is presented in pounds.

Several additional aggregations to the original data have been made most of which are self explanatory. For the Hydrogen/Oxygen/Propellants it should be noted that "Total Tanked" refers to "Total Expended" + "Total Residual", while "Total" refers to "Total Tanked" - "Ground venting/boil-off". Additionally, the "Final Mass" is found as "Payload" + "Total Basic Hardware" + "Total Residuals". The "Report Mass" is defined as "Body" + "Propulsion group" + "Pressurization group" + "Total Propellants" + "Total Helium", which is assumed to be synonymous to the initial mass calculated in this report, as discussed in section 6.8.1.

Centaur Launch	AC-6	AC-9	AC-10	AC-11	AC-15	Average
<b>Payload/Spacecraft</b>	2,084	1,741	2,193	2,294	2,291	2,121
<b>Basic Hardware:</b>						
Body	940	994	972	944	927	955.4
Propulsion group	1,192	1,235	1,194	1,202	1,226	1,210
Guidance group	310	339	341	311	333	326.8
Control group	117	148	140	140	152	139.4
Pressurization group	138	201	139	135	185	159.6
Electrical group	266	276	268	289	286	277
Separation group	80	77	78	81	81	79.4
Flight instrumentation	447	547	274	258	252	355.6
Miscellaneous equipment	153	338	133	145	143	182.4
<b>Total Basic Hardware</b>	<b>3,643</b>	<b>4,155</b>	<b>3,539</b>	<b>3,505</b>	<b>3,585</b>	<b>3,685</b>
<b>Jettisonable Hardware:</b>						
Nose fairing	2,006	2,033	1,964	2,071	2,032	2,021
Insulation panels	1,218	1,218	1,174	1,231	1,224	1,213
Ablated ice		50	50	69	50	54.75
<b>Total Jettisonable Hardware</b>	<b>3,224</b>	<b>3,301</b>	<b>3,188</b>	<b>3,371</b>	<b>3,306</b>	<b>3,278</b>
<b>Residuals:</b>						
Liquid hydrogen	163	150	130	70	207	144
Liquid oxygen	271	290	199	195	662	323.4
Gaseous hydrogen	83	116	83	81	68	86.2
Gaseous oxygen	165	170	164	161	171	166.2
Hydrogen peroxide	52	33	83	67	41	55.2
Helium	5	4	4	5	4	4.4
Ice	12	12	12	19	12	13.4
<b>Total Residual Hydrogen</b>	<b>246</b>	<b>266</b>	<b>213</b>	<b>151</b>	<b>275</b>	<b>230</b>
<b>Total Residual Oxygen</b>	<b>436</b>	<b>460</b>	<b>363</b>	<b>356</b>	<b>833</b>	<b>490</b>
<b>Total Residual Propellants</b>	<b>682</b>	<b>726</b>	<b>576</b>	<b>507</b>	<b>1,108</b>	<b>720</b>
<b>Total Residuals</b>	<b>751</b>	<b>775</b>	<b>675</b>	<b>598</b>	<b>1,165</b>	<b>793</b>

Table D.1: Overview of centaur mass data in pounds. Taken from [18] (Continues next page)

Centaur Launch	AC-6	AC-9	AC-10	AC-11	AC-15	Average
<b>Expandables:</b>						
Main impulse hydrogen	4,966	4,805	4,982	5,015	4,811	4,916
Main impulse oxygen	25,153	24,794	24,793	24,988	24,419	24,829
Gas boiloff on ground hydrogen	27	6	22	0	8	12.6
Gas boiloff on ground oxygen	26	21	24	0	0	14.2
In-flight chill hydrogen	11	65	24	23	71	38.8
In-flight chill oxygen	13	77	33	32	102	51.4
Booster phase vent hydrogen	83	40	40	53	53	53.8
Booster phase vent oxygen	20	80	42	66	66	54.8
Sustainer phase vent hydrogen	46	18	18	30	30	28.4
Sustainer phase vent oxygen	38	30	30	60	60	43.6
Engine shutdown 1 loss hydrogen		6		6	6	6
Engine shutdown 1 loss oxygen		18		18	18	18
Engine shutdown 2 loss hydrogen		6			6	6
Engine shutdown 2 loss oxygen		18			18	18
Parking Orbit Vent, LH2		47			17	32
Parking Orbit Vent, LOX		0			0	0
Parking Orbit Leakage, LH2		0			1	0.5
Parking Orbit Leakage, LOX		0			2	1
Hydrogen peroxide	49	202	49	67	196	112.6
Helium		6	1	1	5	3.25
Ice	50					50
Total Expended Hydrogen	5,133	4,993	5,086	5,127	5,003	5,068
Total Expended Oxygen	25,250	25,038	24,922	25,164	24,685	25,012
Total Expended Propellants	30,383	30,031	30,008	30,291	29,688	30,080
<b>Total Expendables</b>	<b>30,482</b>	<b>30,239</b>	<b>30,058</b>	<b>30,359</b>	<b>29,889</b>	<b>30,205</b>
Total Tanked Hydrogen	5,379	5,259	5,299	5,278	5,278	5,299
Total Tanked Oxygen	25,686	25,498	25,285	25,520	25,518	25,501
Total Tanked Propellants	31,065	30,757	30,584	30,798	30,796	30,800
<b>Total Tanked Weight</b>	<b>40,184</b>	<b>40,211</b>	<b>39,653</b>	<b>40,127</b>	<b>40,236</b>	<b>40,082</b>
<b>Minus ground venting</b>	<b>53</b>	<b>27</b>	<b>46</b>	<b>0</b>	<b>8</b>	<b>26.8</b>
<b>Ground Ignition Weight</b>	<b>40,131</b>	<b>40,184</b>	<b>39,607</b>	<b>40,127</b>	<b>40,228</b>	<b>40,055</b>
Total Hydrogen	5,352	5,253	5,277	5,278	5,270	5,286
Total Oxygen	25,660	25,477	25,261	25,520	25,518	25,487
Total Propellants	31,012	30,730	30,538	30,798	30,788	30,773
Total Helium	5	10	5	6	9	7
Total Hydrogen Peroxide	101	235	132	134	237	168
<b>Final Mass</b>	<b>6,478</b>	<b>6,671</b>	<b>6,407</b>	<b>6,397</b>	<b>7,041</b>	<b>6,599</b>
<b>Report Mass</b>	<b>33,282</b>	<b>33,160</b>	<b>32,843</b>	<b>33,079</b>	<b>33,126</b>	<b>33,098</b>

Table D.2: Continuation of Centaur mass data in pounds. Taken from [18]

Centaur Launch	AC-6	AC-9	AC-10	AC-11	AC-15	Average
<b>Residual/Total</b>						
Hydrogen	0.0460	0.0506	0.0404	0.0286	0.0522	0.0436
Oxygen	0.0170	0.0181	0.0144	0.0139	0.0326	0.0192
Propellants	0.0220	0.0236	0.0189	0.0165	0.0360	0.0234
<b>X / Report Mass</b>						
Ground Weight	1.2058	1.2118	1.2059	1.2131	1.2144	1.2102
Ground Weight - Payload	1.1432	1.1593	1.1392	1.1437	1.1452	1.1461
Jettison	0.0969	0.0995	0.0971	0.1019	0.0998	0.0990

Table D.3: Various mass ratios calculated from tables D.1 and D.2

# Assumptions & Differences

This appendix list the differences between RoCAT and the model given by Kwak et al.[34] and lists the assumptions made for the models used in RoCAT.

## E.1. Differences w.r.t Kwak

- CoolProp fluid properties
- CEA combustion products properties
- GasGenerator O/F-ratio determined by maximum turbine temperature
- Addition of Thrust Chamber (Injector, Combustion Chamber, and Nozzle)
- Addition of regenerative cooling
- Addition of gas generator O/F-ratio estimation
- Account for thrust contribution of turbine exhaust gas
- Minimum material thickness of pressure components
- Inlet/outlet flow state for each component
- Enthalpy change for turbine, pumps, and heat exchanger
- Electric-pump cycle temperature dependence of flow calculation
- Fixed inaccuracies:
  - Electric-pump cycle battery coolant flow efficiencies
  - Gas generator propellant mass margin factor
  - Gas generator required turbine mass flow iteration
- New cycle: open expander cycle
- New configurations:
  - Dual pumps
  - Parallel dual turbine
  - Series dual turbine
  - Dual electric motor
- Modularity:
  - Optional submerged pressurant tank
  - Optional tank shapes (sphere, cylinder with various caps)
  - Optional predefined materials
  - Optional configurations
  - Optional open expander configurations (pre- or post-cooling split or both)
  - Optional nozzle sizing (area ratio, pressure ratio, exit pressure)
  - Optional nozzle shape (conical or bell)
  - Optional propellants (RP-1, LH2, and LCH4 tested with LOX)
  - Optional manual combustion properties
  - Optional nozzle input (pressure ratio, exit pressure, or expansion ratio)
- Additional checks:
  - Pressure balance
  - Pumps NPSH requirement
  - Electric motor leak cooling
  - Choked flow and Summerfield Criterion Check
  - Minimum cooling requirement
- Inputs no longer required:
  - Chamber Characteristic Length
  - Contraction Ratio
  - Gas generator O/F-ratio
  - Fluid Properties

## E.2. List of assumptions

- The mass of pressure components, e.g. tanks, chamber, nozzle, gas generator, is calculated by assuming them to be thin walled pressure vessel (with a minimum thickness)
- CEA set to frozen settings
- The battery heat loss is determined by its inefficiency which is based on burn time
- Fuel is used to regeneratively cool the thrust chamber
- n-Dodecane is comparative to RP1
- Liquid Oxygen is used as oxidizer
- RP1/LH2/LCH4 is used as fuel
- The mass of power components, e.g. pumps, turbine, inverter, electric motor, battery, is calculated by assuming a linear relation between power and mass
- The convergent section of the combustion chamber's volume is simplified to be a truncated cone
- CEA only receives pressure ratio inputs. If an expansion ratio (or exit pressure) is provided IRT is used to find the equivalent pressure ratio, which is subsequently used in the CEA calculations. Using the expansion ratio directly would not give the same results as CEA internally does not use IRT to convert between expansion ratio and pressure ratio
- Temperature changes over "work" components like the pumps, turbine, and heat exchanger are based on enthalpy, which is calculated using CoolProp
- Propellants are assumed to enter the combustion chamber at tank temperatures (could be fixed with another iteration loop)
- Pressure drops over key components such as the injector and heat exchanger are assumed to scale linearly with combustion chamber pressure
- Radiative heat transfer is assumed to be a constant percentage of convective heat transfer (if radiative heat transfer over the whole thrust chamber is 10% of total convective heat transfer, it is assumed that for each section the total is simply 110% of the convective heat transfer)
- Radiative emissivities are taken to be independent of wall material and propellant choice
- Pure propellant flow properties are estimated using CoolProp dynamically
- Combusted flow properties are estimated using CEA and are constant
- Maximum pressure in propellant tanks is determined by initial fluid height and maximum acceleration
- Thrust contribution of turbine exhaust flow is determined by Ideal Rocket Theory equations and decreases the required thrust from the thrust chamber
- Mixture ratio of gas generator is determined through CEA from turbine temperature requirement

# Detailed Gas Generator Validation Data

This appendix contains the validation data for the gas generator cycle in table F.1. It is a complementary data-set to the data provided in table 7.3 and table 7.8. Table F.1a provides the values as calculated by RoCAT, table F.1b provides the values as provided by McHugh [41] and table F.1c provided the percentage difference between the two, i.e.  $(X_{McHugh} - X_{RoCAT}) / X_{McHugh} \cdot 100$ . The absolute average in the last column of table F.1c is obtained by taking the absolute value of each difference and then taking the average.

	<b>HM7B</b>	<b>H-1</b>	<b>RS-27</b>	<b>F-1</b>	<b>HM60</b>	<b>J-2</b>
<b>Thrust Chamber Length [m]</b>	1.93	2.10	2.52	5.68	3.22	3.32
<b>Exit Diameter [m]</b>	0.989	1.20	1.41	3.47	1.77	1.92
<b>Engine Dry Mass [kg]</b>	52.1	363	432	6030	1510	739
<b>Chamber Length [m]</b>	0.279	0.636	0.641	0.796	0.375	0.417
<b>Chamber Diameter [m]</b>	0.181	0.549	0.515	1.16	0.460	0.459
<b>Chamber Mass [kg]</b>	23.2	193	220	3477	378	251
<b>GG Mass Flow [kg/s]</b>	0.238	3.55	4.79	52.5	8.66	3.56
<b>GG Mixture Ratio [-]</b>	0.874	0.331	0.327	0.421	0.886	0.940
<b>Fuel Mass Flow [kg/s]</b>	2.63	103	111	813	42.5	39.1
<b>Oxidizer Mass Flow [kg/s]</b>	11.5	227	243	1777	198	207
<b>Fuel Pump Outlet Pressure [MPa]</b>	5.58	6.39	7.55	12.03	15.50	8.37
<b>Oxidizer Pump Outlet Pressure [MPa]</b>	4.14	4.74	5.60	8.92	11.50	6.21
<b>(Fuel) Turbine Power [kW]</b>	400	2375	2977	35860	13139	6432
<b>Oxidizer Turbine Power [kW]</b>	-	-	-	-	2660	1384
<b>Specific Impulse [s]</b>	447	292	300	306	435	424

(a) As modeled RoCAT

	<b>HM7B</b>	<b>H-1</b>	<b>RS-27</b>	<b>F-1</b>	<b>HM60</b>	<b>J-2</b>
<b>Thrust Chamber Length [m]</b>	2.01	2.67	3.77	6.1	3.1	3.38
<b>Exit Diameter [m]</b>	0.992	1.24	1.44	3.66	1.7	2.05
<b>Engine Dry Mass [kg]</b>	158	878.2	1146.6	8436.8	1719	1542
<b>Chamber Length [m]</b>	0.283	0.78	0.75	1	0.426	0.4572
<b>Chamber Diameter [m]</b>	0.18	0.53	0.52	1.02	0.415	0.47
<b>Chamber Mass [kg]</b>	69	331	415	-	430	446.8
<b>GG Mass Flow [kg/s]</b>	0.25	7.86	9.13	75.7	8.4	3.19
<b>GG Mixture Ratio [-]</b>	0.87	0.342	0.33	0.416	0.9	0.94
<b>Fuel Mass Flow [kg/s]</b>	2.57	102.4	111.3	796	39.7	38.2
<b>Oxidizer Mass Flow [kg/s]</b>	11.7	234.9	251.8	1804	202.5	212.1
<b>Fuel Pump Outlet Pressure [MPa]</b>	5.55	7.1	7.09	13	15.8	8.62
<b>Oxidizer Pump Outlet Pressure [MPa]</b>	5.02	6.3	7.25	11	13	7.64
<b>(Fuel) Turbine Power [kW]</b>	404	2830	3346	40000	11200	6403
<b>Oxidizer Turbine Power [kW]</b>	-	-	-	-	3000	1717
<b>Specific Impulse [s]</b>	445.5	292	301.8	304.8	433.5	425

(b) As given by McHugh [41]

Table F.1: Overview of parameters for various gas generator engines

	HM7B	H-1	RS-27	F-1	HM60	J-2	Abs.Avg.
<b>Thrust Chamber Length [m]</b>	-4.21	-21.38	-33.27	-6.87	3.82	-1.71	11.88
<b>Exit Diameter [m]</b>	-0.31	-2.85	-2.42	-5.16	4.33	-6.54	3.60
<b>Engine Dry Mass [kg]</b>	-67.03	-58.72	-62.28	-28.52	-12.16	-52.09	46.80
<b>Chamber Length [m]</b>	-1.47	-18.46	-14.49	-20.43	-12.08	-8.69	12.60
<b>Chamber Diameter [m]</b>	0.63	3.57	-0.93	14.10	10.90	-2.32	5.41
<b>Chamber Mass [kg]</b>	-66.38	-41.58	-46.95	-	-12.17	-43.72	42.16
<b>GG Mass Flow [kg/s]</b>	-4.7	-54.8	-47.5	-30.7	3.0	11.7	25.4
<b>GG Mixture Ratio [-]</b>	0.49	-3.3	-1.0	1.2	-1.6	0.03	1.3
<b>Fuel Mass Flow [kg/s]</b>	2.4	0.30	-0.08	2.1	7.1	2.4	2.4
<b>Oxidizer Mass Flow [kg/s]</b>	-1.3	-3.4	-3.6	-1.5	-2.4	-2.5	2.5
<b>Fuel Pump Outlet Pressure [MPa]</b>	0.54	-10.1	6.5	-7.5	-1.9	-2.9	4.9
<b>Oxidizer Pump Outlet Pressure [MPa]</b>	-17.5	-24.8	-22.8	-18.9	-11.5	-18.7	19.0
<b>(Fuel) Turbine Power [kW]</b>	-0.9	-16.1	-11.0	-10.4	17.3	0.45	9.4
<b>Oxidizer Turbine Power [kW]</b>	-	-	-	-	-11.3	-19.4	15.4
<b>Specific Impulse [s]</b>	0.41	0.14	-0.43	0.46	0.41	-0.15	0.34

(c) Difference between table F.1b and table F.1a in percent.  
Green-Red gradient between an absolute difference of 0 and 30 %.

Table F.1: Overview of parameters for various gas generator engines



The electric-pump cycle is a rocket engine configuration that uses an electric motor to power the pumps instead of a turbine. This offers several expected advantages such as simpler design, lower development costs, and easier restartability, but comes with reduced performance compared to conventional cycles. Previous research has primarily compared the electric-pump cycle to the gas generator cycle and has been limited to direct comparison. This research aims to extend these studies and to place this new cycle better in the context of conventional cycles. To do so a Rocket Cycle Analysis Tool was developed called RoCAT. It models the last-named cycles as well as the open expander cycle for a broad scope of thrusts, burn times, and chamber pressures, and several propellants. In addition, RoCAT optimizes several inputs for each cycles individually for a fairer comparison. Besides analyzing the electric-pump cycle's current performance, this research also estimates its performance in the future based on historic trends in its key technologies like the battery and electric motor.